Targeted Combination Therapy: Discovery and Evaluation of Synergistic Anticancer Effects of Anti-HER2-Duocarmycin Antibody-Drug Conjugates Combined with ATR Inhibitors

TECHNISCHE UNIVERSITÄT DARMSTADT

vom Fachbereich Chemie

der Technischen Universität Darmstadt

zur Erlangung des Grades

Doctor rerum naturalium (Dr. rer. nat.)

Dissertation

Von

Marcel Rieker, M. Sc.

aus Darmstadt

Erstgutachter: Prof. Dr. Harald Kolmar

Zweitgutachter: Prof. Dr. Felix Hausch

Darmstadt 2018

Rieker, Marcel: Targeted Combination Therapy: Discovery and Evaluation of Synergistic Anticancer Effects of Anti-HER2-Duocarmycin Antibody-Drug Conjugates Combined with ATR Inhibitors
Darmstadt, Technische Universität Darmstadt
Jahr der Veröffentlichung der Dissertation auf TUprints: 2020
Tag der Einreichung: 31. August 2018
Tag der mündlichen Prüfung: 15. Oktober 2018
Veröffentlicht nach den Bestimmungen des UrhG

Die vorliegende Arbeit wurde unter der Leitung von Herrn Prof. Dr. Harald Kolmar am Clemens-Schöpf-Institut für Organische Chemie und Biochemie der Technischen Universität Darmstadt sowie bei Merck KGaA in Darmstadt von Oktober 2015 bis Oktober 2018 angefertigt.

Publications or patents derived from the presented work

Parts of this work have been published or are currently under review.

Publications to related projects

Pirzer, T., Becher, K., Rieker, M., Meckel, T., Mootz, H. D., & Kolmar, H. (2018). Generation of potent anti-HER1/2 immunotoxins by protein ligation using split inteins. *ACS Chemical Biology*, *13*(8), 2058–2066.

1. Content

1. Abstract

While the global cancer burden is still high with 10 million people being diagnosed with cancer and 6 million cancer-related deaths yearly, academia and industry are developing more and more sophisticated therapies to combat cancer. One recent development are antibody-drug conjugates (ADCs) which consist of an antibody portion that mediates tumor selectivity and a highly cytotoxic drug designed to efficiently kill cancer cells. The majority of ADCs in clinical trials today carries payloads targeting the cytoskeleton. However, microtubule-targeting agents often lack clinical efficacy and thus, drugs with other mode of actions are in focus of current ADC research. With Mylotarg and Besponsa for example two ADCs carrying DNA damaging agents are already approved and SYD985 an ADC carrying the DNA-alkylating agent duocarmycin is currently showing promising results in a clinical phase III study. Although ADCs have shown promising anticancer effects and often come along with a broadened therapeutic window compared to conventional chemotherapy, there is still room for improvement regarding e.g. saftey aspects. Establishment of combination therapy for ADCs might pose a strategy for increasing efficacy, diminish side-effects and slow down resistance development especially because single agent therapy has seldom been curative. This work aimed at the discovery of a synergistic drug combination that might enhance the efficacy of duocarmycin-based ADCs like the clinically evaluated ADC SYD985. Therefore, 17 DNA-damage response inhibitors (DDRis), potentially involved in the repair of duocarmycin-induced lesions, were selected based on literature and tested in *in vitro* models. HCC-1954 and MDA-MB-468 cancer cells were treated with a combination of the selected DDRis and duocarmycin and the antiproliferative effects of the combination treatment were compared to the effects of the single agents alone. These experiments clearly demonstrated that inhibitors of the kinase ATR, which plays a central role in the response to replication stress, synergistically enhanced the cytotoxic effects of duocarmycin. This observation was additionally confirmed by treatment of ATR Knock-down cells with duocarmycin. Further drug combination experiments revealed the impact of structural features of different duocarmycins and ATR inhibtors on the synergism level. Besides studying the combinatorial effects of the small molecules alone, it was demonstrated that this combination effect could be translated to a targeted therapy approach like antibody-drug conjugates. Several duocarmycin based ADCs showed strong synergistic effects in combination with different ATR inhibitors *in vitro* as well as *in vivo*. rag2 mice bearing a HER2-expressing NCI-N87 tumor were treated with HER2-targeting duocarmycin-ADC and two different ATR inhibitors. The ATR inhibitors monotreatment showed very mild tumor growth inhibition while the treatment with the ADC at concentrations below the maximum effective dose led to a partial tumor response. The combination treatment, however, resulted in very strong anti-tumor effects while being well tolerated. The present study demonstrates the superiority of combining the targeted delivery of duocarmycin to the tumor using an anti-HER2-duocarmycin ADC with systemic application of ATR inhibitors over the treatment with the drugs as single agents. This might support endeavors of evaluating such combinations in a clinical setting.

2. Zusammenfassung

Jährlich werden 10 Millionen neue Fälle von Krebs diagnostiziert und gleichzeitig sterben 6 Million Menschen an der Krankheit. Deshalb werden durch akademische und industrielle Forschung immer ausgeklügeltere Therapien entwickelt um Krebs zu bekämpfen. Eine neue Entwicklung stellen Antikörper-Wirkstoff Konjugate (AWK) dar, die aus einem tumor-selektiven Antikörper und einem hochpotenten Toxin bestehen um zielgerecht und effizient Krebszellen zu töten. Die meisten AWKs in klinischer Erprobung nutzen dabei Wirkstoffe, die das Zellskelett angreifen. Problematisch ist jedoch, dass es diesen Molekülklassen oft an klinischer Wirksamkeit magelt, wodurch neue Wirkmechanismen gesucht werden. Die beiden bereits zugelassenen AWKs Mylotarg und Besponsa zum Beispiel nutzen DNA-schädigende Wirkstoffe und der in Phase III klinischer Erprobung befindliche AWK SYD985 ist der am weitesten fortgeschrittene AWK mit dem DNA-Alkylator Duocarmycin als Wirkstoff. Obwohl AWKs bereits vielversprechende Wirksamkeit gegen Krebs zeigen konnten und auch ein im Vergleich zu konventioneller Chemotherapie großes therapeutisches Fenster besitzen, gibt es dennoch viel Optimierungsbedarf. Die Etablierung einer Kombinationstherapie für AWKs könnte eine Strategie darstellen um die Wirksamkeit zu erhöhen, Nebeneffekte und auch Resistenzbildung zu verlangsamen, besonders da die Monotherapie zur Behandlung von Krebs bisher selten zur Heilung geführt hat. Die vorliegende Arbeit hat es sich deshalb zum Ziel gemacht, einen Kombinationspartner für Duocarmycin-basierte AWKs wie z.B. SYD985 zu finden, der die Wirksamkeit von Duocarmycin-AWKs synergistisch verstärken kann. Deshalb wurden 17 Inhibitoren der DNA-Schadensantwort selektiert und in *in vitro* Modellen getestet, die basierend auf Literaturdaten möglicherweise bei der Reparatur von Duocarmycin-induzierten DNA-Schäden beteiligt sind. HCC-1954 und MDA-MB-468 Krebszellen wurden mit einer Kombination von Inhibitoren der DNA-Schadensantwort und Duocarmycin behandelt und die zytostatischen Effekte der Kombination wurden mit denen der individuellen Wirkstoffe verglichen. Diese Experimente demonstrierten, dass Inhibitoren der ATR Kinase, die eine zentrale Rolle in der Reaktion auf Replikationsstress spielt, die zytotoxischen Effekte von Duocarmycin synergistisch verstärken können. Diese Beobachtung wurde durch das Herunterregulieren von ATR und anschließender Behandlung mit Duocarmycin bestätigt. Weitere Kombinationseffekte offenbarten den Einfluss der Struktur der Duocarmycine sowie der ATR Inhibitoren auf die synergistischen Effekte. Neben den Untersuchungen der Kombinationseffekte der kleinen Moleküle, konnten die Kombinationseffekte auch auf Kombinationen mit Molekülen der gerichteten Therapie übertragen werden wie z.B. AWKs. Dafür wurden mehrere Duocarmycin-AWKs hergestellt, die in Kombination mit ATR Inhibitoren synergistische Kombinationseffekte *in vitro* und *in vivo* zeigten. Rag2 Mäuse, die einen HER2-exprimierenden NCI-N87 Tumor trugen, wurden mit einem gegen HER2-gerichteten duocarmycin-AWK und zwei verschiedenen ATR Inhibitoren behandelt. Während die ATR Inhibitoren nahezu keinen Effekt auf das Tumorwachstum hatten, konnte der AWK unterhalb der maximalen effektiven Dosis bereits teilweise das Tumorwachstum inhibieren. Die Kombinationsbehandlung jedoch reduzierte stark die Tumorgröße und wurde gleichzeitig gut toleriert. Die

vorliegende Arbeit demonstriert die Überlegenheit der Kombination aus zielgerechter Abgabe des Toxins Duocarmycin an den Tumor mittels anti-HER2-Duocarmycin AWK und systemischer Gabe von ATR Inhibitoren gegenüber der Behandlung mit den Molekülen als Monotherapie. Die Ergebnisse könnten Bestrebungen unterstützen, diese Kombination im klinischen Kontext zu untersuchen.

3. Introduction

3.1. Cancer Prevalence

Cell division is a natural process that assures the replacement of old or damaged cells by new ones. If this process is disturbed, cancer may arise. Cancer is an umbrella term for related diseases that are generally characterized by the uncontrolled division of cells. Most cancers form tissue masses, so called tumors which can be classified as malignant or benign. While malignant tumors can invade and spread into nearby tissue, benign tumors cannot.[1] In 2012, the age-standardized global incidence of cancer was 182 per 100 thousand people with a mortality rate of 56%.[2] This adds up to a global cancer burden of 10 million people being diagnosed with cancer and 6 million cancer-related deaths yearly.[2] The reasons for falling ill with cancer are numerous and the cancer risk is influenced by genetic predispositions and additionally by life-style factors.[2] In the United States of America cancer is caused in approximately 60% of cases by preventable life-style risk factors.[3]

For instance, it was shown that the western life is generally accompanied with a higher risk for lung, colorectum, breast and prostate cancer. A typical risk factor is frequent smoking of tobacco. The risk of developing lung cancer for example increases with the amount of tobacco consumption and it is 20 times higher for smokers than for non-smokers. Another life-style risk factor is the diet. While the consumption of red meat correlates with an increased risk for the development of colon cancer, a diet rich in vegetables and fruits decreases the risk. Furthermore, environmental factors play a major role in the prevalence of cancer. Indoor pollution caused by, as already mentioned, smoking but also cooking and building materials like asbestos increase the cancer risk. Additionally, occupational risks like chemicals encountered at work, or outdoor air pollution caused by traffic and industry play a significant role in the development of cancer. Chronic infections with hepatitis B virus, papillomaviruses or *heliobacter pylori* are leading to higher incidence of liver, cervix or stomach cancer, respectively.[4] A summary of the contribution of preventable life-style factors on cancer incidence is given in figure 1.

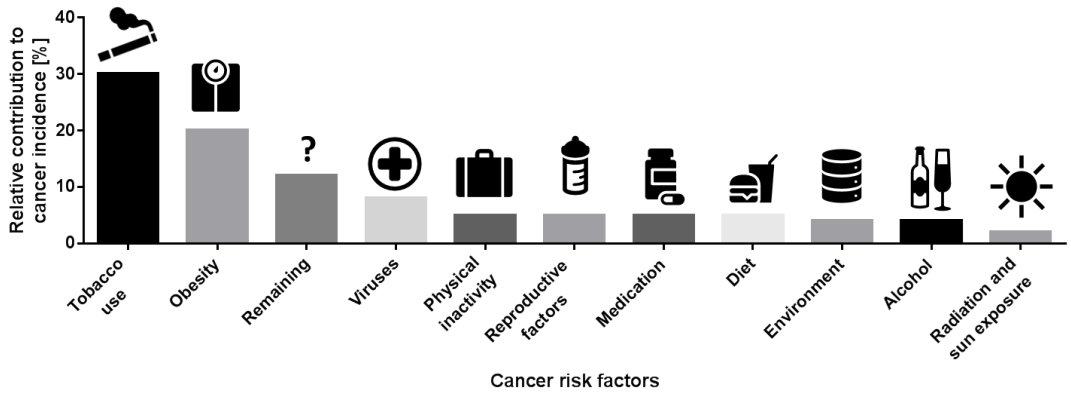

Figure 1: Contribution of live style factors to preventable cancer incidence in the United States of America adapted from Colditz and Wei[3].

An increased cancer risk caused by life-style factors is reflected by an altered physiology on the molecular and cellular level. Given the high incidence and mortality of cancer, extensive research on tumor biology was performed that led to the identification of two major factors that enable tumor growth: genomic instability and tumor-promoting inflammation. Furthermore, tumors exhibit several common characteristics. The following chapter is dedicated to enabling characteristics of tumor growth as well as hallmarks of cancer, because understanding of molecular background of cancer might leverage efforts for the development of a successful anti-cancer therapy.

3.2. Enabling Characteristics of Tumor Development and Hallmarks of Cancer

This chapter shall shed light on the tumorigenesis and the characteristics of cancer. Hanahan and Weinberg postulated two distinct mechnisms – genomic instability and tumor-promoting inflammation – that enable tumor growth in the first place. Although the reasons that lead to genomic instability and tumor-promoting inflammation and subsequently tumor development are numerous as described in the previous chapter, cancer has distinct characteristics in common. Tumor biology research has led to the postulation of eight hallmarks of cancer according to Hanahan and Weinberg: (1) sustained proliferative signaling, (2) deregulated cellular energetics, (3) resistant against cell death, (4) angiogenesis, (5) avoiding immune destruction, (6) replicative immortality, (7) evading growth suppression, (8) invasion and metastasis (Figure 2).[5]

The previously described life-style factors largely influence the development of cancer through genetic alterations, or epigentic factors so called epimutations that regulate gene expression.[5,6] These alterations include mutations like nucleotide changes, chromosomal aberations of structural nature but also the number of chromosomes might be changed leading to loss of heterozygosity and DNA segments be amplified at high frequencies.[6] Genetic predispositions are another aspect that might lead to a cancer vulnerability through genomic instability. However, cells have developed a sophisticated machinery that recognizes DNA damage, directly repairs DNA lesions or inactivates mutagenic molecules before they reach the DNA to prevent mutations. If the repair machinery is impaired in one of these factors, the sensitivity of the cell towards mutagenic molecules but also endogenous stress like replication stress increases.[5] The Li-Fraumeni syndrome for example is characterized by an inactivating germline mutation of either p53 or CHK2 kinase genes. The latter activates p53 in response to DNA-damage. The impaired p53 function leads to escape of cancer cells from apoptosis. The consequense is a high incidence of characteristic tumors such as osteosarcomas, soft tissue sarcomas, leukemias, adrenocortical and breast carcinomas as well as brain tumors. Members of families with Li-Fraumeni syndrome have a 50% cancer risk by the age of 40 and 90% cancer risk by the age of 60.[7]

Mutations might arise that confer evolutionary benefits for the mutated cell leading to dominance in the surrounding tissue. So far, alterations of the genome that might eventually lead to genomic instability have been described.

In addition, the preventable cancer risk factors can trigger the acute activation of immune effector programs[8] leading to "tumor-promoting inflammation".[5] As a result, immune cells invade damaged tissues where a chronic inflammation might arise.[8] In this contex, senescent cells secret inflammatory mediators that should inhibit tumor growth by sustained growth arrest and clearance of senescent cells by the immune cells. In contrast to the intended effect, tumor-supporting inflammatory cells such as macrophages and fibroblasts might be recruited that promote tumor growth[9] by supplying the cancer cells with growth signals, survival factors, matrix-modifying enzmes etc.[10] They also produce reactive oxygen species to kill cancerous cells, which in contrast might damage the DNA of the cancer cell and thus promote mutation of the genome which closes the loop to genomic instability.

The eight hallmarks of cancer will be discussed in detail in the following. Sustained proliferative signaling helps cancer cells to divide uncontrollably. Cancer cells are capable of producing growth-stimulating signals themselves, leading to so called autocrine proliferative stimulation. Besides, surrounding stroma can be stimulated to produce growth stimuli that again lead to the proliferation of the cancer cells. In addition to that, elevated levels of receptors, structural changes of the receptor and mutations of proteins in the downstream signaling have been identified to render the signaling pathway constitutively activated.

Another hallmark of cancer is the evasion of tumor suppression. A prominent example of a tumor suppressor protein is p53, which is mutated in 50% of all human cancers.[7] It is activated in the presence of cellular stress and can stop cell-cycle progression in order to gain time for stress reduction. However, if alarm signals indicate overwhelming or unrepairable damage, the cell might undergo p53-induced cell death by apoptosis. The inactivation of tumor suppressor proteins leads to cell proliferation because the cell lacks growth limiting mechanisms. Cancer cells are able to shutdown apoptosis inducing signaling pathways that enable again the evasion of cell death by the tumor. This is another hallmark of cancer which has been associated with the inactivation of tumor suppressors.[5]

Normal cells can undergo only a limited number of replicative cycles. This limitation is associated with two barriers of replication: senescence and crisis. Sencesence is characterized by the cell being vital but not dividing anymore. If a cell enters the crisis state, this will lead to cell death.[5] Cancer cells on the other hand are immortal which allows the infinite division of the cells. The telomeres, protection caps on the ends of chromosomes, have been identified as crucial for immortalization. If absent, chromosomal DNA might be end-to-end fused followed by bridge-breakage fusion cycles leading to abberant chromosomal structures that threaten cell viability. As a consequence, a cell with critically short telomerase will stop cell division, known as replicative senescence.[11] Hence, the telomeres determine how many cell divisions a cell can run through. While in normal cells telomerase, an enzyme necessary for telomere elongation, is nearly absent, in cancer cells telomerase is expressed at physiologically significant levels[12] and active in 90% of all human cancers[11]. Telomerase expression and activity is one factor that mediates tumor cell immortality and thus is another hallmark of cancer.[11]

In addition, tumor cells have increased throughput of nutrients and oxygen and hence increased need for evacuation of metabolic waste and carbon dioxide. This is accomplished by the ability of tumor cells to stimulate angiogenesis, yet another hallmark of cancer. Through this process new vessels are formed that ensure supply of the tumor with nutrients and oxygen and facilitate waste management.

The ability of cancer cells to invade surrounding tissues and to colonize distant sites of the body has also been described as a hallmark of cancer. This multistep process of invasion and metastasis was termed the invasion-metastasis cascade. First, the cancer cells invade local surrounding tissues and reach the lymphatic and blood vessel system through which they can travel. When a cancer cell manages to escape the vessel, it might invade the tissue at distant sites of the primary lesion.The great majority of cancer-associated deaths – around 90% - can be attributed to the metastasis of the primary tumor rather than the primary tumor itself.[13]

A growing body of evidence suggests, that the defects of the immune system and a switch in metabolism of cancer cells are drivers for tumor development. The cells in our bodies are constantly monitored by the immune system. The vast majority of abberant cells that might eventually become cancerous is eliminated through the aid of the immune cells. However, cancer cells manage to circumvent detection by the immune system which eventually leads to the development of tumors. Tumor cells often express the protein programmed cell death ligand 1 (PD-L1) which binds programmed cell death 1 (PD-1) expressed on the surface of cytotoxic T-cells. Through binding of PD-L1 to the immune inhibitory PD-1 the T-cells are not activated leading to the evastion of cancer cells from cytotoxic activities by immune cells.[14]

Furthermore, it was found that cancer cells especially in regions deeply buried in the tumor mass suffer from oxygen shortage which leads to switching their metabolism. In normal cells under aerobic conditions glycolysis is followed by the transport of pyruvate to the oxygen-consuming mitochondria. Cancer cells often lack sufficient supply with oxygen due to the distance of the cancer cells from blood vessels.[15] Thus, glucose is metabolised using glycolysis and subsequently pyruvate is converted to lactate. Cancer cells often upregulate glucose transporters to increase glucose intake. Although less energy is produced using this pathway, the intermediates can be fed into pathways required for the production of nucleotides and amino acids which are necessary for growth.[5]

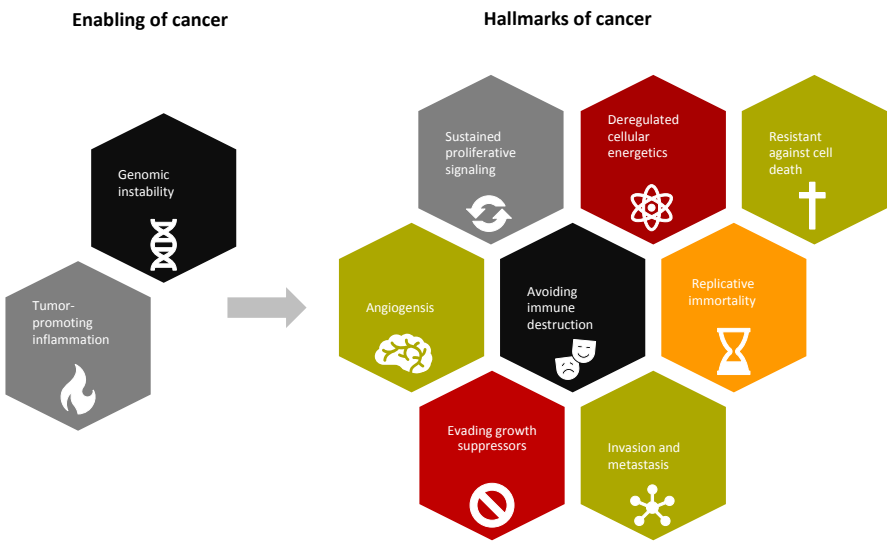

Figure 2: Hallmarks of cancer. Genomic instability and tumor-promoting inflammation enable the development of cancer. Cancer itself is characterized by several hallmarks. While most hallmarks are well-established, the concept of deregulated cellular energy metabolism and the avoidance of destruction by the immune system are emerging concepts supported by a growing body of evidence. Figure adapted according to Hanahan and Weinberg.[5]

The high incidence of cancer and the high mortality rate motivated scientists and companies to develop therapies with the hope to cure cancer patients. Due to extensive research, an increasing knowledge of cancer biology led to more and more sophisticated therapy options and simultaneously to decreasing mortality rates. A historical overview of cancer therapy development will be given in the following chapter.

3.3. Short History of Cancer Therapy

Before 1950 cancer therapy mainly relied on the surgical removal of tumors, until the invention of the linear accelerator added radiotherapy to the portfolio of the oncologist in the 1960s.[16] Although, surgery is still a common strategy to remove the primary tumor and thereby reduce the number of cancer cells and thus diversity it is only infrequently used for the removal of metastases.[13] The reason is that surgery and radiotherapy cannot eradicate metastases,[16] because of the multiple sites of secondary tumors. An effective anti-cancer treatment has alsoways to reach every organ in the body. Thus, small molecule drugs, biological molecules and immunotherapies have become the focus of todays cancer research. During world war I autopsy findings from soldiers dying of exposure to sulphur mustard gas revealed profound lymphoid hypoplasia and myelosuppression. This led Gilman and Goodman to the assumption that another mustard gas, nitrogen mustard, might be suitable to treat lymphatic tumors. After initial mice experiments, the first patient with non-Hodgkin lymphoma (NHL) was treated with the nitrogen mustard in 1942, resulting in a tumor remission. Although the remission only lasted a few weeks before disease progression set in again, these findings demonstrated that tumors might be treated with drugs systemically. Another milestone toward modern chemotherapy was the introduction of combination therapy in 1965. The POMP regimen, a drug cocktail

consisting of methotrexate, vincristine, 6-MP and prednisone could sucessfully induce long-term remission in children with acute lymphoblastic leukaemia (ALL). The growing knowledge of tumor biology led to the establishment of targeted chemotherapy. New targets arose including growth factors, signalling molecules, cell cycle proteins, modulators of apoptosis and molecules promoting apoptosis.[16] Imatinib was one of the landmarks of the targeted revolution. The molecule was a moderately potent inhibitor targeting the protein BCR-ABL. This protein is a fusion protein of a chromosomal translocation of the two genes which was associated with the pathogenesis of chronic myleoid leukaemia (CML). It was shown by Druker, that the imatinib treatment of patients with chronic-phase CML led to complete hematological remission in 90% of all cases.[16]

Beside small molecules, therapeutic antibodies have also been developed for cancer treatment. After initial trials in the 1980 with murine antibodies against carcinoembryonic antigen (CEA) and CD3, two tumor-associated antigens, therapeutic antibodies gained more and more interest. These drugs can selectively bind to antigens presented on the surface of tumor cells and either inhibit intracellular signaling or recruit immune cells to mediate cancer cell killing.[17] Another concept arose that combined the cytotoxicity of chemotherapy drugs with the selectivity of the therapeutic antibodies. These so called antibody-drug conjugates became a relevant cancer treatment option with the first FDA-approval of the ADC Adcetris in the year 2011.[18] A graphical overview of the developments that led to modern chemotherapy is given in figure 3.

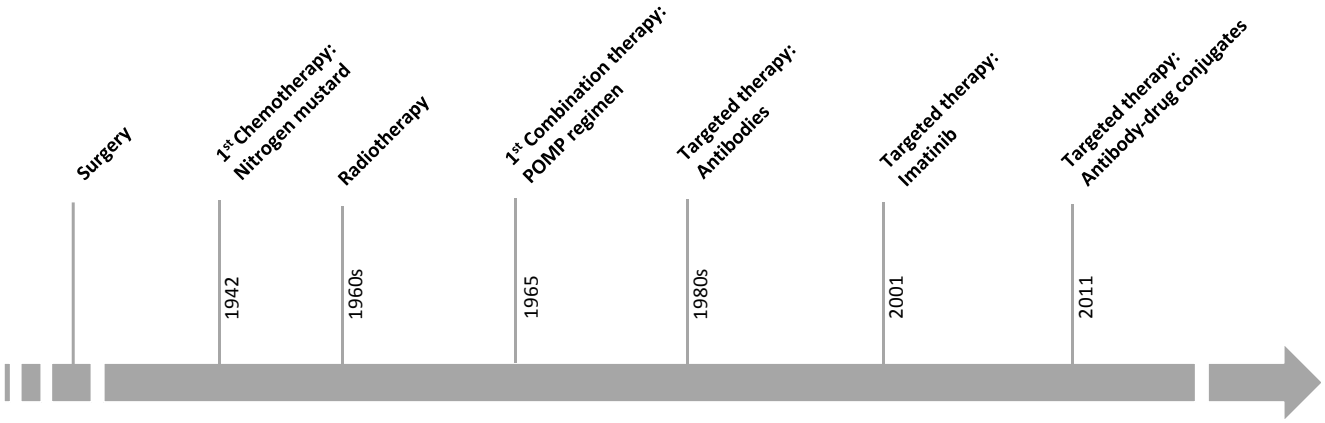

Figure 3: Historical overview of ground-breaking developments in cancer therapy.

Although in the last decades a marked decrease in cancer-associated death rate was observed due to improved therapy and earlier detection, the numbers of total deaths caused by cancer remain high[2] leaving room for improvement. Drug combination therapy has the potential to increase the efficacy of the therapy and slowed down development of resistance.[19] Furthermore, drug combinations might decrease side-effects[19] as do targeted approaches like tumor-specific drug delivery using ADCs.[20] Due to the potential advantages of drug combinations and ADCs for cancer therapy the following chapters will deal with these therapy options.

3.4. Cancer Therapy - Drug Combinations

Conventional chemotherapeutics distribute unspecifically in the body upon administration often leading to severe side-effects like toxicities in healthy tissues, e.g. the bone marrow and gastrointestinal tract. As a result, many anticancer drugs suffer from a narrow therapeutic window. Drug resistance also often occurs when patients are treated with single agents.[21] Combination chemotherapy adresses these issues and is associated with several advantages over conventional single agent chemotherapy: (1) Administration of drugs with non-overlapping toxicites allows the treatment at their individual maxiumum-tolerated dose (MTD), leading to an increased efficacy.[21] (2) The doses of the individual drugs might be reduced in combination while the therapeutic effect can be maintained.[19] (3) combination therapy is associated with a slowed down development of resistance, because cancerous tissue has to become resistant against two drugs simultaneously.[19] (4) Drug combinations tend to have an improved selectivity towards the diseased tissue.[22] Given these advantages, combination therapy promises a surivival benefit of patients treated with a drug combination rather than with single-agents.[23]

Drug combinations can have either additive, antagonistic or synergistic effects. In case of additivity, the effect of a drug combination is exactly the summed up effects of the single agents when given alone. Antagonistic effects are observed when one drug weakens the effects of the other drug. Synergism on the other hand is observed when the effects of the combination exceed the totalled effects of the single agents.[24] Drug combinations are especially powerful for drugs that act synergistically, because therapeutic effects are maximized while adverse events are minimized.[25]

For the identification of synergistic drug combinations several reference models have been developed from which three models are currently widely used: Loewe additivity,[22,26,27] highest single agent (HSA)[28] and Bliss independence[29] model. These models make different assumptions to quantify combination effects.

The Loewe additivity model is based on the sham control experiment, where a drug is combined with itself which by definition can only lead to additive effects.[26] A further development of Loewe additivity is the generalized combination index (CI) theorem, which was derived from Loewe additivity by Chou and Talalay.[19] Mathemathically the CI can be expressed as in eq. 1.[19,25]

$$CI = \frac{D_A}{(D_x)_A} + \frac{D_B}{(D_x)_B} \qquad \text{Eq. 1}$$

The CI can be calculated according to eq. 1 by inserting the dose of drug A (D_A) and drug B (D_B) to achieve a certain effect level when applied in combination as well as the doses of drug A ($(D_x)_A$) and drug B ($(D_x)_B$) when given alone to achieve the very same effect. The doses of the drugs in combination (D_A and D_B) are known from the experimental design and the doses of the single agents to obtain the same effect can be calculated from the dose-response curve. A CI of 1 stands for additivity, while CI<1 implicates synergy and CI>1 antagonism.[19] This

further development of the Loewe additivity model is one of the most widely applied methods to quantify drug synergy with more than 7000 citations.[25]

The HSA model assumes that in case of an additive combination, the effects of the combination equals to the effect of the more active compound, whereas for a synergistic combination the effect is higher than the effect of the more active single agent. One major drawback of this model is that even the combination of a drug with itself can produce an additional effect,[24] because it assumes linear dose-response curves of the individual drugs which are commonly shaped logistically or curvilinearly.[30] Furthermore, synergy is often only observed when one of the compounds is inactive at any concentration,[30] which is only true for a limited subset of drugs.

The Bliss independence model assumes that two drugs exert an effect on their target independently of one another.[31] The drugs both contribute to the overall effect, however, they must not interfere with each other.[30] The mechanistic assumption that the drugs act independently was critisized, because drug combinations often contain compounds with multiple and not fully known modes of action,[30] so acting independently might not be true for a large number of drug combinations.[25] And again, the Bliss independence model fails the sham control experiment,[25] meaning that a combination of a drug with itself might be considered synergistic.

To leverage the great potential of possible drug combinations, sophisticated screening methods have been developed to uncover potential synergistic effects of certain drug combinations (Figure 4). A simple assay set-up is the curve-shift assay. In a first step, a serial dilution of two drugs is studied on cells individually. Then the two drugs can be combined by two different strategies. One drug might be added to a serial dilution of the respective second drug. This might lead to a potentiation, measured as a lowered IC_{50}-value compared to the potency of the single agent. Another strategy is to treat cells with a serial dilution of both drugs simultaneously at a fixed-ratio. Again, combination effects are determined by comparing the potency of the combination treatment with the potency of the individual drugs.

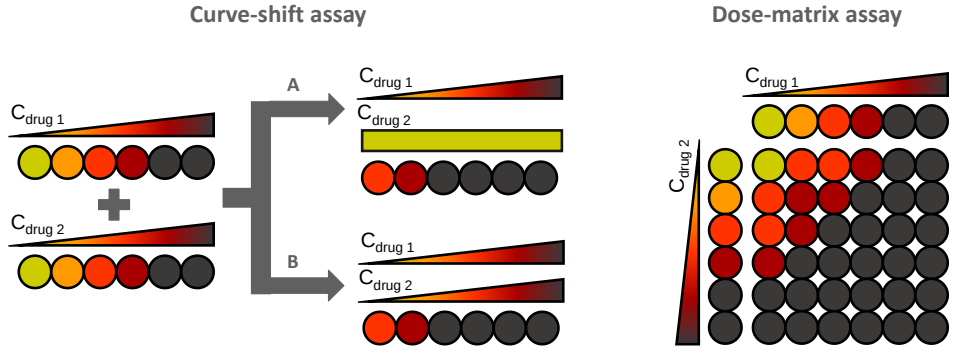

Figure 4: Methods to assess synergistic effects of drug combinations. Curve-shift assays: The dose-response of the individual drugs is assessed separatedly. The combination can be studied by adding a constant concentration of one drug to a serial dilution of the other drug (A) or by adding a serial dilution of both drugs simultaneously to cells at a fixed-ratio (B). Dose-matrix assays: the two drugs are added to cells as serial dilution either alone or in combination resulting in a full matrix of doses where every dose of drug 1 is combined with each dose of drug 2. This figure was adapted according to Ka *et al.*[26]

Some short-comings are associated with this methodology because drugs have different effects on each cell line. An optimal experimental design requires studying the drug combinations at several effect levels and various ratios, since combination effects might depend on the molar ratio between two drugs. Therefore, dose-matrix assays deliver a more complete picture of the combination effects. In a dose-matrix experiment, the two drugs are tested individually by treating cells with a serial dilution of them and at the same time the cells are treated with a mixture of the serial dilutions. As a consequence, every serial dilution of one drug is mixed with varying constant concentrations of the respective second drug and the drugs are tested at several fixed-ratios at once.[26] While the evaluation of curve-shift assays can be accomplished by fitting the individual dose-response curves using e.g. GraphPad Prism, the evalution of dose-matrix assays might become more challenging. The software GeneData Screener might be used for studying dose-matrix assay results.[26] This software uses a scoring function to discriminate between additive, antagonistic and synergistic drug combinations based on e.g. the LOEWE model.

As already mentioned, besides drug combinations, also targeted approaches for anti-cancer treatment might improve efficacy and reduce undesired side-effects. Therefore, the following chapter introduces the concept of antibody-drug conjugates and gives a rough overview of production techniques, molecular build-up and optimization parameters of this drug class.

3.5. Cancer Therapy - Antibody-Drug Conjugates

The term antibody-drug conjugate describes monoclonal antibodies (mAbs) that act as carriers of cytotoxic drugs. The concept behind ADCs is a “biotherapeutic bullet” that specifically targets and kills tumor cells without damaging healthy tissues.[32]

The underlying idea of ADCs dates back to the 1960’s. However, beginning with the approval by the US Food and Drug Administration (FDA) of brentuximab vedotin (Adcetris, Seattle Genetics) in 2011 and trastuzumab emtansine (T-DM1, Kadcyla, Roche) in 2013, ADCs have gained more and more interest in academia and industry. In the year 2017, nearly 100 ADCs were in preclinical or clinical development and with gemtuzumab ozogamicin (Mylotarg, Pfizer) as well inotuzumab ozogamicin (Besponsa, Pfizer) additional ADC approvals followed.[18,33]

The underlying structure of an ADC is the mAb, which is in most of the cases an immunoglobulin G (IgG) molecule. The mAb consists of two identical 50 kDa heavy chains (HCs) and two 25 kDa light chains (LCs) that are connected to each other *via* disulfide bonds. The HCs encompass three constant domains (C_H1-3) and a variable domain (V_H). Similarly, the LCs comprise of a constant domain (C_L) and a variable domain (C_V). Every mAb has a region named “Fragment antigen binding” (Fab) that is formed by the LC and the C_H1 and V_H regions of the heavy chain. This Fab fragment is responsible for the antigen binding. Another important part of a mAb,

the “Fragment crystalline” (Fc), consists of the C_H2 and C_H3 of the HCs. This portion of the antibody mediates effector functions through binding to effector cells of the immune system.[34]

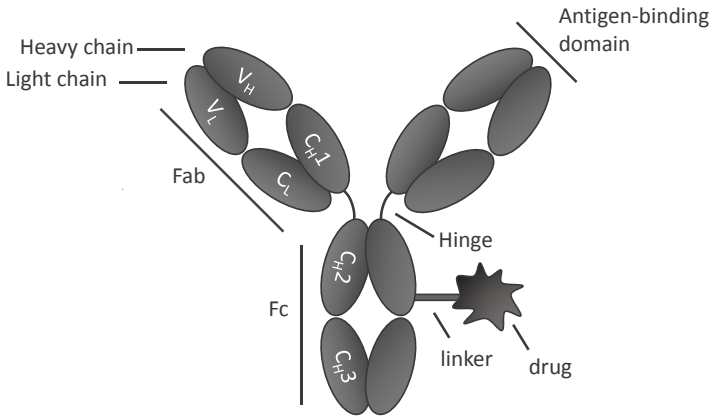

Figure 5: Representation of an antibody-drug conjugate. The molecule consists of a monoclonal antibody and a cytotoxic drug that is attached to the antibody *via* a linker. The antibody is build-up of two identical heavy and light chains. C_H2 and C_H3 of the heavy chains form the “Fragment crystalline” (Fc) and the variable domains of the heavy and light chains (V_H and V_L) together with C_L and C_H1 form the “fragment antigen binding” (Fab) unit. The antigen binding is mediated *via* the variable domains of heavy and light chain.

An ADC can be generated by connecting a cytotoxic drug to an antibody *via* a linker (Figure 5). Target selection for a therapeutic approach using ADCs is crucial. Antigens are selected that are presented on the surface of tumor cells but not or only sparsely on healthy cells.[18] This mediates preferential binding to tumor tissues. Commonly ADCs are chosen that efficiently internalize into the cells. To induce cell death, the cytotoxic drug of the ADC needs to be delivered into the tumor cell. The underlying mode of action of an ADC is depicted in figure 6. Upon binding of the ADC to an antigen, which is often a cell-surface receptor presented on the tumor cell (1), the ADC is internalized into the endosome (2). The endosome can mature to a lysosome (3). Proteolytic restriction and an acidic pH degrade the antibody or cleave the linker. This sets free the cytotoxic drug, which is typically a microtubule inhibitor or DNA-damager. After release of the drug into the cytoplasm, it can enter the nucleus and induce DNA damage (4) or bind and disrupt microtubules (5), which finally leads to cell death.[35] Antibody recycling is a mechanism by which the ADC is trafficked from the endosome back to the cell surface and released again (6), mediating increased half-life.[36]

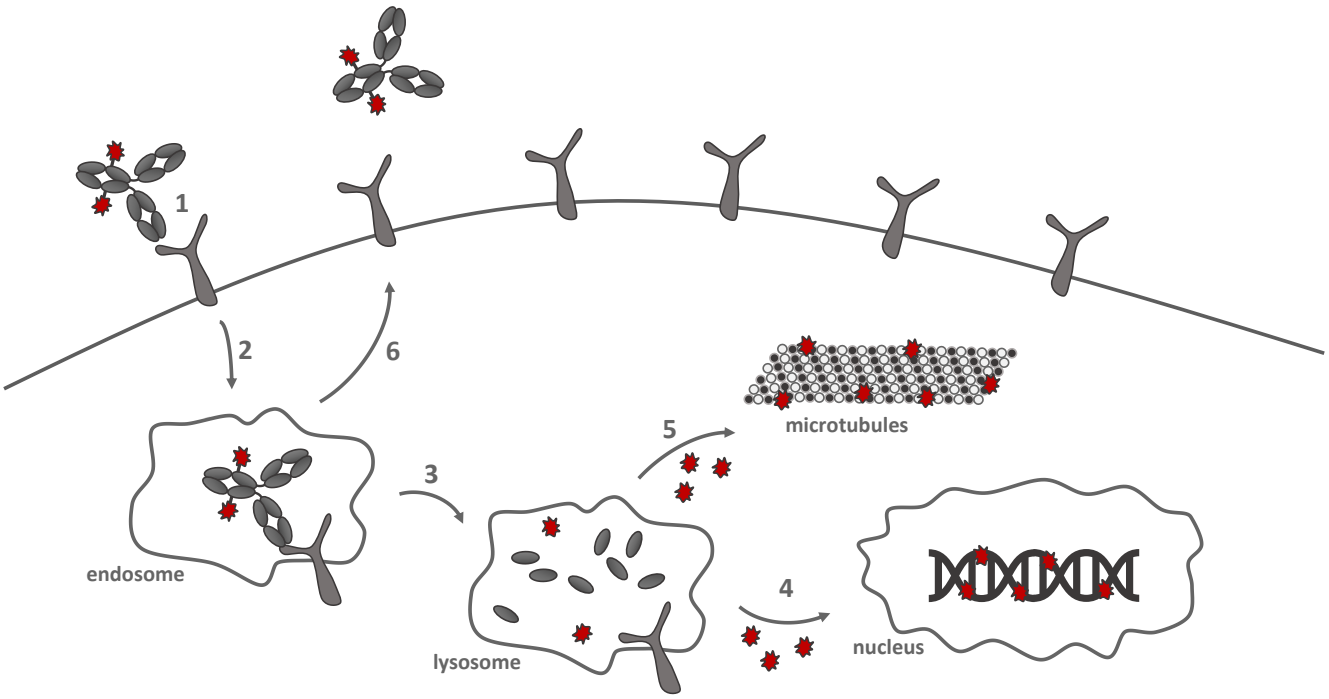

Figure 6: Scheme of internalization route of an ADC. The figure is adapted according to Kitson *et al.*[35] (1) binding of the mAb to a tumor-specific cell-surface antigen. (2) internalization of the ADC into the endosome. (3) maturation of the endosome to the lysosome, where the ADC is degraded and/or the linker is cleaved. The cytotoxic drug is released into the cytoplasm. The drug can diffuse into the nucleus where it induces DNA damage (4) or disrupts microtubules (5). The ADC can be trafficked from the endosome back to the cell surface, where the ADC is released into the circulation again.

Several criteria need to be met by the drugs. The drugs commonly need to be highly potent with potencies in the subnano- to picomolar range, because only a limited amount of ADC finally reaches the tumor site.[37] Furthermore, the drug should have a "chemical handle" that allows modification with the linker. The cytotoxic drugs are often hydrophobic, which limits their application, due to decreased solubility of the conjugate and a tendency to aggregate. In addition to that, a common resistance mechanism to ADCs is the upregulation of efflux pumps. Therefore, the ideal cytotoxic drug is hydrophilic but still efficiently transits into the cytosol, is no efflux pump substrate, chemically modifyable and highly potent.[18,38]

ADCs currently in preclinical or clinical development use cytotoxic drugs mainly based on microtubule inhibitors. 71% of all drugs are auristatins, maytansinoids or advanced tubulin inhibitors and the remaining ADCs mainly carry drugs that induce DNA damage (Figure 7). Auristatins like monomethyl auristatin E (MMAE, **1**) can be found in the clinically approved ADC Adcetris and Maytansinoids are represented in the form of DM1 (**2**) by the marketed ADC Kadcyla. Another microtubule inhibitor used in clinical development is tubulysin (**3**).[18] Although microtubule inhibitors are very widely used in clinical ADC development, robust activity of microtubule inhibitors has only been observed in ALL, Hodgkin's disease and NHL. In other solid cancer indications such as breast or lung cancer, microtubule inhibition has only yielded modest response rates and they are considered inactive in most other solid tumors.[39]

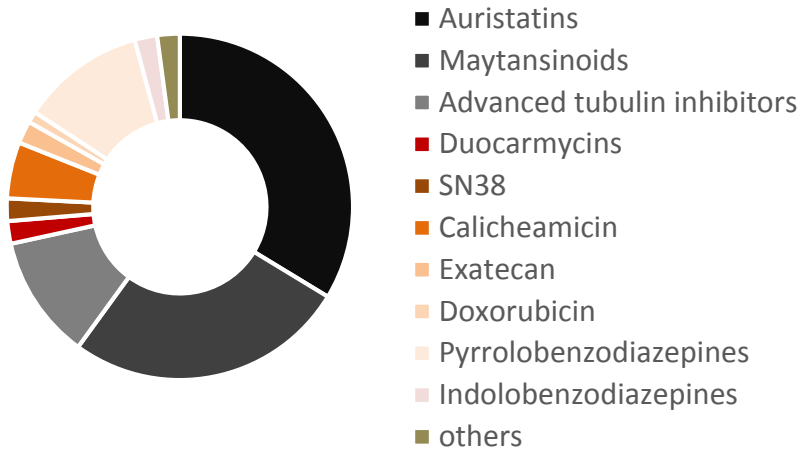

Figure 7: Distribution of drugs used for ADCs in preclinical or clinical development. Microtubule inhibitors like auristatins, maytansinoids or advanced tubulin inhibitors account for the majority of linker-drugs (LDs). The remaining ADCs comprise mostly DNA-damagers.

Given the limited amount of cancer indications in which microtubule inhibiting agents have shown robust activity, other mode of actions need to be exploited. Thus, DNA damagers gain increasing interest. The re-approved ADC gemtuzumab ozogamicin uses the double-strand break inducer calicheamicin (**4**) as cytotoxic drug.[18] Another double-strand inducing agent developed in the ADC context is doxorubicin (**5**), which is already widely applied in anti-tumor therapy as single agent.[18,40] Anthracycline-based molecules like doxorubcin induce double-strand breaks through intercalating properties, but also through inhibition of topoisomerase I and II (TOP1 and TOP2).[40] Topoisomerases are important enzymes involved in decreasing topological stress on DNA during replication. TOP1 creates a single-strand and TOP2 a double-strand break, which is religated once the DNA is relaxed. Upon inhibition of these enzymes, single-strand or double-strand breaks are induced, respectively.[40] Inhibition of topoisomerase I and II finally leads to apoptosis.[41] Exatecan (**6**) and SN-38 (**7**) are two TOP1 inhibitors that are currently used as drugs for ADC development. Finally, alkylating agents are applied as drugs in the ADC field.[18] Bifunctional alkylators like pyrrolobenzodiazepine dimers (PBD dimer, **8**) can alkylate both DNA strands, yielding either intra- or interstrand crosslinks. Monofunctional drugs such as indolinobenzodiazepines (IBD, **9**) or minor-groove binders from the duocarmycin family like *seco*-DUBA (**10**) alkylate one DNA strand.

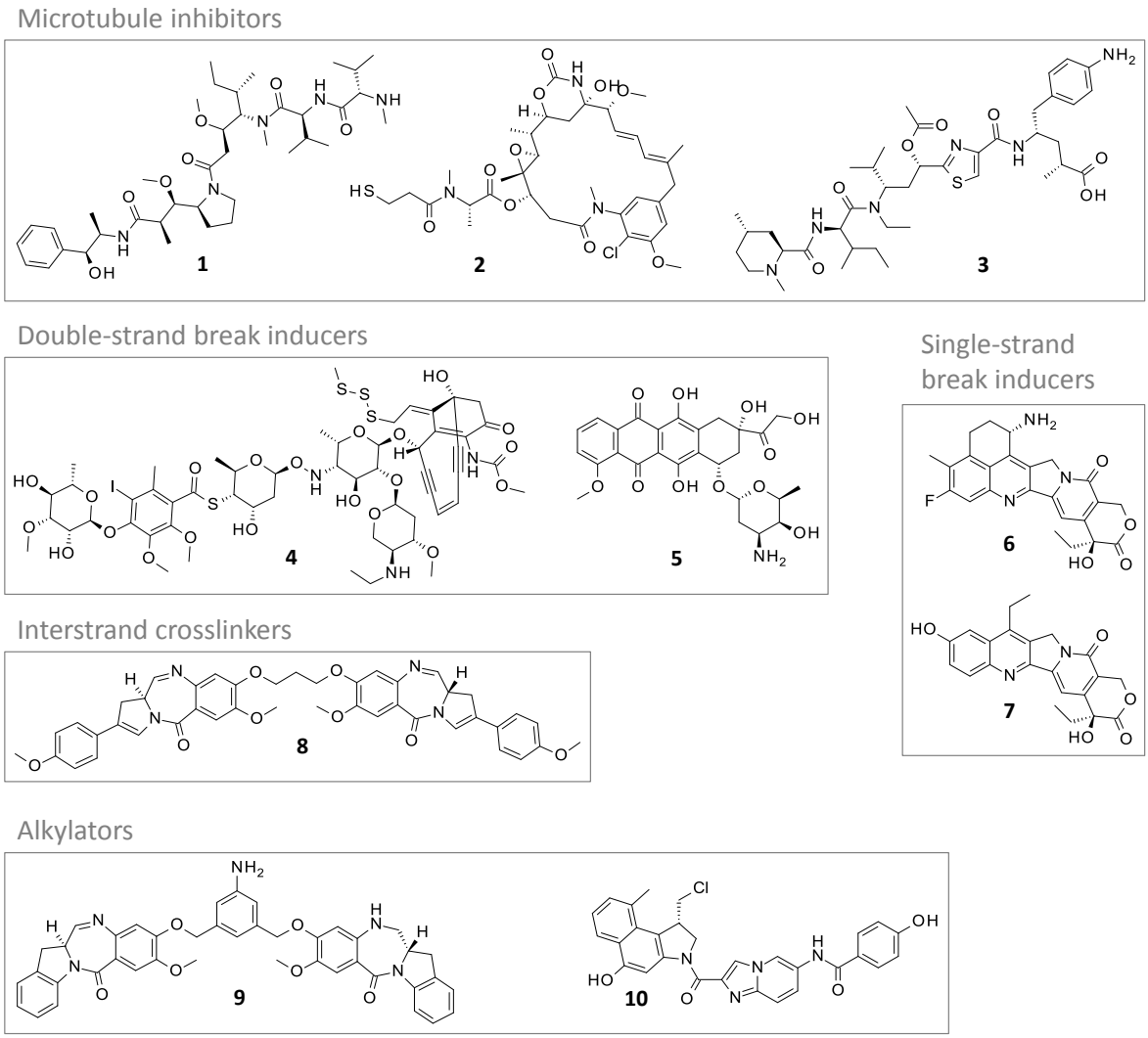

Figure 8: Chemical structures of ADC drugs currently in clinical development. Mono-methylauristatin E (**1**), the maytansinoid DM1 (**2**) and tubulysin (**3**) belong to the microtubule inhibiting agents. The remaining agents cause DNA damage. Double-strand breaks are induced by calicheamcin (**4**) and doxorubicin (**5**) and single-strand breaks by exatecan (**6**) and SN-38 (**7**). Monofunctional alkylators such as indolinobenzodiazepines (9) or minor-groove binders like DUBA (**10**) form a covalent DNA-adduct on one strand. Bifunctional alkylators like the pyrrolobenzodiazepines (8) on the other hand can form intra- or interstrand crosslinks.

Another crucial optimization parameter of an ADC is the linker, because it influences the physicochemical properties of the ADC. The linker determines the stability of the ADC in circulation and on-target. Generally, the linker should be stable in the circulation to ensure that the ADC can accumulate at the tumor site. Premature drug-release can lead to off-target cytotoxicity, which influences the selectivity. However, once the tumor is reached and the ADC is internalized, efficient drug release is important to induce cell death in the target cells. Several linker-chemistries are used in the ADC field that can be classified as non-cleavable linkers and cleavable linkers.[42]

Non-cleavable linkers have a greater stability compared to their cleavable counterparts, which is also reflected as a higher plasma stability. Associated with this are reduced off-target toxicities which might translate into a greater therapeutic window. However, ADCs with non-cleavable linkers rely strongly on efficient internalization

to set free the active drug, because full degradation of the ADC is crucial.[42] One example of an ADC using a non-cleavable linker is the approved ADC Kadcyla. The succinimidyl 4-(*N*-maleimidomethyl)cyclohexane-1-carboxylate (SMCC) portion has two functions; first, to attach DM1 via its free thiol group to the linker and second, to conjugate the linker to the mAb (Figure 9).[43] While some cytotoxic drugs tolerate substitution, like DM1, other drugs are only active in an unsubstituted state like for instance MMAE.[42,44] These drugs require cleavable linkers that tracelessly release the drug upon internalization.[42]

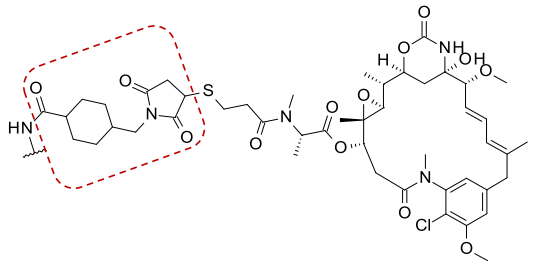

Figure 9: Structure of a non-cleavable linker attached to DM1. The thiol of DM1 is used to form a thioether bond with the SMCC moiety (red). This part cannot be cleaved and remains attached to the drug. The markush indicates the attachment point at the mAb. Figure adapted according to Lu *et al.*[42]

Cleavable linkers often use enzymatic degradation for drug release. Cathepsin B is an ubiquitous cysteine protease, which is usually found intracellularly in the lysosome. Cathepsin B can be found extracellularly only in diseased tissues such as metastatic tumors or rheumatoid arthritis. The intracellular localization of the enzyme should mediate a certain stability against premature cleavage.[45] In addition to that, Cathepsin B was found to be overexpressed in various cancer indications such as adenocarcinomas of the oesophagus and gastic cardia.[46] The approved ADC Adcetris is a conjugate of the mAb brentuximab and the cytotoxic drug MMAE. The linker-drug consists of the dipeptide valine-citrulline, which is recognized and cleaved by Cathepsin B but also other proteases from the cathepsin-family can process the valine-citrulline motif.[47] *para*-aminobenzyl alcohol (PAB) is introduced between the drug and the dipeptide, as a self-immolative module. The PAB module decays upon protease restriction.[48] This ensures that MMAE is set free, without any residual modifications (Figure 10). Besides the dipeptide valine-citrulline, several other dipeptide sequences like phenylalanine-citrulline or alanine-lysine for Cathepsin B-mediated cleavage[45] or alanine-alanine-asparagine for cleavage by the protease legumain[49] have been evaluated for the use as a linker for ADCs. These sequences have different cleavage rate properties[45,50] and open-up opportunities for ADC optimization.

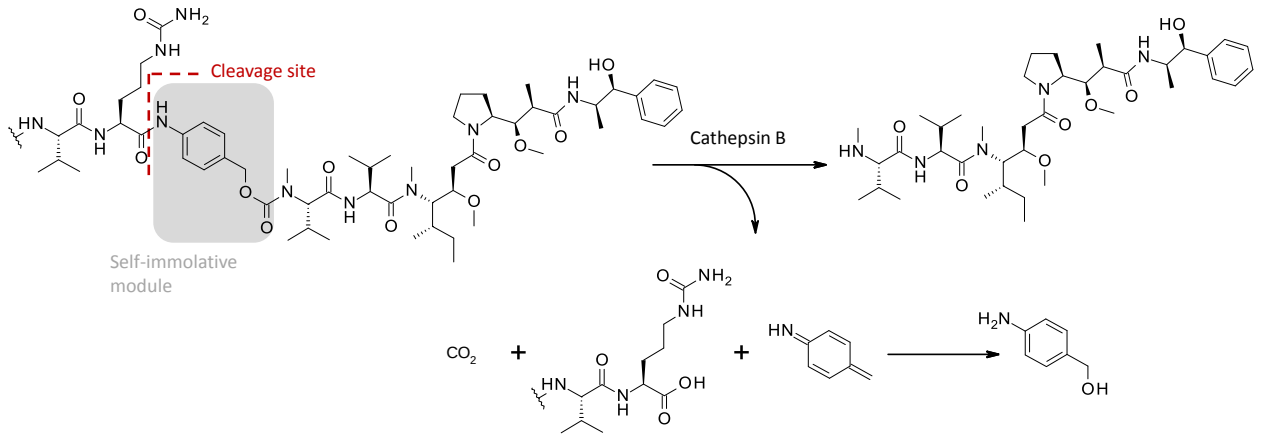

Figure 10: Chemical structure of cleavable dipeptide linker. *N*-terminally of the linker-drug, an attachment site for the linker to the mAb is indicated as markush. It is followed by the dipeptide valine-citrulline, which can be cleaved by the protease Cathepsin B. The self-immolative module decays after cleavage, whereby MMAE is set free.

Besides Cathepsin B-cleavable linkers, there are other enzymatically cleavable linkers as depicted in figure 11. The glucuronide is selectively cleaved by β-glucuronidase. Comparable to the Cathepsin B-cleavable linkers, a self-immolative module is introduced, so that the cleavage occurs tracelessly[51,52] Finally, a minor-groove binder is released. The linker mediated high solubility, which reduced the levels of aggregates. Glucuronide linkers can be considered as an alternative to e.g. dipeptide linkers, because they enable the usage of more hydrophobic drugs.[53]

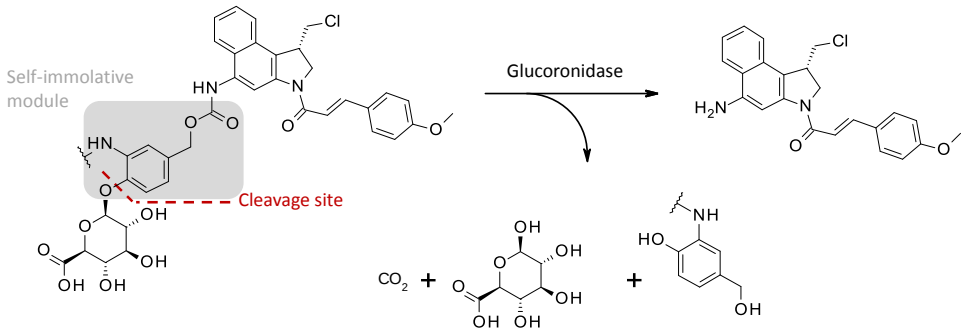

Figure 11: Chemical structures of glucoronide-cleavable linker. The markush indicates the attachment point of the linker to the mAb. The sugar glucuronide is cleaved by β-glucoronidase, which leads to the decay of the self-immolative module. The minor-groove binder is released as free drug and is able to alkylate DNA.

The FDA approved ADCs gemtuzumab-ozagamicin and inotuzumab-ozagamicin are generated using acid-labile hydrazone linkers to connect mAb and the drug calicheamicin (Figure 12).[54] These linkers are designed to be stable in circulation. Internalization of the ADC leads to localization in the lysosome, where the ADC experiences an acidic pH. Consequently, the hydrazone linker hydrolyzes and the drug is released.[55] However, hydrazone linkers have been associated with unspecific drug release.[18]

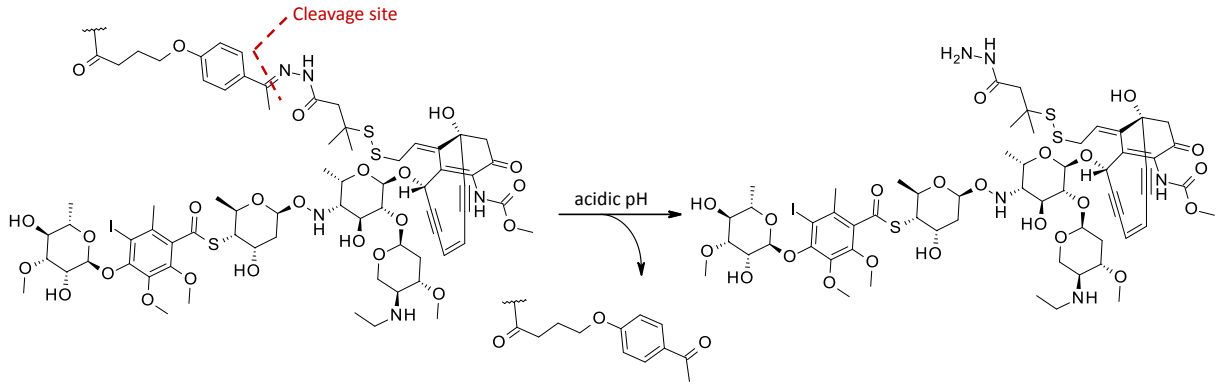

Figure 12: Chemical structure of hydrazone-linked calicheamicin and the product of hydrolysis. The acid-sensitive hydrazone in the linker-calicheamicin is cleaved in the acidic microenvironment of the tumor or the acidic pH of the lysosome. Thereby the carbonyl-function of calicheamicin is regenerated and the free drug is obtained. Figure was adapted according to Beck *et al.*[18]

Another class of ADC linkers uses cleavable disulfide linkage.[18] Due to differences in the reduction potential of plasma and the intracellular compartment, disulfide linkers are only susceptible to cleavage inside the cell. Furthermore, reduced glutathione levels are up to 1000-fold higher in cancerous cells compared to healthy cells.[42]

The cleavage mechanism of disulfide linked drugs is rather complicated, as illustrated by the example of ADC SG3231 in figure 13. Upon internalization of the ADC into the lysosome, the ADC gets proteolytically restricted. This yields an intermediate with a residual cysteine. Then, the drug can enter the cytosol, where reductive conditions lead to the cleavage of the disulfide. A free thiol is generated that mediates a cyclization step, which finally regenerates the free PBD dimer.[56]

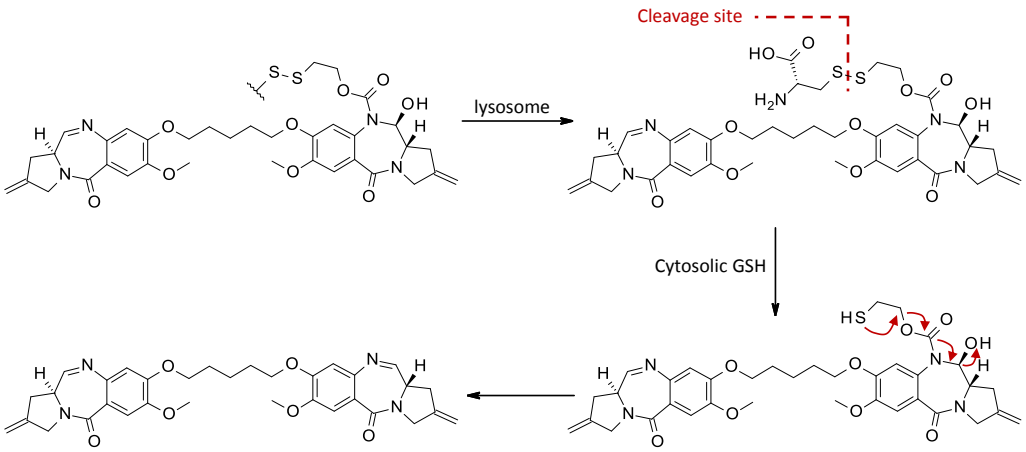

Figure 13: Schematic representation of the decay of disulfide linkers to yield an active PBD dimer. The markush indicates the connection to the mAb. Upon internalization into the lysosome, the mAb is degraded. This leaves the drug with a residual cysteine moiety. The cysteine-modified drug can diffuse into the cytosol, where glutathion mediates the cleavage of the disulfide. A free thiol is generated, which cyclizes and regenerates the active PBD dimer. Figure is adapted according to Pillow *et al.*[56]

All in all, the overall success of an ADC is highly dependent on all three modules of an ADC: the antibody, the linker and the cytotoxic drug. In addition to that, the conjugation technique majorly impacts efficacy,

pharmacokinetics and tolerability.[57] One conjugation method comprises the coupling of the linker-drug to surface lysines of the mAb. A common IgG molecule has about 80 lysines from which around 20 are solvent accessible. As a result, lysine conjugation can lead to an ADC not only varying in the site of drug attachment, the drug-distribution, but also in the drug-to-antibody ratio (DAR), namely the number of drugs attached to the mAb. The generation of Kadcyla for example is realized by coupling the cytotoxic moiety DM1 to lysines on the surface of the mAb, yielding an ADC with an average DAR of 3.5.[44]

Another strategy for ADC generation is the controlled reduction of disulfide bonds and subequent coupling of a maleiimde-containing linker-drug to the reduced interchain cysteines. Such an approach was followed in the production process of Adcetris.[57] In this case 4 interchain cysteines are adressible which again leads to a heterogenous ADC mixture in terms of DAR and drug distribution.[44]

This heterogeneous mixture contains several DAR species that are difficult to purify and characterize.[44] Furthermore, ADC species with high DARs are cleared faster and are prone to aggregate.[58] The ADC species with a low DAR on the other side have a reduced efficacy due to the smaller amount of drug delivered to the tumor cell.[59] Much effort was put into the development of site-specific conjugation techniques to overcome the difficulties asscociated with heterogenous ADCs. By genetic incorporation of cysteines at defined positions, more homogeneous ADCs can be generated as decribed for the THIOMAB approach by Genentech.[60] These molecules have improved PK, similar efficacy and an increased therapeutic index compared to conventionally produced ADCs.[57] Another approach to increase homogeneity of the ADCs is the incorporation of unnatural amino acids which can be adressed orthogonally to the naturally occuring amino acids. Such an ADC displays high efficacy paired with improved PK compared to conventionally generated ADCs.[61] However, the production of such an ADC is complicated.[57] Besides the incorporation of cysteines or unnatural amino acids, enzymatic conjugation strategies can be followed. The enzyme transglutaminase facilitates the formation of an amide bond between a glutamine side chain and small molecules containing a primary amine. Transglutaminase can be used for the conjugation of linker-drugs to Q295, a glutamine in direct proximity of the N-glycan site N297.[62] However, this requires the removal of the glycan structure prior to conjugation by deglycosylation to increase steric accessibility. Another strategy is the incorporation of a LLQG motif into the antibody sequence or the *C*-terminal fusion of the sequence to heavy and light chains.[63] Again, site-specific conjugation yielded ADCs with higher tolerability compared to ADCs with drugs coupled to the interchain cysteines.[64] In addition to transglutaminase, the enzyme sortase A can be used for the conjugation of ADCs.[65–67] Sortase A recognizes the *C*-terminal sequence LPXTG and cleaves the bond between threonine and glycine. Thereby a thioacyl-intermediate is formed, that acceptes *N*-terminal oligo-glycine residues as nucleophile. A new peptide bond is formed between the theonine and the oligo-glycine substrate.[64] An overview of the conjugation strategies commonly applied for the generation of ADCs is provided in figure 14.

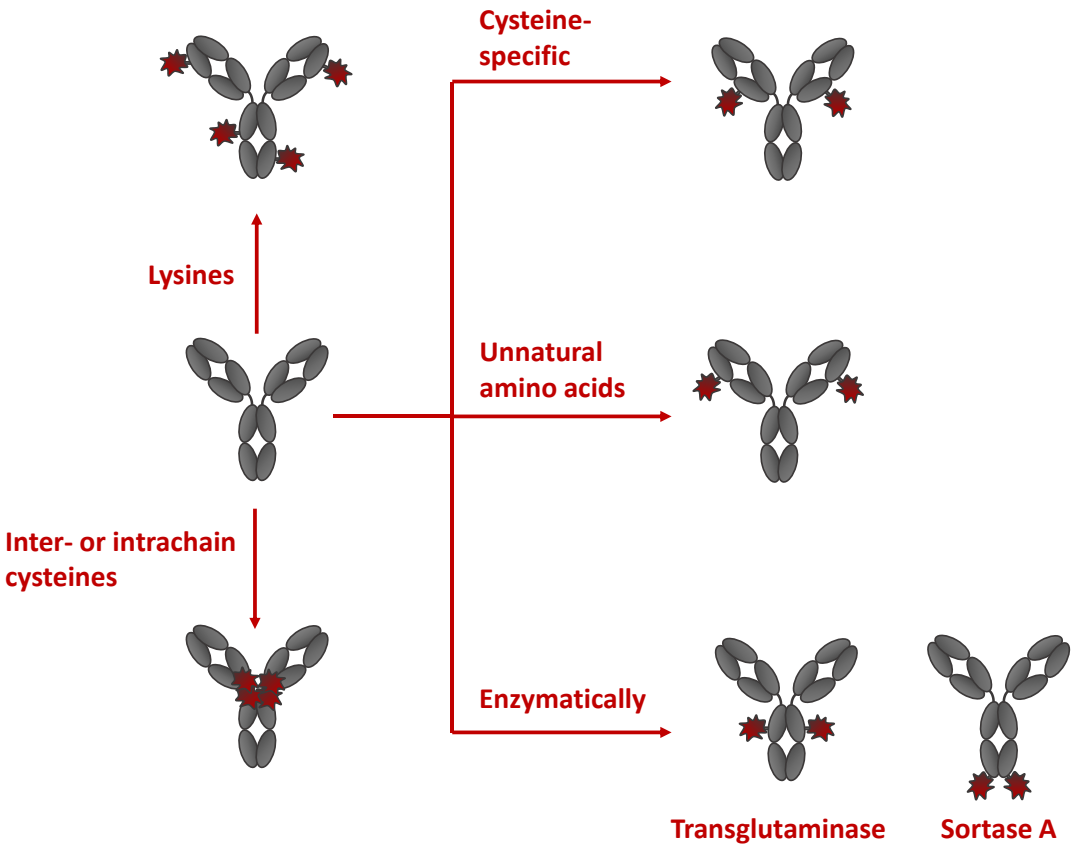

Figure 14: Overview of conjugation techniques for the generation of ADCs. Using chemical methods, lysines or upon reduction inter- and intrachain cysteines can be adressed. By genetically introducing a cysteine or unnatural amino acids, these residues can be used for conjugation. Besides, enzymatic approaches can be applied that use specific recognition sequences for the enzyme. Figure was adapted from Perez *et al.*[57]

Tolcher states in a review that microtubule inhibitors often lack clinical efficacy and that the exploitation of mode of actions other than microtubule inhibition is mandatory to expand the armamentarium of the oncologist.[39] This might not only lead to higher success rates in clinical development of ADCs but also to improved outcomes for anti-cancer treatment of patients. Hence, in this work DNA-damaging ADCs will be studied with a special focus on duocarmycin-bearing ADCs which will be discussed in the following chapters.

3.5.1. Therapeutic Development of Duocarmycin

Duocarmycins are a class of natural compounds originally isolated from *Streptomyces*. These highly potent molecules have a common molecular build-up, consisting of a DNA-alkylating unit and a DNA-binding unit as illustrated by the duocarmycin derivative DUBA (**11**) (Figure 15 A).[68] After binding the minor groove of AT-rich regions of the DNA double strand, an addition of N^3 of adenine to the activated cyclopropane ring of DUBA occurs (Figure 15 B), leading to the alkylation of the DNA (**12**).[69] Although duocarmycins comprise the reactive cyclopropane ring, they are considerably stable in aqueous media. However, duocarmycins exhibit remarkable alkylation efficiencies and rates In the presence of DNA. Complexes of Duocarmycin SA (DSA, **13**) and DNA were studied using nuclear magnetic resonance (NMR) spectroscopy to elucidate this phenomenon.[70] The two subunits of duocarmycins are coplanar in the absence of a ligand. Upon binding in the minor groove of DNA, hydrophobic contacts are maximized, leading to a conformational change of DSA. The two subunits are twisted with respect to each other, activating the molecule for alkylation (Figure 15 C, **14**).[69]

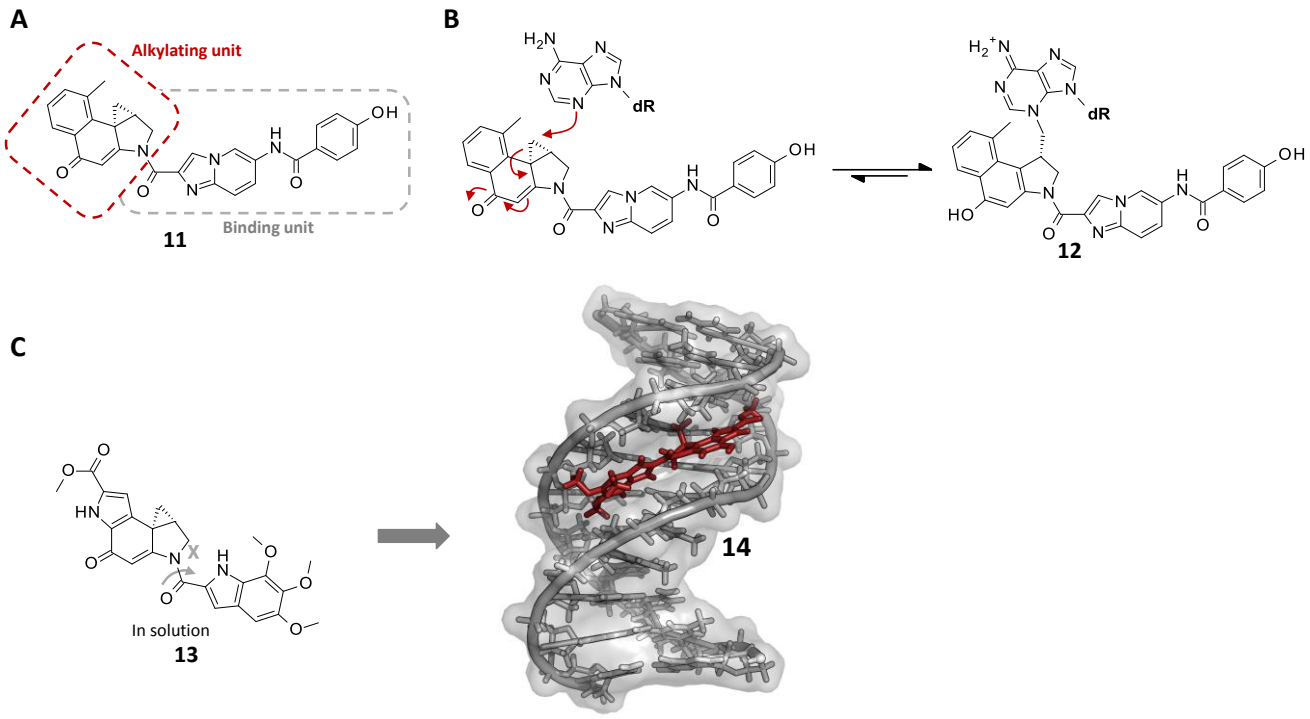

Figure 15: Structural representation of duocarmycin and its alkylation reaction. A) Duocarmycin derivative DUBA depicted with marked alkylation unit (red) and binding unit (gray). B) Scheme of alkylation reaction. N^3 of adenine attacks the least substituted carbon atom of the cyclopropyl ring, which leads to the covalent addition of DUBA to adenine. C) Duocarmycin SA activation for alkylation. DSA is coplanar in solution and therefore considerably stable in solution. Upon binding of the DNA double helix, DSA maximizes hydrophobic interactions with the DNA. As a result, the subunits experience a twist with regard to each other along the X bond which activates the cyclopropyl-ring for alkylation. 3D structure: 1dsa (PDB).

The high cytotoxicity of duocarmycins awoke interest for the application as potential anticancer agents.[71] As a result, extensive research was done to elucidate the structure-activity relationship of the duocarmycin family.[72]

CC-1065 (**15**) was the first compound of the duocarmycin family studied for clinical application (Figure 16 A). Although the drug prolonged the life span of tumor-bearing mice, it was not curative. Furthermore, delayed hepatotoxicity was observed in mice and rabbits at therapeutic doses. As a consequence, efforts were put into the modulation of the alkylating properties to maintain efficacy while avoiding toxicities.[73] One possibility to modulate the alkylation rate is to use a prodrug approach. The duocarmycin derivative carzelesin (**16**) requires a two-step activation to set the active drug free (Figure 16 B). First the phenylurethane promoiety is cleaved either chemically or enzymatically, leading to the formation of the *seco*-prodrug **17** with the chloromethyl-residue. Next, the molecule undergoes an intramolecular Winstein spirocyclization, which leads to the formation of the active drug **18**. Carzelesin was less active *in vitro* than CC-1065 but proved to be more efficacious against several human and murine tumour xenografts.[74]

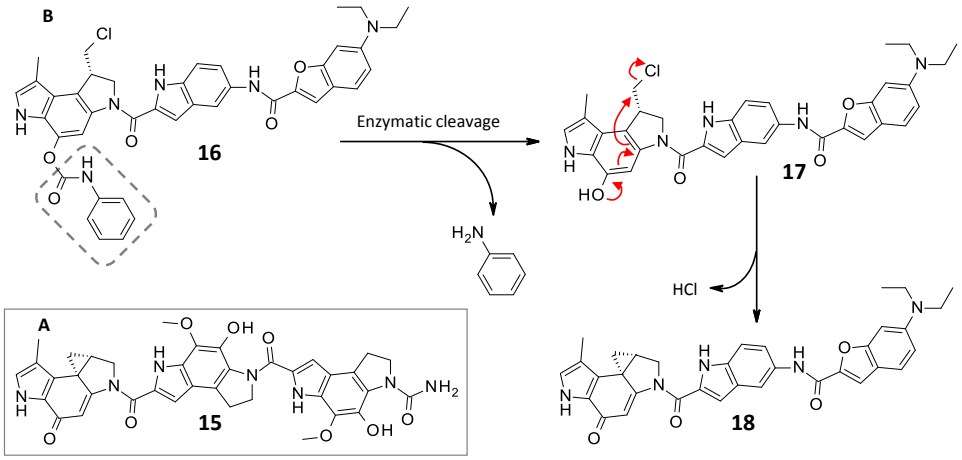

Figure 16: Chemical structures of clinically developed duocarmycin-derivatives. A) Anti-cancer drug CC-1065 B) Activation route of carzelesin (**16**). The promoeity (grey box) of carzelesin is removed chemically or enzymatically. Then an intramolecular spirocyclization step of the *seco*-derivative **17** leads to the formation of the active drug **18**.

Despite promising preclinical data, carzelesin demonstrated no activity in various solid tumors and non-hodghkin lymphoma in a phase II clinical study conducted by the EORTC, while myelotoxicity was found to be the major adverse event.[75] Again, no therapeutic window could be established and no clinical development is ongoing.

Another technology to increase the therapeutic window is the antibody-drug conjugate format. Much effort was put into the development of duocarmycin-based ADCs (Table 1).[53,76–83] A variety of duocarmycin-derivatives was successfully conjugated to antibodies directed against CD19, CD22, CD30, CD56, CD70, CanAg, GD3, human epidermal growth factor receptor 2 (HER2), LeY, LY6E.

Table 1: Overview of duocarmycin-based ADCs reported in literature. ADC identifyer, corresponding target are listed, as well as conjugation technique used for conjugation. The cleavage mechanism is noted and the duocarmycin-derivative studied. The linker is usually attached either to the phenol group of the duocarmycin alkylation unit or to a terminal group on the binding unit. Cytotoxicity is scored as an approximation, beginning with IC_{50}<1x10^{-9} M (+) to IC_{50}<1x10^{-12} M (+++). If *in vivo* experiments were conducted, it is marked by "+", otherwise "N.A.". Abbreviations: minor-groove binder (MGB), binding unit (BU), alkylating unit (AU), not available (N.A.) for data.

ADC	Target	Conju-gation	Cleavage mechanism	Drug	Linker attachment	Cytotoxicity/ selectivity	*In vivo*	Remarks	Source
	CanAg, CD19	Lysine	thioether or disulfide	DC1 (**19**), DC4 (**20**), DC44 (**21**)	BU	+++/+	+	highly hydrophobic LD, modified by phosphate on phenol	[76]
	CanAg	Lysine	thioether or disulfide	DC1 (**19**)	BU	+/+	N.A.	highly hydrophobic LD	[77]
	GD3	Lysine	Ala-Val	DU-257 (**22**)	BU	+/+	N.A.	Linker attached to binding unit	[78]
	CD30, CD70	Thiols	β-Glucuronide	MGB (**23**)	AU	++/+	N.A.	Sugar-cleavable linker studied due to supposedly higher hydrophilicity	[53]
	CD22, LY6E	Thiols	Val-Cit	CBI-TMI (**24**), DSA (**13**)	AU	+/+	N.A.	Ether bond to connect linker and drug	[79]
	CD19	Thiols	Dilsulfide	DC1 (**19**)	BU	+++/+	N.A.		[80]
	CD56	Thiols	Val-Cit	*seco*-DUBA (**25**)		+++/+	+		[81]
	CD30, CD70, LeY	Thiols	Val-Cit or Val-Lys	MGB (**23**), CBI-TMI derivative (**26**)	AU	++/+	N.A.	Extensive research on decreasing the hydrophobicity	[84]
SYD985	HER2	Thiols	Val-Cit	*seco*-DUBA (**10**)	AU	+++/+	+	Clinically developed ADC by Synthon	[82]
BMS-936561	CD70	Thiols	Val-Cit	Duocarmycin-derivative (**27**)	BU	N.A.		Evaluated in phase I clinical trials, development haulted	[18]
MGC-018	B7-H3	Thiols	Val-Cit	*seco*-DUBA (**10**)	AU	N.A.	+	Mice xenograft, well-tolerated in cynomolgus monkeys	[85]

The listed studies used conjugation techniques addressing the cysteines and lysines of the mAb. The linkers encompass non-cleavable, or reductively cleavable disulfides, β-glucoronide cleavable linkers and cathepsin B-cleavable dipeptide linkers with the motifs alanine-valine, valine-citrulline or valine-lysine.

The duocarmycins were connected to the linkers, following two strategies. First, the linker was attached to the alkylating unit *via* a phenolic alcohol or anilinic amine (Figure 17, duocarmycins **10**, **13**, **23**, **24** and **26**). The advantage of this approach was that the drugs were kept in their inactive *seco*-form. Only upon linker cleavage the drug underwent spirocyclization leading to the activation of the duocarmycin. However, the use of stable non-cleavable linkers was only possible with the second approach, where the linker was attached to the binding unit of the duocarmycins (Figure 17, duocarmycins **19**, **20**, **21**, **22** and **27**). Here, already cyclized duocarmycins were often used as exemplified by duocarmycin **22** (Figure 17). This had the disadvantage that the drug was prone to nucleophilic attack at the cyclopropane ring, potentially leading to the inactivation of the drug. Promoieties were attached to the phenolic hydroxyl group of the alkylating unit to avoid premature inactivation of the drug (Figure 17, duocarmycins **20**, **21**, and **27**).

In summary, the ADCs were efficacious *in vitro* against and selective towards antigen-positive cells regardless of antibody, conjugation technique, linker, cleavage mechanism and duocarmycin-variant.

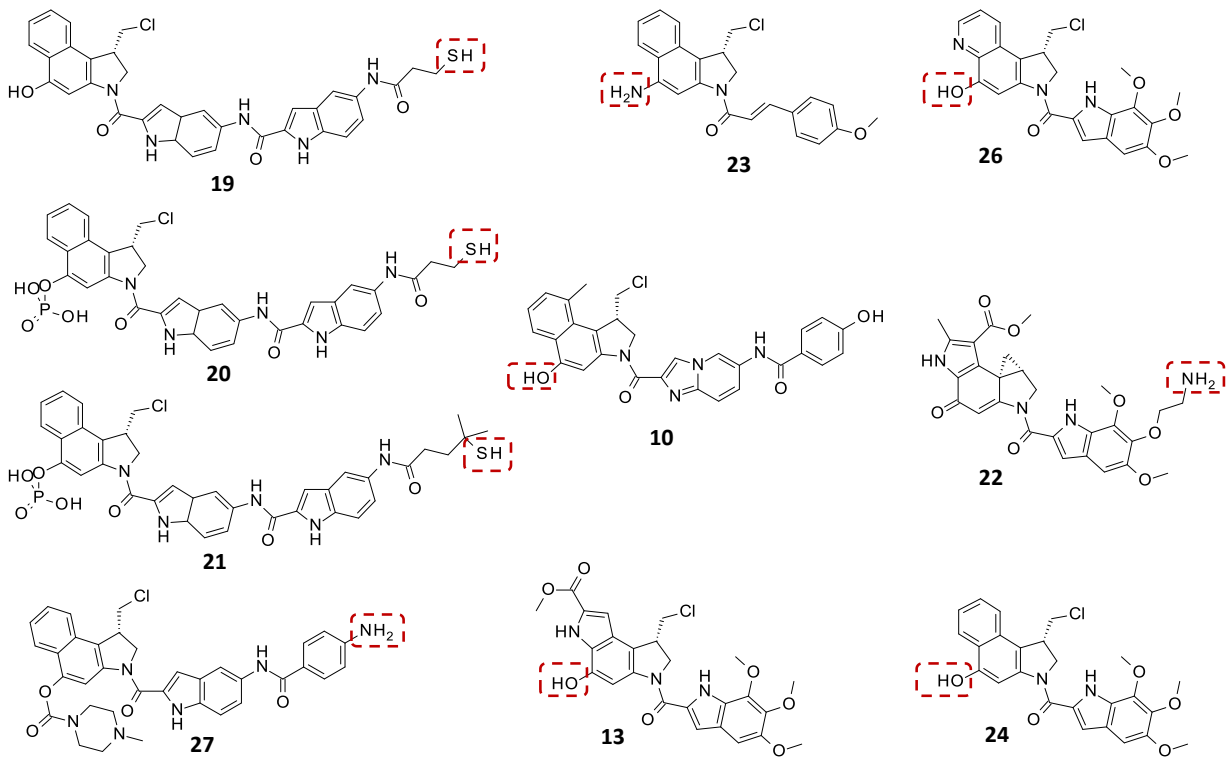

Figure 17: Chemical structures of duocarmycin derivatives applied in the ADC format. The structures of DC1 (**19**), DC4 (**20**), DC44 (**21**), DU-257 (**22**), a minor groove binder (**23**), *seco*-DUBA (**10**), DSA (**13**), CBI-TMI (**24**) and a derivative of this molecule (**26**) are depicted. Red boxes indicate the attachment point of the linker.

A duocarmycin-based ADC currently in clinical development by the dutch pharmaceutical company Synthon is SYD985 (**28**) (Figure 18). This ADC consists of the duocarmycin prodrug *seco*-DUBA (**10**) which is connected *via* a cathepsin B-cleavable dipeptide linker to the anti-HER2 antibody trastuzumab. Upon cleavage of the dipeptide linker the self immolative module decays and the prodrug *seco*-DUBA (**10**) is liberated which spiro-cyclizes to form the active drug DUBA (**11**). The ADC is generated by coupling the maleimide moiety of the linker to the interchain cysteines of the antibody. This results in a rather heterogeneous mixture of ADC species differing in the attachment site as well as in the DAR. In an additional purification step using hydrophobic interaction chromatography the final product SYD985 can be obtained with a DAR of 2.8 consisting mainly of the DAR=2 and DAR=4 species.[82] SYD985 demonstrated superior activity compared to Kadcyla in HER2 over- and low-expressing breast cancers as well as ovarian and uterine carcinosarcoma with HER2/Neu expression.[86,87] In a phase I dose-escalation trial no dose-limiting toxicities and no grade 3 or 4 adverse events were observed, indicating good tolerability.[88] In the expanded study grade 3/4 adverse drug reactions were observed such as neutropenia and conjunctivitis.[89] Nevertheless, SYD985 had a manageable safety profile[89] and as a consequence SYD985 was advanced to clinical phase III trials for metastatic breast cancer in 2017.[90]

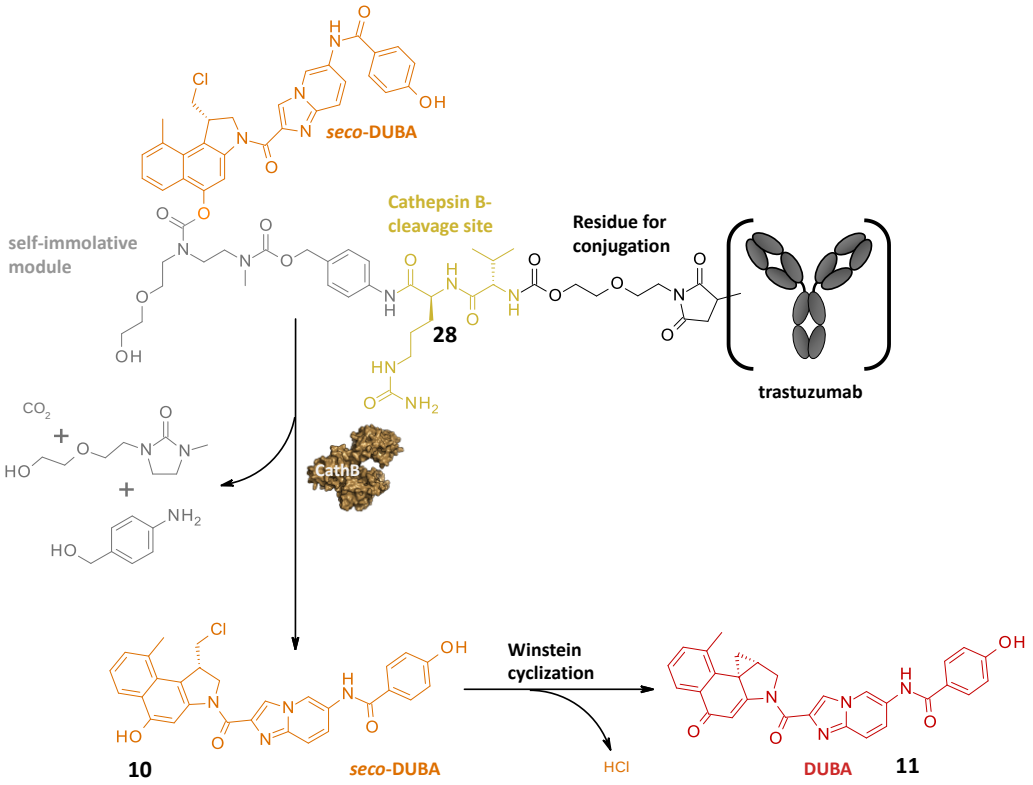

Figure 18: Schematic representation of SYD985 and the mechanism of drug liberation. The ADC **28** consists of the anti-HER2 antibody trastuzumab and a linker-drug. The linker-drug is conjugated to the mAb by addressing the interchain cysteines. Upon *C*-terminal cleavage of the dipeptide valine-citrulline motif (gold), the self-immolative module (gray) decays. This ensures the traceless liberation of the prodrug *seco*-DUBA (**10**, orange). The active species **11** (red) is formed through an intramolecular cyclization step.

As pointed out in the previous chapters, DNA damage can cause severe damage to a cell causing either cell death, senescence or mutations in the genome that might lead to cancer development. Due to the detrimental effects of DNA damage on cell fate, a sophisticated response has evolved to cope with DNA insults. Hence, cells respond to duocarmycin-alkyation lesions with a complex system of DNA-repair, cell cycle regulation, damage tolerance or even apoptosis summarized as DNA-damage response. Due to its complexity, several chapters will be dedicated to the DDR to shed light on the sophisticated mechanisms that have evolved to deal with DNA-damage.

3.6. DNA Damage and Replication Response

Every cell is constantly challenged by thousands of DNA damage events every day. Ultraviolet light, environmental factors like cigarette smoke, industrial chemicals but also the DNA-damaging drugs mentioned in chapter 3.5 cause DNA lesions.[91] Cell division largely relies on the accurate duplication of the genome of a cell and the segregation of the genomic information to the daughter cells.[92] The DNA lesions however can lead to abberations of the DNA like mutations and genome rearrangements, which might have devastating effects on cell fate.[91] In order to deal with the DNA damage the cells have evolved a sophisticated DNA-damage response machinery (Figure 19) that comprises the ability to detect DNA lesions which is followed by a cellular signaling cascade that promotes DNA repair.[93] Cell cycle arrest might be induced which also regulates DNA replication.[94] This is escpecially important, because many DNA lesions become detrimental when the cell replicates its genome.[93] In addition to repair, DNA damage might be also tolerated in order to complete DNA synthesis. If DNA damage is not repaired orderly, the cell will undergo apoptosis or become senescent.[95] The DNA damage response is particularly important since persistant DNA damage might lead to genomic instability which has been described as one of the fundamental reasons for the development of cancer.[96]

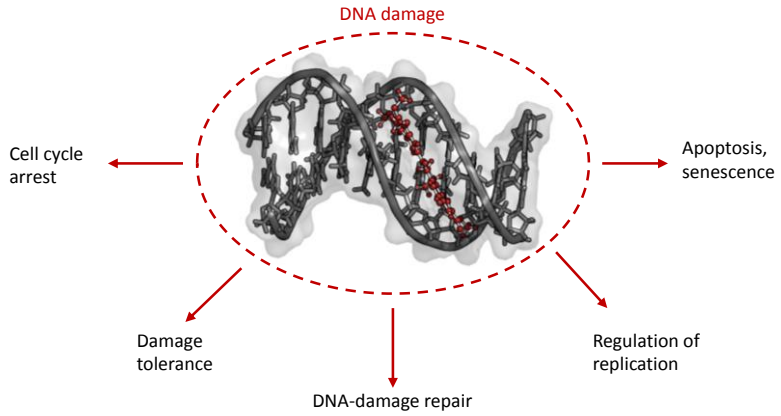

Figure 19: Cellular response to DNA damage. In order to manage DNA damage independently of the form of the lesion, cells have different options. Cells regulate cell cycle to gain time for DNA-damage repair. Cell cycle arrest is also interconnected with the regulation of the replication. If DNA lesions cannot be repaired, the damage might be tolerated to make sure the whole genome is duplicated. If the damage cannot be tolerated, apoptosis or senescence are the consequence.

The cell undergoes a full cell cycle with every cell division. Gap or Growth Phase I (G1) is followed by S phase in which the genome is duplicated. Another growth phase (G2) preceedes cell division in mitosis phase (M). Several checkpoints are present to prevent DNA damage to be taken into the next phase. The G1/S checkpoint makes sure DNA damage is repaired or removed before the genome is replicated in S phase. During S phase the intra-S checkpoint might be triggered to delay replication. This provides additional time for the cell to repair DNA lesions and to ensure the genome is fully replicated. G2/M is the last opportunity to prevent that damage is

taken into cell division. In this critical step underreplicated DNA or DNA-double strand breaks lead to mitotic catastrophe and finally cell death. The cell cycle and cell cycle checkpoints are depicted in figure 20.[95]

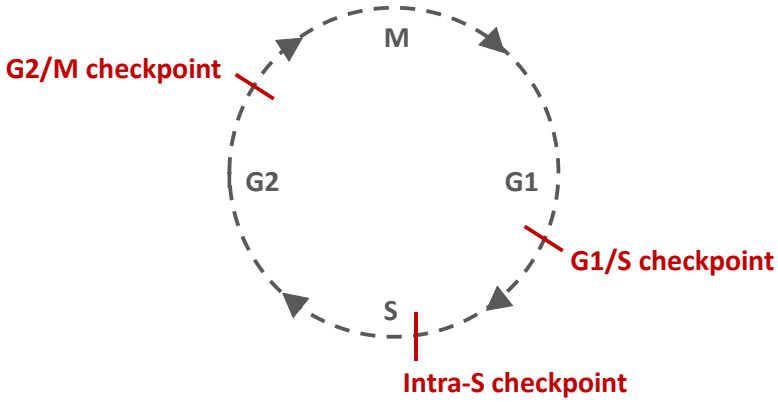

Figure 20: Cell cycle and checkpoints. The cell grows in gap or growth phase (G1) to proceed with the duplication of the genome in S phase (S). Subsequently, another gap or growth phase (G2) prepares the cell for cell division (M). Several checkpoints can be activated to ensure no damage is taken into the next cell cycle phase. Figure adapted from O'Connor.[95]

The repair of DNA lesions however is mediated by several DNA repair pathways (Figure 21), which are activated depending on the type of DNA damage. Although the pathways have distinct roles in repair of DNA damage they are also linked to each other.[95] Oxidative lesions, alkylation lesions and single-strand breaks (SSB) are mainly accomplished by base-excision repair (BER).[91] Double-strand break (DSB) repair however relies on two repair pathways: homologous recombination repair (HRR) and non-homologous end joining (NHEJ).[95] Althouth HRR has a higher fidelity in repair,[95] it requires the presence of a sister chromatid and thus is restricted to S or G2 phase.[97] NHEJ on the other hand does not require the presence of a sister chromatid.[95] The nucleotide-excision repair (NER) pathway is specialized on the removal of bulky DNA lesions that distort the structure of the DNA double helix. During replication wrong base-pairing, nucleotide insertions but also deletions can occur. These lesions are repaired by mismatch repair (MMR). Alklyation damage of nucleobases might be removed by direct reversal pathway. Besides DNA damage caused by exogenous factors the duplication of the genome is prone to DNA damage events during DNA replication as well. To prevent exhaustive DNA damage as a result of replication stress, fork protective measures are induced.

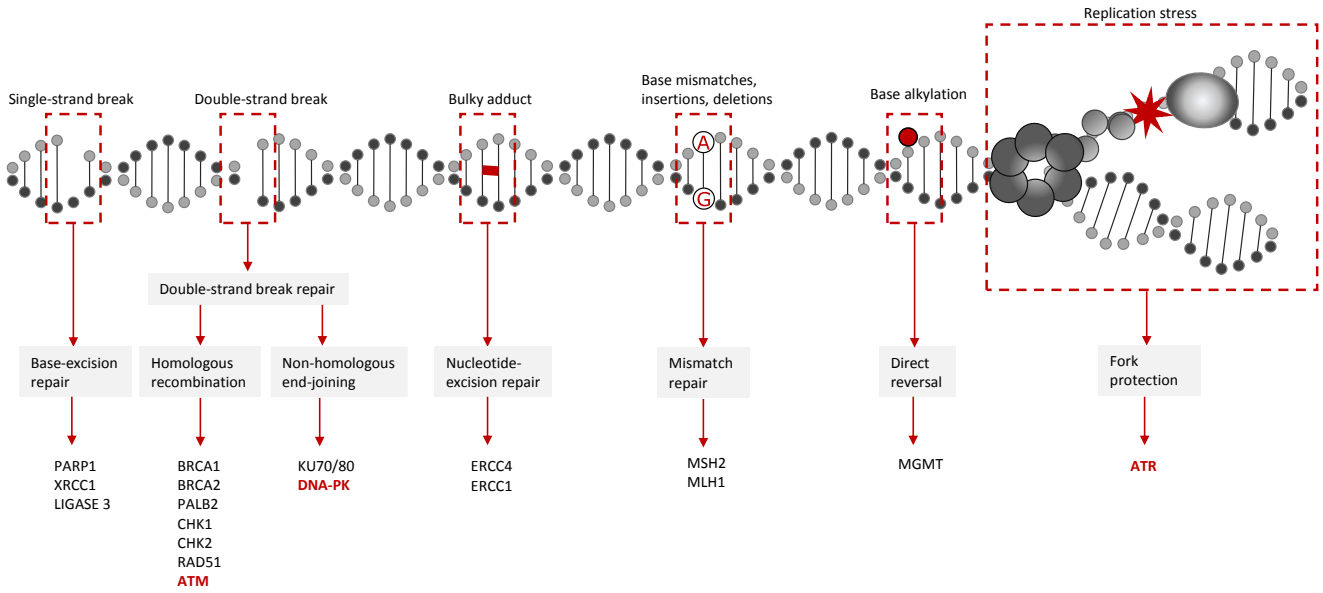

Figure 21: DNA-damage and repair pathways. Depending on the type of DNA-lesions, different DNA repair pathways are recruited that involve several DNA damage repair enzymes. Single-strand breaks are resolved by base-excision repair. Double-strand breaks are repaired by either homologous recombination or non-homologous end joining. Nucleotide excision repair is specialized in the removal of bulky, DNA structure-distorting lesions while mismatch repair corrects base mismatches, insertions or deletions. Alkylation damage on nucleobases is removed by the direct reversal mechanism. Replication stress can induce the stalling of replication forks which activates ATR. The members of the PIKK family ATR, ATM and DNA-PK are marked in red. Figure adapated according to Lord and Ashworth[91] as well as Blackford and Jackson[93].

The three kinases of the phosphoinositide 3-kinase (PI3K)-related kinases (PIKK), namely ataxia telangiectasia-mutated (ATM), ATM and Rad3-related (ATR) and DNA-dependent kinase (DNA-PK) play an essential role in the activation of the DDR (Figure 21, marked in red) and will be discussed in detail in the following.[93]

3.6.1. ATR – Key Kinase in Replication Stress Response

ATR is involved in replication stress response. Thus, the replication process is portrayed as an introduction into the topic.

The survival of a biological organism relies on the replication of the genetic information. This process can be divided into two primary parts that include the melting of the DNA double strand to yield two separate single strands and subsequent semi-conservative replication of each strand. Because the human genome is 3 giga basepairs large, successful replication is a biological masterpiece in which many proteins are involved. Sites of replication initation, so called origins of replication, are distributed over the whole genome to start replication at different site.[98] The origins are often G-rich sequences and CpG islands that form nucleosome-free regions (NFRs) and quadruplex structures. The process of replication is depicted in figure 22. Thus, the origin-recognition complex (ORC) can access DNA and is loaded together with the helicase-loader protein CDC6 to these origins in G1 phase.[99] The pre-replication complex is formed by loading two inactive MCM2-7 helicases together with the chaperone CDT1.[100] At the same time, CDT1 and CDC6 are ejected from the double hexamer, which forms the

pre-replication complex (pre-RC).[101] After the cell enters S phase, the pre-RC is subsequently activated by the formation of the CMG complex consisting of CDC45, the two helicases MCM2-7 and GINS.[102] Finally, a bidirectional replication fork is formed through melting of the DNA-double helix and the recruitment and tethering of the replisome proteins including the polymerase to the MCM2-7[98,102] While MCM2-7 helicase is necessary to open the DNA double helix and to facilitate bidirectional movement, the two polymerases DNA-polymerase ε and δ synthesize the leading and lagging strand, respectively.[103] The process of origin licensing over loading of MCM2-7 helicase onto DNA and formation of the bidirectional replication fork that finally duplicates the DNA is depicted in figure 22.

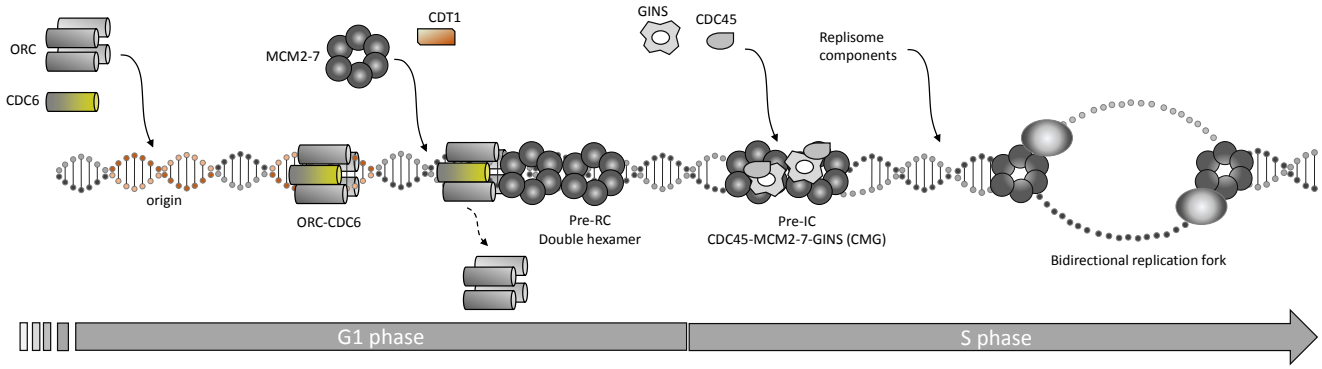

Figure 22: Scheme of replication initiation. The origin recognition complex (ORC) together with CDC6 bind and are loaded onto the origin. The ORC-CDC6 complex facilitates the assembly of the pre-replication complex (pre-RC) consisting of the MCM2-7 double hexamer. Subsequent dissociation of ORC and the loading of GINS and CDC45 to the double hexamer in S phase leads to the formation of the pre-initiation complex, also called CMG. Replisome components are recruited and tethered to the MCM2-7 helicase. A bidirectional replication fork is formed and DNA is replicated.[98]

The replication process frequently encounters challenges such as shortage of dNTPs[104] or histones[105]. In case of depletion of dNTP pools, the DNA-polymerases stall leading to a stalled replication fork. Helicases and DNA-polymerases become uncoupled whereby long stretches of ssDNA are formed.[94] The ssDNA is then coated with replication protein A (RPA) which protects the DNA from nucleolytic restriction.[106] In order to limit damage, the Claspin-TIPIN-Timeless complex restrains helicase movement to keep ssDNA under a certain level.[107] But if this process fails and RPA levels are diminished this might lead to the replication catastrophe which is accompanied by fork collapse and subsequent DNA breaks.[94] Several other sources may lead to replication stress which in this case also manifests in the stalling of replication forks. Stalled replication forks are formed when DNA secondary structures and replicative sequences slow down DNA-polymerization.[108] Furthermore, DNA-RNA hybrids so called R loops formed during transcription pose a barrier for the polymerases.[109] In addition, the DNA suffers from torsional stress during replication which is commonly resolved by topoisomerases.[110] However, these enzymes can pose a replication barrier, too.[111] The physical barries that are encountered by the helicases and DNA-polymerases are depicted in figure 23 A. One common mechanism to resolve replication barriers is the

firing of a neighboring dormant origin to rescue the stalled fork and to complete replication in time. Additionally, a multitude of processes are involved to respond to replication stress.

A central role in replication stress response plays ATR and its downstream target CHK1. Long stretches of ssDNA coated with RPA lead to the recruitment of ATR mediated by ATRIP.[103] The Rad9-Rad1-Hus1 (9-1-1) complex binds to the dsDNA-ssDNA junction through Rad17 with subsequent recruitment of TOPBP1.[108] The interaction of ATR with the 9-1-1 complex and TOPBP1 as well as ETAA1 results in the full activation of ATR. The kinase ATR however has several functions which will be discussed in detail. The processes to overcome these barriers are depicted in figure 23 B.

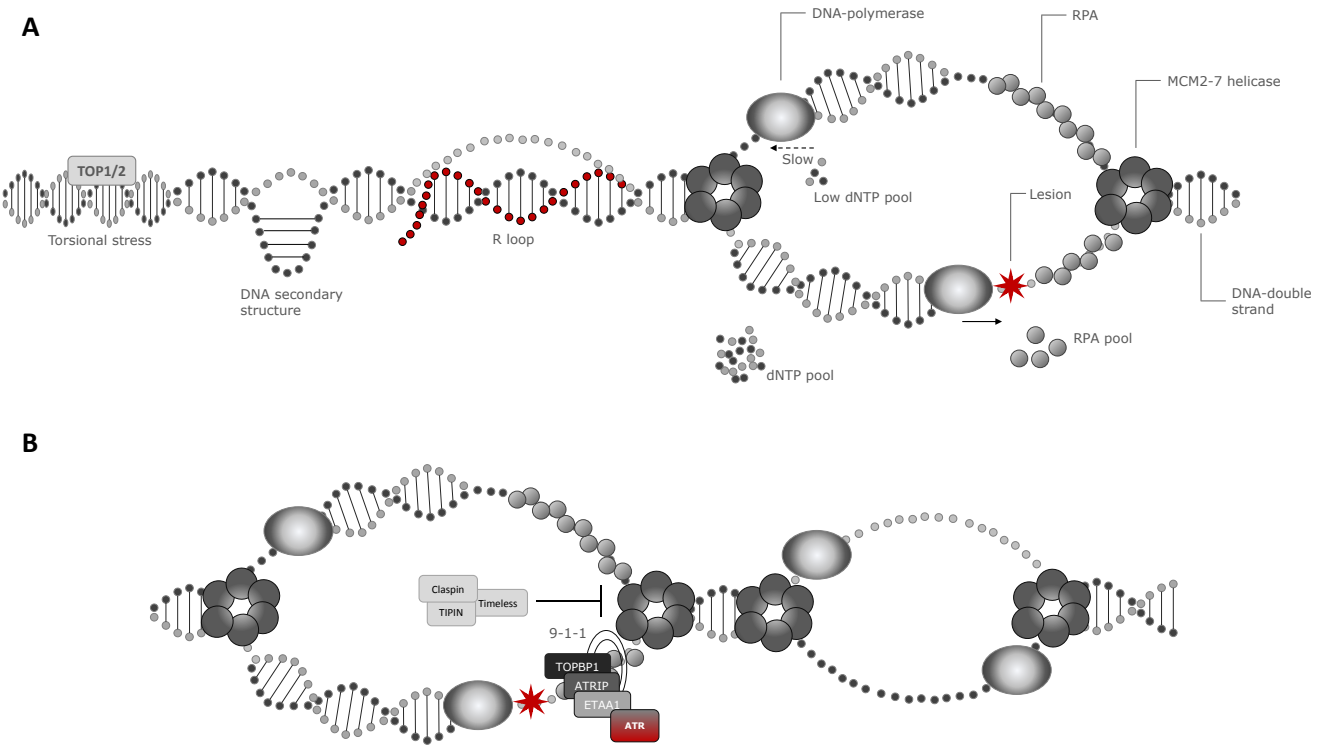

Figure 23: Scheme of replication stress response. A) Representation of types of replication stress. Helicase opens DNA double strand and DNA-polymerases replicate DNA. ssDNA is formed during replication which is coated with RPA to protect the single strand from degradation. The DNA replication encounters torsional stress, DNA secondary structures and R loops that can lead to the stalling of the replisome. Furthermore polymerases might encounter DNA lesions or low dNTP pools that slow down polymerization. These challenges ultimately lead to fork stalling. B) Replication stress response. DNA polymerases stall when they encounter a replication fork barrier. Upon binding of the 9-1-1 complex, TOPBP1 is recruited. ATRIP and ETAA1 bind to the protein complex and ATR is activated leading to several downstream processes. Another possibility of rescuing a stalled fork is the firing of a nearby dormant origin. The Claspin-TIPIN-Timeless complex slows down helicases. Otherwise helicase and DNA-polymerase become uncoupled, leading to the excessive formation of ssDNA. Figure was adapted according to O'Connor and Forment[103].

ATR can activate p53 which induces the transcription of the CDK inhibitor p21 through which G1/S checkpoint is established.[103] Furthermore, ATR phosphorylates CHK1 which again has a multitude of targets that regulate cell cycle and fork stabilization. One target are phosphatases CDC25A, CDC25B and CDC25C. By phosphorylation of the phosphatase CDC25A, it is marked for ubiquitinylation and subsequent degradation. CDC25A removes phosphorylation of CDK1 and CDK2 promoting cell cycle arrest at G1/S transition, in S phase and G2/M transition.

CHK1-mediated phosphorylation of CDC25C leads to the nuclear exclusion of CDC25C. This leads to the inhibition of CDK1 and subsequent G2 arrest. Phosphorylation of CDC25B by CHK1 also results in sequestration of the phosphatase in this case from centromers thereby inhibiting centrosomal CDK1 promoting G2 phase arrest. G2 arrest can also be accomplished by CHK1-mediated phosphorylation of WEE1 which in turn phosphorylates CDK1. Besides the role of CHK1, it is responsible in the recruitment of translesion synthesis which ignores DNA damage to ensure full DNA replication.[108]

It has to be ensured that stalled forks maintain their structure to be able to restart after the replication block is removed by DNA repair enzymes. Abberant remodeling damages the forks which manifests in fork collapse and DNA double strand breaks. Besides their role in cell cycle regulation, ATR and CHK1 have fork-protective functions that include inhibition of fork remodeling.[103] SMARCAL1, an enzyme with remodeling actvity, is inhibited by ATR phosphorylation. This in turn protects DNA from processing by SLX4. CHK1 also phosphorylates Rad51, a key enzyme in homologous recombination repair. Rad51 is recruited to foci of DNA damage promoting repair. Another important function of activated CHK1 is the blockade of replication initiation factor CDC45, which slows down replication. This gains time for the cell to repair damaged DNA and to complete DNA synthesis.[108] If DNA-damage cannot be repaired orderly, persistant cell cycle arrest leads to apoptosis or senescence.[103] The effects of ATR activation are summarized in figure 24.

While the PIKK kinase ATR has proven to be essential for the cellular response to DNA replication stress, two additional kinases of the PIKK family – ATM and DNA-PK – have an important role in the repair of DNA double-strand breaks. Their contribution to DNA maintenance will be described in the following chapter.

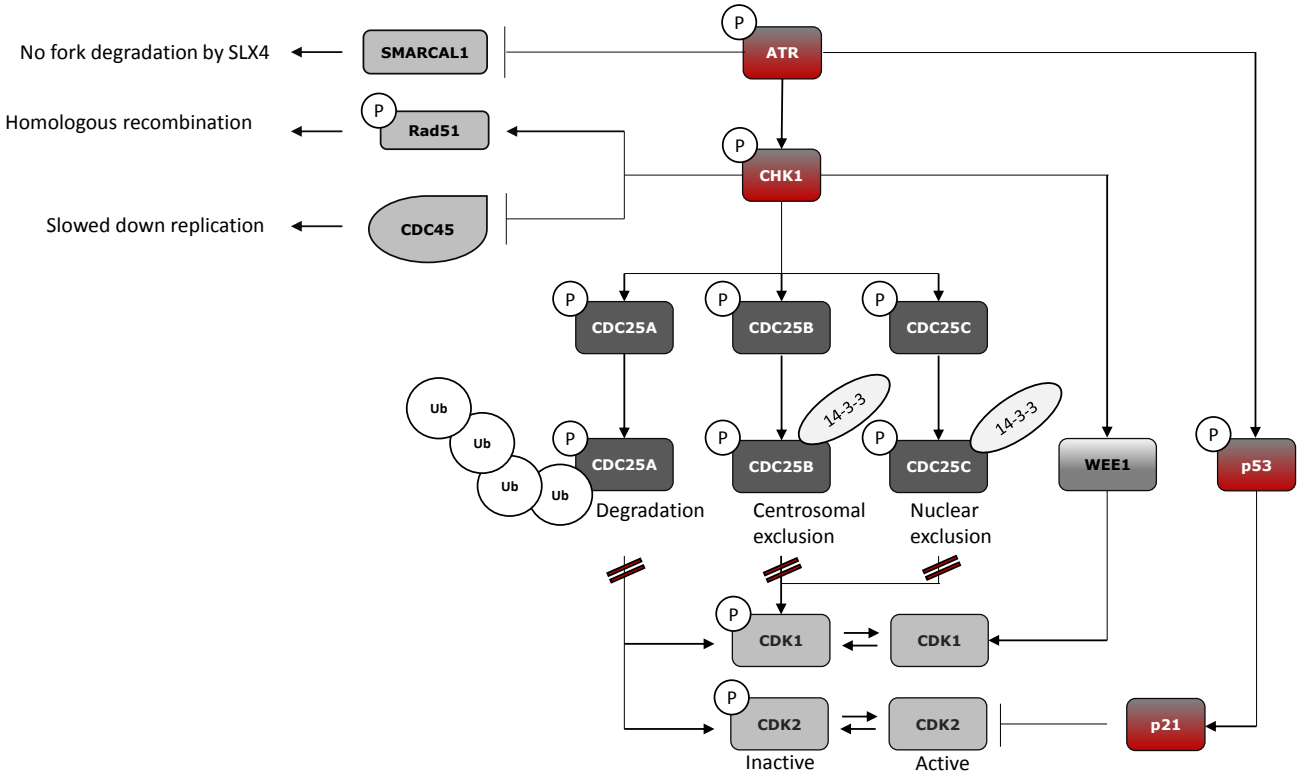

	CDC25A	CDC25B	CDC25C	WEE1	p53
G1 arrest	✓	✗	✗	✗	✓
S delay	✓	✗	✗	✗	
G2 arrest	✓	✓	✓	✓	

Figure 24: ATR downstream signaling. ATR phosphorylates CHK1 which in turn phosphorylates phosphatases CDC25A, CDC25B and CDC25C. Thereby CDC25A is marked for ubiquitinylation and subsequent degradation. CDC25B and CDC25C are excluded from their target CDK1 by centrosomal or nuclear exclusion as result of phosphorylation, respectively. By degrading or relocating the CDC25A/B/C phosphatases CDK1 is kept in its inactive, phosphorylated state. CHK1 also activates WEE1 which phosphorylates CDK1 thereby inhibiting CDK1 activity. ATR activation leads to the activation of p53. As a consequence p21 is transcribed and CDK2 inhibited. Inactivation of CDK1/2 leads to cell cycle arrest. Through these processes cell cycle is regulated as indicated by the check symbol in the table. Phosphorylation of CDC25A by CHK1 leads to cell cycle arrest in G1, S or G2 phase, whereas the phosphorylation of CDC25B or CDC25C by CHK1 effects arrest in G2 as does CHK1-mediated WEE1 activation. p53 phosphorylation results in G1 arrest.

3.6.2. ATM and DNA-PK – Central Kinases in Double-Strand Break Repair

Double-strand breaks can result from endo- and exogenous insults such as radiation, free radicals or radiomimetic drugs. In contrast to single-strand breaks, no template strand is available for the repair of the DSBs rendering DSBs the most hazardous DNA lesion. When DSBs are left unrepaired, termed residual DSBs, they are particularly lethal to the cells.[112] ATM and DNA-PK both are involved in the repair of DNA double-strand breaks however through different molecular mechanisms. DNA-PK promotes the repair mechanism NHEJ which repairs most of the DNA double-strand breaks. Homologous recombination repair, which is promoted by ATM, is mainly used when double-strand breaks occur at replication forks.

NHEJ is initiated when KU70 and KU80 bind to the ends of the double-strand. As a result, DNA-PK is recruited to the double strand and activated. This in turn leads to the recruitment of additional repair factors such as XRCC1, DNA ligase IV, XRCC1-like factor (XLF) and Artemis that help bringing the DNA ends closely together and religating the lesion.[93]

HRR on the other hand is initiated by the MRE11-Rad50-NBS1 (MRN) complex that recruites and activates ATM. As a result, DNA ends are processed so that ssDNA is produced. Then Rad51 binds to the damaged strand and helps invading a sister chromatid strand to use it as a repair template.[93] Activated ATM induces downstream signaling *via* phosphorylation of CHK2. CHK2 subsequently phosphorylates p53 resulting in transcription of CDK inhibitior p21 and G1 arrest. Additionally cell cycle arrest is accomplished through CHK2-mediated phosphorylation of CDC25 phosphatases.[113] The cell cycle regulation mediated by ATM has a crucial role in preventing residual DSBs being taken into the next cell cycle phase.[112]

3.7. Objective of this Work

A common modality to treat cancer besides surgery or radiotherapy is chemotherapy. However, chemotherapeutic agents target not only cancer cells but also normal cells. This lack of specificity towards the diseased tissue leads to off-target toxicities. Furthermore, chemotherapeutic agents often have to be applied at MTD to achieve a therapeutically relevant effect. As a result, chemotherapy is mostly applied as a drug cocktail to increase efficacy. But still, chemotherapy suffers from a narrow therapeutic window.[114]

To overcome toxicity issues of conventional chemotherapy, the concept of ADCs gained momentum. These molecules promised to decrease off-target effects by selectively delivering the cytotoxic drug to the tumor tissues.[115] ADCs open up the possibility to use highly potent drugs, that otherwise could not be used as therapeutic agents.[116] However, second generation ADCs still had a narrow therapeutic window caused by technological problems. The ADCs used for example chemical conjugation techniques such as lysine conjugation or coupling to interchain cysteines. This led to heterogenous ADCs, varying in DAR and drug distribution. The conjugation of highly hydrophobic molecules resulted in ADC aggregation and fast clearance.[18] Technological improvements such as reduction of hydrophobicity[58] or site-specific conjugation techniques[117] contributed to an improved therapeutic window of 3rd generation ADCs.[118] Although much progress has been made, dose-limiting toxicities like neutropenia, thrombocytopenia or ocular toxicity still accompany ADC treatment.[119] A graphical representation of the therapeutic window of ADCs compared to chemotherapy is depicted in figure 25 A.

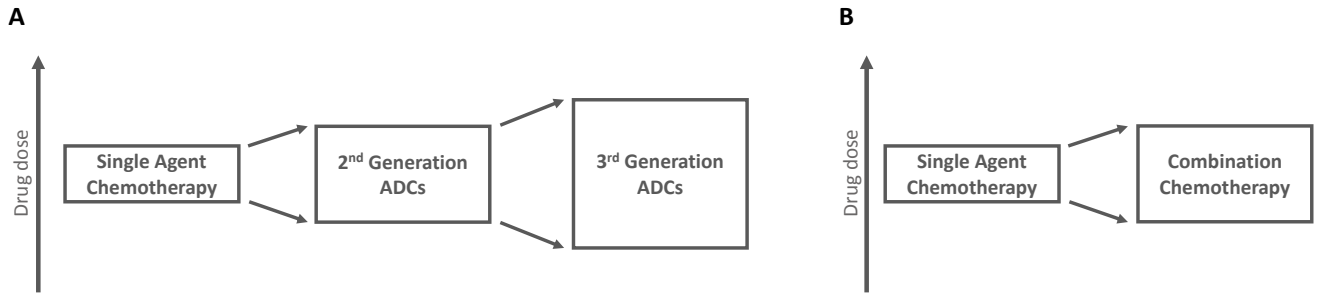

Figure 25: Schematic representation of the therapeutic window of single agent chemotherapy compared to A) 2nd and 3rd generation ADCs or B) combination chemotherapy. A) was adapted from Beck *et al.*[18]

Another way of improving the therapeutic window is the treatment with more than one drug. Synergistic drug combinations have been shown to increase the efficacy of the treatment. This allows to decrease the dose while maintaining the efficacy. Lower doses however might decrease adverse events, especially if the toxicity profiles of the individual drugs differ. Furthermore, combination treatment might be designed to exert a certain selectivity for the diseased tissues.[22] As a result, combination therapy potentially increases the therapeutic window of the therapy when compared to single agent chemotherapy (Figure 25 B).

The goal of this work is the introduction of another treatment modality that combines the advantages of targeted therapy and combination therapy. Therefore ADCs shall be combined with small molecule drugs to

increase the efficacy of both drugs. A schematic representation of the expected therapeutic windows as surrogate for the safety of a treatment is depicted in figure 26.

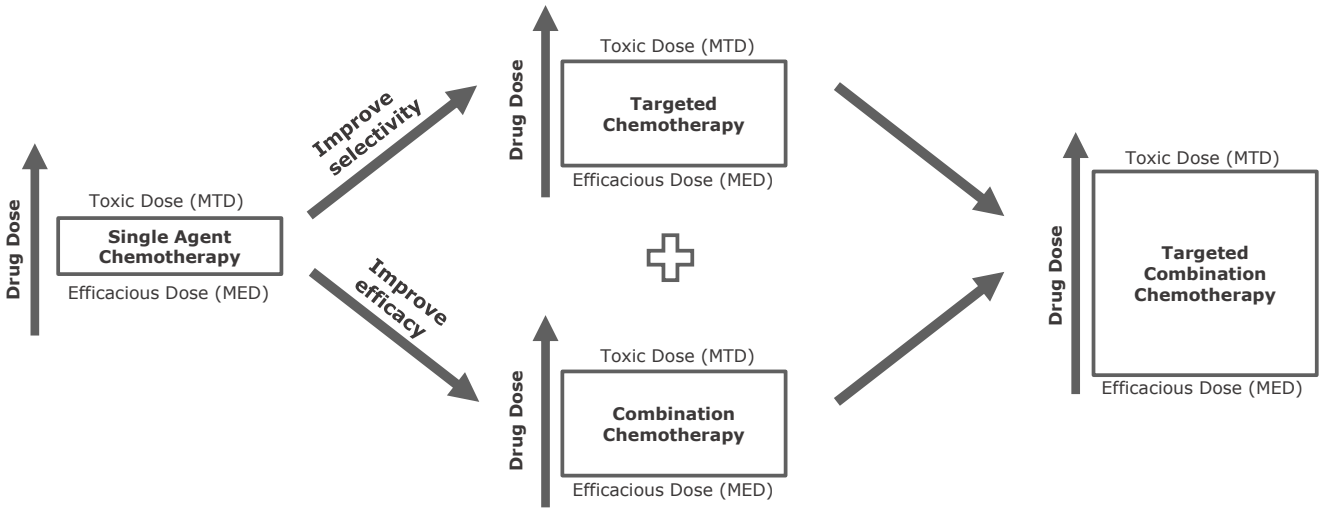

Figure 26: Scheme of expected therapeutic windows. Classical chemotherapy has a rather narrow therapeutic window. The therapeutic window of a drug can be improved by applying combination therapy or by targeting the drug specifically to the tumor tissues. The therapeutic window might be even further increased by using a combination of targeted therapy and combination therapy, namely targeted combination therapy.

Since microtubule-targeting ADCs showed limited efficacy during clinical evaluation,[39] the focus of this work is laid on DNA-damaging payloads. For the DNA-alkylating drug duocarmycin no combination therapy has been reported so far. Therefore, a drug combination screening will be performed with the small molecule DUBA to discover a synergistic combination partner for duocarmycin. The small molecules will be selected based on literature data suggesting a role in duocarmycin lesion repair. Subsequently, ADCs will be generated to study if synergistic drug combinations of small molecules might be translated to the ADC format. Finally, an *in vivo* xenograft model might be established to assess the safety profile of the combination treatment.

4. Methods and Materials

4.1. Reagents

Merck Millipore, Merck KGaA:

Ammonium sulfate, Calcium chloride, Citric acid, Disodium hydrogen phosphate dihydrate, Dithiothreitol, glycerol, Kanamycindisulfate, Sodium chloride, Sodium dihydrogen phosphate hydrate, methanol, sodium azide, MilliQ-water, Triton X-100, Tween-20, hydrochloric acid

Activate Scientific:

Captisol

Colorcon:

K4Premium Methocel

Calbiochem:

Tris(hydroxymethyl)-aminomethan-hydrochloride (Tris-HCl)

Sigma-Aldrich Laborchemikalien GmbH:

Ampicillin sodium salt, Hydroxyurea, propidium iodide,

Thermo Fisher, Gibco:

DMEM high Glucose (no phenol red), DMEM GlutaMax, RPMI-1640 GlutaMax, 100 mM sodium pyruvate, goat serum, phosphate buffered saline (PBS) 1x and 10x, Lipofectamine RNAiMAX, 0,05% Trypsin-EDTA

Invitrogen:

Alexa Fluor® 488 F(ab')2 fragment of goat anti-rabbit IgG (H+L)

Cell Signaling:

Phospho-CHK1 (Ser345, 133D3) rabbit mAb

Roth:

Bovine serum albumin

GE Healthcare:

Accutase,

Dharmacon:

5X siRNA buffer

Pools of siRNA against CHK1 (CHEK1), ATR, PLK1 and a non-targeting siRNA was purchased from Dharmacon with the following sequences:

siGENOME Human CHEK1 (1111) SMARTpool siRNA:

GCAACAGUAUUUCGGUAUA

GGACUUCUCUCCAGUAAAC

AAAGAUAGAUGGUACAACA

AGAUAUGAAGCGUGCCGUA

ON-TARGETplus Human ATR (545) SMARTpool siRNA:

GAGAAAGGAUUGUAGACUA

GCAACUCGCCUAACAGAUA

CCACGAAUGUUAACUCUAU

CCGCUAAUCUUCUAACAUU

ON-TARGETplus Human PLK1 (5347) SMARTpool siRNA:

GCACAUACCGCCUGAGUCU

CCACCAAGGUUUUCGAUUG

GCUCUUCAAUGACUCAACA

UCUCAAGGCCUCCUAAUAG

siGenome Non-Targeting siRNA Pool #1:

UAGCGACUAAACACAUCAA

UAAGGCUAUGAAGAGAUAC

AUGUAUUGGCCUGUAUUAG

AUGAACGUGAAUUGCUCAA

Antibody sequences

Amino acid sequence of αHER2 antibody as published by drug bank accession entry DB00072 in the year 2009.[120] Genetic modifications are marked in bold font.

Heavy chain:

EVQLVESGGGLVQPGGSLRLSCAASGFNIKDTYIHWVRQAPGKGLEWVARIYPTNGYTRYADSVKGRFTISADTSKNTAYLQM

NSLRAEDTAVYYCSRWGGDGFYAMDYWGQGTLVTVSSASTKGPSVFPLAPSSKSTSGGTAALGCLVKDYFPEPVTVSWNSGA

LTSGVHTFPAVLQSSGLYSLSSVVTVPSSSLGTQTYICNVNHKPSNTKVDKKVEPPKSCDKTHTCPPCPAPELLGGPSVFLFPPKP
KDTLMISRTPEVTCVVVDVSHEDPEVKFNWYVDGVEVHNAKTKPREEQYNSTYRVVSVLTVLHQDWLNGKEYKCKVSNKALP
APIEKTISKAKGQPREPQVYTLPPSRDELTKNQVSLTCLVKGFYPSDIAVEWESNGQPENNYKTTPPVLDSDGSFFLYSKLTVDKS
RWQQGNVFSCSVMHEALHNHYTQKSLSLSPGK

Light Chain with SrtA recognition motif:
MKLPVRLLVLMFWIPASLSDIQMTQSPSSLSASVGDRVTITCRASQDVNTAVAWYQQKPGKAPKLLIYSASFLYSGVPSRFSGS
RSGTDFTLTISSLQPEDFATYYCQQHYTTPPTFGQGTKVEIKRTVAAPSVFIFPPSDEQLKSGTASVVCLLNNFYPREAKVQWKV
DNALQSGNSQESVTEQDSKDSTYSLSSTLTLSKADYEKHKVYACEVTHQGLSSPVTKSFNRGEC**GGGGSGGGGSGGGGSLPET
GS**

Amino acid sequence of αEGFR antibody Cetuximab. Genetic modifications are marked in bold font.

Native heavy chain:
QVQLKQSGPGLVQPSQSLSITCTVSGFSLTNYGVHWVRQSPGKGLEWLGVIWSGGNTDYNTPFTSRLSINKDNSKSQVFFKM
NSLQSNDTAIYYCARALTYYDYEFAYWGQGTLVTVSAASTKGPSVFPLAPSSKSTSGGTAALGCLVKDYFPEPVTVSWNSGALT
SGVHTFPAVLQSSGLYSLSSVVTVPSSSLGTQTYICNVNHKPSNTKVDKRVEPKSCDKTHTCPPCPAPELLGGPSVFLFPPKPKDT
LMISRTPEVTCVVVDVSHEDPEVKFNWYVDGVEVHNAKTKPREEQYNSTYRVVSVLTVLHQDWLNGKEYKCKVSNKALPAPIE
KTISKAKGQPREPQVYTLPPSREEMTKNQVSLTCLVKGFYPSDIAVEWESNGQPENNYKTTPPVLDSDGSFFLYSKLTVDKSRW
QQGNVFSCSVMHEALHNHYTQKSLSLSPGK

Heavy chain with SrtA recognition motif
QVQLKQSGPGLVQPSQSLSITCTVSGFSLTNYGVHWVRQSPGKGLEWLGVIWSGGNTDYNTPFTSRLSINKDNSKSQVFFKM
NSLQSNDTAIYYCARALTYYDYEFAYWGQGTLVTVSAASTKGPSVFPLAPSSKSTSGGTAALGCLVKDYFPEPVTVSWNSGALT
SGVHTFPAVLQSSGLYSLSSVVTVPSSSLGTQTYICNVNHKPSNTKVDKRVEPKSCDKTHTCPPCPAPELLGGPSVFLFPPKPKDT
LMISRTPEVTCVVVDVSHEDPEVKFNWYVDGVEVHNAKTKPREEQYNSTYRVVSVLTVLHQDWLNGKEYKCKVSNKALPAPIE
KTISKAKGQPREPQVYTLPPSREEMTKNQVSLTCLVKGFYPSDIAVEWESNGQPENNYKTTPPVLDSDGSFFLYSKLTVDKSRW
QQGNVFSCSVMHEALHNHYTQKSLSLSPGK**LPETGS**

Light chain with spacer and SrtA recognition motif:
DILLTQSPVILSVSPGERVSFSCRASQSIGTNIHWYQQRTNGSPRLLIKYASESISGIPSRFSGSGSGTDFTLSINSVESEDIADYYCQ
QNNNWPTTFGAGTKLELKRTVAAPSVFIFPPSDEQLKSGTASVVCLLNNFYPREAKVQWKVDNALQSGNSQESVTEQDSKDS
TYSLSSTLTLSKADYEKHKVYACEVTHQGLSSPVTKSFNRGEC**GGGGSGGGGSGGGGSLPETGS**

Light chain with SrtA recognition motif:

DILLTQSPVILSVSPGERVSFSCRASQSIGTNIHWYQQRTNGSPRLLIKYASESISGIPSRFSGSGSGTDFTLSINSVESEDIADYYCQ
QNNNWPTTFGAGTKLELKRTVAAPSVFIFPPSDEQLKSGTASVVCLLNNFYPREAKVQWKVDNALQSGNSQESVTEQDSKDS
TYSLSSTLTLSKADYEKHKVYACEVTHQGLSSPVTKSFNRGEC**LPETGS**

Amino acid sequence of αHEL antibody. Genetic modifications are marked in bold font.

Light chain with spacer and SrtA recognition motif:

DIQMTQSPSSLSASVGDRVTITCRASGNIHNYLAWYQQKPGKAPKLLIYYTTTLADGVPSRFSGSGSGTDYTFTISSLQPEDIATY
YCQHFWSTPRTFGQGTKVEIKRTVAAPSVFIFPPSDEQLKSGTASVVCLLNNFYPREAKVQWKVDNALQSGNSQESVTEQDSK
DSTYSLSSTLTLSKADYEKHKVYACEVTHQGLSSPVTKSFNRGEC**GGGGSGGGGSGGGGSLPETGS**

Native heavy chain:

QVQLQESGPGLVRPSQTLSLTCTVSGFSLTGYGVNWVRQPPGRGLEWIGMIWGDGNTDYNSALKSRVTMLKDTSKNQFSLR
LSSVTAADTAVYYCARERDYRLDYWGQGSLVTVSSASTKGPSVFPLAPSSKSTSGGTAALGCLVKDYFPEPVTVSWNSGALTSG
VHTFPAVLQSSGLYSLSSVVTVPSSSLGTQTYICNVNHKPSNTKVDKRVEPKSCDKTHTCPPCPAPELLGGPSVFLFPPKPKDTLM
ISRTPEVTCVVVDVSHEDPEVKFNWYVDGVEVHNAKTKPREEQYNSTYRVVSVLTVLHQDWLNGKEYKCKVSNKALPAPIEKTI
SKAKGQPREPQVYTLPPSREEMTKNQVSLTCLVKGFYPSDIAVEWESNGQPENNYKTTPPVLDSDGSFFLYSKLTVDKSRWQQ
GNVFSCSVMHEALHNHYTQKSLSLSPGK

Amino acid sequence of αMETxEGFR antibody. Genetic modifications are marked in bold font.

SEED GA heavy chain with scFv:

DIQMTQSPSSLSASVGDRVTITCRASQSIGTNIHWYQQKPGKAPKLLIKYASESISGVPSRFSGSGYGTDFTLTISSLQPEDVATYY
CQQNYNWPTTFGQGTKVEIKGGGGSGGGGSGGGGSGGGGSEVQLVQSGAEVKKPGASVKVSCKASGFSLTNYGVHWMR
QAPGQGLEWIGVIWSGGNTDYNTPFTSRVTITSDKSTSTAYMELSSLRSEDTAVYYCARALTYYDYEFAYWGQGTLVTVSS

SEED AG heavy chain:

METDTLLLWVLLLWVPGSTGEVQLVQSGGGLVQPGGSLRLSCAASGFTFSSYAMSWVRQAPGKGLEWVSAISGSGGSTYY
ADSVKGRFTISRDNSKNTLYLQMNSLRAEDTAVYYCAKDRRITHTYWGQGTLVTVSSASTKGPSVFPLAPSSKSTSGGTAALGC
LVKDYFPEPVTVSWNSGALTSGVHTFPAVLQSSGLYSLSSVVTVPSSSLGTQTYICNVNHKPSNTKVDKRVEPKSCDKTHTCPPC
PAPELLGGPSVFLFPPKPKDTLMISRTPEVTCVVVDVSHEDPEVKFNWYVDGVEVHNAKTKPREEQYNSTYRVVSVLTVLHQD
WLNGKEYKCKVSNKALPAPIEKTISKAKGQPFRPEVHLLPPSREEMTKNQVSLTCLARGFYPKDIAVEWESNGQPENNYKTTPS
RQEPSQGTTTFAVTSKLTVDKSRWQQGNVFSCSVMHEALHNHYTQKTISLSPGK

Light chain with SrtA recognition motif:

METDTLLLWVLLLWVPGSTGEPVLTQPPSVSVAPGETATIPCGGDSLGSKIVHWYQQRPGQAPLLVVYDDAARPSGIPERFSG
SKSGTTATLTISSVEAGDEADYFCQVYDYHSDVEVFGGGTKLTVLGQPKAAPSVTLFPPSSEELQANKATLVCLISDFYPGAVTVA
WKADSSPVKAGVETTTPSKQSNNKYAASSYLSLTPEQWKSHKSYSCQVTHEGSTVEKTVAPTECS**LPETGS**

Amino acid sequence of αMET antibody. Genetic modifications are marked in bold font.

Light chain with SrtA recognition motif:

METDTLLLWVLLLWVPGSTGEPVLTQPPSVSVAPGETATIPCGGDSLGSKIVHWYQQRPGQAPLLVVYDDAARPSGIPERFSG
SKSGTTATLTISSVEAGDEADYFCQVYDYHSDVEVFGGGTKLTVLGQPKAAPSVTLFPPSSEELQANKATLVCLISDFYPGAVTVA
WKADSSPVKAGVETTTPSKQSNNKYAASSYLSLTPEQWKSHKSYSCQVTHEGSTVEKTVAPTECS**LPETGS**

Heavy chain:

EVQLVQSGGGLVQPGGSLRLSCAASGFTFSSYAMSWVRQAPGKGLEWVSAISGSGGSTYYADSVKGRFTISRDNSKNTLY
LQMNSLRAEDTAVYYCAKDRRITHTYWGQGTLVTVSSASTKGPSVFPLAPSSKSTSGGTAALGCLVKDYFPEPVTVSWNS
GALTSGVHTFPAVLQSSGLYSLSSVVTVPSSSLGTQTYICNVNHKPSNTKVDKRVEPKSCDKTHTCPPCPAPELLGGPSV
FLFPPKPKDTLMISRTPEVTCVVVDVSHEDPEVKFNWYVDGVEVHNAKTKPREEQYNSTYRVVSVLTVLHQDWLNGKEYK
CKVSNKALPAPIEKTISKAKGQPREPQVYTLPPSREEMTKNQVSLTCLVKGFYPSDIAVEWESNGQPENNYKTTPPVLDS
DGSFFLYSKLTVDKSRWQQGNVFSCSVMHEALHNHYTQKSLSLSPGK

Drugs

Name	No.	Structure	Provided by
ATRi **1**	**1**	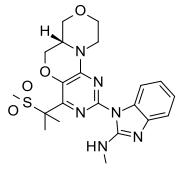	Lab. Dr. Dorsch
AZ20	**2**	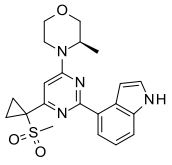	Lab. Dr. Burgdorf
AZD6738	**3**	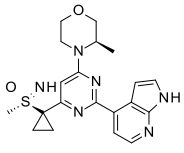	Lab. Dr. Jonczyk, Pharmacon

BAY1895344	**4**	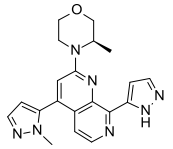	Lab. Dr. Burgdorf
BAY286	**5**	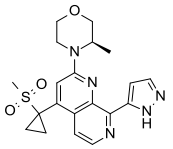	WuXi AppTec
BAY73	**6**	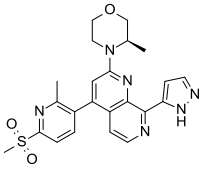	WuXi AppTec
VE-822 (VX-970, M6620 Berzosertib)	**7**	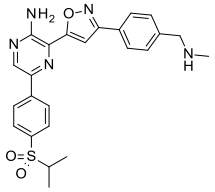	Lab. Dr. Burgdorf, VWR, Vertex Pharmaceuticals Inc.
	13	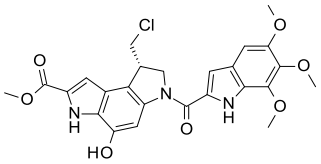	Xdcexplorer Co., LTD.
	24	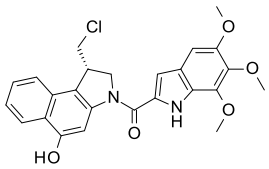	Xdcexplorer Co., LTD.
	29	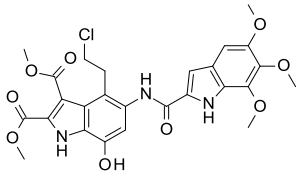	Lab. Dr. Carl Deutsch
	30	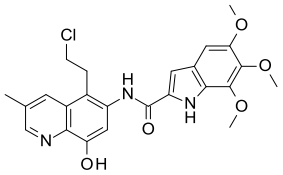	Lab. Dr. Carl Deutsch
	31	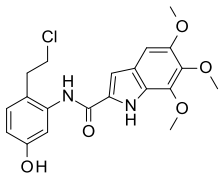	Lab. Dr. Carl Deutsch

	32	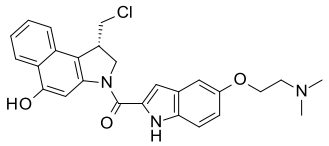	Moradec LLC.
	33	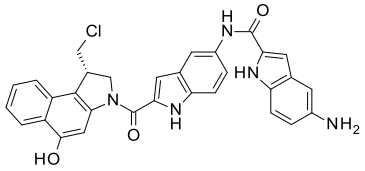	Xdcexplorer Co., LTD.
	34	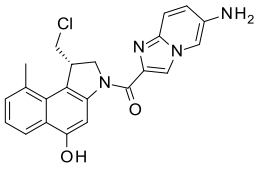	Lab. Dr. Carl Deutsch
	10	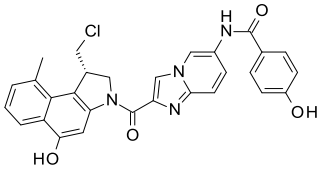	Lab. Dr. Carl Deutsch
KU-55933		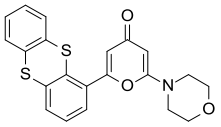	Selleck Chemicals LLC.
M3814		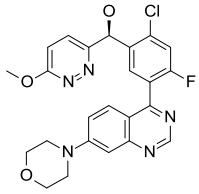	Lab. Dr. Fuchss
NU7441		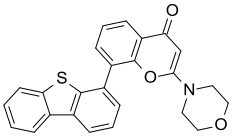	Selleck Chemicals LLC.
AZD7762		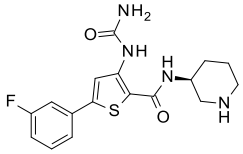	Selleck Chemicals LLC.
LY2603618		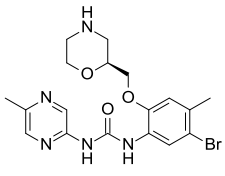	ChemScene

Amuvatinib		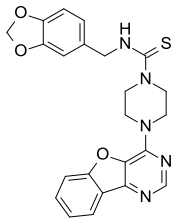	Selleck Chemicals LLC.
AZD1775		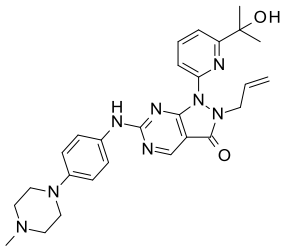	PharmaBlock Inc.
Bleomycin A5		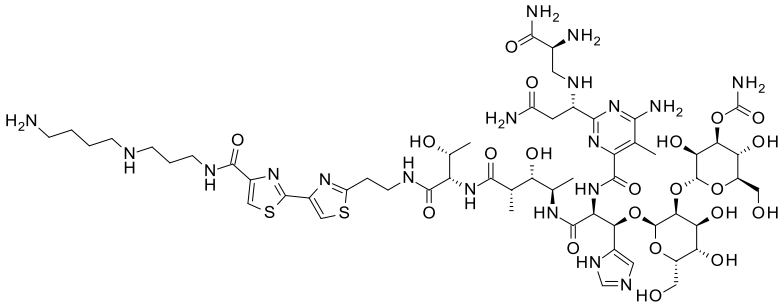	Cayman Chemical Company
Ciliobrevin D		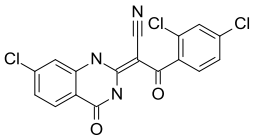	Merck KGaA
Cmpd31		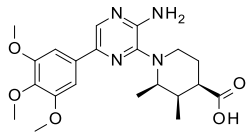	Lab. Dr. Finsinger
CP724714		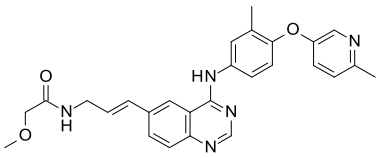	Biomol GmbH
Etoposide		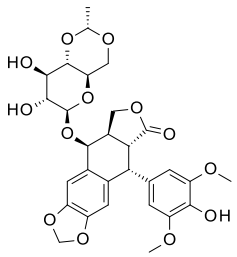	Selleck Chemicals LLC.
Hycanthone		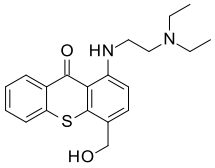	Prestwick Chemical Pc

Lapatinib		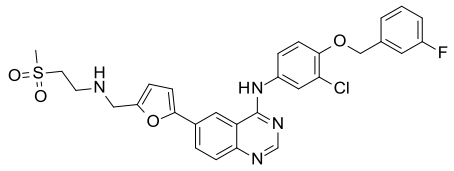	AOKBIO Inc.
Olaparib		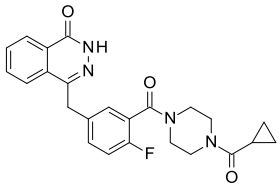	Lab. Dr. Fuchss
Tranespimycin		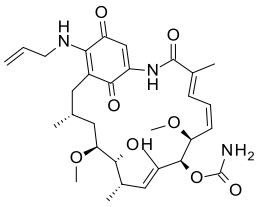	BioTrend Chemikalien GmbH
TH588		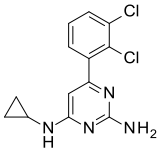	Lab. Dr. Ross
Gemcitabine		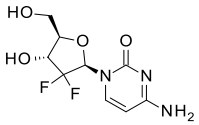	Cayman Chemical Company
SN-38		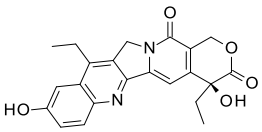	TCI Chemical Industry Co., LTD.
MMAE		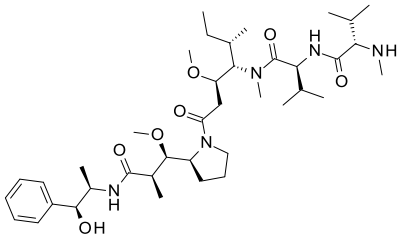	Lab. Dr. Klein
LD-**1**		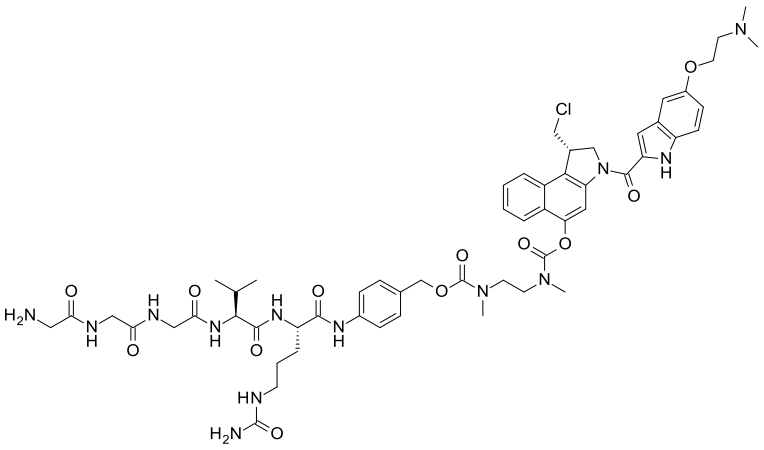	Moradec LLC.

LD-**2**		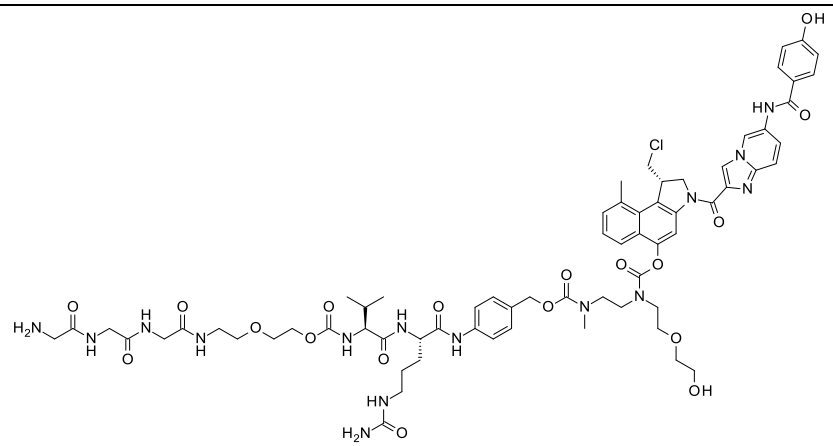	Lab. Dr. Deutsch
LD-**3**		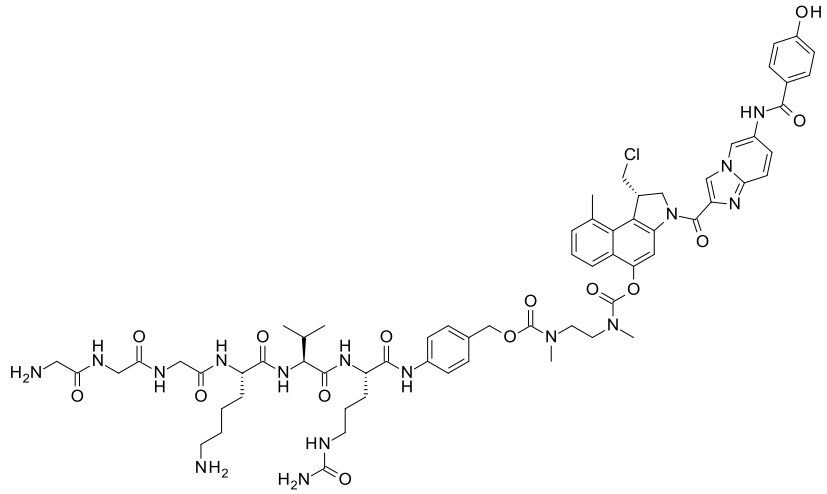	Lab. Dr. Deutsch
LD-**4**		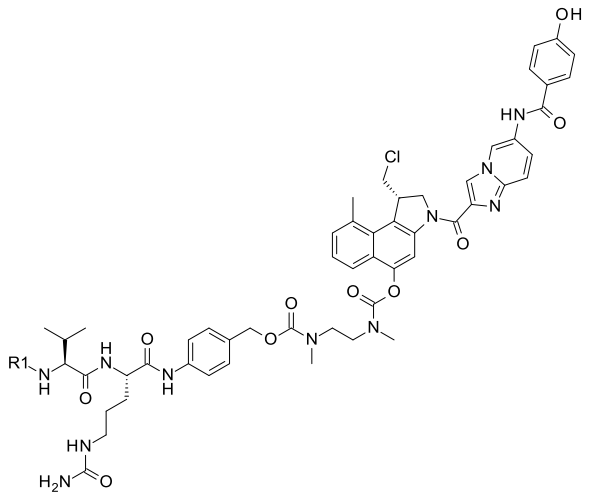	Lab. Dr. Deutsch

LD-**5**		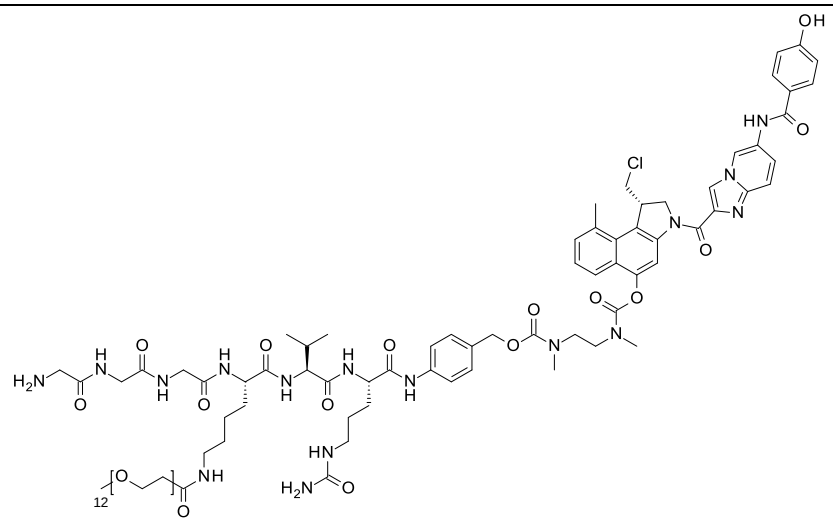	Lab. Dr. Deutsch
LD-**6**		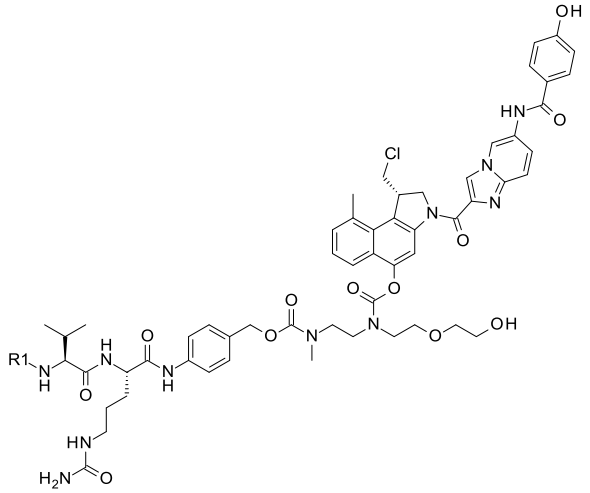	Lab. Dr. Deutsch
LD-**7**		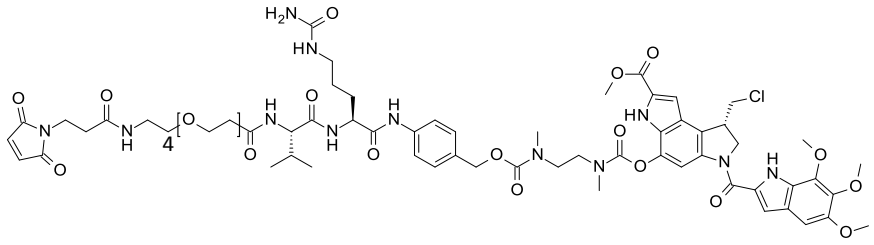	Levena Biopharma
LD-**8**		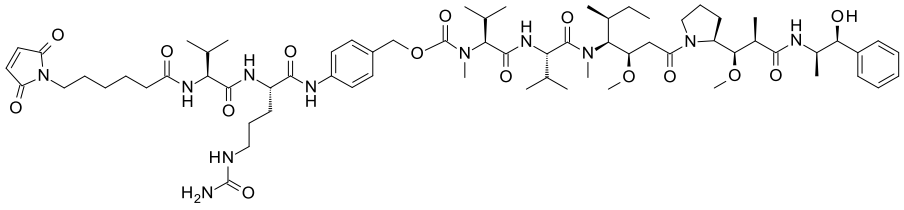	Levena Biopharma

LD-**9**		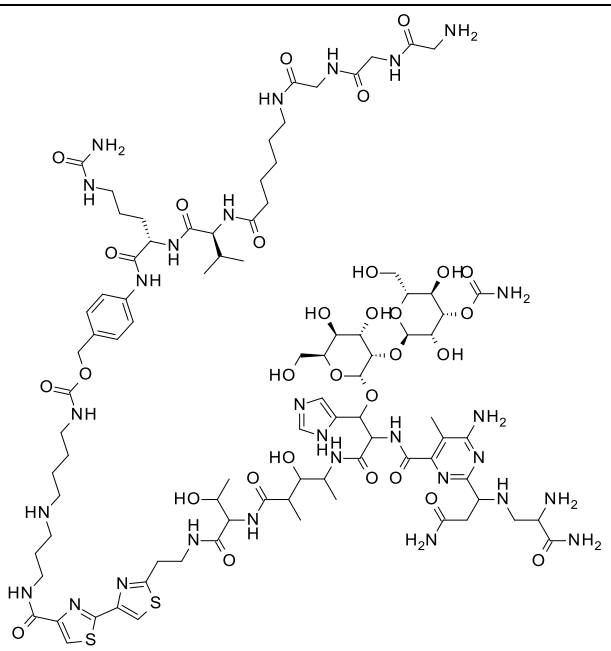	Lab. Dr. Deutsch

Engelhart Pharmacy:

Kadcyla, Herceptin

4.2. Commercially available systems

ExpiFectamine™ 293 *transfection kit*	Life Technologies Corp., Germany
JetStar™ 2.0 Plasmid Purification Kit	Genomed GmbH, Germany
QIAPrep Spin Miniprep Kit	Qiagen, Germany
QuikChange® Site-Directed Mutagenesis Kit	Stratagene, United States of America
Gels and buffers for SDS-PAGE: NuPAGE 4-12% Bis-Tris Gel NuPAGE LDS Sample Buffer (4x) NuPAGE Sample Reducing Agent (10x) NuPAGE MES SDS running buffer (20x)	Life Technologies Corp., Germany

4.3. Consumable material

Cannula, Sterican 27G	B. Braun Melsungen AG, Germany
15 ml, 50 ml falcon tube	Becton Dickinson GmbH, Germany
CellCulture Flasks adherent	Greiner Bio-One GmbH, Austria
Centrifugal filter, Amicon® Ultra-4K and 15K	Merck Millipore, Merck KGaA, Germany
HiLoad™ 16/600 Superdex™ 200 pg column	GE Healthcare Europe GmbH, Germany
HiTrap™ 1 mL Protein A HP column	GE Healthcare Europe GmbH, Germany
HisTrap™ 1 mL HP and HisTrap™ 5 mL HP	GE Healthcare Europe GmbH, Germany
NuPAGE® 4-12% Bis-Tris Gels	Life Technologies Corp., Deutschland
Oral gavage	Fuchigami, Japan
PD-10 column	GE Healthcare Europe GmbH, Germany
Polypropylene cap	Agilent Technologies, United States of America
Polypropylene vial	Agilent Technologies, United States of America
Safe Lock Tubes 0.2, 1.5, 2.0, 5.0 mL	Eppendorf AG, Germany
Steriflip® Sterile filter 50 ml 0.22 and 0.45 µm	Merck Millipore, Merck KGaA, Germany
Syringe, Imnifix-F	B. Braun Melsungen AG, Germany

4.4. Devices

Chromatography system, ÄKTAxpress	GE Healthcare Europe GmbH, Germany
Balance, NewClassic MF	Mettler-Toledo Intl. Inc., Swiss
Cell counter, Vi-CELL™ XR	Beckman Coulter, United States of America
Cell counter, Countess (lab. Blume)	Thermo Scientific GmbH, Germany
Cell disrupter, EmulsiFlex C3	Avestin Inc., Canada
Centrifuge, Megafuge 1.0R	Heraeus Holding, Germany
Centrifuge, Multifuge 3 S-R	Heraeus Holding, Germany
Centrifuge, Sorvall® Evolution RC	Heraeus Holding, Germany
Centrifuge 5415R and 5415D	Eppendorf AG, Germany
Dispenser D300e	Tecan Group Ltd., Switzerland
High performance liquid chromatography, 1260 Infinity (1290 autosampler)	Agilent Technologies, United States of America
Incubator, Heracell 150	Thermo Scientific GmbH, Germany
Cell incubator, Heracell 240 (lab. Blume)	Thermo Scientific GmbH, Germany
Incubator, Kelvitron®	Heraeus Holding, Germany

Incubator, Reach-In CO_2 Incubator Model3951	Thermo Scientific GmbH, Germany
Plate reader, Synergy 4	BioTek, Inc., United States of America
Plate reader, Envision 2104 multiplate reader	Perkin Elmer Inc., United States of America
LaminarAir Flow	Heraeus Holding, Germany
Shaking incubator, Multitron HAT	Infors AG, Germany
Magnetic stirrer, RCT basic	IKA®-Werke GmbH & CO. KG, Germany
Microwave, Inverter	Sharp K.K., Japan
Migration chamber	Life Technologies Corp., Germany
NanoDrop ND-1000 spectrophotometer	Thermo Scientific GmbH, Germany
Single channel pipets	Eppendorf AG, Germany
Shaker, Variomag Monoshake (lab. Blume)	Thermo Scientific GmbH, Germany
16-channel Viaflow II pipets	INTEGRA Biosciences AG
ThermoMixer F1.5	Eppendorf AG, Germany
ThermoMixer comfort	Eppendorf AG, Germany
Ultracentrifuge, Sorvall® RC-5C Plus	Heraeus Holding, Germany
Ultra Confocal High Content Screening System, ImageXpress (lab. Blume)	Molecular Devices, LLC, United States of America
Washer, Powerwasher (lab. Blume)	Tecan Group Ltd., Switzerland

4.5. Buffer and Solutions

Buffer for Hydrophobic Interaction Chromatography

Buffer A: 1.5 M Ammoniumsulfat, 25 mM Tris, pH 7.5

Buffer B: 20 % Isopropanol, 25 mM Tris, pH 7.5

Buffer for Protein A chromatography

Binding buffer: 150 mM NaCl, 20 mM Tris-HCl pH 7.5

Elution buffer: 0.1 M citric acid pH 3.0

Neutralization buffer: Tris-HCl pH 9.0

Buffer for purification via SEC

Mobile phase: PBS, pH 7.0

Buffer for analytical SEC

Mobile phase: 50 mM NaP, 0.4 M Na Perchlorate, pH 6.3

Reaction buffer

150 mM NaCl, 50 mM Tris-HCl pH 7.5

4.6. Antibody Expression

The expression of antibodies is based on the protocol supplied for ExpiFectamineTM 293 Transfection Kit (Life Technologies Corp.). 1250 µL Opti-MEM are mixed with 80 µL Expifectamine and incubate for max. 5 min. Afterwards 12.5 µg of heavy and light chain plasmid are diluted in 1250 µL Opti-MEM. SEED-antibodies carry two different heavy chains. Heavy chain plasmid for GA- and AG-strand and light chain, are mixed in the mass-ratio 1:1:1. Both solutions are united, forming reaction mixture, and incubated for 30 min. Meanwhile cell density of Expi293TM cells is determined using ViCell cell counter (Beckman Coulter). The cells were used if the viability is greater than 95%. Cells are diluted to $3.0x10^6$ cells mL^{-1} in Expi293TM Expression Medium to a total volume of 21 mL, which was tempered at 37 °C. The reaction mixture is added to the cell suspension while shaking. The cells are shaken at 37 °C and 5% CO_2. After 16-18 h 150 µL Enhancer 1 and 1.5 mL Enhancer 2 are added. The expression took place while shaking at 37 °C and 5% CO_2 for four days. The antibodies are isolated by collecting the supernatant after centrifugation (6000 g/10 min/4 °C). The supernatant is filtered sterilely using Steritop 0.22 µm or Steriflip 0.22 µm filters (Merck Millipore, Merck KGaA). Antibodies are purified by proceeding with Protein A chromatography. This procedure can be scaled-up by keeping the ratios of reagents equal.

4.7. Transformation

Transformations were performed using 50 µL chemically competent cells, which were thawed on ice and subsequently mixed with 50 ng plasmid solution. After 30 minutes incubation on ice, the cells were tempered for 30 seconds at 42 °C. Afterwards 250 µL SOC-medium were added, followed by 45 minutes of incubation at 37 °C while shaking. The cell suspension was centrifuged for 1 min at 16 krcf. The supernatant was discarded, whereas the cells were resuspended in the remaining solution. The suspension was plated on agar-plates, containing antibiotic. The plates were incubated overnight at 37 °C.

4.8. Plasmid Amplification

Plasmids were amplified by transformation of One Shot TOP10 Chemically Competent *E. coli*. The purification was performed using JetStar™ 2.0 Plasmid Purification Kit if high plasmid yield is needed for protein expression. The purification procedure began with harvesting of the overnight culture. The cells were lysed, followed by precipitation and centrifugation. The supernatant is applied on a pre-packed anion exchange column. Since the

deoxyribonucleic acid (DNA) backbone is negatively charged, the DNA is bound by the positively charged column matrix. A low salt washing step removes ribonucleic acid (RNA), carbohydrates and proteins. DNA was then eluted under high salt conditions. By precipitation of DNA using alcohol, the DNA was desalted.
For the amplification of plasmid for sequencing purposes QIAPrep Spin Miniprep Kit was used. The purification procedure is comparable to JetStar™ 2.0 Plasmid Purification Kit procedure, but DNA is adsorbed to the silica membrane of QiaPrep columns at high salt concentrations and eluted at low salt concentrations.

4.9. ADC Generation

The conjugation of linker-drugs can be achieved using several techniques. Some of these techniques require prior modification of the antibody. The antibody formats used in this thesis are depicted in figure 27. Formats A, B and C are designed for enzymatic modification using sortase A. In the case of format A and B, a conventional IgG molecule is elongated *C*-terminally by a $(G_4S)_3$-spacer and the sortase A recognition sequence LPETGS or by the sortase A recognition sequence LPETGS only. Format C is a bispecific antibody-format generated using the strand-exchange engineered domain (SEED) technology. This allows to combine a scFv and a Fab portion that bind to different antigens. Additionally, the Fab is elongated *C*-terminally by the sortase A recognition motif LPETGS. Format D enables the production of ADCs with up to four drugs per mAb. Therefore LCs contain $(G_4S)_3$-spacer and the sortase A recognition sequence LPETGS and the HCs are extended *C*-terminally by the SrtA recognition motif LPETGS. For the conjugation of maleimide containing linker-drugs native mAbs (format E) can be utilized.

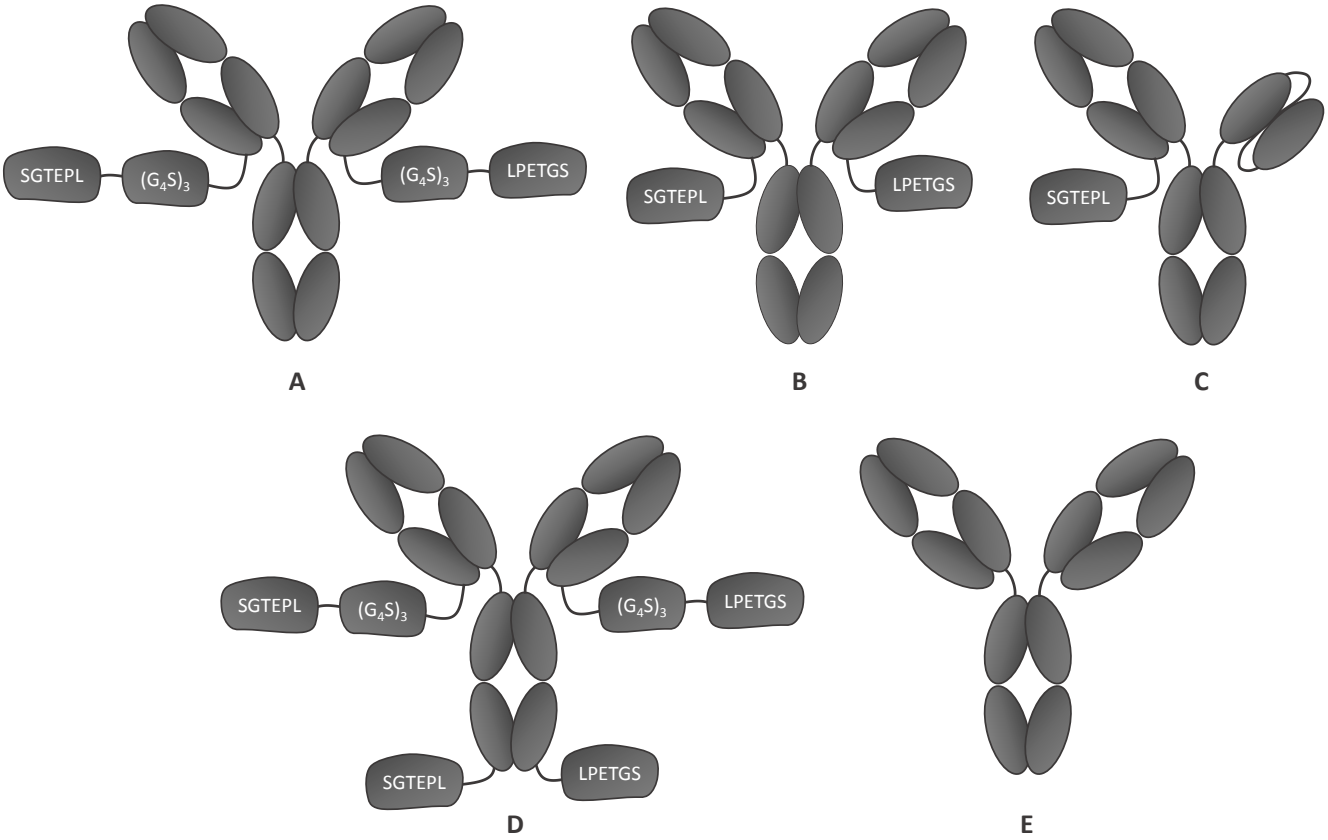

Figure 27: Antibody formats used in this thesis. A) LCs of antibody are elongated *C*-terminally by the motif $(G_4S)_3$LPETGS. B) LCs of antibody are elongated *C*-terminally by the motif LPETGS. C) SEED antibody carrying scFv on one chain, and a Fab on the other chain. The Fab is elongated *C*-terminally by a LPETGS sequence. D) Antibody carrying a total of four SrtA sites. A $(G_4S)_3$LPETGS SrtA recognition motif is fused *C*-terminally to the LCs, and a LPETGS sequence *C*-terminally to the HCs. E) Native mAb.

During this work, several purification methods were used, which are summarized in figure 28. After conjugation of the mAb using either thiol coupling or enzymatic conjugation via SrtA, the crude ADC mixture needs to be purified to deplete excess linker-drug, conjugation reagents or enzymes. A convenient strategy is the purification via preparative SEC (route A), which diretly yields a purified ADC. The use of Protein A chromatography always implies additional purification step that exchange the buffer to ensure ADC storage in an appropriate buffer. Therefore, Protein A chromatography is followed by desalting (route B). However, this method further dilute the sample, which might require a concentration step (route C). Another route uses Protein A chromatography, followed by desalting. If aggregates are present, prepartive SEC can be used to deplete high molecular species. Due to dilution of the sample, concentration yields the purified ADC (route D).

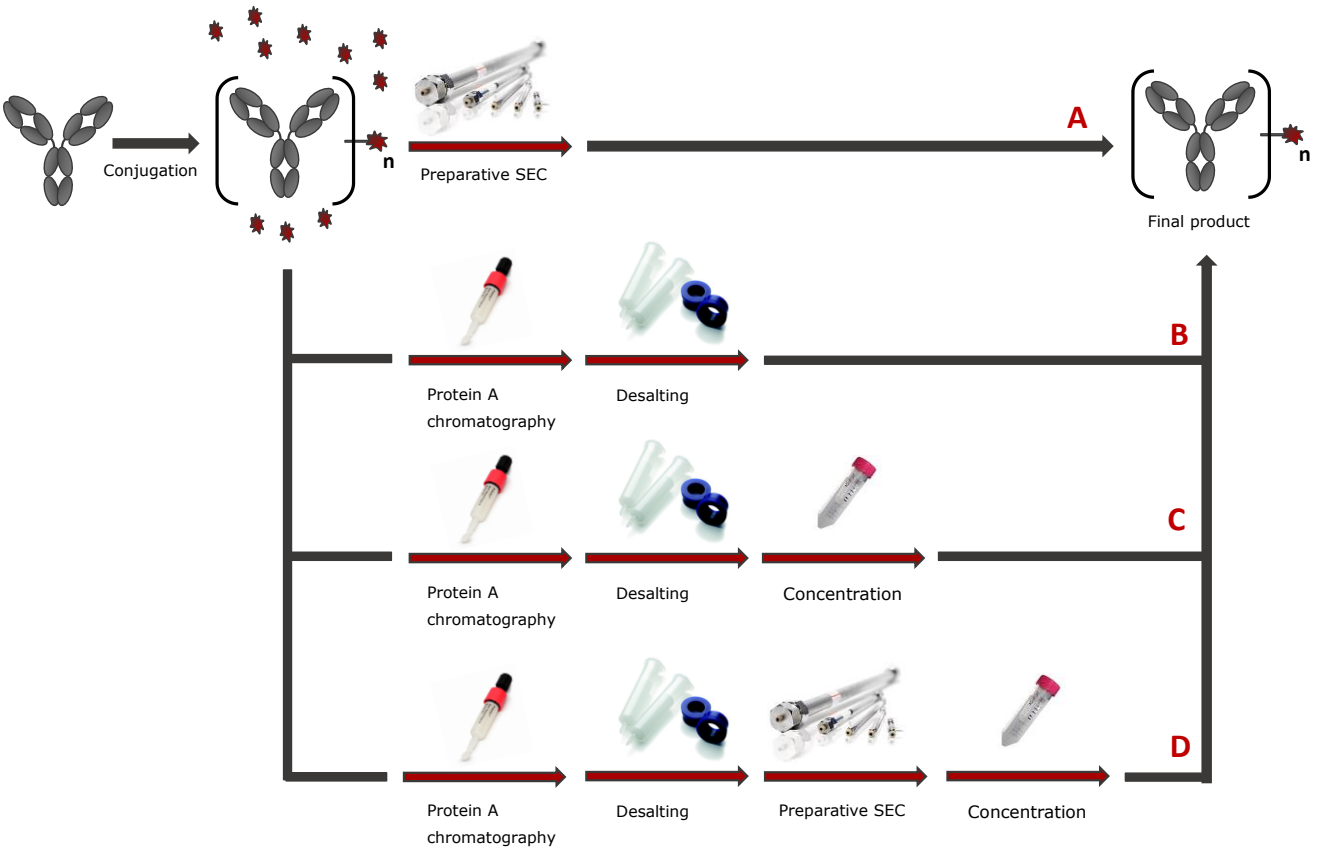

Figure 28: Purification routes for the generation of ADCs. The linker-drug is conjugated to yield a crude ADC mixture. Purification can be achieved via several routes. A) Preparative SEC. B) Protein A chromatography and desalting to change the buffer. C) Protein A chromatography, followed by desalting to exchange the buffer. Subsequently, the ADC mixture can be concentrated again. D) Protein A chromatography, followed by desalting to exchange buffer. Aggregates can be removed by preparative SEC, and the sample can be concentrated. These routes yield a purified ADC.

4.10. Sortase A-Mediated Conjugation Reaction

The reaction is carried out using 10 equivalents of oligo-glycine cytotoxic substrate per SrtA recognition motif of the antibody. 0.37 equivalents Sortase A are applied compared to antibody. Sortase A has a binding site for calcium ions. The binding of calcium ions slows the motion of Sortase A, thereby allowing the binding of the substrate to Sortase A. This leads to an eightfold increase in activity.[121]

13.5 µM (1 eq) antibody construct

5 mM (375 eq) $CaCl_2$

133 µM (10 eq) oligo-glycine substrate per SrtA recognition motif.

5 µM (0.37 eq) eSrtA

The reagents and buffer are mixed in the described manner. The reaction mixture is diluted with reaction buffer to adjust the given concentrations. The reaction is performed by incubation of the mixture at 22 °C for 30 minutes. The addition of SrtA marks the start of reaction. The reaction is stopped by addition of 750 eq EDTA,

which removes free calcium ions from the solution by forming a complex. The final concentration of antibody in solution is adjusted to 13.5 µM by addition of a sufficient amount of buffer.

4.11. Protein A Chromatography

The basis for the purification of IgG antibodies is the high binding affinity of *Staphylococcus aureus* protein A to the Fc region of IgG-type antibodies. The binding between protein A and IgG antibodies takes place at physiological pH and ionic strength, whereas the binding is disrupted at low pH resulting in elution of the antibody. It was shown, that IgG molecules usually elute at pH 3.0.[122]

Antibody purification: Preparative protein A-affinity chromatography was performed on ÄKTAXpress (GE Healthcare) chromatography system using HiTrap™ 1 mL of 5 mL Protein A HP column (GE Healthcare). Upon binding of the antibody to the column, it was washed with binding buffer. Afterwards elution was performed in one step by washing the column with 100 % elution buffer. The antibody was eluted in 1.5 mL fractions onto 100 µL neutralizing buffer into a 96-deepwell plate. The fractions were analyzed using SDS-PAGE regarding purity and pooled accordingly.

ADC purification: ADCs were purified as described before, but on an ÄKTA Purifier (GE Healthcare) chromatography system using HiTrap™ 1 mL 5 mL Protein A HP column (GE Healthcare). The sample was applied on the column using an autosampler by SunChrom. Fractions of 1 mL were eluted into 1.5 mL tubes containing 100 µL neutralization buffer. ADC containing fractions were pooled.

4.12. Preparative SEC

The separation principle of SEC is based on differences in elution time of analytes caused by differences in their size. The stationary phase of the SEC column is composed of spherical particles, which have pores. Small molecules can diffuse into the pores, while larger molecules cannot enter the pores and pass through the matrix directly. This leads to an elution of the largest molecules first, followed by smaller molecules in the order of their size.[122]

In the course of this work SEC was used to remove aggregates from antibody preparations, as well as to separate ADCs from conjugation reagents such as enzyme Sortase A and toxin excess. SEC purification was carried out on a Agilent 1260 HPLC system (Agilent Technologies). The flow rate was 0.5 mL min^{-1} and the samples were separated using a Superdex 200 10/30 increase column (GE Healthcare). Samples were eluted in 0.5 mL fractions and pooled to yield the final product. Preparative SEC for the preparation of αHER2-**1** purified via route D was performed on ÄKTAXpress (GE Healthcare) chromatography system using HiLoadTM 16/600 Superdex™ 200 pg column. Therefore the column was washed with water with subsequent equilibration with the mobile phase. After injection, the sample was eluted isocratically at a flow rate of 1 mL min^{-1} and peaks are collected fractionating.

4.13. Analytical HIC

The drug-to-antibody ratio (DAR) of an ADC can be determined using hydrophobic interaction chromatography (HIC). Therefore, proteins are applied in an aqueous mobile phase containing high concentration of chaotropic salt. The individual proteins bind to the stationary phase based on their hydrophobicty and are eluted by gradual reduction of salt content in the order of least to most hydrophobic.[123] The different ADC species and unreacted mAb are separated based on the drug-load. The weighted area-under-curve of the chromatogram can be used to calculate the DAR of the ADC. A representative chromatogram is depicted in figure 29.

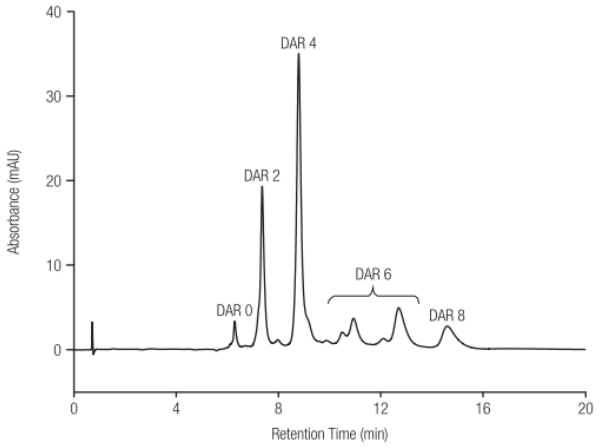

Figure 29: Hydrophobic interaction chromatogram of an ADC. The ADC was prepared using interchain cystein conjugation. This led in the formation of a heterogenous mixture of mAb and ADCs with a DAR of 2,4,6 and 8. Figure copied from HIC column catalogue[123].

All samples were prepared by dilution to a final concentration of 1.5 M ammonium sulfate using sample preparation buffer. Analytical HIC of Sortase A-generated ADCs was performed using HPLC-system (Agilent Technologies) which was equipped with MAB PAK Butyl, 4.6x50 mm column (Thermo Scientific). The UV-VIS detector used wavelengths 220 nm and 280 nm. Measurements were performed at a flow rate of 1 mL min^{-1} applying a gradient of 0 to 100 % buffer B in 20 min. The HPLC-runs were performed at 30 °C. The column was washed subsequently with 100 % buffer B. Data were processed using ChemStation of LC 3D systems (Agilent Technologies).

4.14. Analytical SEC

The monomeric content of mAb and ADC samples was determined by analytical SEC. It was performed on Infinity 1260 HPLC system by Agilent Technologies with a TSK-GEL Super SW 3000 SEC 4.6 x 300 mm column. Elution was performed isocratically at a flow rate of 0.35 mL min^{-1}.

4.15. Buffer Change

The change of buffer is performed using PD-10 Desalting Columns (GE Healthcare), which contain *Sephadex G-25 Medium.* The underlying chromatography method is size exclusion chromatography, where the sample is separated based on the size of the molecules.[122] The elution of proteins often uses harsh buffer conditions that may lead to a decrease in quality of the protein sample. As a consequence buffer has to be changed for storage. For desalting the column was equilibrated by application of three column volumes storage buffer. Then 2.5 mL protein solution were applied on the column, followed by elution using 3.5 mL storage buffer into a fresh falcon.

4.16. Thawing of Mammalian Cancer Cells

The cells provided as cryovial at -80 °C were thawed in a water bath at 37 °C until the ice was dissolved. The cells were resuspended and transferred to a 50 mL falcon tube. The cell suspension was centrifuged (5 min/500 rpm/RT). The supernatant was removed *in vacuo* and the pellet was resuspended in 5 mL cell culture medium. At this point, cells were either used in a cytotoxicity assay directly, or were given into a T75 flask containing 10 mL cell culture medium.

4.17. Culturing of Mammalian Cancer Cells

The cells were usually cultured in T75 cell culturing flasks in an incubator at 37 °C in a 5% CO_2 humid atmosphere and passaged every 3 to 4 days. For passaging, medium was removed in vacuo, cells were washed with PBS (3x) and 1 mL 0.05% Trypsin-EDTA were added. The completion of the detachment reaction was examined visually. When all cells were detached, 9 mL medium were added to the cells to stop the detachment reaction. Depending on the growth rate of the cells, they were splitted 1:2 to 1:4 and reseeded into a fresh T75 flask containing 10 mL of medium. The cells were incubated in an incubator at 37 °C in a 5% CO_2 humid atmosphere afterwards. Cell culturing media and quality control are summarized in appendix 1 and appendix 2, respectively.

4.18. Curve-Shift Assays

In the past chapters, the synergy of duocarmycins and duocarmycin-bearing ADCs with ATR inhibitors was displayed. In this chapter, potentiation effects of duocarmycin-bearing ADCs with ATRi were studied to further elucidate the synergistic effects. Therefore a curve-shift assay system was established which is depicted schematically in figure 30. In a first step, a dose-response curve (DRC) is obtained by treating a certain cell line with an inhibitor. The maximum non-efficacious dose (MNED) can be derived from this DRC. MNED is the highest dose, that can be added to a certain cell line without affecting the viability. The activity of the ADC is confirmed in a separate experiment. Finally, a combination experiment can be conducted. Therefore, the ADC and ADC plus inhibitor at MNED are added to the cells. The inhibitor is tested in parallel at MNED as a control. Due to the

application of inhibitor at MNED, no reduction in cell viability caused by the inhibitor is expected. Three outcomes are possible: 1) The combination of ADC plus inhibitor is equipotent as the ADC only. This would suggest additive effects only. 2) The combination of ADC plus inhibitor is less potent than the ADC alone. Such a result would be interpreted as depotentiation. 3) The combination of ADC plus inhibitor is more potent than the ADC alone. In this case, the potency of the ADC is potentiated.

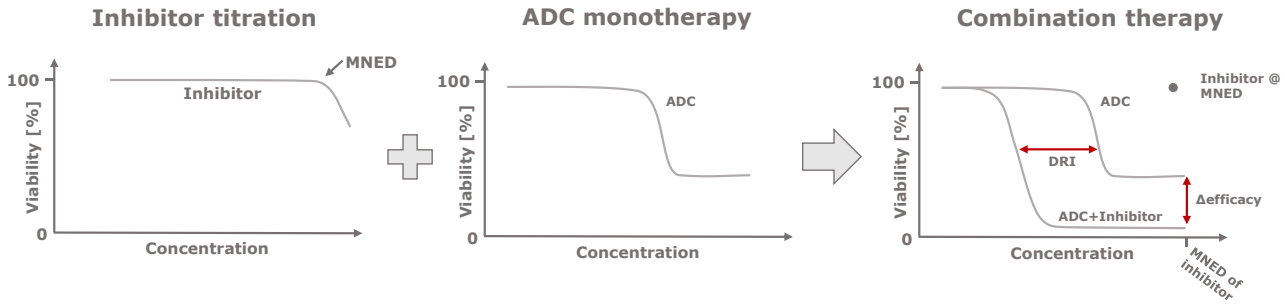

Figure 30: Set-up for curve shift assay. Dose-response curves are depicted to explain the general experimental set-up for curve-shift assays.

Potentiation effects are expressed as dose-reduction indices (DRI), which can be calculated by dividing the IC_{50}-value of ADC by the IC_{50}-value of ADC plus inhibitor according to eq. 2.

$$DRI = \frac{IC_{50}\ of\ ADC}{IC_{50}\ of\ ADC\ plus\ inhibitor} \qquad \text{Eq. 2}$$

Curve-shift assays were conducted as follows: The cell number and viability was determined using ViCell^{TM}-XR (Beckman Coulter) and seeded in opague 96-well plate (10k viable cells/well). After seeding, the plate was incubated (37 °C, 5% CO_2) in a humid chamber overnight. Compounds were diluted in the appropriate medium, added to the cells and the plate was incubated (37 °C, 5% CO_2, 6 d) in a humid chamber. After 30 min equilibration at room temperature, CellTiter-Glo reagent (Promega) was added. After the plate was shaken (3 min, 550 rpm, rt) it was incubated (10 min, rt) and luminescence was read on a synergy 4 plate reader (BioTek). Evaluation was performed using GraphPad Prism version 6.05. Therefor luminescence values were normalized to luminescence values of non-treated cells and dose-response was fitted with 4-point logistic fit.

4.19. Dose-Matrix Assays

Dose-matrix combination assays were performed as described above, but performed in opague 384-well plates (2k viable cells/well). Compounds were added using Tecan D300e liquid. Protein solutions were supplemented with 0.3% Tween-20 (final) and diluted to 1 µM. All wells were normalized to the maximum amount of DMSO (maximum 0.4%) or Tween-20 added. Read out of luminescence was performed on Envision 2104 Multilabel

Reader (Perkin Elmer) and data were evaluated using Genedata Screener® version 14.0.6-Standard (Genedata AG). Luminescence values were normalized to luminescence of non-treated cells and dose-response was fitted using Smart Fit. Synergy scores were calculated using LOEWE synergy model.

4.20. Knock-Down Experiments

$0.7*10^6$ viable cells were seeded in a T25 flask, 5 mL of medium were added and the cells were incubated at 37 °C and 5% CO_2 overnight. The transfection was carried out as follows: 2.5 µL Lipofectamine RNAiMAX were diluted with 247.5 µL OptiMEM and a 0.3 µM siRNA (ATR, CHK1 or non-targeting siRNA) solution was prepared in OptiMEM to yield 250 µL final volume. The solutions were mixed and incubated for 20 min at room temperature, followed by the addition of 500 µL cell culture medium. The cell culture medium was removed from the cells, washed with PBS (3x) and the transfection mix was added to the cells. After 4 h incubation at 37 °C and 5% CO_2, the transfection mix was removed *in vacuo*. The cells were washed with medium (3x), 5 mL medium were added and the cells were incubated for 60 h at 37 °C and 5% CO_2. Then cells were detached, and seeded into 384-well plates. Then a cytotoxicity assay was performed as described before in chapter 0, but with one compound only.

4.21. Statistical Analysis

Statistical analysis was performed using the two-sided T.TEST formula in Microsoft Excel assuming unequal variance. The Null hypothesis for curve-shift assays was that the combination of two compounds is equally cytotoxic as the single agents alone. The Null hypothesis for synergy experiments was that the two combinations are equally synergistic. Graph annotations: *: P<.05, **: P<.01, ***: P<.001, ****: P<.0001.

4.22. Xenograft Experiment

Female H2d Rag2 mice, 6-8 weeks old, were obtained from Taconic Biosciences, LLC. A xenograft was established by harvesting NCI-N87 cells from cell culture, mixing the cells 1:1 with Matrigel and injecting $2.5x10^6$ cells subcutaneously into the flank of the mice. The tumor volume was assessed twice weekly by length measurements in two dimensions using calipers. The volume was calculated following eq. 3 where the length L is the longest tumor length and W is the shortest tumor length.

$$V_{tumor} = \frac{L * W^2}{2} \qquad \text{Eq. 3}$$

After an initial tumor growth phase, mice were randomized and assigned to treatment groups comprising 10 animals. The initial tumor volume amounted to approximately 100 mm^3 when treatment started. Vehicle treated mice obtained a solution of 0.5% Methocel, 0.25% Tween-20 in water. A single dose of 1.0 mg/kg ADC αHER2-**6** dissolved in 10 mM histidine, 8% trehalose, 0.05% Tween-20, pH 6.0 buffer was given intravenously into the tail vein. The 50 mg/kg AZD6738 and ATRi **1** were given per oral dissolved in 0.5% Methocel, 0.25% Tween-20 in water once daily for two weeks. Mice were weighted twice weekly to assess the body-weight during the treatment period. The criteria to terminate the study for single animals were skin ulzerations, tumor length exceeding 15 mm or tumor exceeding 10% of the body weight. In addition, body weight loss was a criterium for termination if body weight loss exceeded 20% accompanied with a haggard appearance, body weight loss exceeded 20% on three successive days or if body weight loss exceeded 25% of the adjusted body weight. Treatment groups were completely terminated if less than eight animals/group were left and therefore no statistical analysis could have been performed. The tumor response criteria were as follows: 1) treatment result was termed tumor progression if the change in tumor volume was > 73% at the end of the observation phase compared to the start of treatment. 2) Tumor stasis was reached if the tumor volume change was between -66% and 73% of initial tumor size at the end of treatment. 3) A tumor reduction of more than 66% at the end of treatment was termed regression. 4) Treatment result was termed complete regression if the tumor was non-palpable or < 20 mm^3 at the end of treatment. The study was executed by Louisa Huettel and directed by Ana Hecht.

4.23. Cellular CHK1 Phosphorylation Inhibition

This assay was performed in the laboratory of Beatrix Blume, department of Cellular Pharmacology, Merck KGaA. 3500 HT29 cells (medium see appendix 1) per well were seeded in 30 µL into a black 384-well plate. Cells were incubated for 1 h at 22 °C followed by overnight incubation at 37 °C, 10% CO_2, and 90% relative humidity. Serial dilutions of ATRi were added to the cells simultaneously with hydroxyurea at a final concentration of 3 mM. 5 µL 7X PBS/HEPES were added and DMSO yielding 0.5% final. The plate was incubated for 4 h at 37 °C, 10% CO_2, and 90% relative humidity. Supernatant was removed using Tecan-Powerwasher. Cells were fixed by the addition of 30 µL/well 4% poly-formaldehyde in PBS and subsequent incubation for 15 min at 22 °C. Cells were washed once with 80 µL PBS and supernatant was removed using Tecan Powerwasher. 40 µL per well -20 °C cold methanol were added and it was incubated 10 min at 22 °C. Cells were washed once with 80 µL PBS and supernatant was removed using Tecan Powerwasher. 30 µL per well of 0.2% Triton solution in PBS were added to the cells and it was incubated for 10 min at 22 °C. Cells were washed once with 80 µL PBS and supernatant was removed using Tecan Powerwasher. 25 µL of 10% goat serum, 1%BSA, 0.1% Tween-20, 0.1% sodium azide in PBS were added and it was incubated for 60 min at 37 °C. The supernatant was removed and it was stained with 25 µL 1° antibody (phospho-CHK1 (Ser345, 133D3) rabbit mAb) in 1% BSA, 0.1% sodium azide in PBS overnight at 4-8 °C. It was

washed trice with 80 µL PBS and the supernatant was removed. 25 µL 2° antibody (Alexa Fluor® 488 goat anti-rabbit F(ab')2 fragment) and 0.2 µg/mL propidium iodide in 1% BSA, 0.1% sodium azide in PBS were added. The plate was incubated for 60-90 min at 37 °C. It was washed trice with 80 µL PBS and 80 µL PBS supplemented with 0.1% sodium azide were added. The plate was sealed with transparent adhesive seals. Images were aquired at IMX Ultra and images were analyzed using Metaexpress 5.3.

5. Results

5.1. Screening for Synergistic Drug Combination Partner for Duocarmycins

The screening of synergistic drug combinations can be accomplished by performing a dose-matrix assay. Therefore, two drugs are serial diluted and mixed at every dose level, yielding a dose-matrix. The drug combination can be additive if the effects of the combination are identical to the added effects of the single agents. However, the effects of the combination might also be stronger than the activity of the single agents. This scenario is termed synergy, whereas weaker combination effects compared to the single agents are termed antagonism. A dose-matrix assay is depicted schematically in figure 31 which illustrates the outcomes of a dose-matrix assay: additivity, antagonism and synergy.

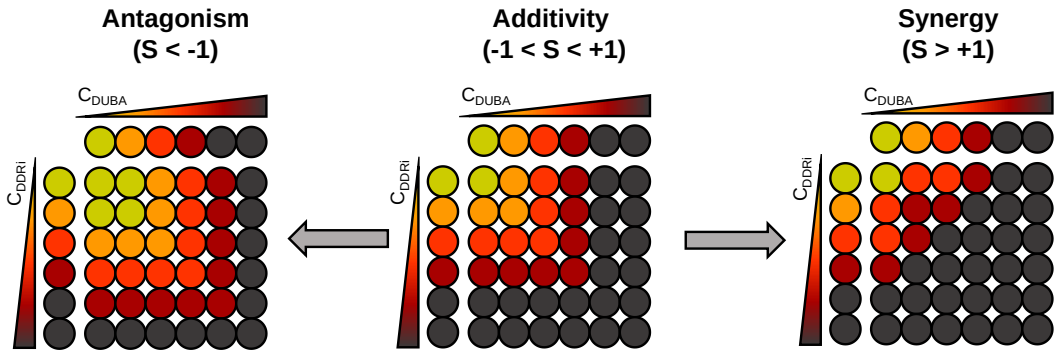

Figure 31: Scheme of experimental set-up of dose-matrix assays for the determination of synergy scores. Serial dilutions of DUBA with increasing concentrations from left to right and serial dilutions of the DDRi from top to bottom are added to cells alone or in combination. The cells respond to the treatment strongly (dark) or weakly (light). Three cases have to be considered: 1) Additivity: The compounds do not interact and the resulting response of the cells does not exceed the response of the single agents. 2) Antagonism: The effect of the combination is weaker than the effect of the single agents. 3) The response to the combination treatment is stronger than the effect of the single agents.

The screening was conducted by serial diluting the duocarmycin derivative DUBA (**10**) and the DDRis. The serial dilutions were added to HCC-1954 or MDA-MB-468 cells either alone or in combination subsequently. Figure 32 illustrates the process of the determination of synergy scores examplarily. DUBA was combined in a dose-matrix assay with hycanthone (Figure 32 A). The cell viability was measured after 6 d of treatment using the CellTiter-Glo assay kit. The signals of the cell viability assay were normalized to untreated cells and fitted. Subsequently, a prediction of additive effects according to Loewe additivity model was calculated for every dose-pair of DUBA and DDRi based on single agent activity. By substracting the modeled data from the fitted data, an excess matrix was generated. The excess matrix can be considered as a visualization of the differences between model and actual data which also highlights spots of either high synergy or antagonism. The quantification of the combination effects, however, was performed by calculating synergy scores. Thererfore, a weighted volume between the model and the fitted actual data was calculated using the GeneData Screener software which is expressed as a synergy score (S) according to the definition of the synergy score by Krueger *et al*.[22] In case of the

combination of DUBA and Hycanthone, the synergy score amounts to 0.1 indicating addtivity. The same procedure was repeated for the combination of DUBA and AZD6738 (Figure 32 B). The excess matrix identified a hotspot of additional cytotoxicity at concentrations of 160 to 630 nM AZD6738 and 0.16 to 0.039 nM DUBA. In this range the activity of the combination killed up to 69% more of the cancer cells than the combination would have killed if the combination was additive. The additional cell cytotoxicity of the combination translated into a synergy score of 7.6. Besides synergy score, the potency of the drugs in monotherapy was obtained from these experiments. When plotting the activity data of the drugs DUBA and AZD6738 against the corresponding concentrations (Figure 32 B, green and violet box), a dose-response is yielded which was fitted using a logistic function. The potency was obtained from this dose-response curve. The resulting dose-response curves are depicted in figure 32 C.

The scattering of S was determined in a sham control experiment to define a cutoff for classifying a combination as truly synergistic or antagonistic. Thus seven different compounds were combined with itself on four different cell lines and the three-σ confidence interval was calculated around the mean of the measurement. According to these experiments, a combination with S in the range 0.6 to -0.7 had a probability of 99.7% to be additive. For the sake of convenience the cutoff was set to a value of ±1.

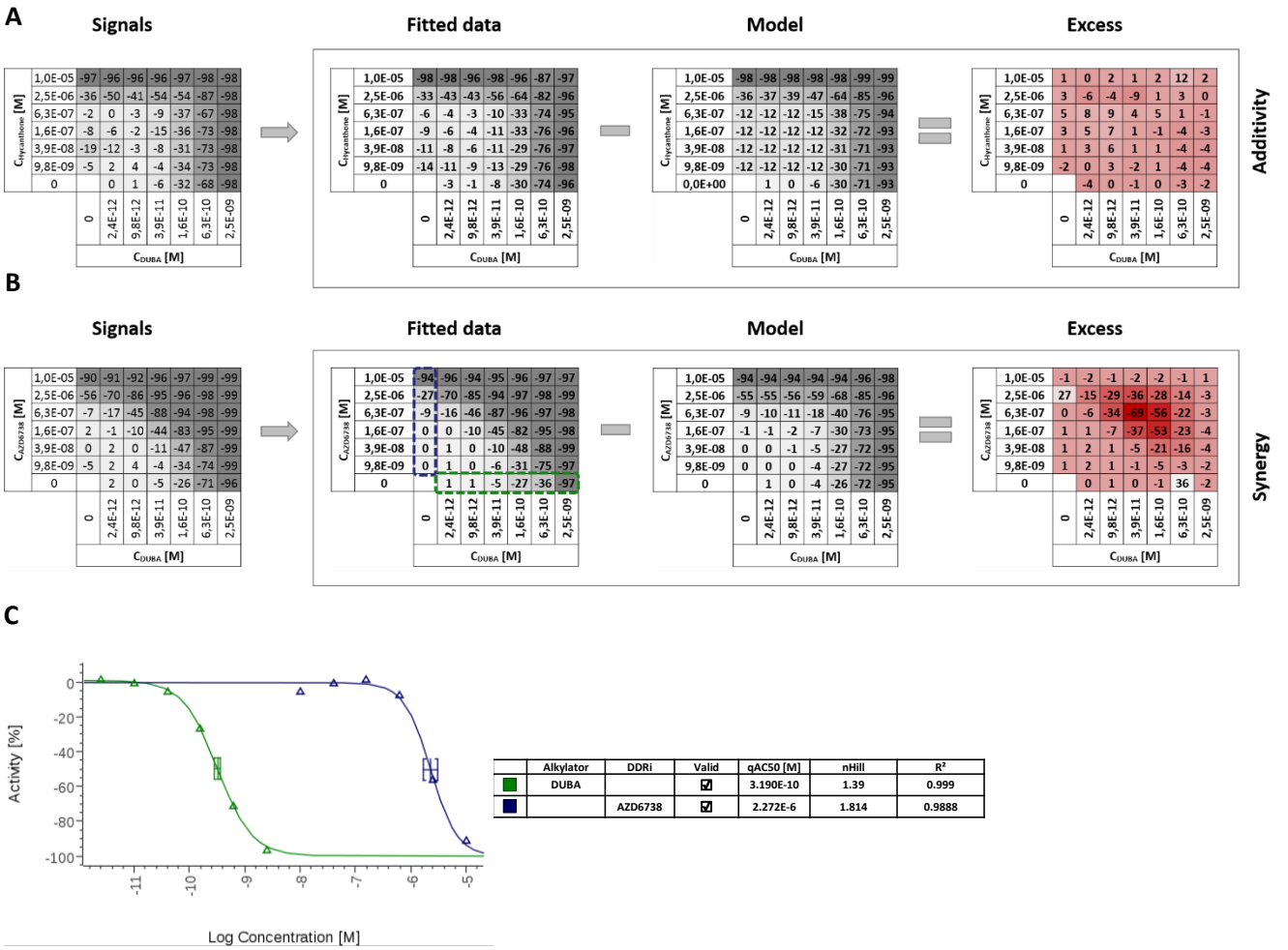

Figure 32: Route to synergy scores based on GeneData Screener data evaluation. Cells were treated with a dose-matrix of Hycanthone and DUBA or AZD6738 and DUBA. The assay was developed using the CellTiter-Glo kit. Finally, data were loaded into GeneData Screener and data were normalized to untreated cells. A) Data of the combination of DUBA plus Hycanthone. The signals were fitted and model data were generated based on LOEWE synergy model. Therefore, single agent data were used to predict signals that would arise if the combination was additive. By subtracting the model from the fitted data, an excess matrix is generated that visualizes differential effects between the data obtained from the experiment and the model of additivity. The excess matrix has excesses ranging from plus to minus single digit activities. The combination of Hycanthone and DUBA led to a synergy score of 0.1 indicating additivity. B) Combination data of DUBA combined with AZD6738. Data were handled as in A. The excess matrix shows maximum excess activities of around -69 indicating a strong deviation of the data from the model. The combination of DUBA with AZD6738 is synergistic with a synergy score of 7.6. C) Dose-response curve of DUBA (green) and AZD6738 (violet). The data are obtained from fitted data in B by plotting the activity of either drug against the logarithm of the dose when given alone to the cells.

Synergy scores (S) were obtained from the combination experiments that indicated additivity (-1>S<+1) if model and actual response were equal. If the actual response exceeded the model, a combination was synergistic (S>1) while it was antagonistic (S<1) if cells treated with the combination responded weaker compared to the single agents than to the combination treatment. The magnitude of the score determined the extent of the combination effects.

A low-throughput screening was performed to identify a synergistic combination partner for duocarmycin. Therefore, 17 small molecule DNA damage response inhibitors (DDRis) were selected that were either interfering with DNA damage repair, cell cycle regulation, DNA remodeling or that induced DNA damage based

on literature data indicating a potential role in the repair of duocarmycin-induced lesions. The inhibitors with corresponding target and mode auf action are summarized in table 2.

Table 2: Inhibitors used in the screening. Target enzyme and mode of action of each inhibitor are listed and a class is assigned according to the function of the enzyme.

Inhibitor	Target	Mode of action	Class
Amuvatinib	multiple tyrosine kinases[124]	Decreased Rad51 expression[124], thus impairing HR[125]	DNA repair
Lomeguatrib	O^6-alkylguanine-DNA-alkyltransferase[126]	Removes alkylation adducts at O^6 of guanine[126]	
NU7441	DNA-PK[127]	Double-strand repair[127]	
Olaparib	PARP[97]	SSB sensing[97]	
Tanespimycin		Downregulation of ERCC1 mRNA[128], required in NER[129]	
TH588	MTH1[130]	Oxidation damage repair[131]	
AZD1775	WEE1[132]	Blocking of G2/M transition for elongated period of time for DNA repair[133]	Cell cycle
AZD6738	ATR[133]	Cell cycle and DNA damage response regulation[133]	
AZD7762	CHK1[133]	Cell cycle arrest, DNA repair regulation[133]	
cmpd31	NEK1[134]	Essential for ATR activity[135]	
KU-55933	ATM[133]	Impaired HR and NHEJ[133]	
LY2603618	CHK1[133]	Cell cycle arrest, DNA repair regulation[133]	
Bleomycin A5		induces double strand breaks[136]	DNA damage
Etoposide	TOP2[137]	Double-strand breaks[137]	DNA remodeling
CP-724714	HER2[138]	HER2 inhibition impairs ATR activation[138]	Other
Hycanthone		RNA synthesis inhibitor	Other
Lapatinib	HER2/EGFR[139]	HER2 inhibition impairs ATR activation[138]	Other
Ciliobrevin D	Cytoplasmic dynein[140]	Intracellular trafficking hinders delivery of repair enzymes[141]	Protein transport

First, inhibitors were selected that were directly involved in DNA repair. Fork collapse as a result of duocarmycin-induced replication fork stalling might lead to double-strand breaks.[142] Thus, it was hypothesized that inhibitors of repair pathways involved in the repair of double-strand breaks might synergize with duocarmycin. Therefore amuvatinib, a down-regulator of homologous recombination repair, the ATM inhibitor KU-55933 or the DNA-PK inhibitor NU7441 were combined with duocarmycin. The synergy score of KU-55933 plus DUBA exceeded the cutoff for synergy on HCC-1954 cells (S=2.1±1.2) barely, indicating either off-target inhibition or the formation of double strand breaks as a result of duocarmycin-treatment. The combination of duocarmycin-variant DUBA with DNA-PKi NU7441 or amuvatinib did not yield a synergy score exeeding the cutoff.

Besides the inhibition of double-strand repair, Bleomycin A5 and the topoisomerase II inhibitor Etoposide were combined with DUBA to overload repair capacities. On HCC-1954 cells Bleomycin A5 combined with DUBA exceeded the cutoff barely (S=1.6±1.0) while the combination was in the range of additivity on MDA-MB-468 cells (S=0.4±1.0). The combination of Etoposide with DUBA led to additive effects on both HCC-1954 (S=-0.7±0.5) and MDA-MB-468 cells (S=-0.3±0.2).

The second group of selected DNA repair inhibitors was involved in the repair of damaged bases. Base excision repair is required for the direct removal of bulky DNA lesions. It was shown, that the base excision repair enzyme DNA glycosylase AlkD of *Bacillus cereus* mediates the removal of lesions caused by the duocarmycin-analogue yatakemycin.[143] Therefore, the effects of inhibiting a human glycosylase using the O^6-alkylguanine-DNA-alkyltransferase inhibitor Lomeguatrib were studied. Only weak synergistic effects with high variance were observed when Lomeguatrib was combined with duocarmycin on the cell line MDA-MB-468 (S=2.8±2.3) while additivity was observed on HCC-1954 cells (S=0.1±1.3). In addition to Lomeguatrib another BER inhibitor, TH588, was combined with DUBA. TH588 inhibits MTH1, which is involved in the resection of oxidatively damaged bases.[130,131] However, on HCC-1954 (S=-0.2±0.3) and MDA-MB-468 cells (S=-0.4±0.3) additive effects were observed.

The repair pathway for the removal of damaged nucleobases is nucleotide excision repair (NER). It plays a role in the repair of duocarmycin alkylation lesions. In the presence of helicase II and DNA polymerase I, CC-1065 (**15**) lesions were excised by ABC excinuclease.[144] However, NER was not recruited of cell extracts of NER-proficient HeLa cells.[145] Only few NER inhibitors were commercially available, so the HSP90 inhibitor Tanespimycin was studied in combination experiments. The inhibitor down-regulated expression of ERCC1, a key enzyme in NER.[128] On HCC-1954 the combination of DUBA with Tanespimycin (S=1.4±0.4) exceeded the cutoff.

A more general approach that impairs DNA damage repair was decreasing the capacity of the cells to import DNA damage response proteins to the nucleus. Microtubule-targeting agents like vincristine inhibited the translocation of the DNA repair enzymes to the nucleus leading to an accumulation of the proteins in the cytoplasm.[141] It was hypothesized that, upon duocarmycin-treatment, the dynein inhibitor ciliobrevin D might hinder the transport of the DNA damage response enzymes to the nucleus and thereby increase the accumulation of DNA damage. However, the combination of ciliobrevin D with duocarmycin-derivative DUBA exceeded the cutoff only barely on the cell line HCC-1954 (S=1.2±0.6) while on MDA-MB-468 cells additive effects were observed (S=0.2±0.5). These results were in line with the combination experiments of the microtubule inhibiting ADC Kadcyla plus AZD6738. The synergy scores of Kadcyla combined with AZD6738 were S=1.1±0.3 on MDA-MB-453 and S=0.3±0.2 on NCI-N87 cells indicating only additivity.

The third group of studied inhibitors included drugs that abrogate checkpoint regulation. The WEE1 kinase is involved in checkpoint regulation. Activity of WEE1 lengthens the G2 phase to gain time for the repair of DNA damage accumulated in S phase. When WEE1 is inhibited by AZD1775, the G2/M checkpoint is abolished which leads to the cells entering mitosis. WEE1 inhibition synergizes with CHK1/2 inhibition in patient-derived xenograft models in mice and generally sensitizes cells for treatment with DNA damaging agents.[133] The combination of DUBA and AZD1775 was additive in our study on HCC-1954 (S=0.8±0.1) and MDA-MB-468 (S=0.1±0.4) cells. The enzyme PARP1 plays an important role in several repair pathways like homologous recombination repair, non-homologous end joining and also base-excision repair. Furthermore, it binds to

stalled-replication forks (SRFs) and is activated by the presence of SRF. Cells lacking PARP1 are sensitive to treatment with hydroxyurea and excess thymidine which causes replication fork collapse or stalling, respectively.[146] Since the treatment with duocarmycin leads to the formation of stalled replication forks,[147,148] this suggests a potential role in the sensing of duocarmycin-induced DNA lesions. In this study, olaparib combined with DUBA displayed additive effects on HCC-1954 (S=0.6±0.4) and minor synergistic effects on MDA-MB-468 cells (S=1.1±0.1).

ATR and CHK1 kinases are crucial enzymes in the cell cycle but also DNA-damage response regulation. In this report, the ATRi AZD6738 and the CHK1i LY2603618 as well as AZD7762 were identified as synergistic combination partners of DUBA. The ATRi AZD6738 strongly synergized with DUBA on HCC-1954 cells (S=6.9±0.7) and MDA-MB-468 cells (S=5.7±1.0). The synergy was stronger for ATRi AZD6738 plus DUBA than for LY2603618 plus DUBA on HCC-1954 (S=4.1±0.3, P=.00002) and MDA-MB-468 cells (S=4.4±1.7, P=.3). Again, the combination of AZD6738 with DUBA also exceeded the synergy observed for AZD7762 combined with DUBA on HCC-1954 (S=3.6±0.4, P=.0002) and on MDA-MB-468 cells (S=2.6±0.2, P=.01).

Functional HER2 was described to be essential for the activation of the G2/M checkpoint following irradiation of MCF7 cells. HER2 inhibition led to abolished ATR and CHK1 signaling following treatment of MCF7 with irradiation.[138] Since in the course of this work, it was shown that ATR and CHK1 synergized with DUBA, it was studied whether the dual-epidermal growth factor receptor and HER2 inhibitor Lapatinib or the HER2 inhibitor CP724714 synergized with DUBA. The combination of both inhibitors with DUBA resulted in additive effects on HCC-1954 and MDA-MB-468 cells.

NEK1 is a kinase associated with ATR and ATRIP that regulates the interplay between these two kinases.[135] Although originally designed for the inhibition of NEK2, cmpd31 inhibits NEK1 with a potency of 0.17 µM.[134] Thus, cmpd31 was combined with DUBA. On HCC-1954 (S=0.3±0.1) and MDA-MB-468 cells (S=0.4±0.2) only additivity was observed. The results of the dose-matrix assays are depicted in figure 33.

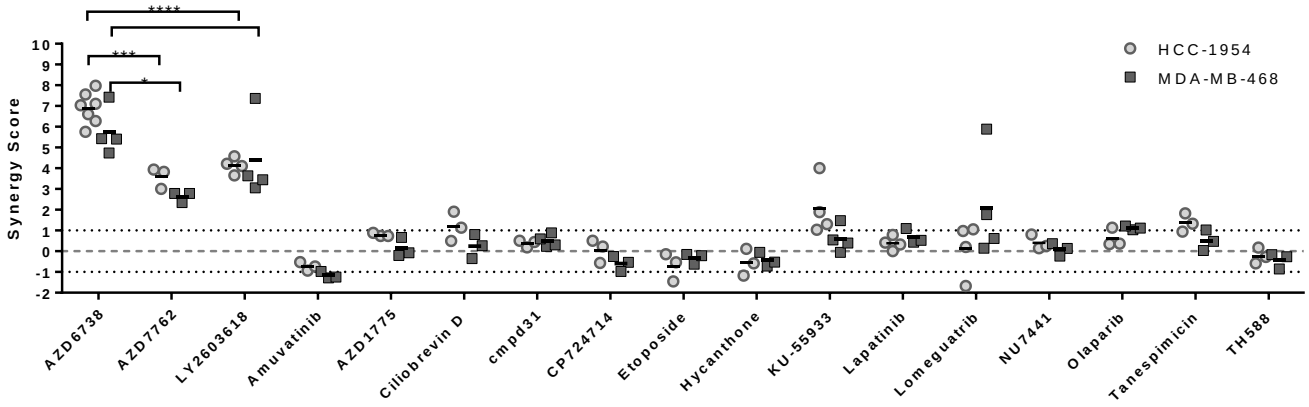

Figure 33: Results of the synergy screening. Duocarmycin variant DUBA was combined with DDRi on HCC-1954 and MDA-MB-468 cells and the combination effect was reported as synergy score. A cutoff synergy score of ±1 was defined. In this range, S of combinations is assumed to be additive, S>1 indicates synergism, S<1 indicates antagonism. Individual data points from independent experiments are depicted as well as the mean of the biological replicates as bar.

Since kinase inhibitors often display off-target effects, ATR and CHK1 levels were decreased using siRNA knock-down to prove the essential role of these enzymes for the survival of the cells treated with duocarmycin. Therefore, HCC-1954 cells were seeded into T25 flasks and left to adhere overnight. Then the cells were washed with PBS, and subsequently ATR, CHK1 and non-targeting siRNA were added. The cells were incubated for 4 h, washed with medium and incubated for 3 d. Cells were detached and seeded into 384-well plates. They were treated with duocarmycins for 6 d. Cell viability was determined via CellTiter-Glo assay kit, and data were evaluated using GraphPad Prism. The knock-down efficiency was evaluated using quantitative PCR (performed by Nicole Hoelzer) (Table 3).

Table 3: Knock-down efficiency of ATR and CHK1 as determined by quantitative PCR. The efficiency of individual experiments is noted.

Cells	Knock-down efficiency [%]
ATR KD	90, 74
CHK1 KD	63, 15

The results are displayed in figure 34. DUBA was more potent on ATR knock-down (IC_{50}=0.25 nM) and CHK1-knock-down cells (IC_{50}=1.1 nM) compared to cells treated with non-targeting siRNA (IC_{50}=1.5 nM). Similar results were obtained for DDM which was again more potent on ATR (IC_{50}=0.014 nM) and CHK1 (IC_{50}=0.133 nM) knock-down cells than on control cells (IC_{50}=0.23 nM). The differences between CHK1 and non-targeting siRNA treated cells were small, but DUBA was 5.8-fold and DDM 17.3-fold more potent on ATR knock-down cells than on control cells.

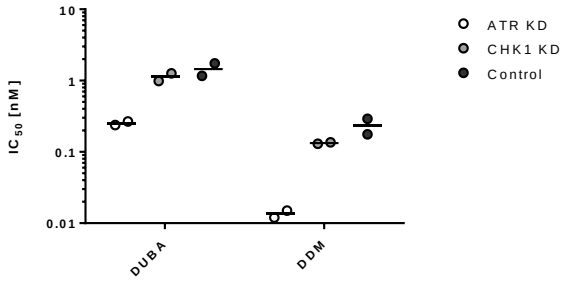

Figure 34: Potency of DDM and DUBA on cells treated with ATR or non-targeting siRNA. Individual data points and mean of IC_{50}-values as black bar are displayed.

All in all, the combination of DUBA with the ATRi AZD6738 yielded superior synergistic effects compared to DUBA plus CHK1i LY2603618 or AZD7762. In addition, the potentiation of the duocarmycins was stronger on ATR knock-down versus CHK1 knock-down cells. Taken together, it was proceeded with studying the drug combination of duocarmycin with ATR inhibitors due to their consistently stronger synergistic effects. So far, only the duocarmycin variant DUBA was studied in combination with ATRi. To ensure that synergistic effects are also observed with other duocarmycin variants, a library of duocarmycins variants with varying properties caused by different alkylating and binding units were evaluated in combination with ATRi in the following experiments.

5.2. Synergistic Drug Combinations of a Duocarmycin library with ATR inhibitor AZD6738

A series of duocarmycin variants was studied after the identification of the synergistic drug combination DUBA plus AZD6738. This should verify that the observed synergy is not an effect caused by DUBA, but duocarmycins in general. Therefore, the duocarmycin variants were clustered into two groups according to their structural features. In the trimethoxy indole (TMI)-series, the binding unit of the duocarmycin is kept constant, while the alkylating unit varies. The alkylating unit of Duocarmycin SA (**13**) and CBI-TMI (**24**) consist of a tricyclus, however, with different stereoelectronic properties. The alkylating unit of the latter have a chiral center. Contrasting this, three achiral duocarmycin variants were investigated. From these, two variants, duocarmycin **35** and **36**, had a bicyclic alykalting unit, while **37** had a monocyclic alkylating unit. The structures of the TMI-series are summarized in table 4.

Table 4: Chemical structures of duocarmycins from the TMI-series. In the trimethoxy indole (TMI)-series, the binding unit is kept constant, while the alkylating unit varies. Cytotoxicity of the duocarmycin variants was determined by treating HCC-1954 cells with the compounds. The potency of the duocarmycin variants is expressed as mean of IC_{50}±SD of N=3 biological replicates except in case of variant **35**, where mean and individual IC_{50} values are noted. Synergy scores were obtained by combination treatment of HCC-1954 cells with the duocarmycin variant and AZD6738. Synergy scores are depicted as S±SD of N=3 biological replicates. Compounds **35** to **37** were kindly provided by the laboratory of Dr. Carl Deutsch, department of ADCs and Targeted NBE Therapeutics, Merck KGaA.

Alkylating unit	Binding unit	No.	IC_{50} [nM]	S
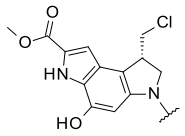	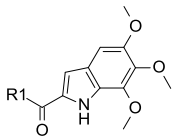	**13**	0.3±0.1	4.1±0.4
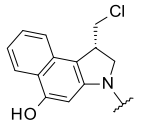		**24**	24±32	6.1±1.2
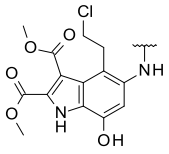		**35**	43.5 (44, 43)	5.2±0.2
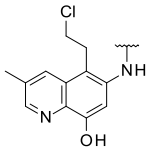		**36**	3.0±0.4	6.7±0.8
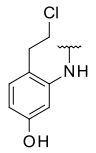		**37**	1200±536	2.8±0.5

The TMI-series might elucidate the influence of the alkylating unit on the synergy between duocarmycins and ATR inhibitors. The cyclopropabenzindole (CBI)-series (Table 5) was used to study the influence of the binding

unit on the synergistic effects between duocarmycin variants and ATRi. In the CBI-series, the alkylating unit is kept constant with only minor modifications like methyl or hydrogen in R1 and the binding unit is varied.

Table 5: Chemical structures of duocarmycins from the CBI-series. In this series, the alkylating unit is a CBI-unit with either methyl- or hydrogen in position R1 of the alkylating unit. The binding unit in position R2 is varied. Cytotoxicity was determined by treating HCC-1954 with the duocarmycins. Synergy scores were obtained by combination treatment of HCC-1954 cells with the duocarmycin variant and AZD6738. Data of **10** and **38** are IC_{50}±SD and S±SD of N=7 or N=9 biological replicates, respectively. For experiments with N=2 biological replicates, mean and individual IC_{50} values are noted in brackets. Compounds **40** and **10** were kindly provided by the laboratory of Dr. Carl Deutsch, department of ADCs and Targeted NBE Therapeutics, Merck KGaA.

Alkylating unit		**Binding unit**		**No.**	**IC_{50} [nM]**	**S**
	R1	R2	R3			
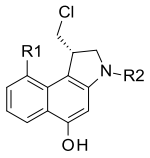	H	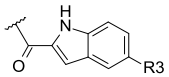	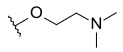	**38**	0.11±0.05	5.6±1.7
	H		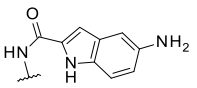	**39**	0.16 (0.21, 0.11)	5.1 (4.8, 5.3)
	Me	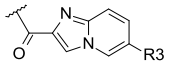		**40**	1.6 (1.7, 1.5)	6.7 (6.3, 7.2)
	Me		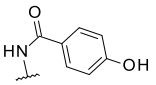	**10**	0.3±0.1	6.9±0.7

To study synergistic effects of the duocarmycin variants in combination with the ATRi AZD6738, HCC-1954 cells were treated either with the single agents or with a combination of the two respective drugs. After 6 d of treatment, CellTiter-Glo luminescent assay was performed and the luminescence was read on Envision Reader. The results were analyzed using GeneData Screener as described before. The outcome of the assay was the potency of the duocarmycin variants and synergy scores for each variant combined with AZD6738.

The potencies in the TMI-series on HCC-1954 cells were scattered strongly (Table 4). While DSA (**13**) had a subnanomolar IC_{50}-value of 0.3±0.1 nM, the duocarmycin variant with the monocyclic alkylating unit **37** had a micromolar IC_{50}-value of 1.2±0.5 µM. The potencies of the remaining duocarmycin variants in the TMI-series lay in between. Duocarmycin **36** had a potency in the single-digit nanomolar range with 3.0±0.5 nM, and **24** and **35** have IC_{50}-values of 24±32 nM and 43.5 nM, respectively. The potencies of the duocarmycins in the CBI-series were distributed more evenly (Table 5). Duocarmycin DM (**38**) had an IC_{50}-value of 0.12±0.03 nM and DUBA (**10**) an IC_{50}-value of 0.2±0.1 nM. Compound **39** had a potency of 0.16 nM and duocarmycin **40** a potency of 1.6 nM. The previously determined cutoff for synergy scores of 1 was exceeded by all compounds tested. However, the synergy scores varied strongly in the TMI-series. While the duocarmycin with the bicyclic, achiral alkylating unit **36** reached a synergy score of 6.7±0.8 in combination with AZD6738, it was followed by the duocarmycins with tricyclic, chiral alkylating units CBI-TMI (**24**) (S=6.1±1.2) and DSA (**13**) (S=4.1±0.4). Drug **35** with the bicyclic, achiral alkylating unit had a score of 5.2±0.2 when given together with AZD6738. The weakest synergistic effects

were reached with the duocarmycin **37** comprising the monocyclic, achiral alkylating unit (S=2.8±0.5). The differences were less pronounced in the CBI-series. The duocarmycins DDM (**38**) and **39** had synergy scores close to each other (S=5.6±1.7 and S=5.1, respectively). The duocarmycins with the methyl-CBI unit as alkylating unit also had comparable synergy scores. While DUBA (**10**) had a synergy score of S=6.9±0.7 when combined with AZD6738, the combination of the DUBA-progenitor **40** with AZD6738 reached S=6.7.

The drugs DDM (**38**) and DUBA (**10**) were chosen for further experiments. After it was proven that duocarmycins synergized with the ATRi AZD6738 regardless of their structural features, it should be investigated whether the duocarmycin variant DUBA also synergizes with other inhibitors of ATR.

5.3. Biological Activity of ATR Inhibitors

In the combination experiments with AZD6738 it was confirmed that the duocarmycin variant plays a role in the extent of the synergistic effects. In this work, several different ATR inhibitors were investigated to elucidate the influence of the ATRi on the combination effects. An overview of the chemical structures of the ATRi studied in this report is given in figure 35. The ATRi were clustered into four groups. The ATRi from Astra Zeneca AZ20 and AZD6378 are closely related with an identical core unit. Bayer ATR inhibitors also had identical core units. The three Bayer ATRi differed only in R1. The phase I ATRi BAY1895344 carried a pyrazole residue and the ATRi BAY73, published as example 73 in a Bayer AG patent[149], was carrying a methanesulfone pyridine residue in R1. The Bayer ATRi BAY286, published as example 286, carried a methanesulfone moitety in R1. While the ATRi **1**, filed in a patent by Fundación Centro Nacional de Investigaciones oncológicals Carlos III (CNIO)[150], was comparable to the Astra Zeneca ATRi series, the compound VE-822 from Vertex was structurally unrelated to the remaining clusters.

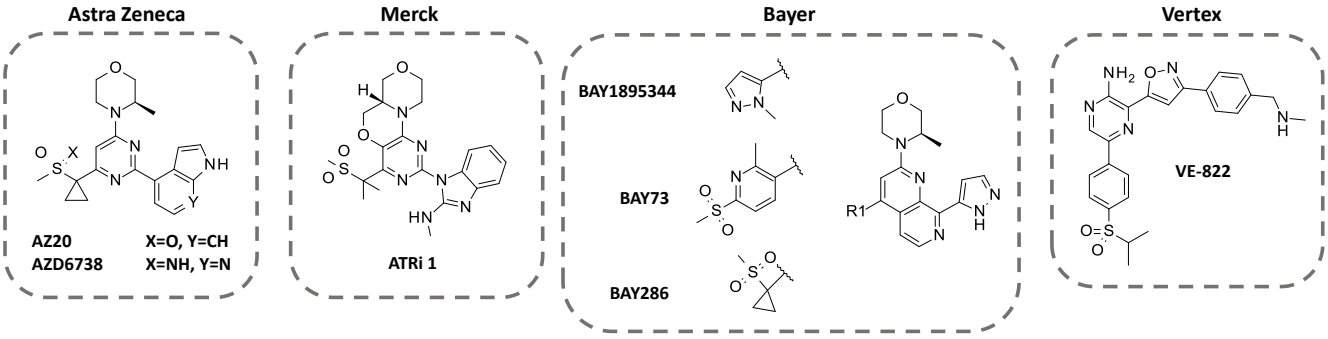

Figure 35: Chemical structures of the ATRi studied in this work. The ATRi can be clustered into four structural groups. In case of the Astra Zeneca series, two closely related drugs were tested. The Bayer cluster comprises three ATRi with a similar core structure. The ATRi from Merck ATRi **1** and VE-822, formerly from Vertex, form distinct clusters.

The structure determines the biological activity of the drugs. Table 6 summarizes characteristic properties and the chemical structures of the ATRi. Two compounds developed by Astra Zeneca were studied, namely AZ20 (ATRi **2**) and phase I ATRi AZD6738 (ATRi **3**). Furthermore, compounds from Bayer were included. The phase I ATRi BAY1895344 (ATRi **1**) was studied, as well as two ATRi, published as example 73 or example 286 in a patent by Bayer AG[149], termed BAY73 (**6**) and BAY286 (ATRi **5**), respectively. In addition, ATRi **1** and Merck's phase I ATRi VE-822 (ATRi **7**) were investigated. Cellular cytotoxicity was represented by the anti-proliferative potency on HCC-1954 cells.

AZD6738 was the least potent ATRi in the panel (2.2±0.7 µM) followed by AZ20 with an IC_{50}-value 1.6±0.5 µM. VE-822 was potent in submicromolar range with a potency of 0.9±0.4 µM. The potency increased with ATRi **1** (0.4±0.2 µM) and the drugs from Bayer BAY1895344 (0.05±0.02 µM), BAY73 (0.12±0.03 µM), BAY286 (0.08±0.02 µM). In addition, cellular cytotoxicity was determined on NCI-N87 and MDA-MB-453 cells. While ATRi **1** was

potent in the same range on NCI-N87 (0.36±0.07 nM) and on MDA-MB-453 (0.32±0.5 nM) cells as on HCC-1954, the potency of BAY1895344 varied stronger between the cell lines. It was remarkably less potent on NCI-N87 (0.3±0.3 nM) and MDA-MB-453 (0.2±0.2 nM) when compared to HCC-1954 cells. AZD6738 on the other hand was more around twice as potent on NCI-N87 (0.98±0.09 nM) and MDA-MB-453 (1.1±0.3 nM) cells compared to the potency on HCC-1954 cells.

Another assay was used to study the cellular effects of the ATRi on the cells according to Kawasumi *et al.*[151] Replication stress is induced in HT29 cells by treatment with hydroxyurea. As a result CHK1 is phosphorylated in an ATR-dependent manner. ATR inhibitors block the ATR-mediated phosphorylation of CHK1. The extent of CHK1 phosphorylation inhibition was assessed subsequently by staining of phospho-CHK1. The assay set-up is depicted in figure 36. The results were kindly provided by the laboratory of Dr. Beatrix Blume.

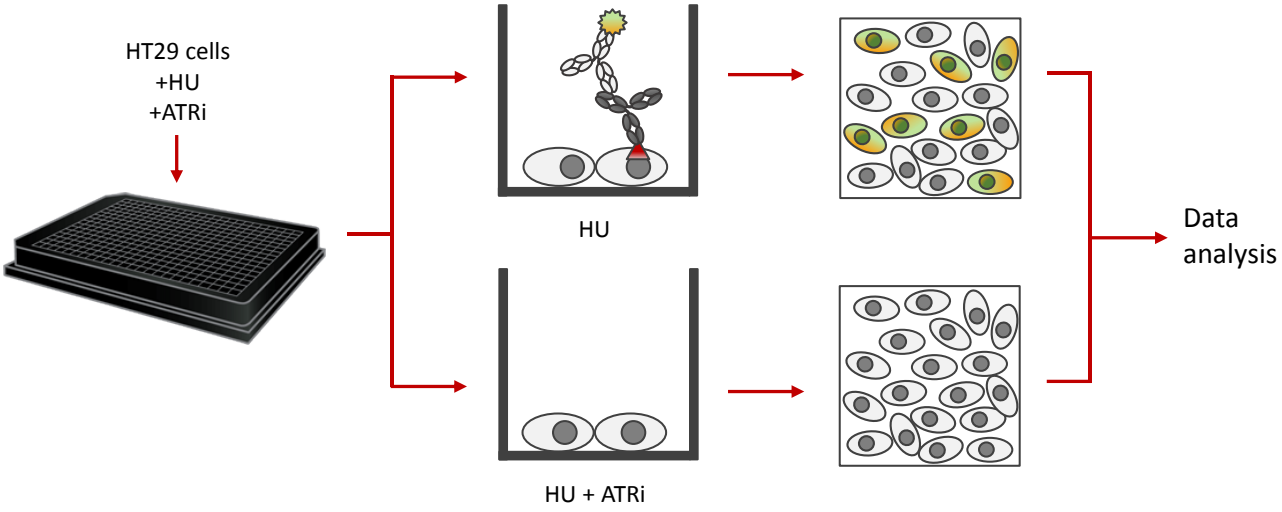

Figure 36: Assay set-up for the determination of CHK1 phosphorylation inhibition by ATRi. HT29 cells were incubated with hydroxyurea with or without ATR inhibitors. Cells were fixed, permeabilized and subsequently stained with an anti-phospho-CHK1 antibody. The latter antibody was stained with a flurescently labeled mAb. While cells stressed with hydroxyurea were positive for anti-phospho-CHK1 staining, the signal was dose-dependently suppressed in cells treated with HU and ATRi. The quantification of cells positive or negative for staining allowed the determination of the potency of the ATRi. Figure adapted according to Kawasumi *et al.*[151] and the picture of the 384-well plate was obtained online from nexelcom[152].

The inhibition of CHK1 phosphorylation upon treatment with hydroxyurea on HT29 cells was used to rank the ATRi. While AZ20, AZD6738 and VE-822 inhibited phosphorylation of CHK1 in the triple-digit nanomolar range (135 nM, 287±153 and 197±78 nM, respectively), ATRi **1** (9±5 nM) and the Bayer ATRi BAY1895344 (7±4 nM), BAY286 (2.4 nM), BAY73 (4±3 nM) showed comparable potencies in the single-digit nanomolar range. The cellular CHK1 inhibition potency data were kindly provided by the laboratory of Beatrix Blume, department of Cellular Pharmacology, Merck KGaA.

Table 6: Summary of ATR inhibitors. Trivial name and structure are depicted. The cellular toxicity on HCC-1954, NCI-N87 and MDA-MB-453 cells and the inhibition of hydroxy urea induced phosphorylation of CHK1 on HT29 cells are noted as mean±SD of IC_{50}-values. The data are displayed as mean±SD and the number of individual experiments is noted in brackets. The cellular CHK1 inhibition potency data were kindly provided by the laboratory of Dr. Beatrix Blume, department of Cellular Pharmacology, Merck KGaA.

			Cytotoxicity IC_{50}			**Inhibition of CHK1 phosphorylation IC_{50}**
ATRi	**No.**	**Structure**	**HCC-1954**	**NCI-N87**	**MDA-MB-453**	**HT29**
			μM			nM
ATRi **1**	**1**	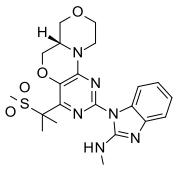	0.4±0.2 (9)	0.36±0.07 (3)	0.32±0.5 (3)	9±5 (9)
AZ20	**2**	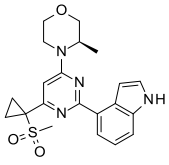	1.6±0.5 (7)	-	-	135 (130, 140)
AZD6738	**3**	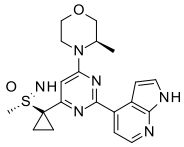	2.2±0.7 (21)	0.98±0.09 (3)	1.1±0.3 (6)	287±153 (9)
BAY1895344	**4**	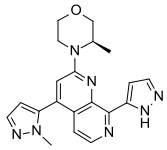	0.05±0.02 (9)	0.3±0.3 (3)	0.2±0.2 (4)	7±4 (4)
BAY286	**5**	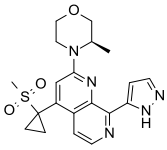	0.08±0.02 (5)	-	-	2.4 (3.8, 0.95)
BAY73	**6**	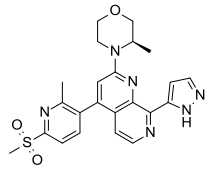	0.12±0.03 (7)	-	-	4±3 (4)
VE-822 (VX-970, M6620 Berzosertib)	**7**	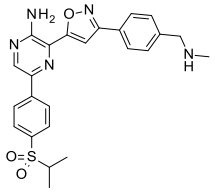	0.9±0.4 (7)	-	-	197±78 (95)

5.4. ADC generation

5.4.1. Generation of Duocarmycin-Bearing ADCs

In this work, several duocarmycin-bearing ADCs were generated based on antibodies targeting cancer-related receptor-tyrosine kinases HER2, EGFR and mesenchymal–epithelial transition (MET). The linker-drugs that were coupled to these antibodies were specified by the tag LD-X, where X refers to the index number of a specific structure. The name of the resulting ADC was composed of the target or the name of the antibody and the linker-drug index number. For instance, an ADC composed of linker-drug **1** (LD-**1**) and the anti-EGFR (αEGFR) antibody or anti-HER2 (αHER2) carried the name αEGFR-**1** or αHER2-**1**, respectively.

The linker-drugs for the generation of duocarmycin-bearing ADCs are summarized in table 7. The basic structure of the linker-drugs utilizes a dipeptide valine-citrulline linker, which can be cleaved by cathepsin B. The dipeptide is followed by a self-immolative module, which ensures efficient drug release upon cleavage. The self-immolative module carries either a methyl group or a diethylgycol moiety in R2 position. The basic structure is elongated *N*-terminally at R1. The linker-drugs LD-**1** to LD-**5** contain a *N*-terminal triple-glycine sequence to enable Sortase A (SrtA)-mediated conjugation. Several modifications were introduced to increase the solubility of the linker-drugs. LD-**2** and LD-**5** are modified with ethyleneglycol. Since charge can also mediate solubility, LD-**3** contains a lysine which is positively charged at physiologial pH. LD-**6** was conjugated *via* chemical conjugation techniques. LD-**7** is modified *N*-terminally by a maleiimde motif for the conjugation to thiols. In both linkers, an ethyleneglycol unit is incorporated to increase solubility. The duocarmycin-variants DDM (LD-**1**), DUBA (LD-**2** to LD-**6**) and DSA (LD-**7**) were used as drugs in R3.

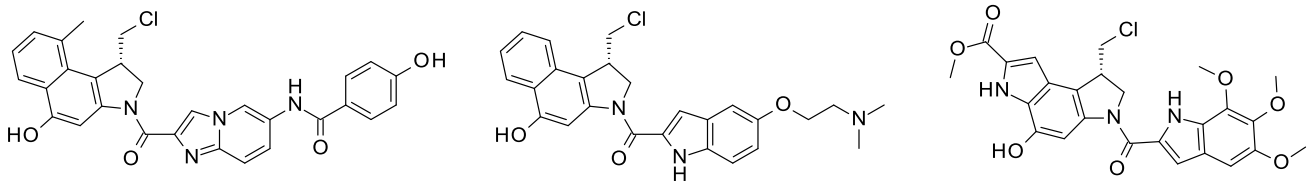

10 **38** **13**

Figure 37: Chemical structures of the duocarmycin-variants DUBA (**10**), DDM (**38**) and DSA (**13**) studied in the ADC format. The drugs are displayed in the *seco*-form.

Table 7: Duocarmycin-based linker-drugs used for ADC preparation in this thesis. R1: Linker-drugs LD-**1** to LD-**5** are modified *N*-terminally with a triple-glycine motif that is recognized by SrtA. LD-**2** to LD-**5** contain modifications that increase the hydrophilicity. Thus, ethyleneglycol units are introduced in LD-**2** and LD-**5**. LD-**3** comprises a lysine residue and hence is positively charged at a physiological pH. LD-**6** was prepared by chemical conjugation to the αHER2 antibody. LD-**7** carries a *N*-terminal maleimde residue for conjugation using thiol coupling and ethyleneglycol units for increased solubility. R2: Methyl group or diethyleneglycol is used. Diethyleneglycol increases solubility. R3: Linker-drugs contain Duocarmycin DM (LD-**1**), DUBA (LD-**2** to LD-**6**) or DSA (LD-**7**). The linker-drugs **2** to **6** were kindly provided by the laboratory of Dr. Carl Deutsch, department of ADCs and Targeted NBE Therapeutics, Merck KGaA.

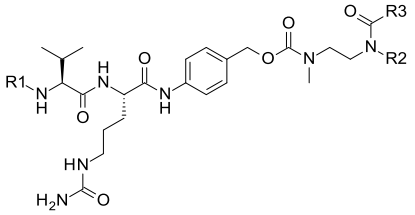

Linker-drugs	R1	R2	R3
1	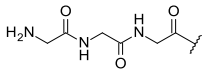	Me	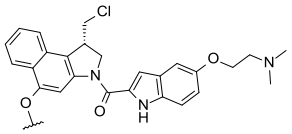
2	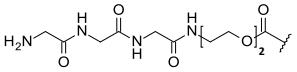	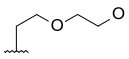	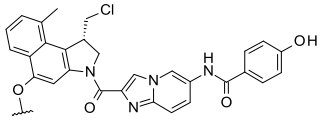
3	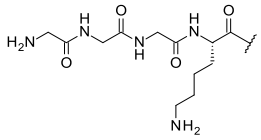	Me	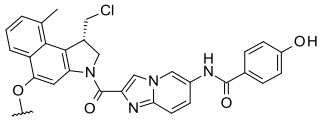
4	Not disclosed	Me	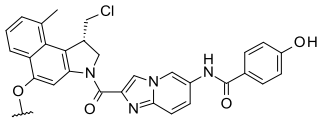
5	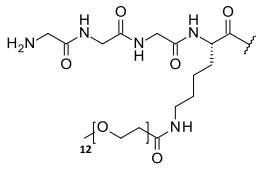	Me	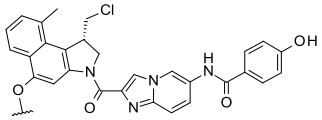
6	Not disclosed	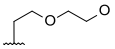	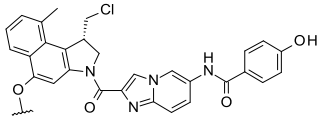
7	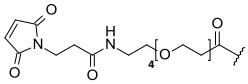	Me	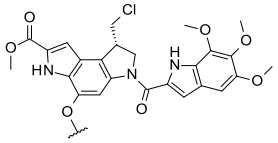

The conjugation of LD-**1** to the αHER2 mAb was performed using SrtA-conjugation. Therefore, antibody modified *C*-terminally with $(G_4S)_3$-LPETGS was mixed with LD-**1**, $CaCl_2$ solution and buffer. Then SrtA was added to start the reaction. After 30 min of shaking at 22 °C, the reaction was stopped by adding an excess of EDTA. The sample was then subjected to Protein A chromatography. The flow through was discarded, and after a

washing section, the ADC was eluted using an acidic pH shift. After buffer exchange and concentration, the resulting purified ADC was analyzed by analytical HIC and SEC. The chromatograms of such a purification are exemplarily shown in figure 38.

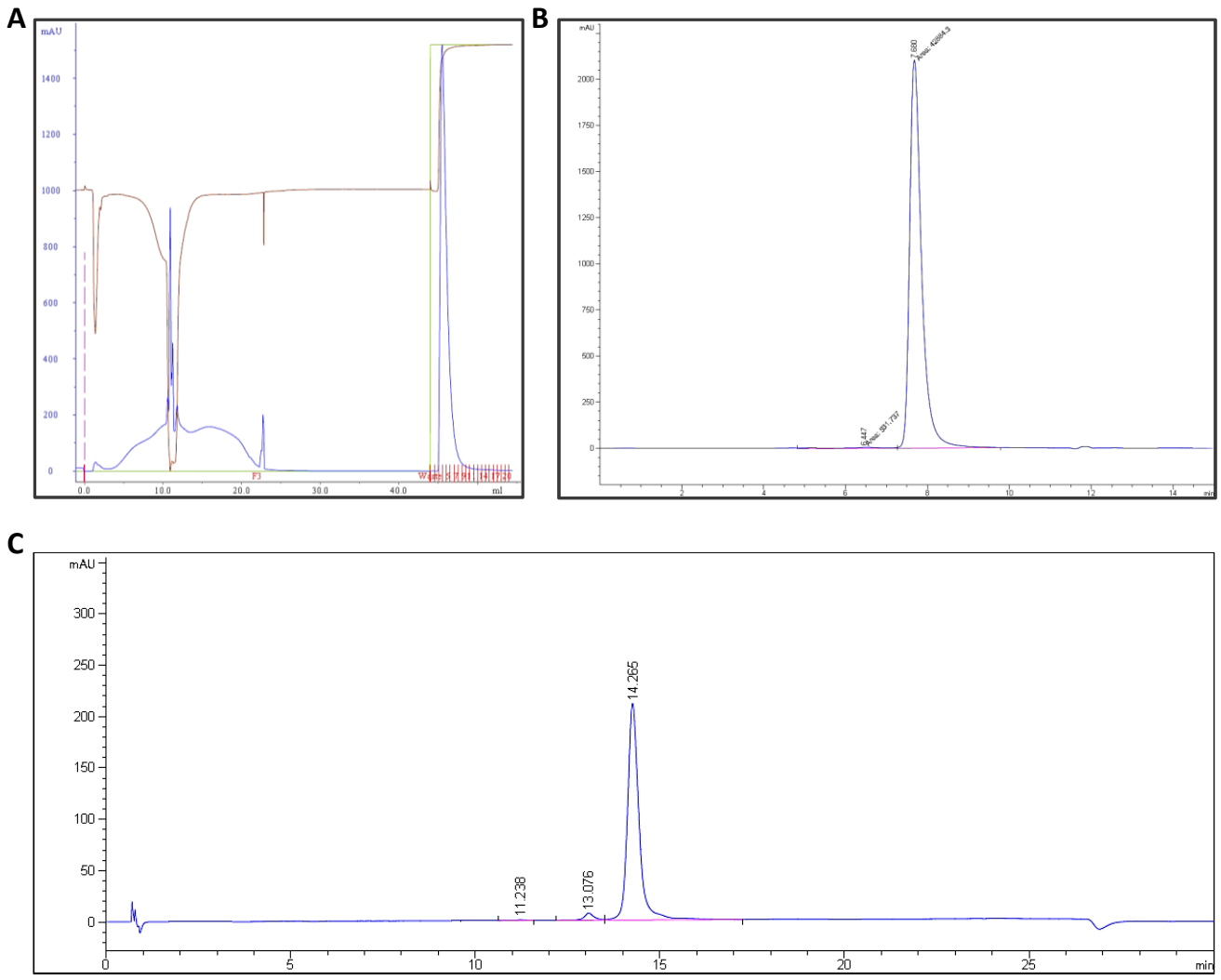

Figure 38: Chromatograms of ADC preparation and analysis. A) Chromatogram of preparative Protein A chromatography. The sample was subjected to a protein A column. Up to 20 mL eluent flew through before the ADC was washed and eluted by an acidic pH shift. Fractions were collected and pooled. The UV-signal is shown in blue, the conductivity in brown. In green, ratio buffer B/buffer A is displayed. B) Chromatogram of analytical scale SEC. The blue signal is the UV-absorption. 98.8 % of the ADC was monomeric. C) HIC chromatogram of purified ADC. The blue signal is the UV-absorption. 0.27% unconjugated mAb at retention time 11.238 min, 2.87% of monofunctionalized ADC at retention time 13.076 min and ADC with a DAR of 2 at retention time 14.265 min were detected. This ADC composition had an overall DAR of 1.97.

The αHER2 mAb was used as a tool antibody in the course of this work to study the impact of duocarmycin linker-drugs on the producibility of ADCs. Therefore, LD-**1** to LD-**5** were conjugated to the αHER2 mAb via SrtA-mediated conjugation in analytical scale reactions at first. The LD-**4** could not be conjugated to the αHER2 mAb, since the resulting product was precipitated. LD-**5** was successfully conjugated to the αHER2 mAb in an analytical scale reaction. However, the conjugation reaction was incomplete, leading to an ADC with a DAR of

approximately 1. The linker-drugs LD-**1**, LD-**2**, and LD-**3** were successfully coupled to the αHER2 mAb using antibody-format A in preparative scale. In this setting, homogeneous ADCs with a DAR>1.85 were prepared and the monomer content of the ADC was at least 95%. While the DUBA-based linker-drugs LD-**2** and LD-**3** were conjugated to the αHER2 mAb in excellent or very good yield, respectively, the preparation of αHER2-**1** was performed in poor to good yield.

In addition to that, LD-**1** was conjugated to the αEGFR mAb cetuximab, and the mAbs αMET, αMETxEGFR and αHEL. The resulting ADCs were prepared in acceptable yields. While a DAR von 1.90 was achieved in the preparation of αHEL-**1**, the preparation of αEGFR-**1** and αMET-**1** yielded ADCs with a DAR of 1.70 and 1.68, respectively. In the case of the αMETxEGFR-**1** ADC a DAR of 0.89 and 0.95, respectively, was achieved. The monomer content of these ADCs was acceptable, except for αMET-**1**, where the monomer content was the lowest with 93.6%.

Table 8: Overview of generated duocarmycin-based ADCs using SrtA conjugation. The column "App." contains the appendix number under which data such as HIC and SEC profile can be found.

mAb	mAb format	Linker-drug	Purification route	Yield [µg] (%)	Yield [%]	DAR	Monomer [%]	App.
αHER2	A	**1**	D/C/C	2760/1443/2850	34.4/28.8/71.0	1.97/1.89/1.96	98.8/95.6/96.7	4/5/6
αEGFR	B	**1**	C	1350	66.5	1.70	98.2	7
αMET	B	**1**	B	1064	52.4	1.68	93.6	8
αMETxEGFR	C	**1**	A/A	503/620	57%/74.3	0.95/0.89	98.4/98.4	9/10
αHEL	A	**1**	C	2400	47.8	1.90	97.2	11
αHER2	A	**2**	B	1984	97.8	1.85	97.4	12
αHER2	A	**3**	A	2150	81.1	1.93	99.3	13
αHER2	A	**4**	-	-	-	Precipitated	-	
αHER2	A	**5**	-	-	-	0.99	-	14
α-GP	B	**1**	D	1215	60.0	1.57	89.4	15

The duocarmycin-bearing ADCs αHER2-**6** and αEGFR-**7** were kindly provided by the laboratory of Dr. Nicolas Rasche. The results of the characterization are summarized in table 9. The ADC αHER2-**6** was generated using chemical conjugation techniqes resulting in an ADC with a DAR of 1.90. αEGFR-**7** was produced by conjugation of LD-**7** to the interchain cysteines. A DAR of 1.54 was achieved. Both ADCs did only contain negligible amounts of aggregates.

Table 9: Overview of duocarmycin-based ADCs which were kindly provided by the laboratory of Dr. Nicolas Rasche, department of ADCs and Targeted NBE Therapeutics, Merck KGaA. αEGFR-**7** was generated using thiol coupling.

mAb	mAb format	Linker-drug	DAR	Monomer [%]
αHER2	Not disclosed	**6**	1.90	98.8
αEGFR	Native (E)	**7**	1.54	99.7

5.4.2. Generation of Control ADCs

As a negative control for combination experiments, a MMAE linker-drug **8** was conjugated to cetuximab using cysteine conjugation. The LD was purchased from Levena Biopharma. This ADC was kindly provided by the laboratory of Dr. Nicolas Rasche, department of ADCs and Targeted NBE Therapeutics, Merck KGaA.

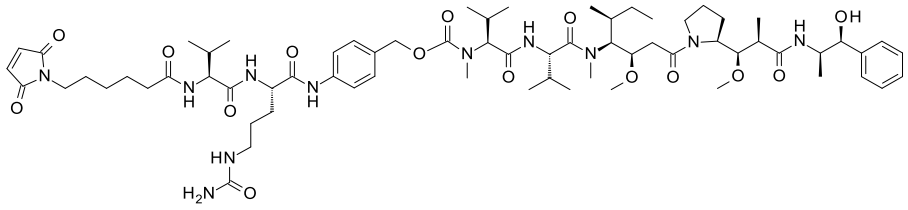

Figure 39: chemical structure of control linker-drug **8**. The linker-drug consists of a maleimide for cystein conjugation, a valine-citrulline dipeptide sequence for Cathepsin B-mediated cleavage and the cytotoxic drug MMAE (**1**).

5.5. Cytotoxicity of Duocarmycin-Based ADCs

In this chapter, the anti-proliferative effects of duocarmycin-based ADCs are described. The cytotoxicity of ADC αHER2-**1** was studied on HER2-positive cells. The cell panel encompassed the breast-cancer cell lines BT-474, HCC-1954, JIMT-1, MDA-MB-361, MDA-MB-453 and SK-BR-3 as well as the lung adenocarcinoma cell line Calu-3. Furthermore, the ADC was tested on a HER2-negative breast cancer cell line MDA-MB-468. αHER2-**1** was active in the double-digit picomolar to single-digit nanomolar range on the HER2-positive cell lines and showed only weak cytotoxicity on HER2-negative cell line MDA-MB-468 in the lower triple-digit nanomolar range. The ADCs αHER2-**2** and αHER2-**3** were as cytotoxic as αHER2-**1** on Calu-3, HCC-1954 and SK-BR-3 cells. However, Kadcyla was 5- to 45-fold less potent on Calu-3 compared to the duocarmycin-based ADCs. Kadcyla, as well as αHER2-**2** and αHER2-**3** were potent in the double-digit nanomolar range on antigen-negative cells. The non-targeting ADC αHEL-**1** exhibited weak anti-proliferative effects on HER2-positive cells in the double- to triple digit nanomolar range. The ADC αHER2-**6** had subnanomolar IC_{50}-values on NCI-N87 and MDA-MB-453, which was comparable to the effects of Kadcyla. αHER2-**6** was comparably as potent as αHER2-**2** on NCI-N87 cells.

Table 10: Cell killing potencies of αHER2-duocarmycin ADCs αHER2-**1**, αHER2-**2** and αHER2-**3** on HER2-positive cell lines and the HER2-negative cell line MDA-MB-468. The control ADCs Kadcyla and αHEL-**1** were tested in parallel. HER2-positive cell lines are indicated by plus sign independently of the total amount of receptor on the surface. Data: IC_{50}±SD of N≥3 biological replicates or if less than three indpendent experiments were performed, mean and individual IC_{50}-values in brackets. Cytotoxicity data are obtained from assays in the 96-well format. a: Assay performed in 384-well format.

		IC_{50} in nM							
	HER2	αHER2-**1**	αHER2-**2**	αHER2-**3**	αHER2-**6**	Kadcyla	αHEL-**1**	DDM (**38**)	DUBA (**10**)
BT-474	+	1.0 (1.2, 0.70)	-	-	-	-	-	-	-
Calu-3	+	0.9±0.4	4±2	1.5±0.9	-	41±22	-	-	-
HCC-1954	+	1±1	2±1	1±1	-	0.50±0.03	230±35	0.11±0.07[a]	0.30±0.07[a]
JIMT-1	+	0.41±0.07	-	-	-	-	-	0.14 (0.20, 0.074)[a]	3±2[a]
MDA-MB-361	+	0.1±0.02	-	-	-	-	29±3	-	-
MDA-MB-453	+	0.3±0.1	-	-	0.5±0.4[a]	0.23±0.04[a]	339±179	0.14 (0.15, 0.13)[a]	0.3±0.1[a]
NCI-N87	+	-	0.15±0.03[a]	-	0.3±0.4[a]	0.10±0.02[a]	-	-	1.2±0.5[a]
SK-BR-3	+	0.08±0.03	0.16±0.05	0.15±0.05	-	0.2±0.1	42±14	-	-
SK-OV-3	+	0.2±0.1	-	-	-	-	-	-	-
MDA-MB-468	-	140±47	28±7	17±4	-	43±9	56	0.02±0.01[a]	0.06±0.02[a]

Muller and Milton stated that at early drug development stages, where only *in vitro* data are available, the therapeutic index might be assessed on the basis of on- and off-target selectivity. Although the target selectivity does not necessarily correlate with an increased therapeutic index *in vivo*, there are many examples where higher target selectivity also led to improved therapeutic window.[153] Therefore, the selectivity indices (SI) of an ADC towards antigen-expressing cells were calculated according to eq. 4 to rank the ADCs. The selectivity index

of an idividual ADC was determined by dividing the IC_{50} on target negative cells by the IC_{50} on target-positive cells.

$$selectivity\ index = \frac{IC_{50}\ of\ ADC\ on\ target\ negative\ cells}{IC_{50}\ of\ ADC\ on\ target\ positive\ cells} \qquad \text{Eq. 4}$$

Selectivity indices for the individual ADCs are depicted in figure 40. The ADC αHER2-**1** is the most selective ADC tested with a mean selectivity index of 639. The ADCs αHER2-**2** and αHER2-**3** with mean selectivtiy indices of 67 and 43 are weakly less selective than Kadcyla with a mean selectivity index of 110. The non-targeting ADC αHEL-**1** has a mean selectivity index of approximately one, which indicates that αHEL-**1** exerts cell killing properties target-independent. The small molecule drugs DDM and DUBA killed MDA-MB-468 cells at lower doses than other cell lines studied, leading to selectivity indices of 0.15 and 0.14, respectively.

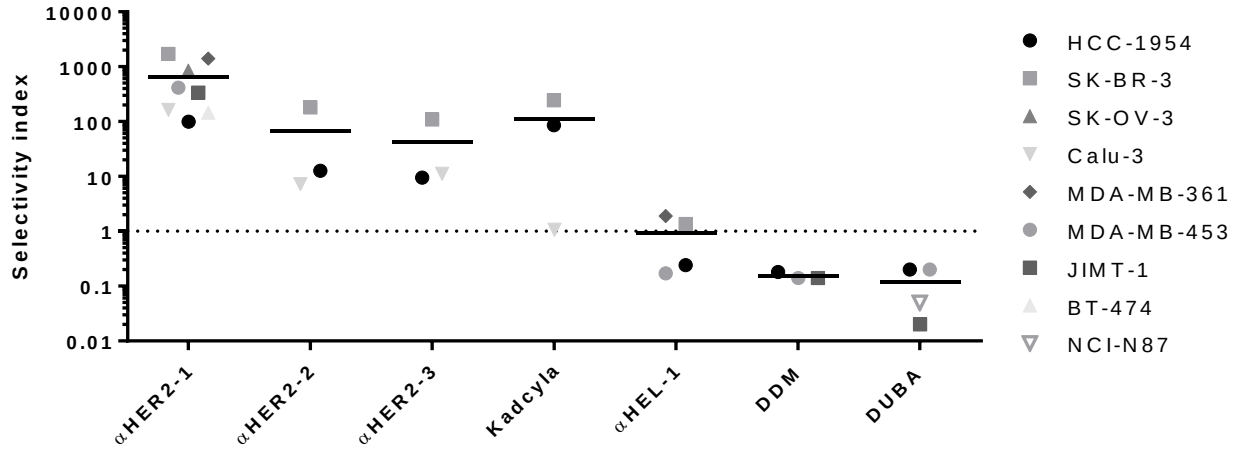

Figure 40: Selectivity indices of αHER2-duocarmycin ADCs αHER2-**1**, αHER2-**2** and αHER2-**3** carrying different linker-drugs, Kadcyla and aHEL-**1** on HER2-presenting cell lines. The selectivity indices were calculated by dividing the IC_{50}-value of the individual molecule on HER2-negative cell line MDA-MB-468 by the IC_{50}-value of the molecule on the indicated HER2-positive cell lines. The bar represents the mean of the selectivity indices for every ADC.

Besides the αHER2 and αEGFR mAb, an αMET and a bispecific αMETxEGFR mAb were used for ADC generation. The resulting ADCs were studied for their anti-proliferative properties (Table 11). The surface expression of the receptors EGFR and MET was reported in literature[67] and classified as positive for 10- to 100 thousand copies, as double-positive for 100 to 1000 copies and as triple positive for >1000 copies per cell. The ADCs αEGFR-**1** and αMET-**1** were potent on EGFR- and MET-postive cells in the subnanomolar range, except for αEGFR-**1** on MKN-45, where the ADC had an IC_{50} value of 45 nM. αMETxEGFR-**1** was less potent on the studied cell lines with IC_{50} values in the single-digit nanomolar range. The ADC αEGFR-**7** killed A431 and MDA-MB-468 cells in the subnanomolar range. On EGFR-negative MCF7 cells, the Duocarmycin DM-bearing ADC αEGFR-**1** and the DSA-

carrying αEGFR-**7** were considerably less potent in the single- to doubledigit nanomolar range. The free drugs DDM and DSA were potent on all cell lines regardless of surface receptor status in the subnanomolar range.

Table 11: Cell killing potencies of αMET-**1**, αEGFR-**1** and αMETxEGFR-1 ADC on cell lines with differential expression of EGFR and MET. For N<3 biological replicates the potency is reported as mean of IC_{50} with individual measurements in brackets. Asteriks indicate that an assay was performed, but the fit was ambigous and no IC_{50}-value was obtained. Receptor densities were classified according to literature[67]. Receptor densities of $10x10^3$-$100x10^3$ copies were classified as "+", $100x10^3$-$1000x10^3$ classified as "++" and densities >$1000x10^3$ were classified as "+++". a: receptor densitiy obtained from internal data. The IC_{50}-values of DDM were already presented in table 10.

			IC_{50} in nM					
	EGFR	**MET**	αMET-**1**	αMETxEGFR-**1**	C-**1**	C-**7**	DDM	DSA (**13**)
A431	++	+	-	-	0.17±0.04	0.21±0.02	0.055±0.005	0.21±0.02
A549	+	+	-	-	*	*	0.1±0.1	0.33±0.07
HepG2	-	(+)	-	-	*	*	-	-
MCF7	-[a]	-[a]	-	-	27±8	9±5	0.164±0.004	0.06±0.02
MKN-45	+	++	0.80 (1.2, 0.41)	2.7 (3.8, 1.6)	45 (0.72, 88)	-	-	-
MDA-MB-468	+++	+	0.91 (0.12, 0.59)	1.9±0.2	0.12±0.08	0.06±0.02	0.02±0.01	0.14±0.07
NCI-H1975	+	+	0.14 (0.20, 0.077)	7.7 (9.3, 6.2)	0.11 (0.15,0.058)	-	-	-

To further elucidate differences between the individual cetuximab-duocarmycin ADCs, selectivity indices were calculated according to eq. 4 using the IC_{50}-values of the ADCs αEGFR-**1** and αEGFR-**7** and the respective small molecule counterparts on EGFR-positive cell lines and the EGFR-negative cell line MCF7. The results are depicted in figure 41. The ADC αEGFR-**1** was more selective towards the cell lines A431 (SI=162) and MDA-MB-468 (SI=222) compared to ADC αEGFR-**7** (SI=40 on A431 and 148 on MDA-MB-468). αEGFR-**1** was selective towards NCI-H1975 cells (SI=257) but showed no selectivity for MKN-45 cells (SI=0.6). The mean selectivity indices for αEGFR-**1** accounted to 161 and for αEGFR-**7** to 94. The small molecule duocarmycins DDM and DSA did not show selectivity for EGFR-overexpressing cell lines (SI_{mean}=0.5 and 0.3, respectively).

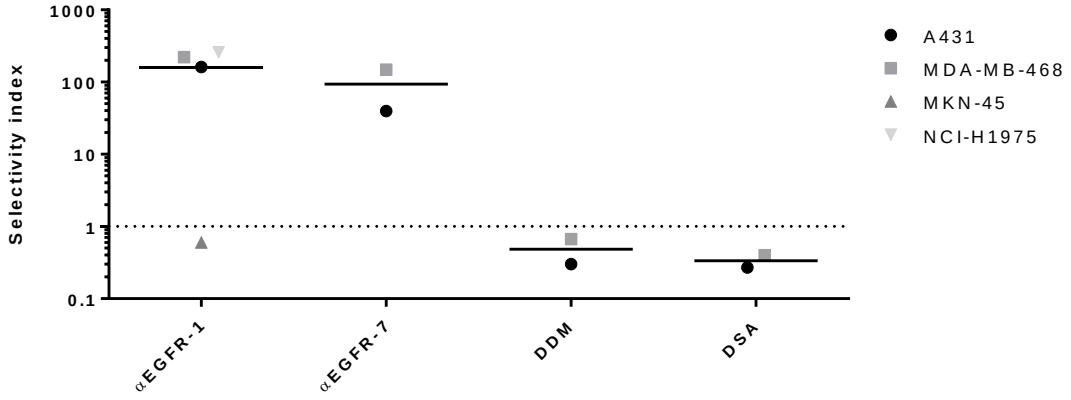

Figure 41: Selectivity indices of anti-EGFR αEGFR-**1** and αEGFR-**7** ADCs for EGFR-overexpressing cell lines. The selectivity was calculated by dividing the IC_{50}-value of the individual molecules on EGFR-negative cell line MCF7 by the IC_{50}-value on the indicated EGFR-positive cell lines. Selectivity for different EGFR-positive cell lines is indicated by shades of grey. The bar represents the mean of selectivity indices over the cell lines treated with a certain ADC.

5.6. Synergy of Duocarmycin-ADCs with ATRi

The small molecule duocarmycins synergized with ATR inhibitors on HCC-1954. ADCs were generated to study the translatabiliy of the combination effects observed with the small molecule combinations with ATRi to duocarmycin-carrying ADCs.

5.6.1. Synergy of Combinations of αHER2-Duocarmycin ADCs and ATRi

HCC-1954 were treated with DDM, DUBA and the corresponding DDM-bearing αHER2-**1** and DUBA-carrying ADC αHER2-**2** (Figure 42) in combination with AZD6738 for 6 d. Then, cell cytotoxicity was determined using CellTiter-Glo kit. Luminescence was read on Envision reader and data were evaluated using GeneData Screener. The combination of DDM with AZD6738 (S=5.6±1.7) was comparably synergistic as the corresponding ADC αHER2-**1** (S=5.1±2.0). The same conclusion can be drawn for the combination of DUBA with AZD6738 (6.9±0.7) and αHER2-**2** plus AZD6738 (7.2±1.0).

As positive controls, SN-38 and Gemcitabine were combined with AZD6738 on HCC-1954 cells. SN-38 as well as Gemcitabine synergized with AZD6738 (S=7.2±0.8 and S=6.9±0.3). The microtubule inhibitor MMAE, however, synergized weakly with the ATRi AZD6738 (S=2.2±0.1) as well as microtubule inhibiting ADC Kadcyla combined with AZD6738 (S=1.3±0.7) on HCC-1954 cells. In this case, one measurement was excluded that yielded a synergy score of 6.4. Thus, αHER2 mAb trastuzumab and DM1 were combined with AZD6738 to elucidate the influence of the two molecular portions on the synergistic effects. Trastuzumab did not synergize with AZD6738 on HCC-1954 cells (S=-0.2±0.2) while DM1 and AZD6738 led to synergistic cell killing (S=2.8±0.5).

Furthermore, the influence of different ATRi on the synergistic effects of the combination with ADC αHER2-**2** or the corresponding small molecule DUBA was studied on HCC-1954 cells. The combination of αHER2-**2** with ATRi **1** was significantly stronger (P=.03) with a score of 12.5±1.7 than the combination of αHER2-**2** with AZD6738 on HCC-1954 cells. When combining the ADC αHER2-**2** with BAY1895344 it was also significantly stronger (P=.003) with a synergy score of 13.1±1.0 than αHER2-**2** combined with AZD6738. The ATRi VE-822 and AZ20 synergized with αHER2-**2** comparable to AZD6738 with synergy scores of 5.7±0.3 and 5.8±0.4, respectively. BAY73 combined with αHER2-**2** had the highest synergy score with 14.4±1.1. BAY286 plus αHER2-**2** had a synergy score in the mid range of 10.4±0.2. The synergy scores of DUBA combined with the ATRi AZ20 (S=5.1±0.5), ATRi **1** (S=12.0±0.6), BAY1895344 (S=12.8±0.5), BAY73 (S=12.4±0.8), BAY286 (S=9.5±0.8) and VE-822 (S=5.3±0.6) on HCC-1954 cells were in good comparison to the ADC αHER2-**2** combined with the respective same ATRi.

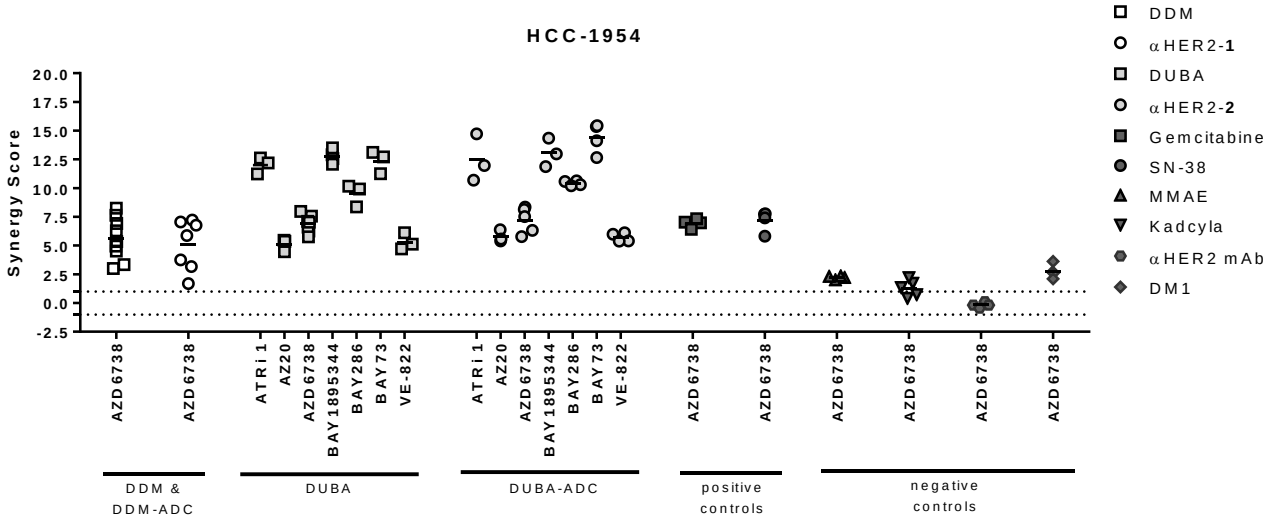

Figure 42: Synergy scores of duocarmycin-based ADCs and small molecules in combination with AZD6738 on HCC-1954. Individual data points are displayed as well as the mean of the individual points represented by a bar.

In a next experiment, the ADCs αHER2-**2** and αHER2-**6** were combined with the three ATR inhibitors AZD6738, ATRi **1** and BAY1895344 on NCI-N87 and MDA-MB-453 cells. As a control, the small molecules DUBA and Gemcitabine and as ADC control Kadcyla were combined with the ATRi AZD6738 (Figure 43). On NCI-N87 cells αHER2-**2** synergized in increasing order with the ATRi AZD6738 (S=3.7±0.7), ATRi **1** (S=7.1±0.8) and BAY1895344 (S=7.6±0.4). The combination of αHER2-**2** plus ATRi **1** (P=.008) and BAY1895344 (P=.0007) were significantly more synergistic than the combination of the ADC plus ATRi AZD6738. The same trend was observed for the combination of another DUBA-ADC αHER2-**6**. Again, the combination with AZD6738 (S=3.0±0.05) showed the lowest score, ATRi **1** (S=6.1±0.4) a mid-range and BAY1895344 (S=7.0±0.2) the highest score. In direct comparison, S of the combination of αHER2-**6** with AZD6378 was significantly lower than the combination of αHER2-**6** with ATRi **1** (P=.009) and BAY1895344 (P=.0002). As a positive control, DUBA was combined with the

ATRi AZD6738. A synergy score of S=3.1±0.6 proves the synergy between the duocarmycin-derivative and the ATRi. The combination of αHER2-**6** with AZD6738 was comparably synergistic as the combination of its small molecule counterpart DUBA with AZD6738 (P=.3). The negative control Kadcyla showed only additive effects when combined with AZD6738 (S=0.3±0.2), while the benchmark Gemcitabine barely exceeded the cutoff score when combined with the ATRi AZD6378 (S=1.1±0.5). The duocarmycin-ADC αHER2-**6** synergized significantly stronger with the ATRi AZD6738 compared to the negative control Kadcyla (P=.003) and the positive control Gemcitabine (P=.001).

Similar results were obtained on MDA-MB-453 cells. Here, αHER2-**2** synergized with the ATRi AZD6738 (S=9.1±2.1), ATRi **1** (S=13.3±0.3) and BAY1895344 (S=14.7±2.3) in increasing order. The same trend was observed for αHER2-**6** plus AZD6738 (S=9.5±0.9), ATRi **1** (S=11.4±1.4) and BAY1895344 (S=15.8±0.5). Gemcitabine synergized slightly stronger with AZD6738 on MDA-MB-453 (S=1.6±1.2) than on NCI-N87. The negative control combination of Kadcyla with AZD6738 reached a synergy score of 1.1±0.3 which is just above the cutoff score indicating very weak synergy. The positive control DUBA synergized with AZD6738 also on MDA-MB-453 cells (S=5.0±0.5) but significantly weaker than the combination of αHER2-**6** with the corresponding ATRi (P=.01).

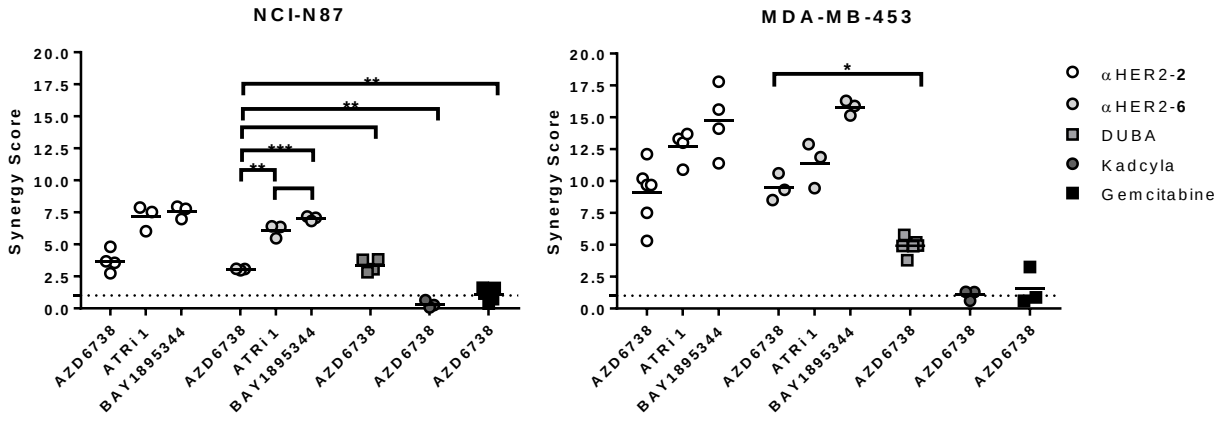

Figure 43: Synergy scores of combinations of duocarmycin-bearing ADCs αHER2-**2** and αHER2-**6** with different ATRi on NCI-N87 or MDA-MB-453 cells. As controls, the small molecules DUBA and Gemcitabine and, as negative control, Kadcyla were included. Bars represent the mean of independent biological replicates.

A total of seven ATRi were investigated in this study to elucidate the effect of the ATRi on the combination effects with duocarmycin and duocarmycin-based ADCs on HCC-1954, MDA-MB-453 and NCI-N87 cells. The synergy scores of the individual ATRi (as presented in figure 42 and figure 43) combined with the duocarmycin DUBA or DUBA-based ADCs were plotted against their potency to inhibit the phosphorylation and thus activation of CHK1 after HT29 were stressed by treatment with hydroxyurea. The plots are depicted in figure 44. A correlation between the ATRi potency and the synergy scores was observed for the small molecule DUBA with the ATRi on HCC-1954. This finding was confirmed with the ADC αHER2-**2** combined with the ATRi library on

HCC-1954. The same correlation was observed for αHER2-**2** and αHER2-**6** combined with a subset of ATRi on MDA-MB-453 and NCI-N87 cells.

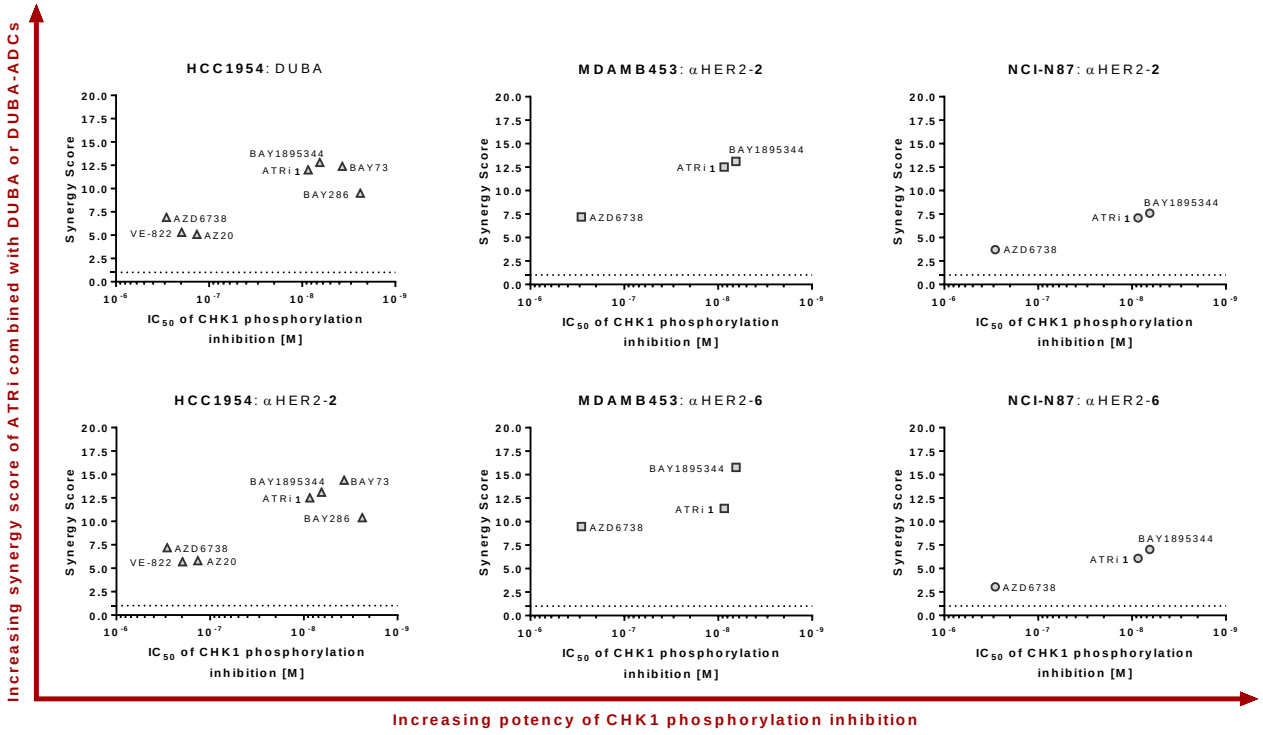

Figure 44: Correlation between synergy score and cellular CHK1 phosphorylation inhibition on HT29 cells. The more potent the ATRi in terms of CHK1 phosphorylation inhibition the higher the synergy score. This correlation was shown for combinations of the small molecule drug DUBA with several ATRi on HCC-1954 cells. The correlation was reproduced for the same ATRi combined with the ADC αHER2-**2** on HCC-1954. A subset of the ATRi was combined with αHER2-**2** and another DUBA-based ADC αHER2-**6** on MDA-MB-453 and NCI-N87 cells.

5.6.2. Synergy of Combinations of αEGFR-Duocarmycin ADCs and ATRi

In the previous chapters, the combination of αHER2-duocarmycin ADCs with ATRi was studied. To validate that the concept of combining duocarmycin-modified ADCs with ATRi can be translated to additional antibodies, cetuximab-based duocarmycin-ADCs were investigated. Therefore, the EGFR-positive cell lines A549, A431 and MDA-MB-468 as well as EGFR-negative MCF7 cells were treated with DDM-based αEGFR-**1**, DSA-based αEGFR-**7** in combination with AZD6738. As controls, the cells were also treated with the MMAE-ADC αEGFR-**8** and the small molecule duocarmycins DDM and DSA. After 6 d of treatment, cell viability was determined using CellTiter-Glo reagent. Luminescence was read on an Envision reader and evaluation took place using GeneData Screener. Data are depicted in figure 45. The negative control ADC αEGFR-**8** had synergy scores in the range of additivity. The positive control DDM had synergy scores ranging from 2.0±1.1 on A549 to 6.0±1.0 on MDA-MB-468 cells. The synergy scores of the small molecule DSA were comparable on A431, MDA-MB-468 and MCF7. However, DSA did not synergize with AZD6738 on A549 cells but showed additive effects. While the synergy of the combination of αEGFR-**1** plus AZD6738 was very similar on A549 (S=3.9±1.0), A431 (S=3.9±0.3) and MDA-MB-468 (S=4.2±0.3) cells, the synergy score on MCF7 (S=2.2±0.1) was significantly lower compared to αEGFR-**1** combined with AZD6738 on MDA-MB-468 (P=.006) or A431 (P=.01). However, the effects were less distinct for the combination of the DSA-ADC αEGFR-**7** combined with the ATRi. The synergy score of C-**7** plus AZD6738 amounted to 4.4±0.6 on A431, 2.9±1.1 on A549 and 3.2±0.4 on MDA-MB-468 cells. This combination reached a synergy score of 2.3±0.1 on the EGFR-negative cell line MCF7, which is significantly lower than the combination given to A431 cells (P=.03).

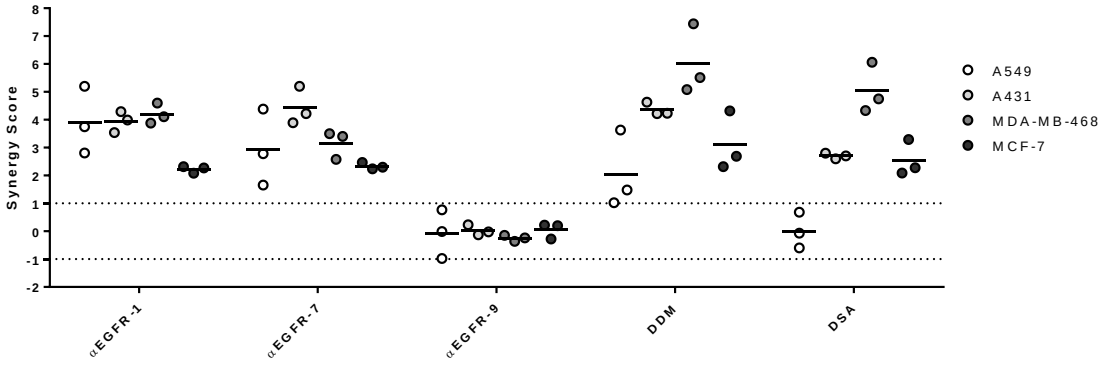

Figure 45: Synergy scores of combinations of cetuximab-duocarmycin ADCs with the ATRi AZD6738 on EGFR-positive cell lines and the EGFR-negative cell line MCF7. As a control, Cetuximab-MMAE was combined with the ATRi AZD6738. Individual data points are displayed as well as the mean of the experiments.

5.6.3. Dose-Reduction of αHER2-Duocarmycin Combinations with ATRi

A strategy for improved safety of a combination therapy is the reduction of the administered doses. It was demonstrated in the previous chapters that duocarmycin-bearing ADCs combined with ATRi unfolded synergistic toxic effects towards cancer cells. But the expression of synergistic effects in terms of a synergy score did not allow an estimation on how much the dose of the drugs in a combination might be lowered while maintaining the same cellular effects. Therefore, it was studied how strong the potency of the duocarmycin-bearing ADCs was increased when ATRi were added at sub-efficacious doses.

The determination of dose-reduction indices (DRI) in a maximum non-efficacious dose (MNED) curve-shift assay is a 3-step process as depicted exemplarily in figure 46. The cytotoxicity of the ADC is confirmed in a cell viability assay in an initial step. Here, HCC-1954 cells were treated with αHER2-**1**, the αHER2 mAb trastuzumab (T) and a control ADC αHEL-**1** for 6 d and cell viability was measured using CellTiter-Glo kit. While αHER2-**1** had an IC_{50}-value of 1.1 nM, the naked mAb did not show any anti-proliferative effects. The isotype control ADC αHEL-**1** reduced the cell viability at 250 nM to 75% but was considerably less cytotoxic as αHER2-**1**. In the second step, the MNED of the ATRi was determined. Therefore, the cells were treated with ATRi **1** and the dose-response curve (DRC) was plotted to identify MNED which was in this case 40 nM. It was proceeded to the last step qith these data, the MNED curve-shift assay. Therefore, HCC-1954 cells were treated with a serial dilution of αHER2-**1** or a serial dilution of αHER2-**1** supplemented with 40 nM ATRi **1**. In order to obtain a full DRC for the combination, the starting concentration of the ADC was lowered compared to the experiment in step 1. The IC_{50}-value of αHER2-**1** was 2.5 nM. The combination of αHER2-**1** with 40 nM ATRi **1** had a potency of 0.059 nM. This potentiation of the combination compared to the ADC alone can be expressed as a DRI of 42. ATRi **1** did not reduce cell viability at 40 nM.

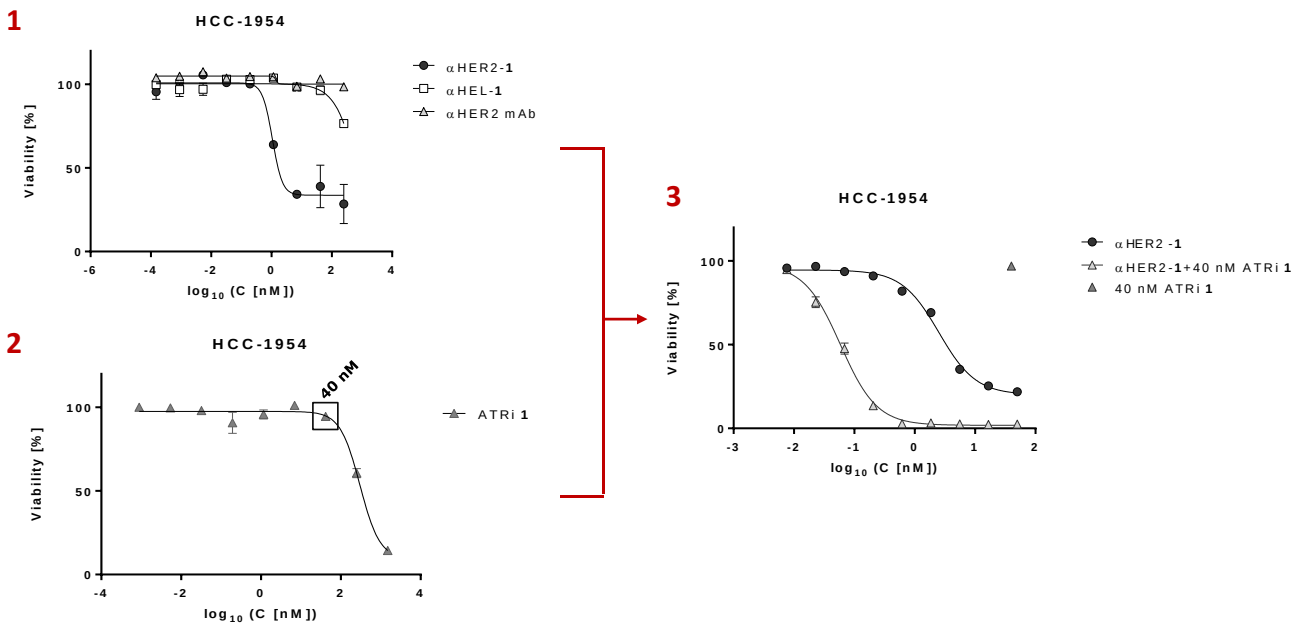

Figure 46: MNED-curve shift assay for the determination of dose-reduction indices as a 3-step process. 1) Cytoxocity of the ADC αHER2-**1** was confirmed in a cell viability experiment. 2) The inhibitor potency of ATRi **1** was titrated to identify the MNED. 3) MNED-curve shift assay is performed by serial diluting the ADC αHER2-**1**. The serial dilution of αHER2-**1** was added to HCC-1954 cells either alone or with ATRi **1** at the previously determined MNED. This led to a leftward shift of the ADC toward lower potencies. The inhibitor was added at MNED to the cells as a quality control demonstrating no effect on cell viability.

MNEDs were determined for AZD6738 and VE-822 on a panel of HER2-positive cell lines and on the HER2-negative cell line MDA-MB-468, because cell lines might respond differently to the combination treatment of αHER2-**1** and ATRi. In addition, the MNED of BAY73 and ATRi **1** were determined on HCC-1954 cells. The MNEDs for the HER2-positive cell lines and the HER2-negative cell line MDA-MB-468 are summarized in table 12.

Table 12: Summary of maximum non-efficacious doses on HER2-positive cell lines and HER2-negative cell line MDA-MB-468.

	MNED in nM			
Cell line	**AZD6738**	**BAY73**	**ATRi 1**	**VE-822**
BT-474	1000	-	-	1000
Calu-3	400	-	-	80
HCC-1954	250	14	40	250
JIMT-1	80	-	-	80
MDA-MB-361	111	-	-	-
MDA-MB-453	111	-	-	40
MDA-MB-468	300	-	-	300
SK-OV-3	150	-	-	125
SK-BR-3	150	-	-	125

Then, the cells were treated with either ADC alone or with a combination of αHER2-**1** with AZD6738 or VE-822 at the corresponding MNED. The IC_{50}-values of the monotreatment and the combination treatment are summarized in table 13. Although, in all cases the IC_{50}-values of the combination was lower than the IC_{50}-value of the ADC alone, only in few cases the difference was significant. The potency of the ADC alone was 1±1 nM on HCC-1954 cells. In combination with 250 nM AZD6738 or 250 nM VE-822, the potency of the combination was lowered to 0.3±0.3 nM or 0.3±0.2 nM, respectively. The potentiation effect was significant in both cases (P=.03 and P=.03, respectively). The IC_{50}-value of αHER2-**1** on JIMT-1 was 0.41±0.07 nM. The combination of αHER2-**1** with 80 nM of the ATRi AZD6738 led to a significant higher potency with an IC_{50}-value of 0.19±0.03 nM (P=.03). The potency of the combination of αHER2-**1** with 111 nM AZD6738 on MDA-MB-361 (IC_{50}=0.03±0.01) was also significantly more potent than the monotreatment with αHER2-**1** (IC_{50}=0.10±0.02). The potentiation effects were also studied on the HER2-negative cell line MDA-MB-468. The potency of the ADC alone was 140±47 nM. If 300 nM AZD6738 or 300 nM VE-822 were added, the potency was 19±4 nM or 44±17 nM. The combination of αHER2-**1** with AZD6738 or VE-822 was significantly more potent than the monotherapy with αHER2-**1** alone (P=.00009 or P=.0004, respectively).

Table 13: Potencies of ADC αHER2-**1** alone or in combination with AZD6738 and VE-822 on a HER2-positive cell panel and a HER2-negative cell line MDA-MB-468. The ATRi were added at constant concentration to the ADC αHER2-**1** (MNED, see table 12). Potencies of the ADC αHER2-**1** on the cell panel are already listed in chapter 5.5, table 10, but repeated for comparison. Data are mean±SD for N≥3 biological replicates (except for BT-474 where experiments were conducted twice). P-values were added if the combination treatment was significantly more potent than the monotreatment.

		IC_{50} in nM		
	HER2	αHER2-**1**	αHER2-**1**+AZD6738	αHER2-**1**+VE-822
BT-474	+	1.0 (1.2, 0.70)	0.086 (0.095, 0.077)	0.079 (0.10, 0.057)
Calu-3	+	0.9±0.4	0.3±0.1	0.6±0.2
HCC-1954	+	1±1	0.3±0.3 (P=.03)	0.3±0.2 (P=.03)
JIMT-1	+	0.41±0.07	0.19±0.03 (P=.03)	0.24±0.02
MDA-MB-361	+	0.10±0.02	0.03±0.01 (P=.02)	N/D
MDA-MB-453	+	0.3±0.1	0.05±0.01	0.13±0.03
SK-BR-3	+	0.08±0.03	0.036±0.006	0.05±0.02
SK-OV-3	+	0.2±0.1	0.07±0.04	0.05±0.02
MDA-MB-468	-	140±47	19±4 (P=.00009)	44±17 (P=.0004)

The potentiation effects of combination treatment versus monotreatment can be elucidated in a more detailed fashion by calculating dose-reduction indices using eq. 2. The potency of a combination is enhanced compared to the monotherapy with increasing DRI. The results of this calculation are displayed in figure 47. The DRIs of the combination αHER2-**1** plus VE-822 on Calu-3, JIMT-1 and SK-BR-3 were below two. In most of the cases, DRIs of two to five were reached. The combination of αHER2-**1** with AZD6738 exceeded a DRI of five on HCC-1954

(DRI=5.4), MDA-MB-453 (DRI=6.4) and MDA-MB-468 (DRI=7.4). DRIs greater then ten were reached for αHER2-**1** combined with AZD6738 (DRI=11.1) and VE-822 (DRI=12.0) on BT-474 cells.

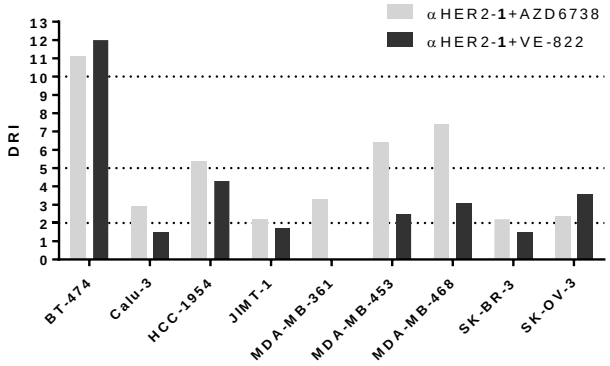

Figure 47: Dose-reduction indices of the combination of αHER2-**1** with AZD6738 or VE-822 on a panel of HER2-positive cell lines and the HER2-negative cell line MDA-MB-468. The ATRi were given at their individual MNED (Table 12) in the combination groups.

Furthermore, HCC-1954 cells were co-treated with ADC αHER2-**1** and the ATRi AZD6738, VE-822, ATRi **1** and BAY73 to study the effect of the ATRi on the DRI (Figure 48). The ADC alone had an IC_{50}-value of 1.4±1.2 nM, while the combination of ADC with 250 nM AZD6738 was 5.4-fold more potent with IC_{50}=0.26±0.33 nM (P=.03). The combination of αHER2-**1** with VE-822 was comparably potent (IC_{50}=0.33±0.17 nM) and again significantly more potent than the monotreatment with αHER2-**1** (P=.03). A DRI of 4.3 was obtained for αHER2-**1** combined with VE-822. The combination of ADC with 40 nM ATRi **1** or 14 nM BAY73 strongly potentiated ADC potency (IC_{50}=0.074±0.022 nM and IC_{50}=0.030±0.008 nM, respectively). The combination of αHER2-**1** and ATRi **1** achieved a DRI of 27.1, while the combination of the ADC with BAY73 led to a 47.1-fold potentiation. It can be stated that αHER2-**1** plus BAY73 or ATRi **1** are significantly more potent than αHER2-**1** alone (P=.01 and P=.01, respectively) based on these data. For clarity, the DRIs of the combinations of αHER2-**1** with the four different ATRi AZD6738, VE-822, ATRi **1** and BAY73 are depicted in figure 48 B.

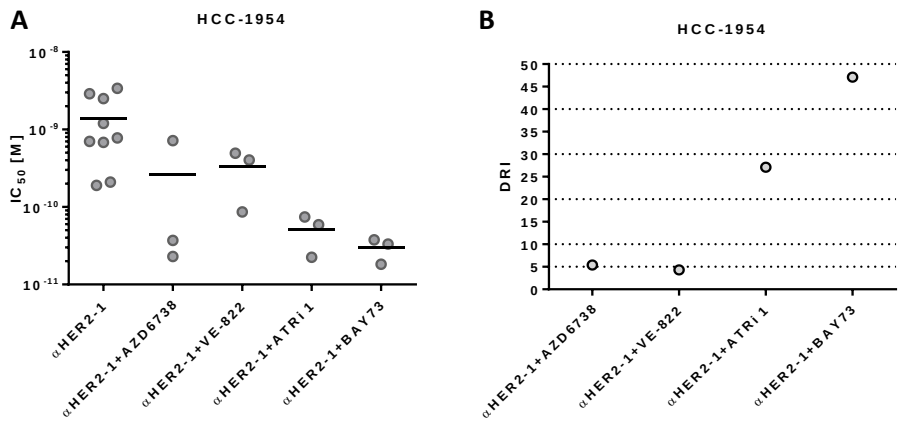

Figure 48: Combination of ADC αHER2-**1** with ATRi AZD6738, VE-822, ATRi **1** and BAY73 on HCC-1954 cells. The ATRi are given at their individual MNEDs in the combination treatment groups as summarized in table 12. A) The IC_{50}-values of the single agent and combination groups are depicted as individual data points. The black bar indicates the mean of the IC_{50}-values for each group. B) DRI of αHER2-**1** combined with the ATRi are plotted. The DRI were calculated from the IC_{50}-values shown in A).

Major differences in the synergy scores were observed when combining small molecule duocarmycins with AZD6738. Thus, potentiation effects of DUBA-based ADCs should be compared to potentiation effects of DDM-carrying ADCs when combined with different ATRi. The potencies of DDM-based ADC αHER2-**1** alone or in combination with AZD6738 and VE-822 are already summarized in table 13. In addition to these experiments, potencies of DUBA-based ADCs αHER2-**2** and αHER2-**3** alone or in combination with AZD6738 and VE-822 were studied on HER2-positive cell lines HCC-1954, Calu-3 and SK-BR-3 and HER2-negative cell line MDA-MB-468. While αHER2-**2** and αHER2-**3** had IC_{50}-values in the single-digit nanomolar range on HCC-1954 and Calu-3 cells, the ADCs were potent in the subnanomolar range on SK-BR-3 cells. On MDA-MB-468 cells, the DUBA-based ADCs were considerably less potent than on the HER2-positive cell lines, with IC_{50}-values in the double digit nanomolar range. The effects of the ADCs were potentiated when adding AZD6738 or VE-822 at their respective MNED for every cell line to the ADCs. Although this trend was observed for all the combinations of αHER2-**2** and αHER2-**3** with AZD6738 and VE-822, the effects were significant only for the potentiation effects of αHER2-**2** plus AZD6738 (P=.04) and VE-822 (P=.04).

Table 14: Potencies of the DUBA-bearing ADCs αHER2-**2** and αHER2-**3** as well as control ADC Kadcyla alone or in combination with constant doses of AZD6738 and VE-822 at MNED. The MNEDs of ATD6738 and VE-822 for each are summarized in table 12. Data are mean±SD of N≥3 biological replicates.

		IC_{50} in nM								
		αHER2-**2**			αHER2-**3**			Kadcyla		
	HER2	-	AZD6738	VE-822	-	AZD6738	VE-822	-	AZD6738	VE-822
HCC-1954	+	2±1	0.10±0.02	0.097±0.006	2±1	0.09±0.02	0.15±0.04	0.50±0.03	0.4±0.2	0.3±0.2
Calu-3	+	4±2	0.7±0.4	0.931±0.164	1.5±0.9	0.4±0.1	0.6±0.2	41±22	37±22	41±23
SK-BR-3	+	0.16±0.05	0.035±0.007	0.061±0.015	0.15±0.05	0.039±0.001	0.071±0.005	0.2±0.1	0.19±0.02	0.12±0.07
MDA-MB-468	-	28±6	2.3±0.4	5.14±2.056	17±4	1.4±0.3	5±3	43±9	30±1	31±1

The control ADC Kadcyla was comparably potent HCC-1954, SK-BR-3 and MDA-MB-468. On Calu-3, Kadcyla was considerably less potent than the duocarmycin-carrying ADCs αHER2-**2** and αHER2-**3**. However, this effect was not significant.

A summary of DRIs of DDM-bearing ADC αHER2-**1**, DUBA-carrying αHER2-**2** and αHER2-**3** and control ADC Kadcyla combined with AZD6738 and VE-822 at constant dose on HCC-1954, Calu-3, SK-BR-3 and MDA-MB-468 is displayed in figure 49. On HCC-1954 cells, the highest DRIs were reached with the DUBA-ADCs. The potency of αHER2-**2** was enhanced strongly by addition of AZD6738 (21.5-fold) or VE-822 (22.9-fold). Weaker potentiation effects were achieved by combining αHER2-**3** with AZD6738 (18.5-fold) or VE-822 (11.7-fold) at MNED. The combination of DDM-bearing ADC αHER2-**1** with AZD6738 reached considerably lower DRIs of 5.4 or 4.3 when AZD6378 or VE-822 were added, respectively. The negative control ADC Kadcyla had DRIs of 1.4 and 1.5 when combined with AZD6738 or VE-822, respectively. The trend of DUBA-bearing ADCs combined with ATRi being superior to DDM-bearing ADC αHER2-**1** plus ATRi was reproduced on Calu-3, SK-BR-3 and MDA-MB-468 although less pronounced. Kadcyla combinations with the ATRi had consistently DRIs<2.

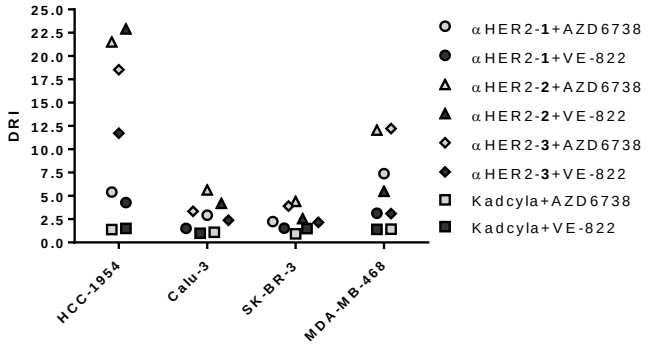

Figure 49: Comparison of DRIs of αHER2-**1**, αHER2-**2** and αHER2-**3** and Kadcyla when combined with constant concentrations of the ATRi AZD6738 and VE-822. The DRIs were calculated using the IC_{50}-values in table 13 and table 14. The ATRi were added to the ADC at MNED (Table 12).

In order to compare the potentiation effects of DDM-bearing ADCs with DUBA-carrying ADCs and the negative control Kadcyla, DRIs were condensed and depicted in figure 50 A. The potentiation effects of DUBA-based ADCs αHER2-**2** and αHER2-**3** when combined with ATRi were stronger (DRI=9.8 and 7.2, respectively) than the potentiation of DDM-based αHER2-**1** combinations with ATRi (DRI=3.6). The mean DRI of Kadcyla plus ATRi amounts to 1.3. Furthermore, the potentiation effects of the ATRi AZD6738 and VE-822 when added to the duocarmycin-bearing ADCs on the different cell lines were compared (Figure 50 B). In all cases, the mean of DRIs of the combination AZD6738 with duocarmycin-ADCs was higher compared to the combination of VE-822 with duocarmycin-based ADCs.

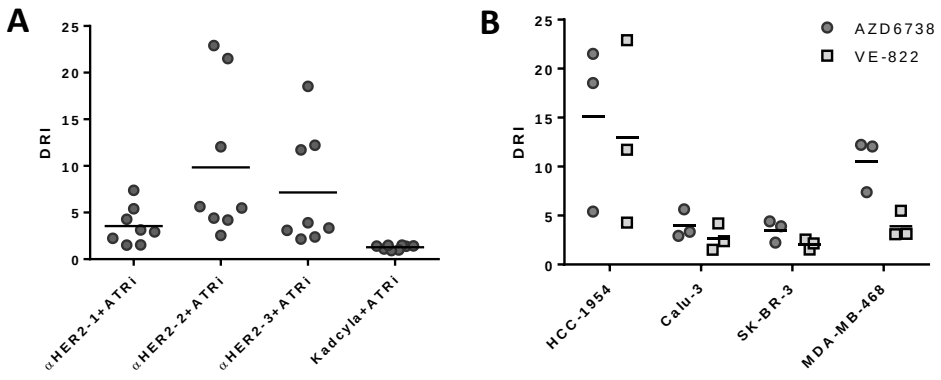

Figure 50: DRIs of duocarmycin-bearing ADCs combined with ATRi. A) DRI of the combination of ATRi with duocarmycin-bearing ADCs αHER2-**1**, αHER2-**2** and αHER2-**3** as well as Kadcyla were condensed regardless of cell line. Individual data points are displayed and the mean is indicated by a black bar. These data are already presented in figure 49. B) DRI of ATRi combined with duocarmycin-bearing ADCs. The results were condensed regardless of which ADC-variant was used. Individual data points are displayed and the mean is indicated by a black bar.

Every cell line studied in the course of this work had a differential tolerability of the ATR inhibitors, reflected by the different MNEDs. In chapter 5.5 selectivity indices were introduced that allowed the comparison of different ADCs. However, in the case of combination treatment, varying constant concentrations of ATRi were added to the cells together with the duocarmycin-ADC. This impaired the calculation of selectivtiy indices for drug combinations. As a result, it was necessary to determine the potency of ADC combined with constant concentrations of ATRi on MDA-MB-468. In the following experiments the dependency of the DRI on the constant dose of ATRi added to the ADC in combination experiments was investigated. Figure 51 illustrates that the IC_{50}-value of the ADC alone was decreased by the addition of either VE-822 or AZD6738 in a dose-dependent manner.

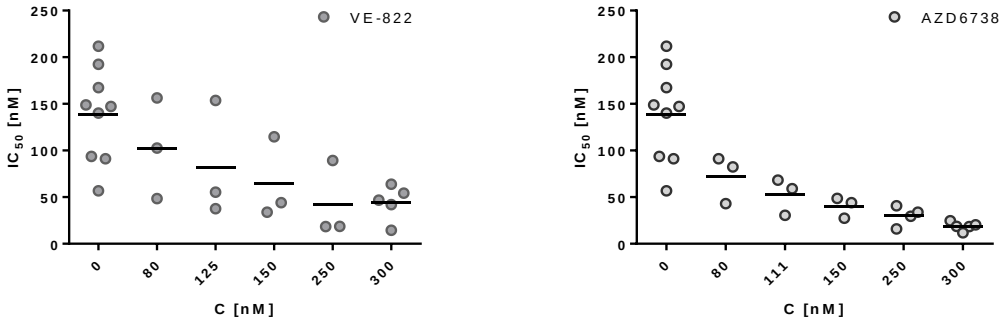

Figure 51: Dose-dependency of potentiation effects. MDA-MB-468 cells were treated with ADC αHER2-**1** and increasing doses of VE-822 (left) or AZD6738 (right). Individual data points are displayed and the mean is represented by a black bar.

The data presented in figure 51 enabled the calculation of selectivity indices according to eq. 4. Therefore, the IC_{50}-value of αHER2-**1** combined with a constant concentration of 111 nM AZD6378 on MDA-MB-468 (53±16 nM) was divided by the IC_{50}-value of αHER2-**1** combined with 111 nM AZD6738 on MDA-MB-453

(0.05±0.01 nM). This resulted in a selectivity index of 1010 for the combination treatment at that specific dose of ATRi. In comparison to that, the selectivity index of the monotherapy using αHER2-**1** amounted to 414. Selectivity indices for the monotherapy, combination treatment of αHER2-**1** with AZD6738 or VE-822 are depicted in figure 52. Since the MNED of the ATRi on BT-474 and the MNED of AZD6738 on Calu-3 exceeded the MNED of the HER2-negative cell line MDA-MB-468, no selectivity index was calculated in these cases. Furthermore, MDA-MB-468 cells were not treated with 40 nM VE-822, so no SI was calculated for that case.

The selectivity of αHER2-**1** was 153 towards Calu-3 cells, 138 towards HCC-1954 cells and 337 towards JIMT-1 cells. Higher selectivity indices were reached for αHER2-**1** on MDA-MB-453 (SI=460) and SK-OV-3 (SI=690). Triple digit indices were obtained when MDA-MB-361 cells or SK-BR-3 cells were treated with αHER2-**1** (SI=1380 or 1725, respectively). When treating HCC-1954, SK-BR-3 and SK-OV-3 cells with αHER2-**1** and AZD6738 simultaneously, the SI were decreased compared to monotherapy. The SI towards HCC-1954 amounts to 100, towards SK-BR-3 to 1105 and towards SK-OV-3 cells to 571 when treated with the combination. The selectivity was increased when αHER2-**1** and AZD6738 were given to JIMT-1 (SI=379), MDA-MB-361 (SI=1749) or MDA-MB-453 cells (SI=1060) at the same time. The combination treatment of Calu-3 cells with VE-822 and αHER2-**1** had slighly increased selectivity towards Calu-3 (SI=172) compared to monotherapy. On HCC-1954 cells the selectivity of the monotherapy (SI=138) and the combination therapy (SI=140) was equal. On JIMT-1 cells the combination of αHER2-**1** with VE-822 was more selective towards antigen-positive cells (SI=429) than the treatment with αHER2-**1** alone, while on SK-BR-3 cells a lower SI of 1640 was obtained for the combination when compared to monotherapy. αHER2-**1** combined with VE-822 was comparably more selective towards SK-OV-3 cells (SI=1640) than the ADC alone.

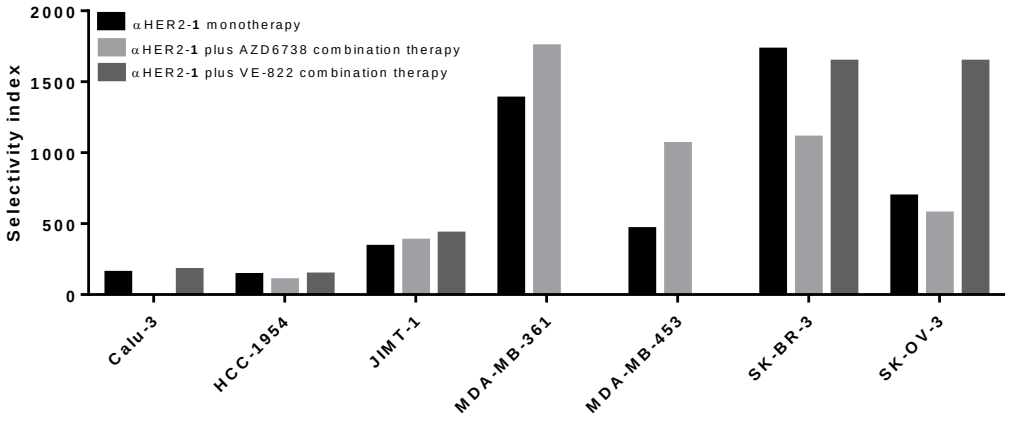

Figure 52: Comparison of selectivity indices for monotherapy and combination therapy for αHER2-**1** combined with either AZD6378 or VE-822 at the respective MNED. Selectivity indices were calculated according to eq. 4 for cells treated with ADC only.

5.6.4. Potentiation Effects of Glycoprotein Binding-Duocarmycin DM ADC when Combined with ATRi

Furthermore, it was studied whether the potentiation effects observed with the αHER2-based ADCs on HER2-positive cells might be translated to other targeted antigens, two glycoprotein (GP)-expressing cell lines were treated with GP-binding ADC αGP-**1** alone or ADC combined with the ATRi AZD6738 and VE-822 at their respective MNED for 6 d. Afterwards, the cell viability was determined using CellTiter-Glo assay. The potencies of the cell viability assays are summarized in figure 53. The ADC as single agent had an IC_{50}-value of 5±2 nM on GP-expressing cell line 1 and 1.4±0.6 nM on GP-expressing cell line 2. The potency of the ADC αGP-**1** was enhanced 7.5-fold on GP-expressing cell line 1 cells by the addition of 300 nM AZD6738, which resulted in an IC_{50}-value of 0.7±0.3 nM. The addition of 300 nM VE-822 decreased the potency of the combination to 1.1±0.5 nM which is 4.7-fold more potent than the single agent. On GP-expressing cell line 2 similar results were obtained. αGP-**1** combined with 300 nM AZD6738 had an IC_{50}-value of 0.3±0.2 nM, which is the equivalent of a 4.2-fold dose-reduction. The addition of 300 nM VE-822 to the ADC decreased the potency 4.5-fold leading to a potency of 0.3±0.2 nM.

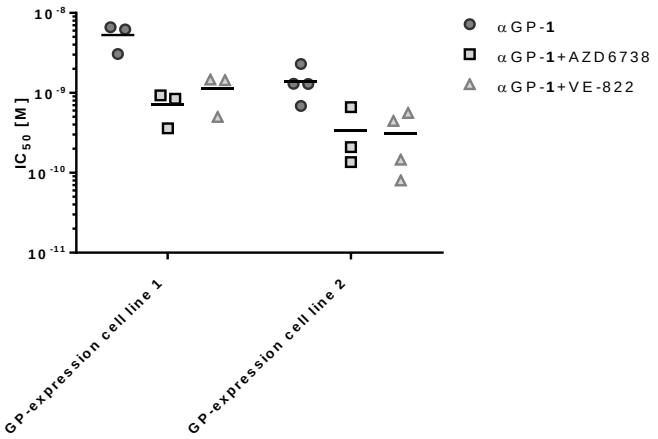

Figure 53: Potencies of αGP-**1** as single agent or combined with constant doses of ATRi AZD6738 and VE-822 on GP-positive cells MDA-MB-468 and WISH. The inhibitors were given at MNED to the cells. The individual IC_{50}-values of biological replicate experiments are displayed.

5.7. In Depth Investigation of Drug Combinations of ATRi with Duocarmycin

The combination effects of a drug combination were quantified in previous experiments *via* synergy scores. Therefore, six doses of each compound were mixed with each other to obtain a 6x6-dose-matrix from which a synergy score was derived by calculating the weighted volume between the expected response for an additive drug combination according to the Loewe additivity model and the actual measured response of the drug combination. It was defined that synergy scores S < -1 were indicative of antagonistic drug combinations, scores between -1 and 1 were additive and drug combinations yielding S > 1 were termed synergistic. However, synergy scores reduce the data obtained into one single value, leading to the loss of information. In this chapter, it was aimed at improving the amount of information obtained from one experiment. Thus, a dilution series of 13 dilution steps was generated for each compound of a drug combination and the dilution series were mixed subsequently yielding a 13x13-dose-matrix. Besides the synergy score, curve-shift data were obtained from a dose-matrix assay as illustrated in figure 54. The horizontal data of a dose-matrix yielded the curve-shift of drug A supplemented with constant concentrations of drug B. The vertical data were considered as a curve-shift assay of drug B with different concentrations of drug A being added. The diagonals of the matrix were used to obtain information about curve-shifts of drug A and B when given simultaneously to the cells at varying fixed-ratios where the ratio of each combination-curve was calculated according to eq. 5.

$$ratio = \frac{C_{drug\ A}}{C_{drug\ B}} \qquad \text{Eq. 5}$$

In addition, the data of a curve-shift assay were used to calculate dose-reduction indices and combination indices according to eq. 2 and eq. 1, respectively.

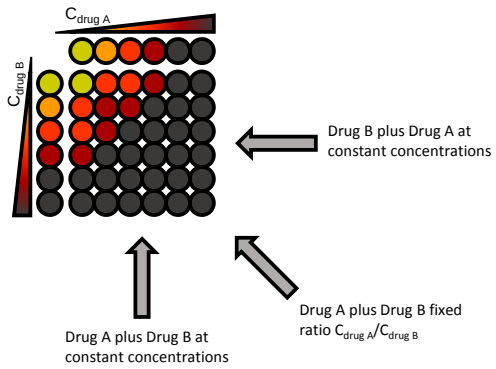

Figure 54: 6x6-dose-matrix assay set-up. A serial dilution with 6 dose-levels of drug A and B are mixed to yield a dose-matrix. A cell viability assay can be used to determine a synergy score from this dose-matrix assay. Furthermore, curve-shift data can be derived for serial-dilutions of drug B supplemented with a constant concentration of drug A and *vice versa*. In addition, curve-shifts of drug combinations of drug A plus drug B at a fixed-ratio can be derived from the diagonals of the dose-matrix.

Genedata Screener, which was used in the course of this work to calculate synergy scores, has no integrated solution for the calculation of the curve-shift assay data, DRIs or CIs.

A R-based program was written that first fits the vertical, horizontal and diagonal data of the dose-matrix. This way full dose-response curves for the single agents and the combinations of drug A plus constant concentrations of drug B, and *vice versa*, were obtained as well as the drug combinations at a fixed-ratio between drug A and B. The DRCs were fitted using the logisitc fitting function LL.4 (Eq. 6) of the DRC package by inserting the viability of the cells f(x) for every dose x.[154] This equation describes a 4-parameter logistic (4PL) curve and reads as follows:

$$f(x) = Bottom + \frac{Top - Bottom}{1 + e^{HillSlope(\log x - \log IC_{50})}} \qquad \text{Eq. 6}$$

By fitting the cell-viability data, the parameters “Bottom”, “Top”, “HillSlope” and “IC_{50}” are obtained that fully define the DRC at any given dose x. “Bottom” and “Top” describe the level of cell viability reached in saturation. “HillSlope” describes the slope of the curve and the “IC_{50}” decribes the turning point of the curve. Another way to plot dose-response curves is based on the median effect equation (MEE) given in eq. 7.[19]

$$\frac{fa}{fu} = \left(\frac{D}{D_m}\right)^m \qquad \text{Eq. 7}$$

The effect level of a certain drug dose D is expressed as fraction of affected cells (fa) divided by the fraction of unaffected cells (fu), where the latter corresponds to the cell viability. The fraction of affected cells and unaffected cells adds up to one, representing the whole cell population (Eq. 8).

$$1 = fa + fu \qquad \text{Eq. 8}$$

The parameter Dm corresponds to the IC_{50}-value of the 4PL equation and m corresponds to the HillSlope of the 4PL equation. Examples of DRCs using the 4-parameter logistic equation or the median effect equation are given in figure 55.

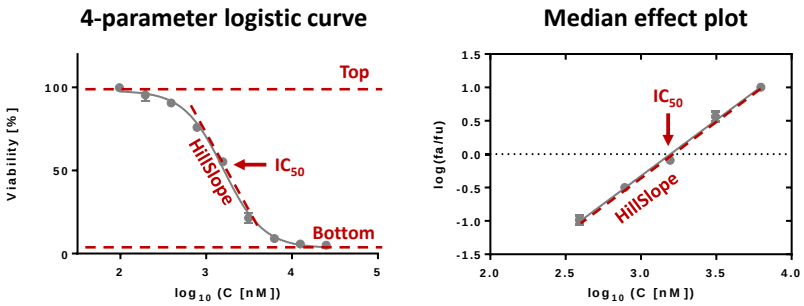

Figure 55: Examples of dose-response curves following 4-point logistic and median effect equation. A certain drug dose induces a certain cellular effect. The data pairs of drug dose and drug response can be used to fit a dose-response curve using the 4-point logistic equation or the median effect equation. Left: The DRC is defined by four parameters "Top", "Bottom", "HillSlope" and "IC_{50}". Right: The median effect equation is defined by the IC_{50} and the HillSlope.

As a proof of concept experiment, MDA-MB-453 cells were treated for 6 d with αHER2-**2** and AZD6738 in a 13x13-dose-matrix format. The cell viability was determined using CellTiter-Glo reagent and luminescence was read using Envision reader. This experiment was performed twice and similar results were obtained.

The validity of the fit data was checked by comparing the IC_{50}-values obtained from fitting the data with the LL.4 function and the IC_{50}-values calculated by GeneData Screener software. Therefore, the mean of IC_{50}-values of the two biological replicate experiments was plotted and fitted using a linear regression model in Microsoft Excel. The slope of the linear regression was m=0.9935 with a coefficient of determination R^2=0.9812, indicating that IC_{50}-values obtained through fitting with GeneData Screener or the LL.4 function of the DRC package are comparable (Appendix 3).

The fitting results were stored in a table for the calculation of DRI. Next, the dose-reduction indices at the IC_{50}-value of the combination αHER2-**2** plus AZD6738 were calculated and plotted against the amount of αHER2-**2** or AZD6738 added to the respective other compound. A linear regression was performed. Representative graphs are displayed in figure 56.

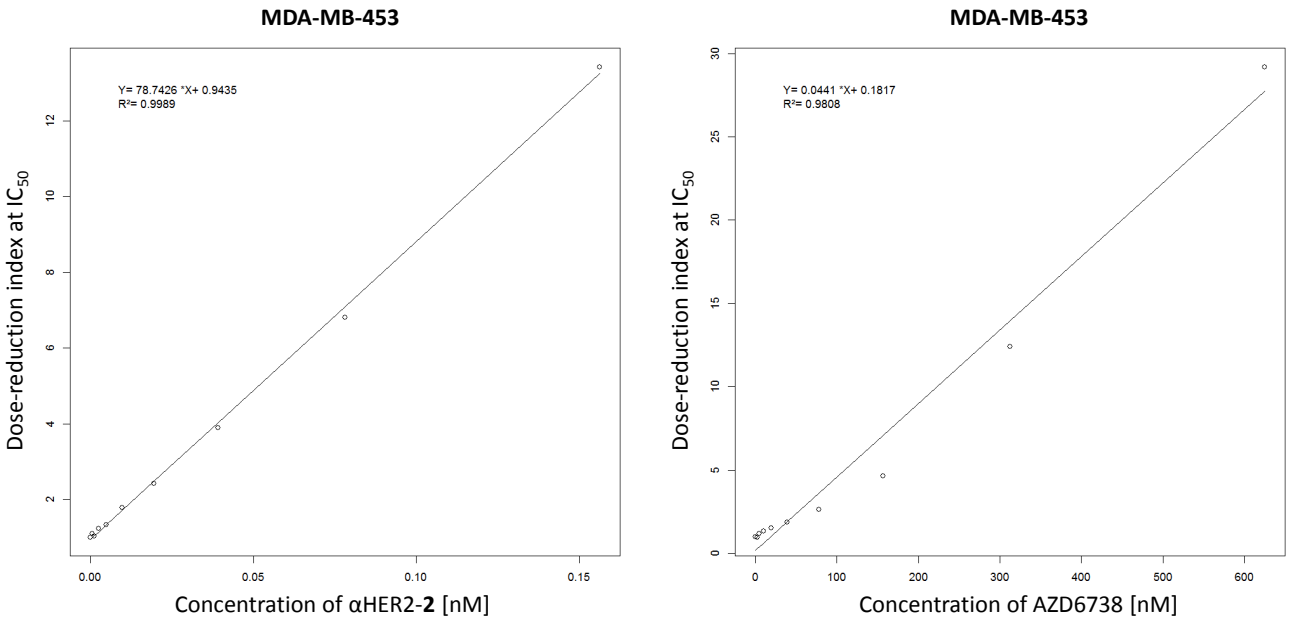

Figure 56: DRI at IC_{50} of MDA-MB-453 cells treated with a combination of αHER2-**2** and AZD6738. Left: The DRI of cells treated with serial dilutions of AZD6738 plus constant concentrations of αHER2-**2** was plotted against the constant concentration of αHER2-**2** added to the ATRi. Right: The DRI of combinations of αHER2-**2** plus AZD6738 was plotted dependent on the concentration of AZD6738 that was added to the ADC.

Slope and intercept of the linear regressions of two biological replicate experiments were averaged, yielding the linear equations eq. 9 for the DRI of the ADC αHER2-**2** as a function of the amount of ATRi AZD6738 added and eq. 10 for the DRI of the ATRi AZD6738 depending on the amount of αHER2-**2** added to the ATRi. Furthermore, combinations of αHER2-**2** with ATRi **1** and BAY1895344 were studied on MDA-MB-453 cells and the DRIs at the IC_{50}-value was plotted against the concentration of ADC or ATRi. The results of the linear regressions are summarized in table 15. The linear regression equations illustrated that the DRIs of the combinations were dependent on the amount of αHER2-**2** or ATRi AZD6738, ATRi **1** and BAY1895344 added to the combination on MDA-MB-453. While the DRI of αHER2-**2** was increased by m=0.0349/nM with growing concentration of AZD6738, the effect was 12-fold stronger if ATRi **1** was added (m=0.427/nM) or 90-fold stronger for the combination with BAY1895344 (m=3.13/nM). The same trend was observed considering the potentiation effects of the ATRi when adding constant concentrations of the ADC. The addition of αHER2-**2** to AZD6738 led to an increase of m=75.2/nM with increasing ADC concentrations. Again, the addition of constant concentrations αHER2-**2** to ATRi **1** led to stronger potentiation effects (4-fold, m=304/nM) and the effects of adding αHER2-**2** to BAY1895344 were even more pronounced (8-fold regarding AZD6738, m=560/nM).

Table 15: Summary of equations of linear regressions for combination experiments of ATRi combined with αHER2-**2** on MDA-MB-453 cells at the half-maximum inhibitory concentration. The equations are depicted either as a function of the constant concentration of ATRi added or dependent on the constant concentration of αHER2-**2** given to the cells. The parameters slope and y-axis intercept are the mean of N replicate experiments as stated in the table. The coeffcients of determination of the individual linear regressions are R^2>.974.

ADC	ATRi	Cell line	Equation	Eq. No.	N
αHER2-**2**	AZD6738	MDA-MB-453	$DRI_{\alpha HER2-\mathbf{2}} = \frac{0.0349}{nM} * C_{AZD6738} + 0.280$	Eq. 9	2
			$DRI_{AZD6738} = \frac{75.2}{nM} * C_{\alpha HER2-\mathbf{2}} + 1.00$	Eq. 10	
	ATRi **1**		$DRI_{\alpha HER2-\mathbf{2}} = \frac{0.427}{nM} * C_{Merck\ 331} - 0.124$	Eq. 11	2
			$DRI_{Merck\ 331} = \frac{304}{nM} * C_{\alpha HER2-\mathbf{2}} + 1.02$	Eq. 12	
	BAY1895344		$DRI_{\alpha HER2-\mathbf{2}} = \frac{3.13}{nM} * C_{BAY1895344} - 1.08$	Eq. 13	1
			$DRI_{BAY1895344} = \frac{560}{nM} * C_{\alpha HER2-\mathbf{2}} + 0.81$	Eq. 14	

These calculations of the DRI for combinations of ATRi with αHER2-**2** on MDA-MB-453 cells were performed for the IC_{50}-values. In order to calculate the DRI at any given effect level it was necessary to calculate the dose needed to achieve a certain cellular response. Therefore, the MEE was solved for the dose D as shown in in eq. 15.

$$D = D_m * \left(\frac{1-fu}{fu}\right)^{\frac{1}{m}} \quad \text{Eq. 15}$$

Eq. 15 is defined by using the parameters obtained from fitting the cell viability data. Potentiation effects expressed as DRI can be calculated using eq. 2 as stated in materials and methods (chapter 4.18). This equation, however, is restricted to calculations using the dose at the IC_{50}-value of mono- or combination therapy. A generalized equation is given in eq. 16, that allows the calculation of a DRI for every effect level for drug A combined with constant concentrations of drug B.

$$DRI_{drug\ A} = \frac{D_{drug\ A}}{D_{drug\ A+C_{drug\ B}}} \quad \text{Eq. 16}$$

Eq. 17 was yielded by inserting eq. 15 into eq. 2. This equation allowed the calculation of the DRI for a drug combination at every effect level.

$$DRI_{drug\ A} = \frac{D_{m_{drug\ A}} * \left(\frac{1-fu}{fu}\right)^{\frac{1}{m_{drug\ A}}}}{D_{m_{drug\ A+C_{drug\ B}}} * \left(\frac{1-fu}{fu}\right)^{\frac{1}{m_{drug\ A+C_{drug\ B}}}}} \quad \text{Eq. 17}$$

The fit results obtained from the cell viability assay for combinations of αHER2-**2** and AZD6738 on MDA-MB-453 were used to generate the DRI-surface displayed in figure 57. The DRI-surface was plotted dependent on the amount of drug at constant concentration added to serial dilutions of the respective other drug and on the effect level expressed as viability. The DRI of ATRi was calculated as a function of the amount of ADC added (Figure 57 A1) In these combination experiments. Another, complementary set-up calculated the DRI of the ADC as a function of the constant concentration of ADC that was added to the cells (Figure 57 A2). The same calculations were performed for the addition of constant concentrations of ATRi to serial dilutions of the ADC. The DRI-surfaces of AZD6738 plus constant concentrations of αHER2-**2**, and αHER2-**2** combined with constant concentrations of AZD6738 were in line with the results of the DRI calculated at IC_{50} (Figure 56). Two trends were deduced from the calculations. Firstly, the DRI increased in these cases (Figure 57 A1 and B1) with increasing constant concentrations of the respective second drug. Secondly, the DRI depended on cell viability in a way that high cell viability correlated with strong potentiation effects. In contrast to that, the dose-reduction indices of αHER2-**2** as a function of the constant concentration of αHER2-**2** showed the highest values at low concentrations of αHER2-**2** and low cell viabilities (Figure 57 A2). The same trend was found for the dependency of DRIs of AZD6738 on the concentration of AZD6738 added (Figure 57 B2).

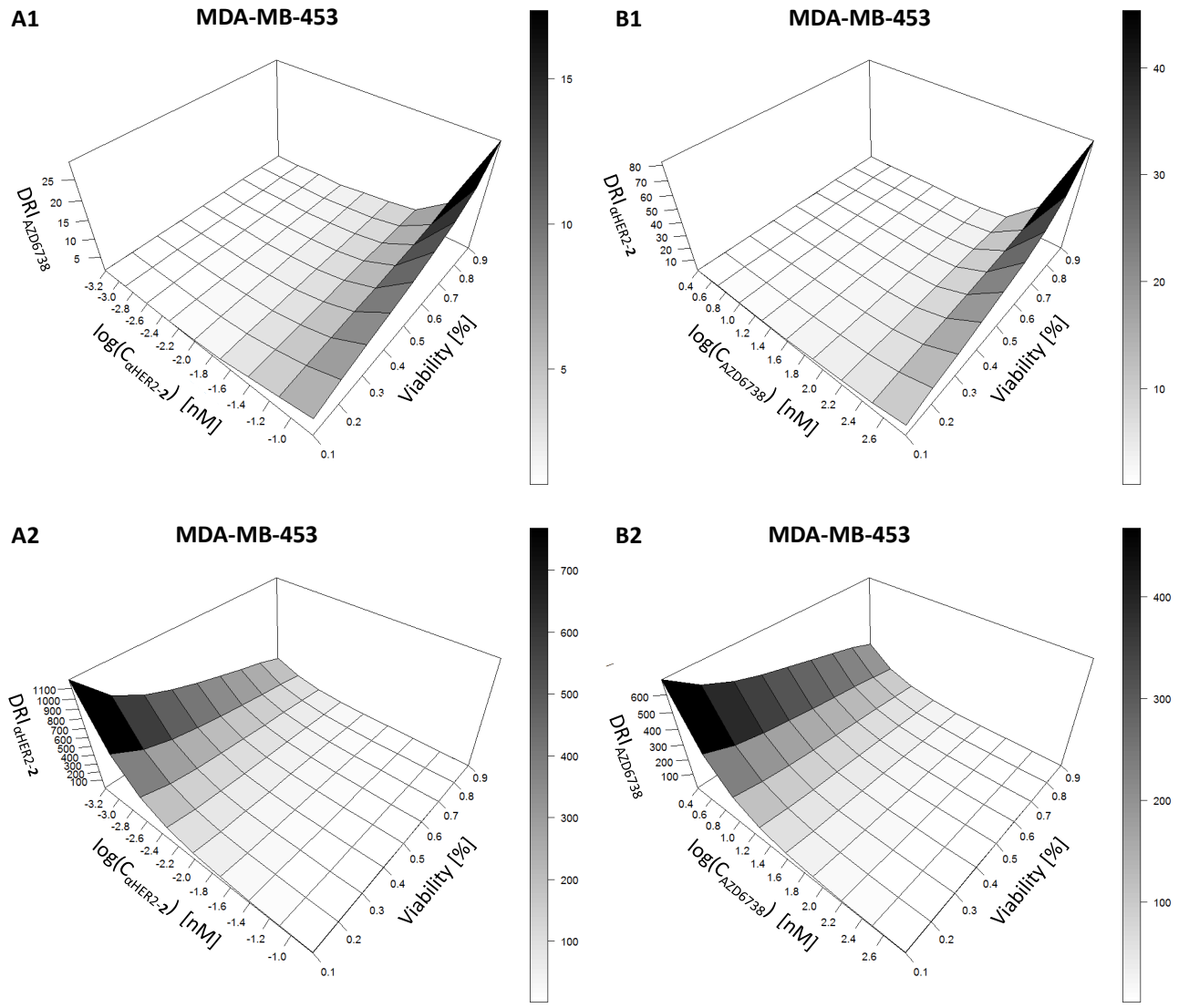

Figure 57: DRI-surface of MDA-MB-453 cells treated with αHER2-**2** and AZD6738. The DRI-surface was modeled using the DRC data obtained from a cell viability assay. These graphs are representative for two independent experiments. **A1**) Constant concentrations of αHER2-**2** were added to serial dilutions of AZD6738 on MDA-MB-453. DRI of αHER2-**2** was plotted as a function of the concentration of AZD6738. **B1**) Serial dilutions of αHER2-**2** were supplemented with increasing constant concentrations of AZD6738 to treat MDA-MB-453 cells. DRI of AZD6738 was plotted as a function of the concentration of αHER2-**2**. **A2**) Same data set as in A1, but DRI was calculated for the constant concentration of αHER2-**2** that was given to the ATRi. **B2**) Same data set as in B1, but the DRI of AZD6738 was calculated for the constant concentration of AZD6738 that was added to the ADC αHER2-**2**. The surface is shaded in white to black, where white indicates low DRI and black indicates high DRI.

The equation that defines the combination index for drug combinations (Eq. 1) was already introduced in the introduction. According to eq. 1, the CI can be calculated by dividing the doses of the individual drugs A and B in combination by the doses that are needed to achieve the same cellular effect when applying A or B as single agents. Subsequently, the sum of the fractions is formed to determine the CI. Another way to calculate the CI sums up the reciprocal DRI of drug A and B, which is expressed in eq. 18.

$$CI = \frac{D_A}{(D_x)_A} + \frac{D_B}{(D_x)_B} = \frac{1}{DRI_{drug\ A}} + \frac{1}{DRI_{drug\ B}} \qquad \text{Eq. 18}$$

Eq. 18 was used to generate a combination index surface that depends on viability of the cells as well as on the ratio between AZD6738 and αHER2-**2**. Figure 58 depicts the CI surface calculated using eq. 18 (left) and the CIcomp function implemented in the DRC package (right). The CI decreased at high effect levels or low cell viabilities. The ratio between the drugs strongly influenced the CI. Decreasing the ratio of AZD6738 to T-**2** decreased the CI simultaneously.

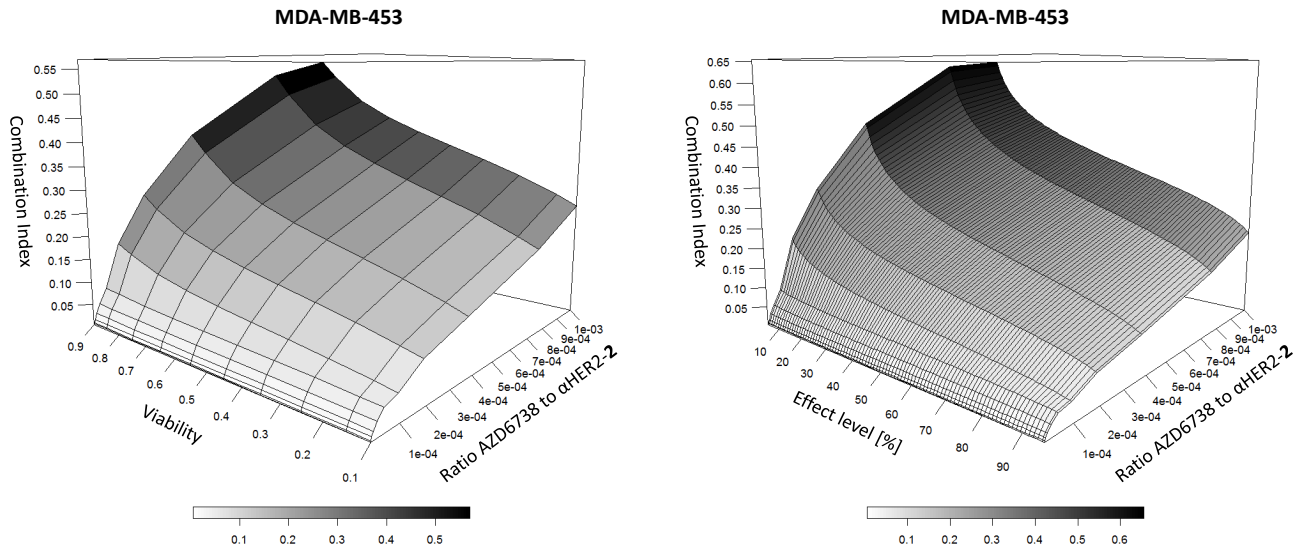

Figure 58: Combination index surface of αHER2-**2** combined with AZD6738 on MDA-MB-453 cells at a fixed-ratio for a range of effect levels. Left: CI surface derived from eq. 18. CI depends on viability and the ratio between the two drugs added to MDA-MB-453 cells. Right: CI surface calculated using the CIcomp function from DRC model. The CI depends on the effect level, which is the complement to cell viability, and the ratio between the compounds αHER2-**2** and AZD6738. The surface is shaded in white to black, where white indicates low CI and black indicates high CI. The graphs are representative of two replicate experiments.

Next, the CI was determined for the combination of αHER2-**2** with AZD6738 on MDA-MB-453 at either constant concentration of the ADC or the ATRi for varying effect levels dependent on constant concentrations of ATRi or ADC added to the combination (Figure 59). The CI reached a minimum when T-**2** was added at a constant concentration of 1.2 pM. In general, the CI decreased with increasing effect levels or decreasing cell viabilites, respectively. Although the CI increased with increasing constant concentrations of T-**2** in the mixture, it remained smaller than one, indicating synergy. One exception is found at an effect level of 10% and a concentration of 0.6 pM ADC where the CI was 1.2, indicating antagonism. Similar results were obtained for the combination of αHER2-**2** and AZD6738 dependent on the constant concentration of AZD6738 added to the cells. The minimal CI was reached when 9.8 nM of the ATRi were present. The combination was synergistic over the whole range of doses and effect levels except for the combinations of 625 nM AZD6738 with serial dilutions of αHER2-**2** and at low effect levels when 2.4 nM ATRi were added to αHER2-**2**.

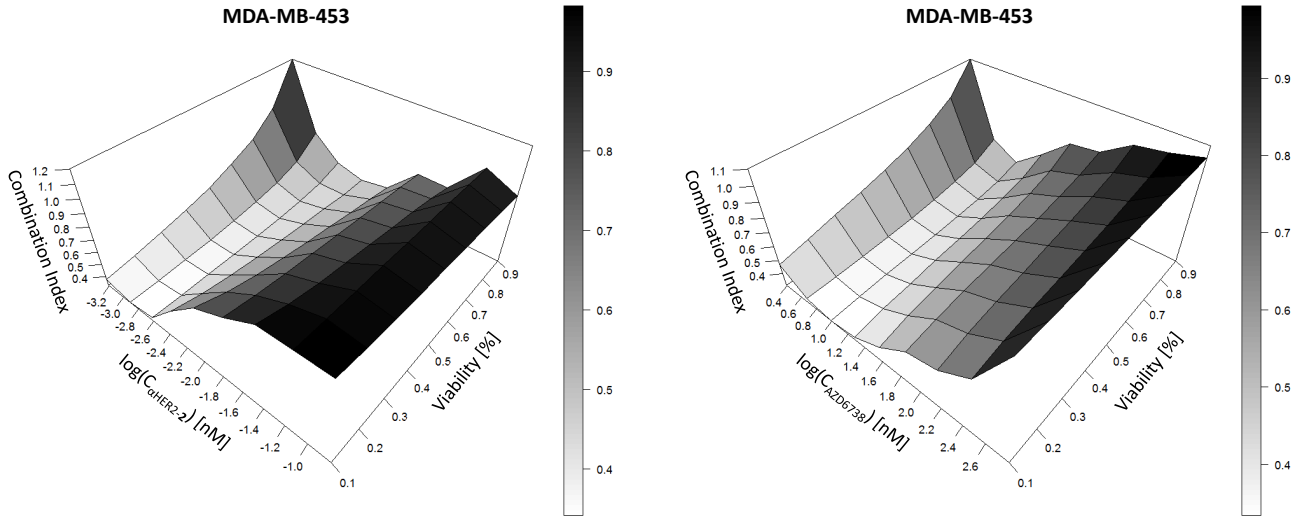

Figure 59: Combination index surface of αHER2-**2** combined with AZD6738 on MDA-MB-453. The CI was determined as a function of the constant concentration of either αHER2-**2** or AZD6738 added to the combination and of the cell viability. The surface is shaded in white to black, where white indicates low CI and black indicates high CI. The graphs are representative of two replicate experiments.

In addition, the CI surfaces were modeled for the combination of αHER2-**2** with ATRi **1** on MDA-MB-453 cells (Figure 60 A) and for the combination of αHER2-**2** with BAY1895344 on MDA-MB-453 cells (Figure 60 B). When comparing the CI surfaces for αHER2-**2** combined with either AZD6738, ATRi **1** or BAY1895344 on MDA-MB-453 it became apparent, that the course of the CI surface of the ATRi combined with constant concentrations of ADC remained largely unaffected by the choice of the ATRi. The CIs of αHER2-**2** plus BAY1895344 were the lowest, the CIs of αHER2-**2** combined with ATRi **1** were nearly equally low and the CI values of the combination of αHER2-**2** with AZD6738 displayed the highest CI values over the range of tested concentrations. While the combination of αHER2-**2** with varying constant concentrations of ATRi **1** had the minimum CI value at 9.8 nM ATR,i which is comparable to the combination of αHER2-**2** with AZD6738, the minimum CI of αHER2-**2** plus constant concentrations of BAY1895344 was 3.9 nM. The R-based script, that was written for the evaluation of the 13x13-dose-matrices, is attached in appendix 20.

.

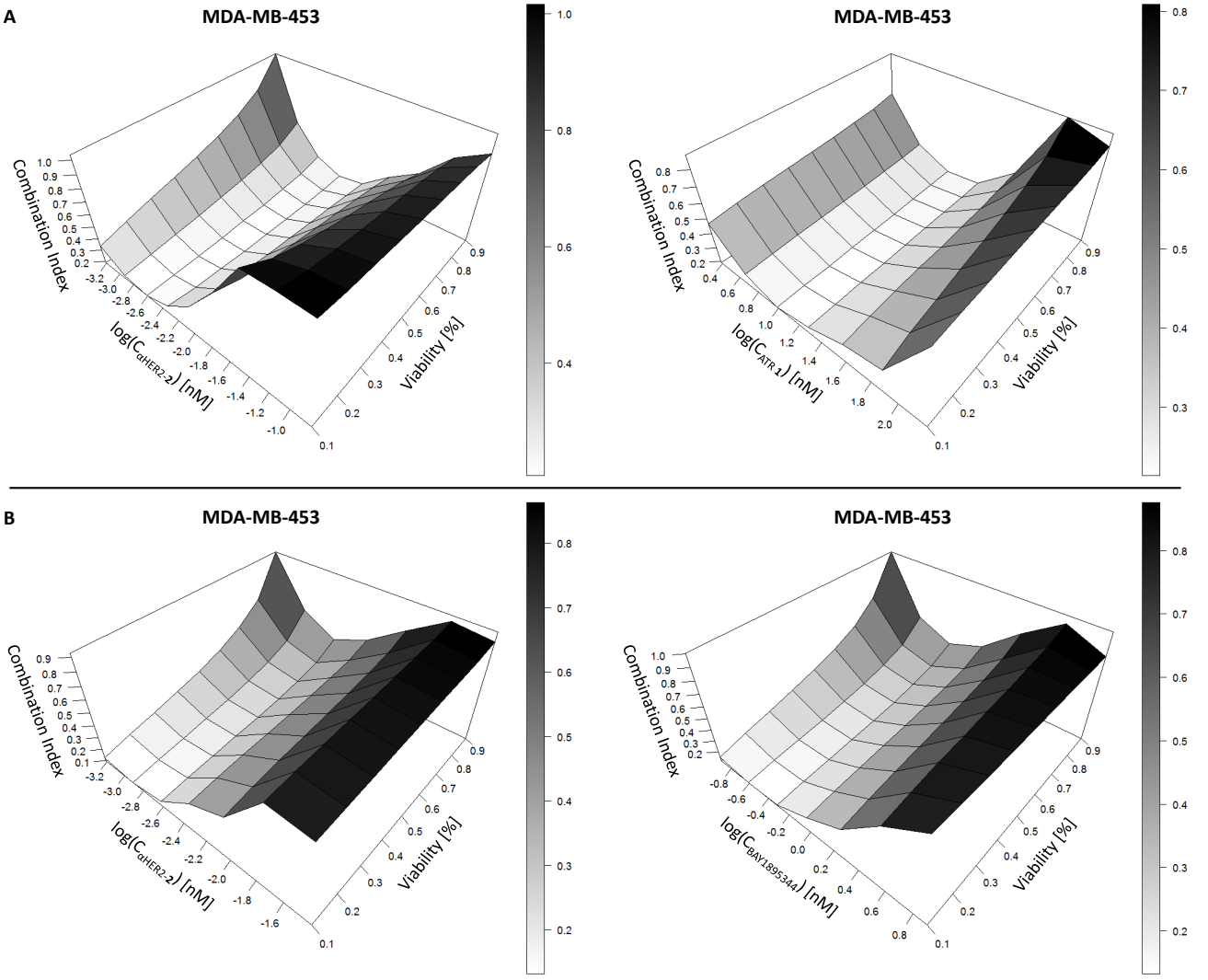

Figure 60: Combination index surface of αHER2-**2** combined with ATRi on MDA-MB-453. The CI was determined as a function of the constant concentration of either αHER2-**2** or ATRi added to the combination and of the cell viability. The surface is shaded in white to black, where white indicates low CI and black indicates high CI. A) CI surface for αHER2-**2** plus ATRi **1**. The graphs are representative of two replicate experiments. B) CI surface of αHER2-**2** combined with BAY1895344 on MDA-MB-453. The graphs are representative of one experiment.

5.8. *In vivo* Efficacy and Tolerability of αHER2-6 Combination with ATR Inhibitors AZD6738 and ATRi 1

After it was sucessfully confirmed that duocarmycins also synergize with ATRi when conjugated to an antibody the combination was investigated *in vivo* to study efficacy and tolerability of the combination treatment. 10 days after subcutaneous injection of NCI-N87 cells into H2d Rag2 mice, animals were randomized and treated either with vehicle, with a single intravenous dose of 1.0 mg kg^{-1} αHER2-**6** or with 50 mg kg^{-1} ATRi AZD6738 or ATRi **1**, given once daily over 14 days per oral. The combination effects were studied by giving αHER2-**6** combined with AZD6738 or αHER2-**6** plus ATRi **1** at the same dosing and schedule as the single agents.

The vehicle group was terminated on day 24, because the tumor volumes met the criterium for termination. The treatment with AZD6738 was not statistically different from the vehicle-treated group (P=.2). In case of the ATR Inhibitor ATRi **1**, a transient tumor stasis was induced until day 8 but the tumor rapidly progressed to reach the endpoint. However, the tumor-growth inhibition was statistically significantly stronger compared to the vehicle group (P=.003). The administration of the single agent αHER2-**6** led to transient tumor stasis until day 9 when the tumor progressed. ADC-treatment resulted in statistically significant reduction of tumor volume compared to the vehicle-receiving group (P=.0002) and the ATRi monotherapy groups treated with AZD6738 ($P=9x10^{-9}$) and ATRi **1** (P=.006).

The combination therapy groups αHER-**6** plus AZD6738 or ATRi **1** however induced stastistically significantly stronger anti-tumoral effects than the vehicle-treated group (P=.00003 or P=.00002, respectively). The combination αHER-**6** plus AZD6738 induced tumor stasis until day 66 when this group was terminated because three animals had skin lesions on the tumors. The treatment of mice with a combination of αHER-**6** and ATRi **1** led to tumor regression until day 63 when the tumors began to progress again. Remarkably, in the combination treatment group that received αHER-**6** plus AZD6738, one mouse showed a complete response ($V_{tumor}<20\ mm^3$) which lasted until the group was terminated (day 66). In the group treated with αHER-**6** plus ATRi **1** a total of three complete responses were observed. In one mouse, this effect was transient lasting around 90 days until the tumor progressed and in case of the other two mice, the animals showed tumor free survival until the end of the observation period (15 weeks). The data are displayed in figure 61 at the level of the treatment groups (Figure 61 A) and at the level of individual animals in the combination groups (Figure 61 B).

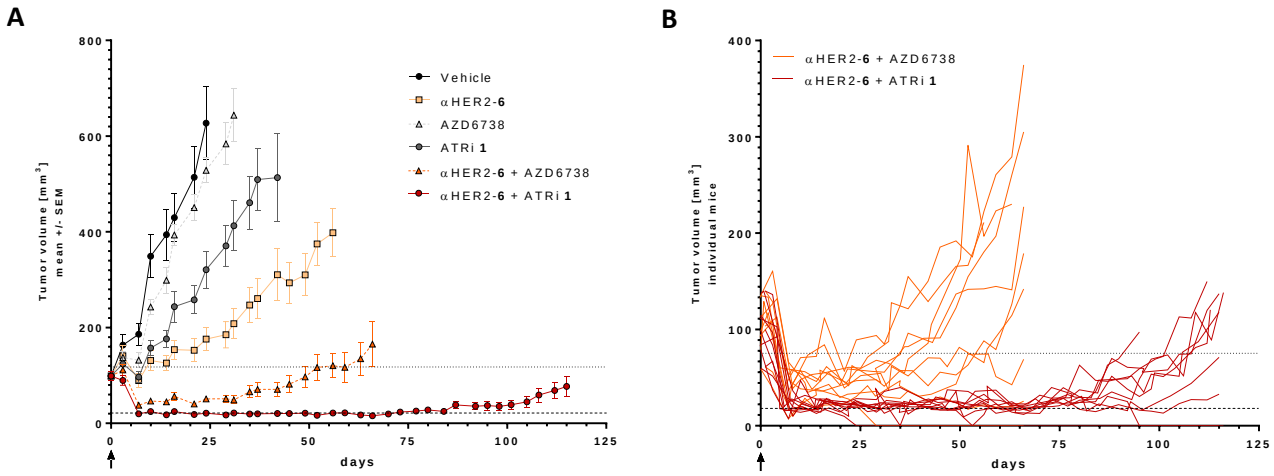

Figure 61: Therapeutic efficacy of αHER2-**6** combined with the ATR inhibitors AZD6738 and ATRi **1** in H2d Rag2 mice bearing NCI-N87 xenografts. **A)** Antitumor activity was assessed as change in tumor volume compared to vehicle, and the single agents αHER2-**6**, AZD6738 and ATRi **1**. Therefore mice (N=10 per group) were treated with 1.0 mg kg^{-1} αHER2-**6** intravenously, 50 mg kg^{-1} AZD6738 or ATRi **1** per oral once daily for two weeks or a combination of αHER2-**6** plus AZD6738 or αHER2-**6** plus ATRi **1** at the same doses and schedules as the single agents beginning at day 0 as indicated by the arrow. The upper dotted line indicates an increase in tumor volume of 73%, while the lower dotted line indicates a decrease in tumor volume by 66% as compared to day 0. The range between the dotted lines indicates tumor stasis and below the lower line tumor regression. **B)** Tumor volume of the combination groups αHER2-**6** plus AZD6738 or αHER2-**6** plus ATRi **1** at the level of individual animals. Treatment with αHER2-**6** plus AZD6738 led to 1/10 cures, while the treatment with αHER2-**6** plus ATRi **1** led to 2/10 cures.

The tolerability of the anti-cancer treatment was assessed considering the overall condition of the animal as well as body-weight changes of the mice (Figure 62). The body-weight of mice treated with the ADC αHER2-**6** did not decrease and was comparable to the body-weight of the vehicle-treated group at all time points. However, mice treated with the ATRi AZD6738 and ATRi **1** lost weight compared to the vehicle group but body-weight loss was still below 5%. Mice receiving combination treatment with αHER2-**6** and AZD6738 or ATRi **1** showed a body-weight profile comparable to mice treated with the ATRi AZD6738 or ATRi **1** as single agents.

It can be concluded that the ADC αHER2-**6**, the ATRi AZD6738 and ATRi **1** as well as the combination treatments were well tolerated.

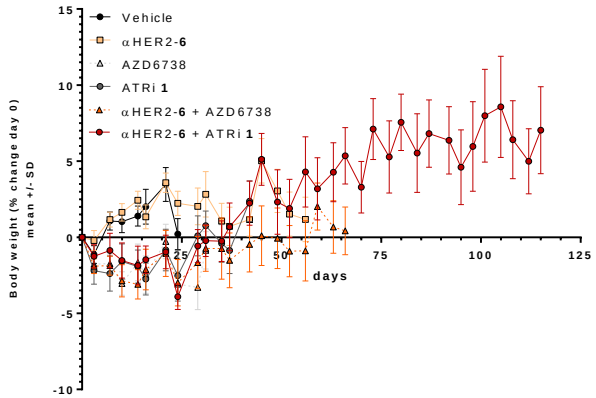

Figure 62: Therapeutic tolerability of αHER2-**6** combined with the ATR inhibitors AZD6738 and ATRi **1** in H2d Rag2 mice bearing NCI-N87-xenografts.The body weight was assessed as a measure of tolerability of the combination treatment as well as the corresponding single agents αHER2-**6**, AZD6738 and ATRi **1**.

5.9. Bleomycin A5-ADCs

In preceeding chapters it was discovered that drugs of the duocarmycin family synergized with ATRi and that ATR knock-down cells were sensitized towards duocarmycin treatment. Furthermore, duocarmycins were coupled to antibodies and the resulting ADCs were studied in depth in combination with ATRi. It was proven, that the synergy observed with the combinations of small molecule duocarmycins could be translated to the ADC context. ATR belongs to the PIKK kinase family and is responsible for replication and DNA-damage response. DNA-PK and ATM are two other enzymes of the PIKK family that are both involved in DNA-damage response, specifically in the repair of double-strand breaks. It was hypothesized that synergistic drug combinations might be discovered for these members of the PIKK family. In this chapter double-strand break inducing Bleomycin A5-based ADCs were generated and subsequently combined with DNA-PK inhibitors NU7441 and M3814.

5.9.1. Generation of Bleomycin A5-Bearing ADCs

Linker-drug **9** was synthesized (laboratory Dr. Carl Deutsch, department of ADCs and Targeted NBE Therapeutics, Merck KGaA), which carried the double-strand break inducer Bleomycin A5 (BA5). LD-**9** consisted of several structural units. A triple-glycine motif for SrtA-mediated conjugation was introduced *N*-terminally, followed by a spacer. A valine-citrulline dipeptide coupled with a self-immolative PAB module ensured efficient release of the drug Bleomycin A5 (Figure 63).

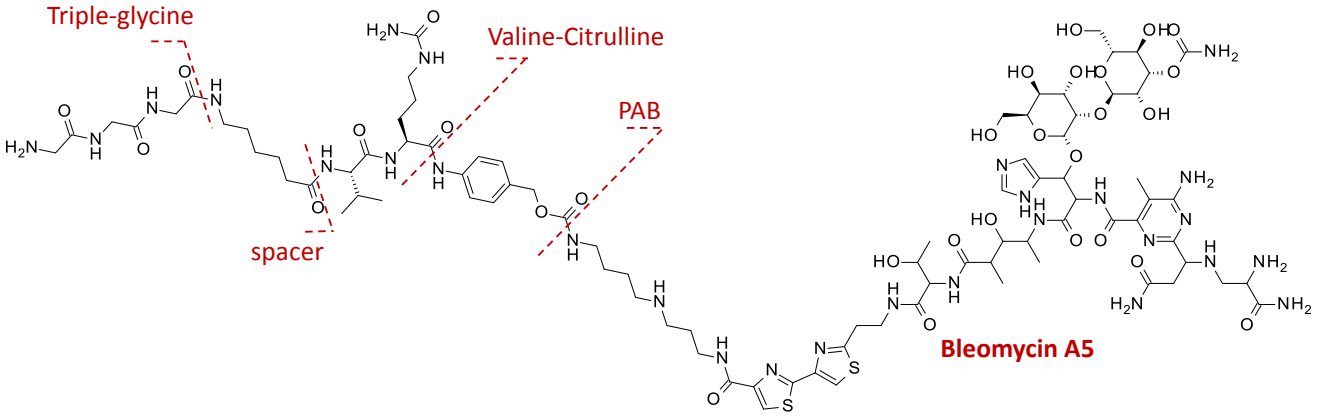

Figure 63: Bleomycin A5 linker-drug **9**. The linker-drug can be structured into five units. Beginning *N*-terminally, a triple-glycine for SrtA conjugation is introduced, followed by a spacer. The dipeptide valine-citrulline paired with the self-immolative module PAB ensures efficient, traceless release of Bleomycin A5.

LD-**9** was conjugated to the LCs of the αHER2 and the αEGFR mAb (format A) via SrtA-mediated ligation. A DAR of 1.78 was achieved in both cases. Furthermore, LD-**9** was conjugated to trastuzumab in the mAb format D, which allowed the conjugation of up to four drugs per mAb. The preparation yielded αHER2-**9** with a DAR of 3.38. The theoretical yield of the preparation of αHER2-**9** with SrtA-site at HC and LC and the preparation of

αEGFR-**9** was exceeded (>100%). The yield of the generation of αHER2-**9** with 1.78 drugs per mAb was excellent. The monomeric content was high with >99.0%. Table 16 gives an overview of the produced ADCs.

Table 16: Overview of preparations of Bleomycin-A5 ADCs. The column "App." contains the appendix number under which data such as HIC and SEC profile can be found.

Target	mAb format	Linker-drug	Purification route	Yield [µg]	Yield [%]	DAR	Monomer [%]	App.
αHER2	A	**9**	A	2240	93.0	1.78	99.8	17
αHER2	D	**9**	A	4430	116.0	3.38	99.2	16
αEGFR	A	**9**	A	5240	122.2	1.78	99.8	18
αHEL	A	**9**	A	1530	65.0	1.81	99.7	19

5.9.2. Cytotoxicity of Bleomycin A5-Based ADCs

Anti-proliferative effects of Bleomycin A5-ADC αEGFR-**9** in mAb format A were studied on an EGFR-postive cell line panel. However, only on EGFR-positve cell lines MDA-MB-468 and A431 the effects of Cetuximab alone were exceeded (Figure 64). On MDA-MB-468, the potency of αEGFR-**9** was 1.4±0.4 nM (N=6) and on A431 a potency of 5±1 nM (N=3) was reached. On EGFR-negative MCF7 cells, no effect was observed (N=1). In addition, on the EGFR-positive cell lines A549, Capan-2, MDA-MB-231 and SK-OV-3 no effect was observed up to 250 nM (N=1, each). The small molecule Bleomycin A5 was considerably less potent on MDA-MB-468 with an IC_{50}-value of 1973±387 nM (N=4).

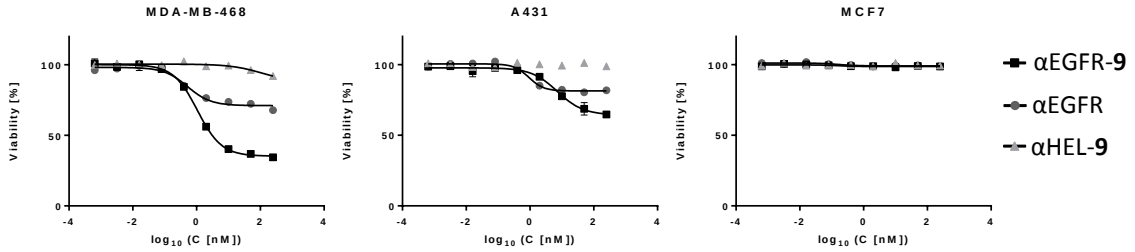

Figure 64: Representative dose-reduction curves of Bleomycin A5-ADC αEGFR-**9** and αHEL-**9** and mAb cetuximab on EGFR-positive cell lines MDA-MB-468, A431 and EGFR-negative cell line MCF7.

The Bleomycin A5-ADC αHER2-**9** was active on HCC-1954 cells with an IC_{50} value of 1.2±0.5 nM (N=3). At 250 nM, the highest concentration used in the assays, 42±4% of the cells were killed. In comparison to this, the small molecule Bleomycin A5 had an IC_{50}-value of 567±21 nM (N=3). To exclude, that the effect is mediated by the αHER2 mAb itself, the mAb was tested on the cells. The αHER2 mAb alone killed 4±4% (N=3) of the cells at 250 nM. On the negative cell line MDA-MB-468 αHER2-**9** affected 7±4% (N=3) of the cells at C=250 nM. No

cytotoxic effect was observed up to 250 nM on BxPC3 and LNCaP cells when treated with αHER2-**9**. The potencies of Bleomycin A5-based ADCs are summarized in table 17.

Table 17: Overview of cytotoxicity of Bleomycin A5-based ADCs. Isotype control ADC αHEL-**9**, αEGFR-**9** and αHER2-**9** as well as small molecule BA5 were studied on several cell lines. EGFR and HER2 levels are indicated by plus or minus sign for postive or negative cell lines, respectively. If no cytotoxic effect was observed up to 250 nM, it is indicated by "No Effect (N/E)". Experiments were conducted in singlicates, except it is stated otherwise.

			IC_{50} in nM			
	EGFR	**HER2**	αHEL-**9**	αEGFR-**9**	αHER2-**9**	BA5
A431	+	N/E	N/E	5±1 (N=3)	-	-
A549	+	N/E	N/E	N/E	-	-
BxPC3	+	N/E	-	-	N/E	-
Capan-2	+	N/E	-	N/E	-	-
HCC-1954	+	+	-	N/E	1.2±0.5 (N=3)	567±21 (N=3)
LNCaP	+	N/E	N/E	-	N/E	-
MCF7	-	N/E	N/E	N/E	-	4152 (N=1)
MDA-MB-231	+	N/E	-	N/E	-	-
MDA-MB-468	+	+	N/E	1.4±0.4 (N=6)	N/E	1973±387 (N=4)
SK-OV-3	+	+	-	N/E	-	-
SK-BR-3	+	+	-	-	N/E	-

5.9.3. Synergistic Effects of Bleomycin A5-ADC Combinations with DDRi

The Bleomycin A5-bearing ADC was active on MDA-MB-468 in the nanomolar range. As a next step, it was studied whether the Bleomycin A5-ADC synergizes with DDRi known to be involved in double-strand break repair. Therefore, αEGFR-**9** was combined with the DNA-PKi NU7441 and M3814 on MDA-MB-468 in a dose-matrix assay. As controls, the small molecule Bleomycin A5 and the antibody cetuximab were combined with the DDRi NU7441. After 6 d, the cell viability was read out as luminescence on an Envision reader. The data were analyzed via GeneData Screener and synergistic effects were expressed as synergy scores. All combinations exceeded the cutoff synergy score that indcated additivity. The small molecule Bleomycin A5 combined with NU7441 had a mean synergy sycore of 2.7, however, the values scattered strongly. The combination of cetuximab with NU7441 also exceeded the cutoff with S=1.8. The synergy of ADC αEGFR-**9** combined with the DNA-PKi NU7441 (S=5.7) was stronger than the synergy between αEGFR-**9** and M3814 (S=4.7). The synergy scores are summarized in figure 65.

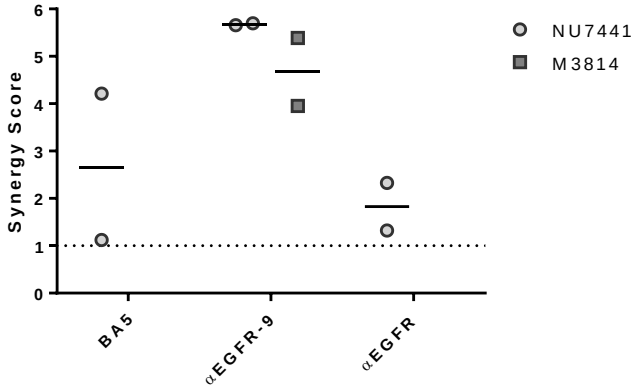

Figure 65: Synergy scores of αEGFR-**9** when combined with DNA-PKi NU7441 or M3814 on EGFR-positive MDA-MB-468 cells. Control groups were combinations of cetuximab (C) or Bleomycin A5 combined with DNA-PKi NU7441. Individual data points are displayed as well as a black bar indicating the mean of the individual points.

5.9.4. Potentiation Effects of Bleomycin A5-ADC Combined with NU7441 or KU-55933

The ADC αEGFR-**9** was added to MDA-MB-468 cells either alone or together with a constant concentration of the DNA-PKi NU7441. The DDRi was given at its respective MNED of 1.2 µM. The potency amounts to 0.07±0.01 nM when 1.2 µM NU7441 and αEGFR-**9** were added to MDA-MB-468 cells simultaneously. This is a significant (P=.0007) 19.3-fold potentiation of the ADC potency (IC_{50}=1.4±0.4 nM).

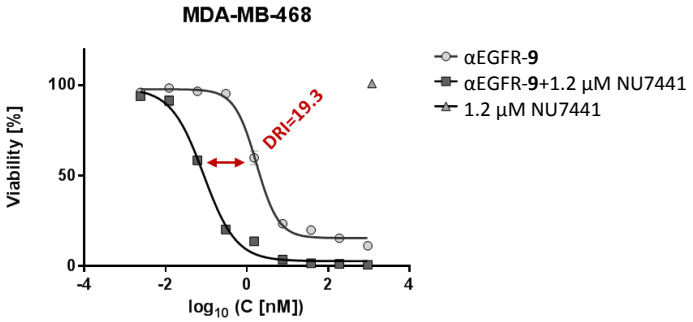

Figure 66: Dose-response curves of αEGFR-**9** combined with constant doses of DNA-PKi NU7441 on MDA-MB-468. The combination of αEGFR-**9** with 1.2 µM NU7441 led to a curve-shift of 19.3 as calculated from the mean of the mono- and combination treatment.

6. Discussion

6.1. Screening for a Synergistic Drug Combination Partner for Duocarmycin

A total of 17 DDRi were combined with DUBA on the two cancer cell lines HCC-1954 and MDA-MB-468. While most of the DDRi yielded only additive effects when combined with DUBA, some exceeded the cutoff for synergy barely. Two targets were identified whose inhibition led to strong synergistic anti-proliferative effects in combination with DUBA, namely ATR and CHK1. These enzymes play a major role in the replication stress response in the same pathway, where CHK1 is the downstream kinase of ATR.

In order to prove the observed synergy between DUBA and the ATRi and CHK1i in the dose-matrix assay, the enzymes were downregulated by transfection of HCC-1954 cells with ATR and CHK1 siRNA. The potency of DUBA and DDM was substantially higher on ATR knock-down cells than on cells treated with non-targeting siRNA. However, only a minor potentiation was observed in case of CHK1 siRNA treated cells compared to control cells. One explanation for this might be that the CHK1i LY2603618 and AZD7762 have off-target effects on ATR. Although LY2603618 was described as a specific CHK1i based on a screening on 51 kinases, inhibitory effects regarding ATR were not studied.[155] In case of the CHK1i AZD7762, it was tested for inhibitory effects on a total of 164 kinases, but again, ATR was not studied.[156] Based on these reports it cannot be fully excluded, that the CHK1i have off-target effects on ATR. However, in case of CHK1 siRNA treatment, the knock-down efficiency was considerably lower compared to ATR knock-down, leading to residual CHK1 levels that might be sufficient for cell cycle regulation. This might also explain the differentially strong potentiation effects of ATR or CHK1 knock-down versus control cells.

Taken together, this work identified a synergistic drug combination of ATRi combined with the duocarmycin-derivative DUBA. However, at this point it was not clear which influence the duocarmycin variant and also the type of the ATRi have on the synergistic cell killing effects.

6.2. Impact of Duocarmycin Structure on Synergistic Effects

During the screening procedure only one distinct molecule from the duocarmycin familiy was used, namely DUBA. In order to elucidate the influence of the structure of the duocarmycin on synergistic effects, a duocarmycin library was combined with the ATRi AZD6738 to treat HCC-1954 cells. Duocarmycins consist of two structural subunits – the binding and alkylating unit. It was aimed at identifying the distinct influence of these two structural subunits. The results are summarized in figure 67. Figure 67 A ranks compounds with a trimethoxyindole (TMI) binding moiety and five varying alkylating units. While the duocarmycins with bi- and tricyclic alkylating units had synergy scores in the same range when combined with AZD6738, the monocyclic variant synergized with the ATRi only weakly. Apparently, whether the achiral or chiral variants were combined with AZD6738 did not have a major impact on the synergy score for duocarmycins with the bi- and tricyclic

alkylating units. In figure 67 B and C, the duocarmycin variants from the CBI-series were ranked. Here, the alkylating unit was a CBI-unit or a methyl-CBI-unit. These duocarmycins comprised different binding units. Although small differences were observed for the combination of these compounds with the ATRi AZD6738 on HCC-1954, the differences were less distinct compared to the TMI-series, suggesting a larger impact of the alkylating unit on the synergistic effects than the binding unit.

Members of the duocarmycin family have distinct properties that largely depend on their structure. These properties include stability, cytotoxicity and alkylation rate. It was reported that the choice of the alkylation unit as well as the binding unit influences the alkylation properties of the duocarmycin.[157,158] In this report, no correlation between potency and synergy score for duocarmycins combined with ATRi was established. It is possible that the synergy between duocarmycins and ATRi depends on several factors such as the alkylation efficiency, the timing of the alkylation as well as the stabilization of DNA helix.

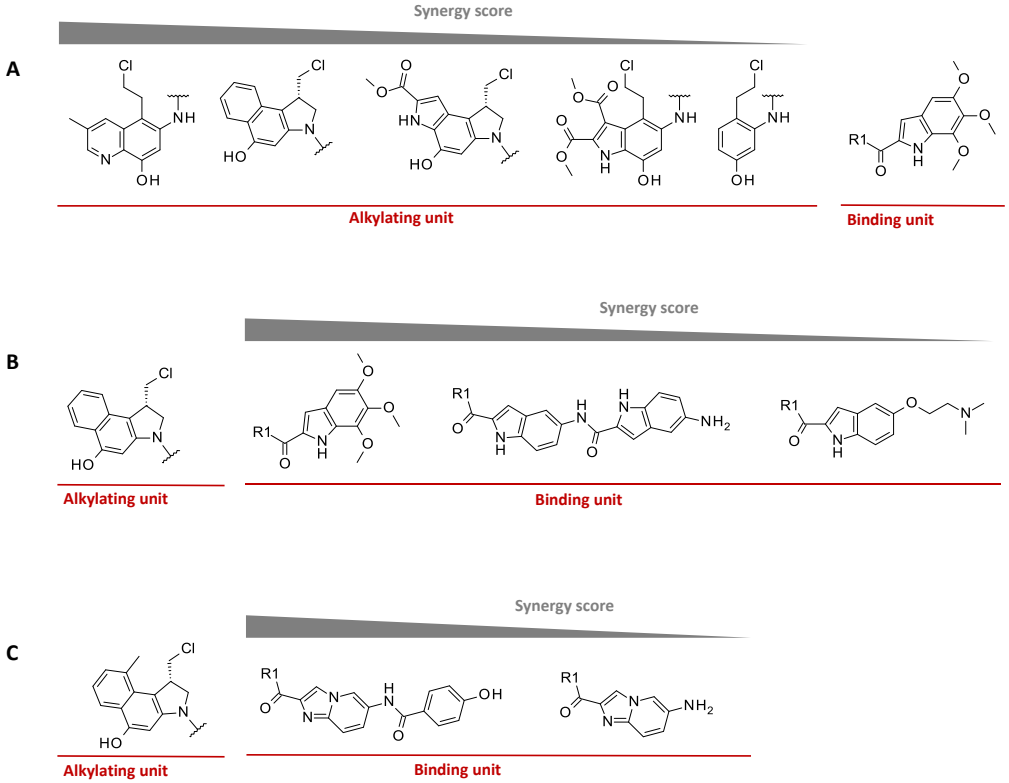

Figure 67: Ranking of synergistic effects of a duocarmycin library combined with ATRi AZD6738 on HCC-1954 cells. A) Schematic representation of the influence of the alkylating unit on the synergy score upon keeping the binding unit constant. The binding unit was a trimethoxyindole moiety in all cases. B) Schematic representation of the influence of binding unit on synergy score. The alkylating unit was a CBI-unit, which was extended by three different binding units. C) Influence of binding unit on synergy score. Methyl-CBI unit as alkylating unit was extended by two distinct binding units.

6.3. ADC-Generation to Modulate the Therapeutic Window of Duocarmycin

Adozelesin and Carzelesin, two molecules of the duocarmycin family, have been in clinical development for anti-cancer therapy. However, both compounds failed because no therapeutic window could be established.[75,159] Duocarmycins were therefore conjugated to antibodies in order to increase the therapeutic window by mediating drug delivery to tumor cells specifically through the antibody portion.

ADCs were conjugated using linker-drugs comprising the duocarmycins Duocarmycin DM, DUBA and Duocarmycin SA. The Duocarmycin DM linker-drug **1** was successfully conjugated using SrtA to the αHER2 antibody, the αEGFR antibody as well as to an αHEL, αMET, a bispecific αMETxEGFR antibody and a glycoprotein binding antibody. No clear dependency of yield or physicochemical properties of the ADC on purification route or mAb format was found. In all cases the conjugation efficency was high, leading to ADCs with >75% of available conjugation sites covered, meaning that ADCs with two conjugation sites carried at least 1.5 drugs per antibody. The ADCs generally had high monomeric contents.

The αHER2 mAb was used as model antibody to generate four additional ADCs comprising DUBA-based linker-drugs **2**, **3**, **4** and **5**. The conjugations of LD-**2** and LD-**3** were successful with yields as high as 97.8% and 81.1%, respectively and high DARs at low levels of aggregates <3%. However, the conjugation of LD-**4** and LD-**5** was considerably difficult. The analytical scale conjugation of LD-**4** to the αHER2 mAb led to the precipitation of the reaction product so the conjugation of this linker-drug was not pursued any further. The analytical scale coupling of LD-**5** to the αHER2 mAb was comparably slow. Even elongation of reaction time did not lead to a significant increase in conversion, hence, the ADC was not conjugated in preparative scale. The DUBA-ADC αHER2-**6** and the DSA-ADC αEGFR-**7** were kindly provided by the laboratory of Dr. Nicolas Rasche.

The preparation of the clinically developed ADC SYD985 was performed according to literature upon conjugating the maleimide-containing LD-**28** to reduced cysteines of the αHER2 mAb trastuzumab. The conjugation procedure led to the formation of a heterogeneous ADC mixture consisting of species with varying drug-loads including unconjugated mAb and also high molecular weight (HMW) species. Preparative HIC was applied to remove the high DAR and HWM species, finally yielding an ADC with a DAR of 2.8. However, the ADC SYD985 was still a mixture comprising DAR=2 and DAR=4 species in a 2:1 ratio.[82] In this work, the DUBA-based LD-**2** which was closely related to the linker-drug of Synthon's ADC SYD985 was used for ADC generation. The only difference between the two linkers was that LD-**2** carried a triple-glycine tag *N*-terminally of the linker-drug in contrast to Synthon's linker-drug bearing a maleimide (Figure 68). The oligo-glycine tag enabled site-specific conjugation of the linker-drug LD-**2** to the genetically modified light chains of the αHER2 mAb *via* the enzyme Sortase A. This led to the formation of a homogenous ADC with a DAR of 1.85 and 97.4% monomeric content at a high yield of 60.0%. Thus, site-specific drug conjugation might be beneficial for the generation of DUBA-based ADCs, because the drug product was considerably more homogeneous.

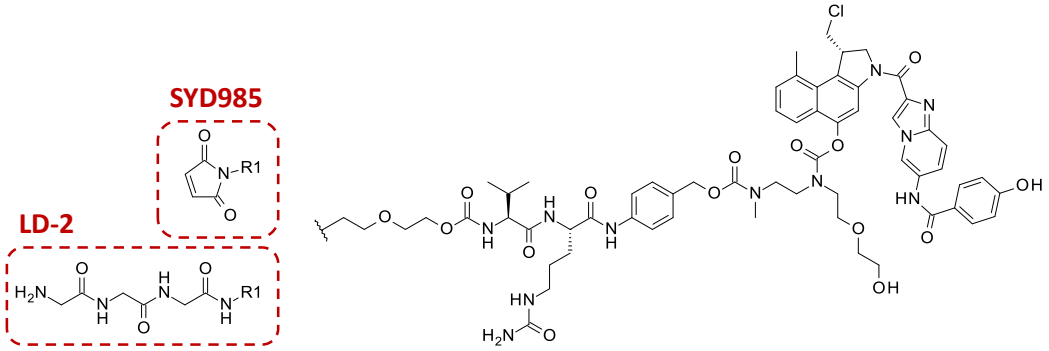

Figure 68: Chemical structures of LD-**2** in comparison with the linker-drug of SYD985. The coupling strategy was changed from thiol coupling *via* maleimide as in the linker-drug of SYD985 to SrtA-mediated coupling via an oligo-glycine tag as in LD-**2**.

After the successful conjugation of the ADCs, it was studied whether the cytotoxicity of the duocarmycins was retained in the ADC format. All the αHER2 ADCs (αHER2-**1**, αHER2-**2**, αHER2-**3** and αHER2-**6**) were potent in the single-digit to subnanomolar range on HER2-positive cell lines reaching double-digit picomolar IC_{50}-values in some cases. αHER2-**1** comprised the drug Duocarmycin DM and the ADCs αHER2-**2**, αHER2-**3** and αHER2-**6** carried DUBA as payload. The DUBA-ADCs differed in the linker-structure and conjugation technique. There was no clear connection between linker-drug and potency of the conjugate. In addition, the αHER2-duocarmycin ADCs were comparably cytotoxic as Kadcyla, except on Calu-3 cells, where Kadcyla was considerably less potent in the double-digit nanomolar range. As an isotype control, αHEL-**1** was tested. This non-binding ADC was less toxic to the cells than the binding counterpart ADC αHER2-**1**, generally killing cells in the double- to triple-digit nanomolar range. Table 18 compares the results of the cell viability assays reported in this work for Kadcyla, and DUBA-based ADCs αHER2-**2** and αHER2-**6** with the cytotoxicity of SYD985 and Kadcyla reported by van der Lee *et al.*[87] The IC_{50}-values of Kadcyla reported in this work and in literature differed only to a minor extent although the linkers of αHER2-**2** and αHER2-**6** were not identical to the linker of SYD985.

Table 18: Comparison between potencies of Kadcyla obtained from literature and determined in this work.

	IC_{50}-values reported in literature[87] [nM]		IC_{50}-values reported in this work [nM]		
	SYD985	Kadcyla	Kadcyla	αHER2-**2**	αHER2-**6**
SK-BR-3	0.046	0.11	0.2±0.1	0.16±0.05	
NCI-N87	0.16	0.30	0.08970±0.00003	0.18±0.01	0.3±0.4

In order to evaluate whether the low potencies of the αHER2-duocarmycin ADCs were dependent on the target HER2 or if the cytotoxicity was target-independent, further ADCs based on other antibodies like the αEGFR mAb cetuximab and also αMET and a bispecific mAb directed against both EGFR and MET were studied regarding their anti-proliferative effects.

DDM-carrying αEGFR-**1** and DSA-bearing αEGFR-**7** as well as αMET-**1** and the bispecific molecule αMETxEGFR-**1** were investigated on target-positive cells. Again, all ADCs were potent in the nano- to subnanomolar range on target-positive cells. The least potent ADC was αMETxEGFR-**1** which was probably caused by the ADC carrying only ~0.9 drugs per mAb, while the cetuximab and αMET ADCs had a DAR>1.68.

Besides studying the ADCs on target-positive cells, the ADCs were also tested for unspecific cell cytotoxicity on target negative cells. In case of αHER-ADCs, the IC_{50}-values were in the double- to triple-digit nanomolar range. As a result, the ADCs were considerably less potent on HER2-negative MDA-MB-468 cells. Cetuximab-based ADCs showed similar results on EGFR-negative MCF7 cells with IC_{50}-values in the single- to double-digit nanomolar range.

During the drug development process it is important to assess the safety of a drug. A common measure for drug safety is the therapeutic index, which quantitatively correlates desired on-target pharmacological effects with off-target side-effects. Although, testing in animals or humans leads to a more accurate determination of the therapeutic index and also the safety of the drug, biochemical and *in vitro* methods can also be applied in early development to rank drug candidates. One such early estimation of the therapeutic index uses the on-target versus off-target selectivity of a drug.[153]

Hence, the differential cytotoxic effects induced by ADCs towards target-negative versus target-positive cells was expressed in the form of a selectivity index (Eq. 4). The selectivity index is a measure of the selectivity of an ADC towards antigen-expressing cells. In general, a high selectivity index indicates a strong cell toxicity on antigen-positive cells uponbeing considerably less toxicity towards antigen-negative cells. The results presented in this work indicated that the Duocarmycin DM-bearing ADC αHER2-**1** was approximately one order of magnitude more selective than the DUBA-based ADCs αHER2-**2** and αHER2-**3**, which were almost equally selective. The DUBA-based ADCs were as selective as Kadcyla. The non-binding ADC anti-HEL-**1** and the small molecules DDM and DUBA however did not show any selectivity towards HER2-expressing cells, as was expected.

These results suggested a major impact of the duocarmycin variant conjugated to the mAb on the selectivity but only a minor influence of the linker regarding the selectivity of an ADC at least in the HER2-context. In addition, it was shown, that the cetuximab-based ADCs αEGFR-**1** and αEGFR-**7** were selective towards EGFR-expressing cells. However, Duocarmycin DM-bearing and DSA-carrying ADCs αEGFR-**1** and αEGFR-**7**, respectively, were nearly equally selective towards EGFR-expressing cells. The small molecules DDM and DSA on these cell lines did not exert any selectivity for EGFR-positive cell lines, as expected.

These results demonstrated very clearly that the cytotoxicity of the small molecule duocarmycins was retained in duocarmycin-bearing ADCs. In addition, the results suggested that the cytotoxicity was largely independent of the target antigen of the ADC. Furthermore, the ADCs specifically killed antigen-positive cells while antigen-negative cells were affected only to a minor degree.

6.4. Synergistic Effects of Combinations of Duocarmycin-ADCs with ATRi

After it was proven that ATRi AZD6738 synergized with duocarmycins independently of the structure of the duocarmycin, it was studied whether the synergy was also retained in the ADC format. The duocarmycin-bearing ADCs αHER2-**1**, αHER2-**2** and αHER2-**6** were applied together with AZD6738 to three cancer cell lines HCC-1954, NCI-N87 and MDA-MB-453. In all cases, the duocarmycin-carrying ADCs synergized comparably to the small molecule duocarmycin. On MDA-MB-453, the synergy of the ADC plus AZD6738 was higher than the synergy between DUBA and AZD6738. This observation might be explained as follows:
The small molecule DUBA is highly efficacious on this cell line, while the ADC is only capable of affecting 70% of the cells. However, in combination the efficacy of the ADC is enhanced, leading to death of the entire cancer cell population. Since DUBA already affects all cells, the efficacy cannot be further increased, leading to a smaller synergy score (Figure 69). This indicated that the combination therapy might have the potential to increase the overall response of the cell population to the treatment.

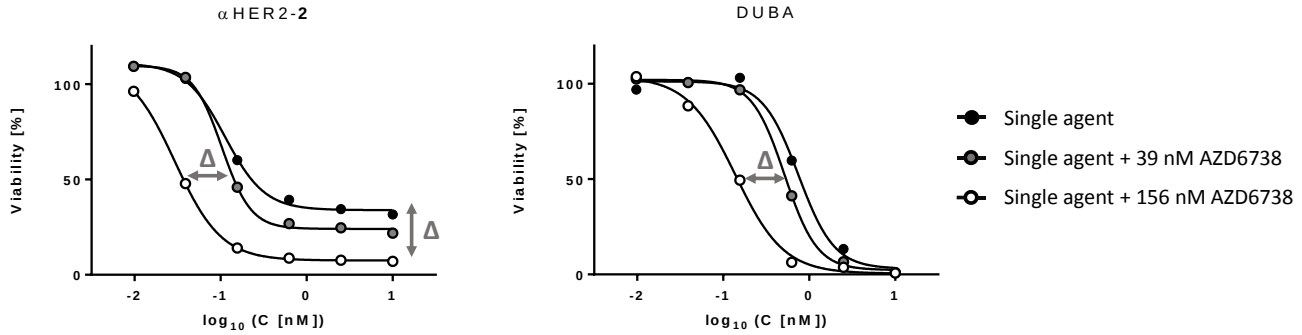

Figure 69: Cell viability of MDA-MB-453 after treatment with αHER2-**2** or DUBA alone or in combination with constant doses of AZD6738. If MDA-MB-453 cells were treated with αHER2-**2** alone, the cell viability was only reduced to 30%, while DUBA as single agents had 100% efficacy. In combination with AZD6738, the efficacy of αHER2-**2** was enhanced leading to the death of an increased number of cells while the combination of DUBA with AZD6738 might only increase the potency.

It was published by Wallez *et al.* that gemcitabine synergizes with the ATRi AZD6738.[160] The synergistic effects of gemcitabine when combined with AZD6738 were reproduced on HCC-1954 cells. However, on NCI-N87 and MDA-MB-453 cells no or weak synergistic effects were observed, respectively, for the combination treatment. This indicated a strong dependency of gemcitabine-ATRi combinations on the cellular background. In another study by Thomas *et al.* a synthetic lethal screen with siRNA revealed that ATR depletion sensitized cells to TOP1 poisons. Drug combinations of TOP1i irinotecan with ATRi VE-822 were investigated *in vitro* and *in vivo*. Synergistic anti-tumor effects were observed for the combination of irinotecan with VE-822. In this study, SN-38, an active metabolite of irinotecan was combined with another ATRi AZD6738 as a benchmark. The synergistic effects of TOP1i combined with ATRi published by Thomas *et al.* were reproduced on HCC-1954 cells but not NCI-N87 and MDA-MB-453 cells.

As negative controls, a microtubule-targeting agent (MTA), MMAE, and the MTA-carrying ADC Kadcyla were studied. On HCC-1954 cells, both drugs had weak synergistic effects when combined with the ATRi AZD6738, which is in line with the observation that ciliobrevin D had weak synergistic effects in the screening when combined with AZD6738 on HCC-1954 cells. However, on NCI-N87 and MDA-MB-453 cells no synergy between Kadcyla and the ATRi AZD6738 were observed. Interestingly, the positive controls Gemcitabine, SN-38 as well as DUBA and the DUBA-ADC αHER2-**2** had nearly identical synergy scores when combined with AZD6738. By treating EGFR-positive cells with combinations of αEGFR-**1** or αEGFR-**7** and the ATRi AZD6738 it was proven that the synergistic effects of duocarmycins with ATRi were not exclusive for HER2-targeting ADCs but could also be translated to ADCs targeting different antigens and thus potentially other indications.

A total of seven ATRi were investigated in this study to eludidate the effect of the ATRi on the combination effects. The ATRi were ranked according to their ability to inhibit the phosphorylation and thus activation of CHK1 after HT29 cells were stressed by treatment with hydroxyurea. The results allowed the establishment of a correlation between synergy scores and the potency of CHK1 phosphorylation inhibtion. Ultimately, it was observed that, the more potent the ATRi in terms of CHK1 phosphorylation inhibition, the higher the synergy score when combined with DUBA or DUBA-ADCs.

By comparing the synergy scores of small molecule duocarmycins with ATR on several cell lines, the sensitivity of different cell lines toward combined treatment could be estimated. MCF7 and A549 cells e.g. responded comparably weak to the drug combination, while the same combination led to 2-3 fold higher synergy scores on HCC-1954 and MDA-MB-468 cells. These data suggested a strong dependency on the cellular background. A review by Forment and O'Connor described several genes that rendered cells resistant or sensitive for treatment with ATR inhibitors.[94] Increased sensitivity or resistance toward ATR inhibition might account for the differences between the cell lines.

The synergistic effects between duocarmycins and duocarmycin-ADCs combined with ATRi were elucidated using a curve-shift assay system. The potentiation effects were reproduced on nine HER2-positive cell lines using a combination of αHER2-**1** with AZD6738 or VE-822. However, the extent of the potentiation effects varied strongly which is not surprising given the different synergy scores of the small molecules combined with the ATRi on several cell lines. Besides, a strong dependency of the potentiation effects on the choice of ATRi AZD6738, VE-822, ATRi **1** or BAY73 in the combination with αHER2-**1** was observed on HCC-1954. Again, the potentiation effects were dependent on the potency of the ATRi to inhibit CHK1 phosphorylation. Furthermore, also the duocarmycin variant had an influence on the potentiation effects if ATRi were added. DUBA-variants displayed greater potentiation effects than DDM-based ADCs combined with ATRi. Additionally, the potency of a glycoprotein binding ADC combined with the ATRi AZD6738 and VE-822 was potentiated. All in all, the results of the curve-shift assay underpinned the results obtained from the dose-matrix assays.

The dose-reduction effects were used to study whether the combination treatment of duocarmycin-ADC with ATRi might lead to a beneficial therapeutic window compared to monotherapy. The combination of αHER2-**1**

with AZD6738 or VE-822 led to an increased selectivity index over monotherapy on around half of the cell lines. Lehár *et al.*[22] reported that synergistic drug combinations tended to be more selective towards diseased tissues compared to the single agents. The fact that only on half of the cell lines combination treatment posed a selectivity benefit over monotherapy might be explained in part by the crosstalk between HER2 and ATR. HER2 inhibition and also knock-down leads to the inhibtion of ATR activation and abrogation of G2/M checkpoint following treatment of cells with IR.[138] This suggests that HER2-negative cancer cell lines might be particularly sensitive to ATR inhibition and thus combination treatment. Furthermore, the HER2-negative cell line MDA-MB-468 responded comparably strong to combined treatment with ATRi and duocarmycin. MDA-MB-468 cells are mutated in the PTEN gene leading to loss of function of the enzyme.[161] PTEN plays an important role in replication fork recovery and checkpoint response after cells were stressed with replication inhibitors.[162] In addition, PTEN dephosphorylates MCM2 upon replication stress and thereby restricts the progression of the fork.[163] Hence, PTEN loss of function might lead to formation of long stretches of ssDNA due to uncoupling of helicase and DNA polymerases which might result in depletion of RPA pools. Besides, fork stabilization is impaired in PTEN loss cells, whereby fork collapse and subsequent formation of DSBs might be promoted. Thus, the selectivity index might be underestimated.

Overall, these results demonstrated the translatability of the combination effects of small molecule duocarmycins to the ADC format. Furthermore, the synergistic effects of gemcitabine, SN-38 and DUBA or DUBA-ADCs with ATRi were in good comparison on HCC-1954 cells. Thirdly, synergistic effects of duocarmycin-ADCs with ATRi can be observed independently of the cancer indication, although the extent of the synergistic effects strongly depended on the molecular background of the cancer cell. Fourthly, more potent ATRi led to stronger synergistic anti-cancer effects when given simultaneously with duocarmycin-ADCs.

6.5. Therapeutic Relevance of the Synergistic Combination of Duocarmycin-ADCs with ATR Inhibitors

Combination therapy brings along several benefits over single agent therapy such as increased efficacy or equal efficacy at lower doses. Through the administration of lower doses, side effects might be reduced and in addition, the development of resistance might be slowed down.[19]

Several ATRi such as AZ20, AZD6738 or VE-822 are in clinical evaluation as combination therapy combined with radiotherapy, or chemotherapy agents like TOP1i topotecan or cisplatin.[164] VE-822 combined with irinotecan was studied in a subcutanous COLO205 mouse xenograft model. While VE-822 had no anti-tumor effect as single agent, irinotecan led to tumor growth delay. The combination of VE-822 with irinotecan had substantially stronger anti-tumor effects, inducing transient tumor shrinkage. The combined treatment resulted in no additional body-weight loss over irinotecan alone.[165] In a phase I dose-escalation study, VE-822 was combined with topotecan. Although partial responses and stable diseases were observed, one patient suffered from dose-limiting grade 4 thrombocytopenia. Furthermore, grade 3 and 4 adverse events were observed such as neutropenia, anemia and leukopenia.[166] These dose-limiting toxicities and grade 3 and 4 adverse events

observed in the clinical setting might be circumvented by targeted delivery of the cytotoxic drug to the tumor using an ADC, because exposure of healthy tissue would be minimized. The effects of the ADC might be enhanced by the addition of chemotherapeutic drugs.

Several combinations of ADCs with small molecules or antibodies have been published (Table 19). The antitumor effects of the MMAE-bearing ADC SGN-35 when combined with ABVD (doxorubicin, bleomycin, vinblastine, dacarbazine) or Gemcitabine were assessed in xenograft mouse models. The combination groups had 9/9 or 5/5 durable tumor regressions for SGN-35 plus ABVC or gemcitabine, respectively. No significant body-weight loss and no morbidity was observed in the combination groups.[167] The approved ADC Kadcyla was studied in combination with several chemotherapeutic agents such as lapatinib, docetaxel, gemcitabine, carboplatin, 5-fluorouracil etc. The combination groups showed stronger tumor regression compared to single agents and in case of Kadcyla plus lapatinib or 5-fluorouracil it was proven that the combination acted synergistically. Besides microtubule-targeting ADCs, also DNA-targeting ADCs were investigated for potential use in combination therapy. The calicheamicin-ADCs Mylotarg and inotuzumab ozagamicin were or are currently evaluated in clinical studies in combination with chemotherapy. Inotuzumab ozagamicin is studied in combination with rituximab or standard chemotherapy regimens R-CVP (Rituximab, cyclophosphamide, vincristine, prednisolone) and R-GDP (rituximab, gemcitabine, dexamethasone, cisplatin). While mylotarg plus chemotherapy did not yield a clinical benefit as first-line treatment over chemotherapy alone for patients with relapsed ALL, rituximab plus inotuzumab ozagamicin is currently evaluated in an open-label phase III study for relapsed or refractory B-cell NHL.[168]

Furthermore, the SN-38 ADC IMMU-132 was intensively studied in combination therapy. Since SN-38 is substrate for ABC transporters, overexpression of these transporters is a mechanism of resistance development against IMMU-132. SN-38-resistant cell lines were established and treated with IMMU-132 or IMMU-132 plus ABCG2 inhibitor YHO-13351. The combination resensitized SN-38-resistant cells for IMMU-132 *in vitro* and *in vivo*.[169]

The ADC IMMU-132 plus PARP inhibitor olaparib was the first published combination of an ADC plus DNA-damage response inhibitor. The combination was evaluated for anti-cancer treatment and proved to synergistically inhibit cancer cell proliferation *in vitro*. Subsequently the results were translated to an *in vivo* xenograft model in mice. Since it was known that topoismerase I inhibition is synthetic lethal with PARP1 inhibition in BRCA1/2-deficient cells, the combination was studied in BRCA1/2-deficient and BRCA1/2 wildtype cells. The ADC alone as well as olaparib had only minor anti-tumor effects. The combination of IMMU-132 plus olaparib however led to a tumor remission in BRCA1/2-deficient xenograft models and provided a survival benefit of treated mice in BRCA1/2-wildtype xenograft mice. No severe side-effects were observed as assessed by body-weight change. Toxicity studies revealed that the combination of the ADC with olaparib decreased platelet, lymphocyte and neutrophil count stronger than the single agents. However, the counts were still in the tolerated range.[170] In addition, the monoalkylating anti-CD33 ADC IMGN779 was combined in preclinical studies with cytarabine yielding additive anti-tumor effects[171] but also with several PARP inhibitors which led to

synergistic anti-proliferative effects.[172,173] So far, two DNA-damaging ADCs, IMMU-132 and IMGN779, were combined with PARPi and synergistic anti-tumor effects were observed.

In this work, a synergistic combination of a DNA-targeting ADC plus DNA-damage response inhibitor was discovered. Therefore, an *in vivo* xenograft model was established to prove the therapeutic relevance of the αHER2-duocarmycin-ATRi combination. Rag 2 mice bearing subcutaneous NCI-N87 tumors were treated with αHER2-**6**, and two ATRi AZD6738 and ATRi **1** either alone or in combination. While the ATRi AZD6738 had no significant effect on tumor growth, ATRi **1** given as single agent delayed tumor growth. Although a low dose of ADC was chosen to better resolve combination effects, the ADC had tumor growth inhibiting effects after initial tumor stasis. The combination of αHER2-**6** with AZD6738 led to durable tumor stasis where one mouse experienced tumor free survival and αHER2-**6** combined with ATRi **1** induced tumor regressifon with two mice showing tumor free survival until the endpoint was reached. The antitumor effects of ATRi **1** plus αHER2-**6** were stronger compared to AZD6738 combined with αHER2-**6** which reflects the finding that ATRi **1** synergized stronger with duocarmycin-ADCs than AZD6738 on the cellular level. This gives rise to the assumption that the combination treatment can be optimized *in vitro* to yield improved efficacy *in vivo*. However, so far a quantitative assessment of the combination effects is missing. Fu *et al.* described a detailed method for the quantification of *in vivo* combination effects. Therefore, it is necessary to determine a dose-response relationship for the individual compounds as well as the combination at e.g. a fixed ratio of doses. The dose-response data can be fitted using the median-effect equation and a combination index can be calculated as a proof of synergy.[174]

In addition to the efficacy data, the xenograft model revealed that the mice in the combination groups did not suffer body-weight loss, suggesting that the therapy was well tolerated. This is of particular importance because it is often suggested, that synergistic drug combination do also lead to synergistic side effects,[22] which was not the case for combination treatment with αHER2-**6** and the ATRi AZD6738 and ATRi **1** in this study.

The DUBA-based αHER2-**6** ADC used in this study was closely related to the phase III clinically evaluated ADC SYD985,[90] which was studied in monotherapy only so far. In a phase I expanded cohorts study, SYD985 led to grade 3 and 4 adverse events such as neutropenia and conjunctivitis.[89] Besides duocarmycin-ADC SYD985 also ATRi are currently under clinical development. The ATRi VE-822 was studied in a phase I dose-escalation study and no toxicity was observed up to a dose level of 480 mg/m².[175] On the contrary, patients treated with the ATRi AZD6738 had grade 3 and 4 toxicities such as thrombocytopenia, pancytopenia, elevated amylase, photosensitivity, mucositis, anemia when treated with 240 mg/m² BD for 21 of a 28 day cycle and 5 days on, 2 days off. At a dose level of 160 mg/m² only anaemia was observed with the same scheduling.[176] The findings reported in this work provide the rationale for the clinical evaluation of SYD985 in combination with ATRi. The combination of ATRi with targeted delivery of duocarmycin mediated by an ADC might boost anti-tumor effects. This would give room for lowering the doses and hence combination therapy might lead to less adverse events, especially since the toxicity profiles do not overlap for SYD985 and the ATRi AZD6738 or VE-822.

Table 19: Summary of ADC combination therapies.

ADC				Combination		
Identifyer	**Target**	**Payload**	**MoA**	**Drug**	**MoA**	**Source**
Besponsa	CD22	Calicheamicin	DSB	**R-CVP/R-GDP/R**	MTA/DTA	[168]
Mylotarg	CD33	Calicheamicin	DSB	**Chemotherapy**	CD20	[168]
SGN-35	CD30	MMAE	MTA	**ABVD/Gemcitabine**	MTA/DTA	[167]
Kadcyla	HER2	DM1	MTA	**Chemotherapy**		[177]
IMMU-132	TROP2	SN-38	TOP1i	**YHO13351**	ABCG2	[169]
IMMU-132	TROP2	SN-38	TOP1i	**Olaparib**	PARPi	[170]
IMGN779	CD33		Alkylation	**Cytarabine**	Antimetabolite	[171]
IMGN779	CD33		Alkylation		PARPi	[172,173]

6.6. Mechanism of ATR-Mediated Sensitization for Duocarmyin Treatment

As already lined out, the combined treatment with duocarmycin-ADCs and ATR inhibitors might lead to improved efficacy of anti-cancer treament. Therefore, profound knowledge of the underlying mechanism of action of the synergy between duocarmycin and ATRi is important because it facilitates the selection of patients based on e.g. biomarkers with potentially high response rates and also to anticipate resistance mechanisms. Thus, a mechanism of action for the syneristic cytotoxicity between duocarmycins and ATRi will be proposed in this chaper which might serve as a basis for detailed mechanistic studies.

The repair of Duocarmycin-induced DNA-damage is not fully unraveled yet. It was reported, that the duocarmycin variant CC-1065 was not recognized by the nucleotide excision repair apparatus, propably due to the thermodynamic stabilization effects on double-stranded DNA.[145] However, CHO cells deficient in components of the NER were more sensitive to treatment with duocarmycin-derivative AS-I-145 than their NER proficient counterparts.[147] Treatment of HCT116 cells with adozelesin led to increased expression of p53 and stabilization by phosphorylation at serine S15. As a result, p21 was transcribed which led to G2 arrest after adozelesin treatment with low doses. High doses of adozelesin however arrested cells in S phase and at the same time p21 levels were decreased. A consequence of adozelesin-treatment was that cells entered apoptosis.[178] Liu *et al.* studied the cellular responses upon duocarmycin treatment. Cells treated with adozelesin showed phosphorylation of ssDNA-binding protein RPA and also histone H2AX, which was supressed by addition of aphidicholin prior to adozelesin treatment. The cells formed RPA and γ-H2AX foci which colocalized. By incubating the cells with BUdR, a fluorescent nucleotide analogon, cells were labeled that were actively synthesizing DNA. Cells actively incorporating BUdR were also positive for RPA foci formation upon adozelesin treatment. In another experiment, cells were arrested by overnight treatment with aphidicholin. While arrested cells showed not RPA foci formation, released cells did. Taken together these data suggest that adozelesin-

alkylation lesions were S phase specific and relied on active fork progression.[148] Furthermore, the phosphorylation of DNA-damage marker γ-H2AX was mediated by ATR. This was proven by overexpression of a kinase dead mutant of ATR and subsequent treatment of kinase dead ATR and ATR wildtype cells with HU, UV or IR. It was observed that γ-H2AX foci formation was largely suppressed in ATR kinase dead cells.[179] Besides, adozelesin treatment of HeLa cells induced CHK1 phosphorylation.[180]

The synergy between duocarmycins and ATRi can best be described as anti-counteractive synergy. In case of anti-counteractive synergistic drug combinations a drug induces a cellular response that would decrease its efficacy and a second drug is added that suppresses the cellular response to the first drug.[28] Literature data suggest that duocarmycin might induce ATR phosphorylation. ATR activity however can be suppressed by adding an ATR inhibitor. This leads, as demonstrated in this work, to an increased response to duocarmycin-ATRi combination treatment compared to the single agents.

Based on the cellular response discussed in this chapter and the functions of ATR upon replication stress and DNA damage, a mechanism of synergy between duocarmycin and ATR inhibitors is proposed as depicted in figure 70. When cells enter S phase and start replication of the genome, the DNA polymerase eventually collides with a duocarmycin-lesion. The MCM2-7 replicative helicase and DNA-polymerase become uncoupled whereby stretches of ssDNA are formed. These are protected against nucleolytic restriction by coating the ssDNA with RPA. The 9-1-1 complex binds to ssDNA-dsDNA junctions, and TOPBP1, ETAA1 and ATRIP are recruited, ultimatively leading to the activation of ATR. ATR in turn has several functions that include the induction of cell cycle arrest by activation of p53, WEE1 and CHK1. ATR also regulates the activity of SMARCAL1 translocase which is required for fork maintenance and fork restart.[181] Through SMARCAL1 inactivation, the stalled replication fork is protected from fork remodeling which otherwise would result in restriction by SLX4/MUS81 endonucleases. In addtion, ATR downstream kinase CHK1 inhibits CDC45, which is required for the initiation of a bidirectional replication fork, to suppress the firing of not-yet fired late origins. This process limits the use of RPA as does the slowing-down of helicase movement by Claspin-TIPIN-Timeless complex. Through the ATR-mediated response, the cell cycle progression is slowed down, the replication fork is protected, the firing of late origins is prevented and finally the RPA level is kept at an acceptable level. In contrast to that, in the absence of functional ATR, forks are no longer protected against SLX4/MUS81-mediated degradation. More importantly, cell cycle checkpoints are abrogated and late origins fired. DNA synthesis occurs at multiple sites whereby ssDNA is formed excessively. The ssDNA stretches are coated by RPA until RPA-levels fall below a certain level. A sudden pan-nuclear appearance of DNA double-strand breaks at replicons is associated with the depletion of RPA and this finally leads to the so called “replication catastrophe”.[92]

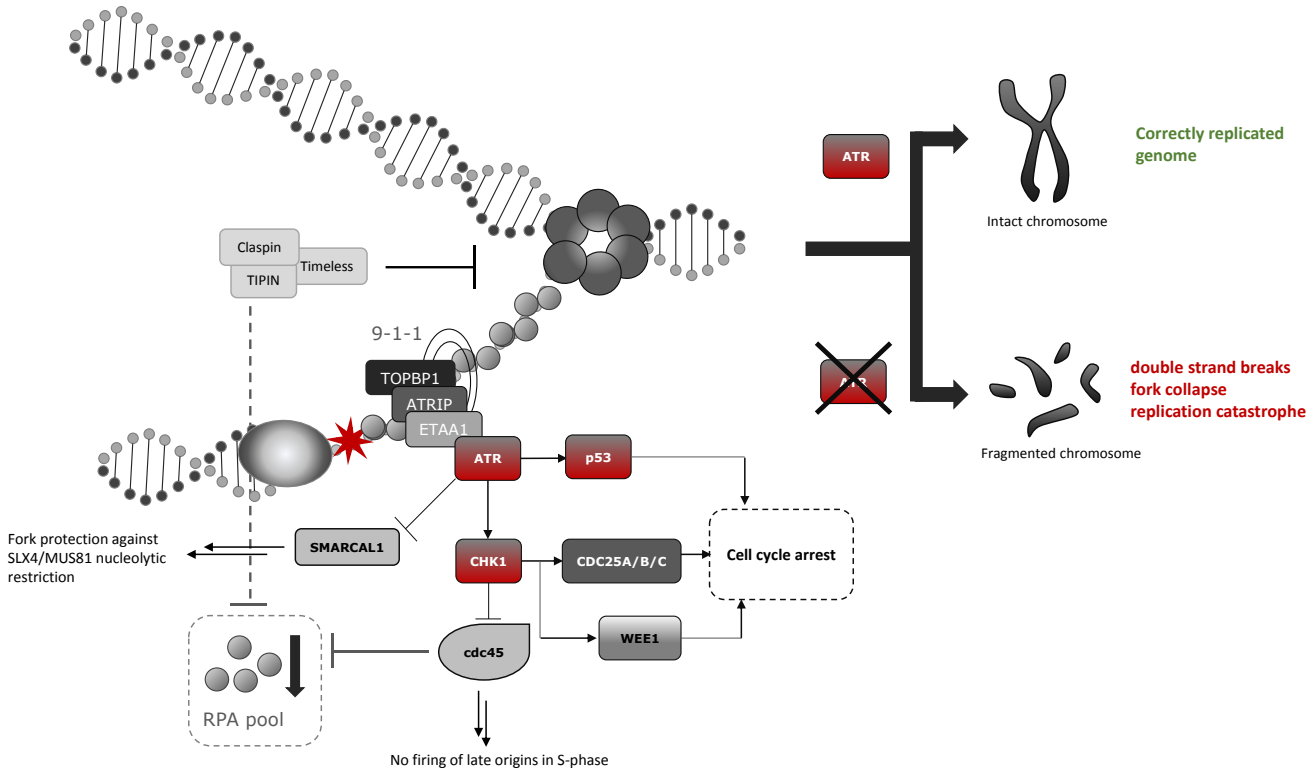

Figure 70: Proposal of mechanism of synergy between duocarmycin and ATR inhibitors. Duocarmycin poses a replication fork barrier, leading to the inhibition of the DNA-polymerase. As a result, DNA-polymerase and MCM2-7 helicase might be uncoupled leading the formation of ssDNA, which is coated by RPA. In order to keep RPA levels above a threshold level, the Claspin-TIPIN-Timeless complex blocks the movement of the helicase. RPA-coated ssDNA is recognized by the 9-1-1 complex. Subsequently, TOPBP1, ETAA1 and ATRIP are recruited. The latte activates ATR which mediates fork-protective actions and also cell cycle regulation *via* p53 and CHK1. By inhibition of SMARCAL1, the stalled replication fork is protected from fork remodeling and subsequent nucleolytic restriction. Through these mechanisms, correct replication of the genome is mediated. In the absence of ATR, SRF might be nucleolytically cleaved, and also cell cycle is not slowed down to assure correct genome duplication and maintain RPA levels. The result is the replication catastrophe if the cell tries to replicate despite the DNA-damage which is accompanied by fork collapse and DSBs.

In a head-to-head comparison by Liu *et al*., it was found that Adozelesin treatment led to the same cellular response as camptothecin treatment[148] indicating that the cells cannot discriminate between a replication block induced by duocarmycin-derivative adozelesin or TOP1 poison camptothecin. The combination of camptothecin with ATRi was studied in detail by Jossé *et al*. Camptothecin treatment induced cell cycle arrest and at the same time the firing of late origins in S phase. Furthermore, chain elongation was inhibited which was associated with a slower fork progression. The addition of the ATRi VE-821 however abrogated cell cycle checkpoint, led to firing of late origins during S phase and increased fork velocity when compared to camptothecin-treated cells alone. Furthermore, camptothecin treatment induced CHK1, CHK2 and H2AX phosphorylation.[165] Adozelesin treatment was also reported to induce CHK1 and H2AX phosphorylation.[180] The finding, that cellular response to adozelesin and camptothecin treatment was comparable, might in part explain why the combinations of DUBA or SN-38 with AZD6738 led to equal synergy scores on HCC-1954 cells.

Sensitivity of cancer cell lines toward combined treatment with duocarmycin or duocarmycin-ADC and ATRi and mutational status of respective cell lines is summarized in table 20. p53-wildtype cell lines were not sensitive to the combination treatment with duocarmycin and ATRi. At the same time, p53-mutated cell lines were

frequently sensitive toward combination treatment. p53-binding protein 1 (p53BP1) is important for p53 function. It was shown, that p21 expression was impaired in p53-wildtype but p53BP1-deficient cells[182], propably contributing to the sensitivity of MDA-MB-453 cells to duocarmycin-ATRi combination treatment. MDA-MB-468 were also sensitive toward combination treatment, which might be mediated by its PTEN loss of function mutation as discussed earlier. Sensitivity was reduced for p53-mutated cell lines that simultaneously carried an ARID1A mutation. ARID1A is a protein involved in the modification of chromatin structure by sliding or ejecting nucleosomes from DNA leading to the modulation of replication, transcription and DNA-repair.[183] Williamson *et al.* reported a synthetic lethality relationship between ARID1A-deficiency and ATR inhibition. Treatment of cells deficient in ARID1A with ATRi VE-822 led to increased levels of apoptosis, DNA-damage and also fragmentation of chromosomes when compared to ARID1A-proficient cells.[183] Hence, ARID1A-deficient cells are already sensitive to ATR inhibitor treatment. Appearently, combination treatment with duocarmycin and ATRi does not bring along an additional benefit over ATR inhibitor treatment alone.

Table 20: Summary of sensitivity of cell lines studied in this work and mutational status. Sensitivity was classified on A549, HCC-1954, MCF-7, MDA-MB-453, MDA-MB-468 and NCI-N87 cells after treatment with small molecule duocarmycins DUBA, Duocarmycin DM or Duocarmycin SA and ATRi AZD6738 as follows: Synergy score > 3 was termed sensitive ("+") and synergy score < 3 was termined non-sensitive ("-"). Senstivity toward treatment of BT-474, Calu-3, JIMT-1, MDA-MB-361, SK-BR-3 and SK-OV-3 cells with αHER2-**1** and constant doses of AZD6738 was classified as follows: DRI > 3 was termed sensitive ("+"), DRI < 3 was termed insensitive ("-"). The DRI data were extracted from figure 47. Mutational status of genes in the headline were extracted from the ancer Cell Line Encyclopedia (CCLE) database. It was marked with "mut" if the proteins were mutated. Tolerated mutations were denoted with "mut (tol)". TP53 and PTEN status of MDA-MB-468 cell line was extracted from literature.[184] p21 has another gene symbol CDKN1A.

Cell line	Sensitivity	ARID1A	ATR	ATM	p21	PTEN	p53	p53BP1
A549	-		mut					
BT-474	+						mut	
Calu-3	-				mut		mut	
HCC1954	+						mut	
JIMT-1	-	mut					mut	
MCF7	-							
MDA-MB-361	-	mut					mut	
MDA-MB-453	+							mut
MDA-MB-468	+					mut		
NCI-N87	+						mut	
SK-BR-3	-						mut (tol)	
SK-OV-3	-	mut		mut				

However, the proposed mechanism is solely based on the finding, that duocarmycins synergized with ATR and CHK1 inhibitors leading to improved tumor cell killing and data from literature. This allows only to speculate about the mechanism of synergy between duocarmycin and ATRi. In the outlook section, methods are described that allow the refinement of the proposed mechanism.

6.7. DNA-PK Inhibition for ADC Combination Therapy

After it was discovered that duocarmycin-ADCs synergize with inhibitors of ATR, a member of the PIKK enzyme family, the question arose whether the concept might be translated to other members of the PIKK family. Therefore, Bleomycin A5-based ADCs were generated by conjugation to the αHER2 mAb, αEGFR mAb cetuximab and isotype control αHEL. The conjugation of BA5 to these antibodies had good to excellent yields. Since yields greater than 100% were observed, it might be hypothesized that BA5 absorbs in the same range as the antibody and this way influenced the measurement of the concentration. In all cases, more than 80% of the available conjugation sites were covered. The monomeric content was greater than 99% in all cases. The ADCs were studied on several cell lines subsequently. While the HER2-targeting ADC αHER2-**9** (DAR=1.78) was active on HCC-1954 cells in the nanomolar range, no cytotoxicity was observed on LNCaP and BxPC3 cells. αEGFR-**9** was studied on the cell lines A549, Capan-2, MDA-MB-231 and SK-OV-3, A431, MDA-MB-468 and EGFR-negative cell line MCF7. The ADC was exceeding the effects of the mAb alone only on A431 and MDA-MB-468 cells. The treatment of HCC-1954 cells with αHER2-**9** or MDA-MB-468 cells with αEGFR-**9** led to a substantial increase in potency of the small molecule drug Bleomycin A5 of approximately 470 and 1400, respectively.

Another ADC was described in literature that used a Bleomycin-derivative as payload.[185] The ADC was based on the antibody BR96 that targets Lewis Y antigen which was associated with colon, breast, ovary and lung carcinomas but not normal tissues. Tallysomycin S_{10b}, the already mentioned Bleomycin analogue, was conjugated to BR96 and cancer cells were treated with the conjugate. The ADC was potent in the single- to double-digit nanomolar range. An non-targeting Tallysomycin S_{10b}-ADC was considerably less potent, and Tallysomycin S_{10b} alone was 13-875-fold less potent than the corresponding ADC.[185] The potencies of the Bleomycin A5-ADCs αHER2-**9** and αEGFR-**9** were in the same range as that described in literature, and also an increased potency was observed for the conjugates compared to the drug alone. However, it was surprising that the conjugates αHER2-**9** and αEGFR-**9** were inactive in the vast majority of cell lines studied. This might be explained by differences in the cellular uptake and subsequent trafficking between the antibodies cetuximab and BR96. Furthermore, the synthesis of the linker-drug containing Tallysomycin S_{10b} reported in literture involved the complexation of the drug with copper(II)-ions. The synthesis of LD-**9**, however, was performed without the complexation step. Thus, the formation of a complex of ADC with bivalent cations prior to treatment of cells with the ADCs might be of importance for unfolding the cytotoxic activity.

Nevertheless, synergistic effects were studied on MDA-MB-468 cells. Therefore αEGFR-**9** was combined with two DNA-PKi in a dose-matrix assay. The combination of αEGFR-**9** with the DNA-PKi NU7441 and M3814 was synergistic on MDA-MB-468 cells. A control experiment was conducted wherein the small molecule Bleomycin A5 and the antibody cetuximab were combined with DNA-PKi NU7441. The synergy score of BA5 plus NU7441 was around two-fold lower than αEGFR-**9** plus NU7441. Interestingly, the antibody cetuximab also weakly synergized with NU7441 (S=1.8). A role of the surface receptor EGFR in DNA repair has been described

by Dittmacher *et al.*[186] EGFR is translocated to the nucleus upon irradation. As a result, EGFR forms a complex with DNA-PK, which led to an increased DNA-PK activity. DNA-PK activity was again suppressed by addition of cetuximab.[186] Apparently, simultaneous inhibition of DNA-PK by cetuximab and NU7441 led to synergistic shutdown of DNA-PK-mediated DNA-damage repair. The synergy between the bleomycin A5-ADC and the DNA-PKi NU7441 translated also in 19.3-fold potentiation of ADC potency as determined using the MNED-curve-shift assay.

Bleomycin-ADC have not been clinically evaluated. However, several ADCs with double-strand break inducing payloads are clinically studied. The company Pfizer has a strong pipeline of calicheamicin-based ADCs. PF-06647263, inotuzumab ozogamicin, gemtuzumab ozogamicin are currently in clinical development in all clinical phases.[119] Inotuzumab ozogamicin, gemtuzumab ozogamicin are clinically studied when combined with standard chemotherapy[168], however not with targeted chemotherapy agents such as DNA-PK inhibitors. It was demonstrated by Bouquet *et al.* that calicheamicin induced DNA-PK and ATM phosphorylation in HeLa cells[187] underpinning the potential benefit of combining calicheamicin-ADCs with DDRi on a cellular level. Furthermore, IMMU-110, a doxorubicin-carrying ADC, is currently evaluated in a phase II clinical study. The data reported in this study pose a rationale for the further evaluation of combinations of double-strand inducing ADCs with DNA-PK inhibitors.

7. Outlook

7.1. Biomarker Identification and Refinement of Proposed Mechanism of Synergy

In regard of a therapeutic application of combinations of duocarmycin-ADCs with ATRi, it would be essential to identify a biomarker to increase the response toward treatment. A biomarker is important to select patient populations that are in particular reponsive regarding combination therapy. Biomarker identification and refinement of the proposed mechanism of synergy between duocarmycin and ATRi go hand in hand. The efforts put into biomarker identification might also improve the mechanistic understanding of the synergy between duocarmycins and ATR inhibitors, because key enzymes might potentially be identified that in- or decreased sensitivity toward the combination of the drugs.

Therefore two approaches might be followed. First, the combination might be studied on a large cancer cell panel. Bioinformatic data bases contain information about mRNA levels, that correspond to protein expression, and also mutations of specific genes. A correlation between high or low synergy scores and mutation or expression levels of specific genes might be established. Secondly, genes known to mediate sensitivity or resistance toward ATRi treatment as published by e.g. Forment and O'Connor[94] might be downregulated using siRNA knock-down. The knockdown cells would be treated with a combination of duocarmycin and ATRi and synergy scores would be determined, possibly revealing key enzymes that are involved in the response to duocarmycin plus ATRi treatment.

Additional insight into the model might be gained by studying expression levels and phosphorylation status of the kinases and phosphatases mentioned in the model after treatment of cells with duocarmycin or duocarmycin plus ATRi by western blotting. This might help to elucidate the signalling pathways that are activated upon stressing the cells with the drugs. Additionally, compensatory mechanisms might be identified that support cells in surviving the cellular stress induced by treatment with ATRi and duocarmycins.

In this work, replication catastrophe was assumed to be the main reason for cell death upon combined treatment of cells with duocarmycin and ATR inhibitors. To test whether this hypothesis was correct, replication catastrophe can be assessed by quantification of DNA-damage and RPA1 as well as RPA2 levels on chromatin after pre-extraction according to Toledo *et al*.[92]

One promising starting point for biomarker studies might be p53. This was already indicated by a correlation between sensitivity of the cells towards combination treatment and p53 status. Furthermore, Hall *et al.* reported increased sensitivity of A549 p53-knockdown cells toward combined treatment with VE-822 and DNA-damaging drugs cisplatin, etoposide, gemcitabine, oxaliplatin and irinotecan compared to p53-wildtype cells.[188] Although duocarmycin was not included in the study by Hall *et al.*, the work published by Liu *et al.*[148] strongly suggests that the cellular response to duocarmycin and irinotecan treatment are similar.

This underpins the possible role of p53 in sensitivity to duocarmycin and ATRi treatment. To prove the hypothesis, that p53-mutations render cells sensitive toward combination treatment with duocarmycin and ATRi, p53-knock-out cells might be generated to compare their sensitivity toward the treatment with isogenic p53-proficient cells in cell viability assays and ideally in a xenograft model.

7.2. Improvement of Anti-Tumor Effects of Duocarmycin-ADCs Combined with ATR Inhibitors

It was demonstrated in the NCI-N87 xenograft model that the combination of the DUBA-ADC αHER2-**6** with ATR inhibitors led to improved anti-tumor effects compared to the drugs as single agents. However, there is still room for improving the outcome of further xenograft studies. The combination effects might largely depend on the constant supply with both drugs, especially because ADCs often cannot penetrate the tumor leading to the saturation of the tumor surface only.[189] Therefore, the dosing and scheduling poses an important optimization parameter. A study by Elgersma *et al.* suggested that multiple administration of SYD985 has an improved anti-tumor efficacy compared to a single administration at the very same dose.[82] Therefore, a repeated administration of the ADC e.g. might not only improve anti-tumor effects of the single agent but also of the combination. In addition, the good tolerability of the ADC allows the administration of a higher ADC dose in further experiments to increase the exposure of the tumor to the drug.

Besides the optimization of the dosing and scheduling, the model cell line potentially has a great influence on the tumor killing effects of the combination *in vivo*. In this work it was shown that for example the synergy score of αHER2-**6** combined with ATRi AZD6738 is 3-times higher on MDA-MB-453 cells than on NCI-N87 cells which might also translate into stronger anti-tumor effects.

Furthermore, it was reported by Ubink *et al.* that a certain carbamate in the structure of the linker-drug is subject to proteolytic cleavage by carboxylesterase 1c (ces1c), which is a protease found in the sera of rodents.[190] The ces1c-mediated cleavage impacts the pharmacokinetic properties of the ADC and by this means limits tumor-specific delivery of duocarmycin to the tumor. In order to overcome this issue, either the linker-drug might be modified or a ces1c-knock-out mouse model might be established that would also allow for a more precise prediction a the clinical dose.[190]

All in all, although the combination results reported in this work are encouraging, potential for improvement was identified which might be evaluated in upcoming studies.

8. Appendix

Appendix 1: Cell lines and corresponding cell culturing medium.

Cell line	Medium
BT-474	Ham's F12, 2 mM L-Glutamine, 10 µg/mL insulin, 10% FBS
Calu-3	DMEM, 10% FBS
HCC-1954	RPMI-1640, 2 mM L-Glutamine, 1 mM Na-pyruvate, 10% FBS
Hela Silencix ATR	DMEM, 2 mM L-Glutamine, 1 mM Na-pyruvate, 4.5 g/L Glucose, 125 µg/mL Hygromycin B, 10% FBS
Hela Silencix control	DMEM, 2 mM L-Glutamine, 1 mM Na-pyruvate, 4.5 g/L Glucose, 125 µg/mL Hygromycin B, 10% FBS
HT-29	DMEM high glucose, GlutaMax w/o phenol red, 1 mM Na-pyruvate
JIMT-1	DMEM, 10% FBS
MDA-MB-361	DMEM, 10% FBS
MDA-MB-453	DMEM, 2 mM L-Glutamine, 1 mM Na-pyruvate, 10% FBS
NCI-N87	RPMI-1640, 2 mM L-Glutamine, 1 mM Na-pyruvate, 10 mM HEPES, 4.5 g/L glucose, 10% FBS
SK-BR-3	DMEM, 2 mM L-Glutamine, 1 mM Na-pyruvate, 10% FBS
SK-OV-3	DMEM, 2 mM L-Glutamine, 1 mM Na-pyruvate, 10% FBS
MDA-MB-468	RPMI-1640, 2 mM L-Glutamine, 1 mM Na-pyruvate, 10% FBS

Appendix 2: Overview of cell line origin and quality controls. The quality controls were performed by the department Molecular Biology, Merck KGaA.

Cell line	Origin	Accession number	Mycoplasma (qPCR)	Cross-contamination (nested PCR)	STR	Sterility (last test)
BT-474	ATCC	HTB-20	negative	negative	yes	Yes (04.05.2017)
Calu-3	ATCC	HTB-55	negative	negative		Yes (08.08.2016)
HCC-1954	ATCC	CRL-2338	negative	negative	yes	Yes (14.11.2017)
Hela Silencix ATR	Tebu-bio laboratories		negative	negative	yes	Yes (24.02.2012)
Hela Silencix control	Tebu-bio laboratories		negative	negative	yes	Yes (24.02.2012)
JIMT-1	DSMZ	ACC589	negative	negative	yes	Yes (06.09.2012)
MDA-MB-361	ATCC	HTB-27	negative	negative	yes	Yes (17.01.2013)
MDA-MB-453	DSMZ	ACC65	negative	negative	yes	Yes (18.04.2013)
NCI-N87	ATCC	CRL-5822	negative	negative	yes	Yes (19.02.2017)
SK-BR-3	ATCC	HTB-30	negative	negative	yes	Yes (09.03.2017)
SK-OV-3	ATCC	HTB-77	negative	negative	yes	Yes (05.03.2013)
MDA-MB-468	ATCC	HTB-132	negative	negative	yes	Yes (14.02.2016)

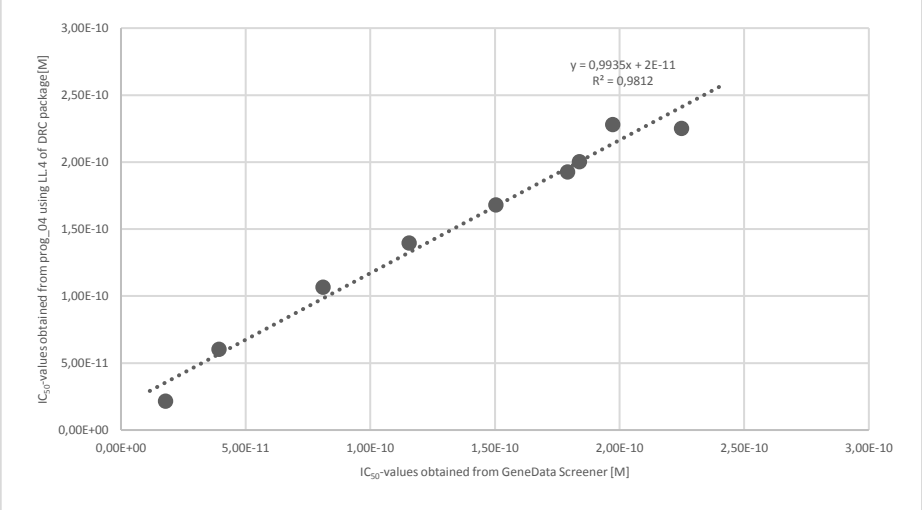

Appendix 3: Plot of IC_{50}-values obtained from own code using LL.4 function of the DRC package against the IC_{50}-values obtained from GeneData Screener software. A linear regression was performed and the equation as well as coefficient of determination are displayed in the graph.

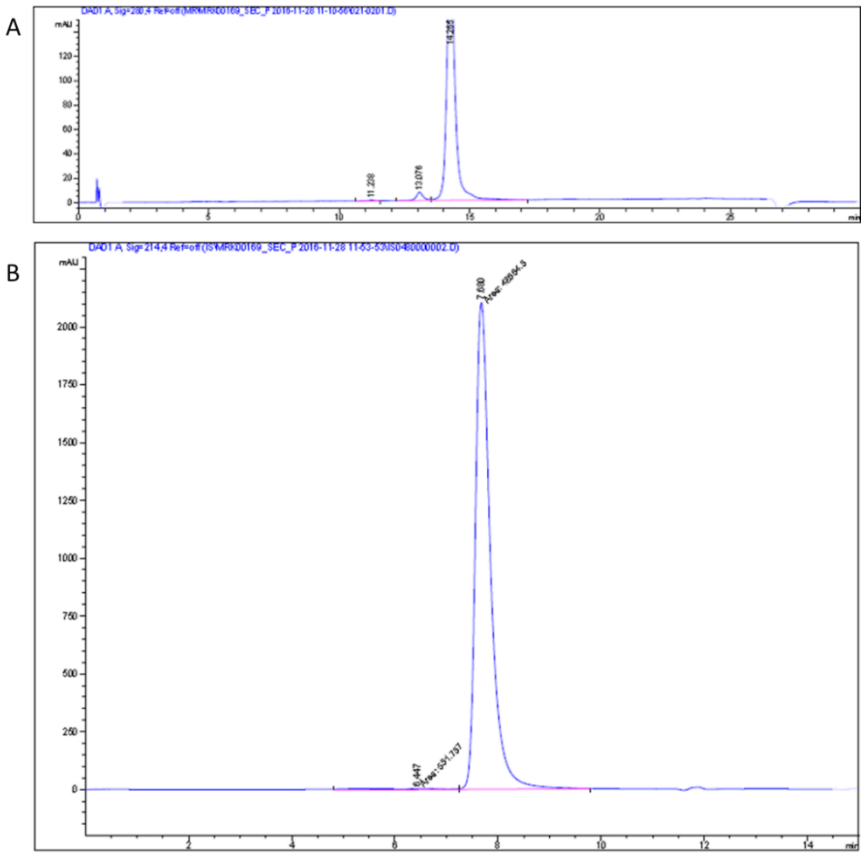

Appendix 4: Analytical data for the preparation of αHER2-**1**. A) HIC profile of the ADC at 280 nm. B) SEC chromatogram at 214 nm.

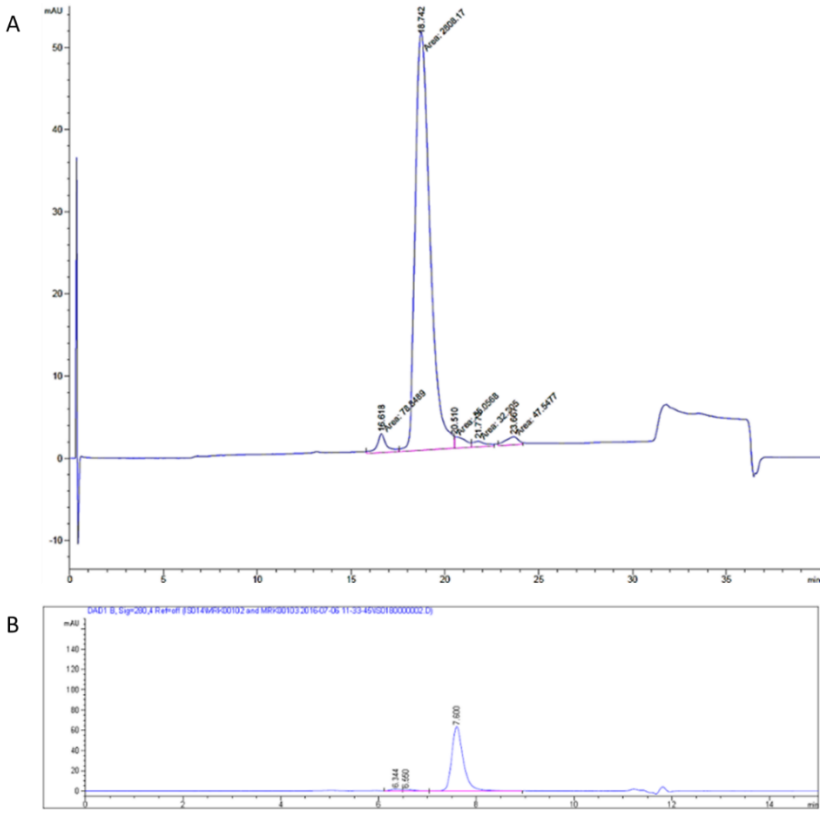

Appendix 5: Analytical data for the preparation of αHER2-**1**. A) HIC profile of the ADC at 214 nm. B) SEC chromatogram at 280 nm.

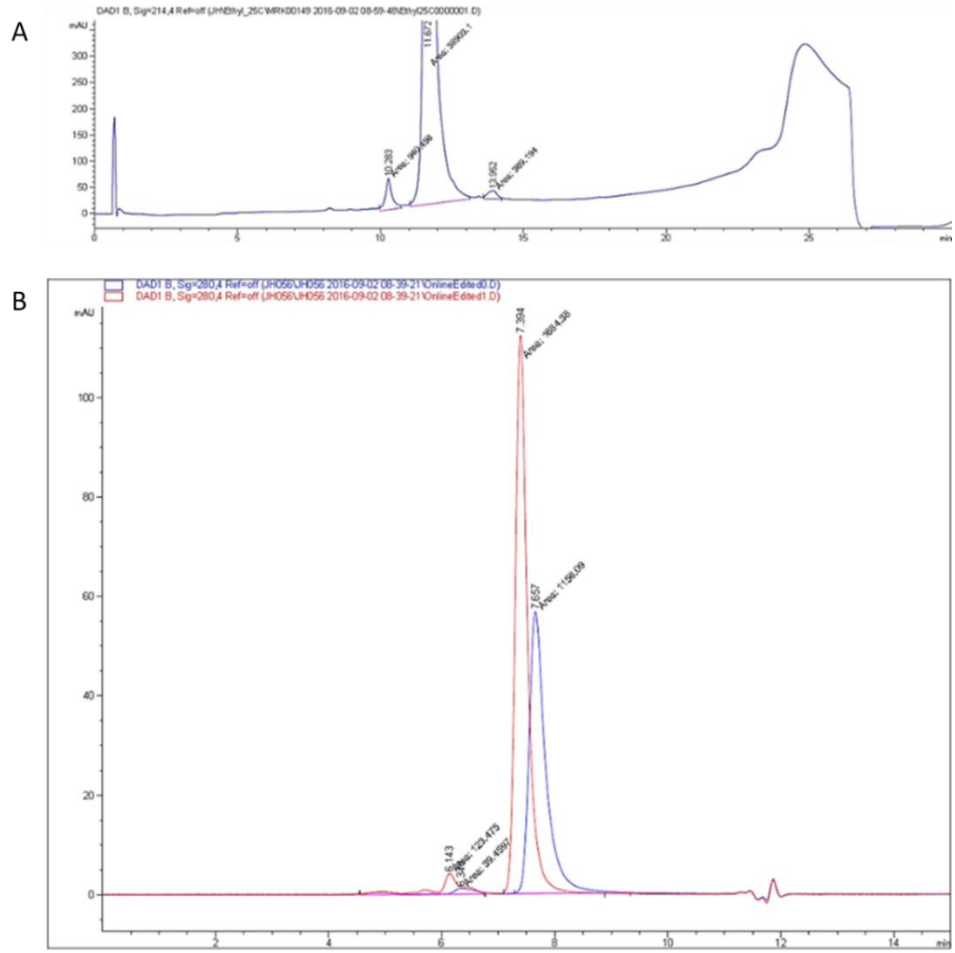

Appendix 6: Analytical data for the preparation of αHER2-**1**. A) HIC profile of the ADC at 214 nm. B) SEC chromatogram at 280 nm. Red: αHER2-1; Blue: αHER2 mAb.

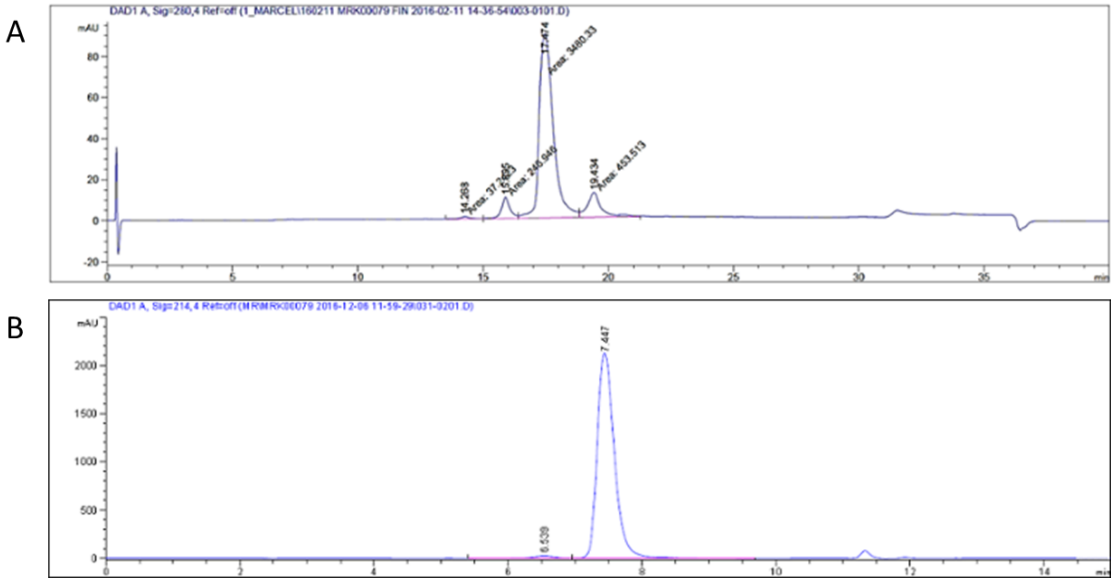

Appendix 7: Analytical data for the preparation of αEGFR-**1**. A) HIC profile of the ADC at 280 nm. B) SEC chromatogram at 214 nm.

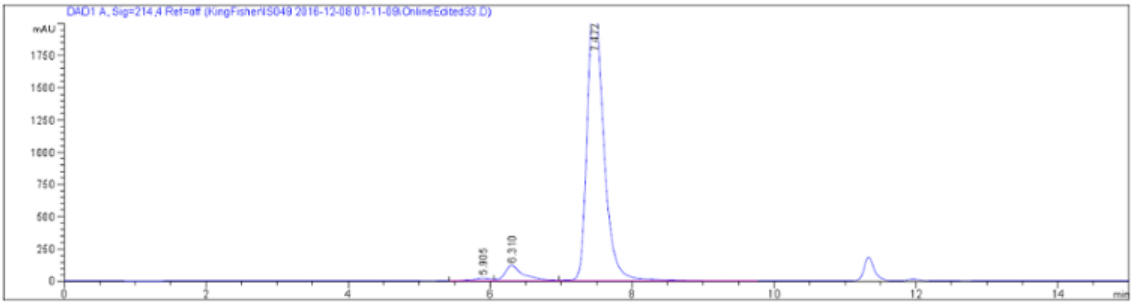

Appendix 8: Analytical data for the preparation of αMET-**1**. SEC profile of the ADC at 214 nm. HIC profile was not transferred. The integrals were evaluated online and only the DAR was noted.

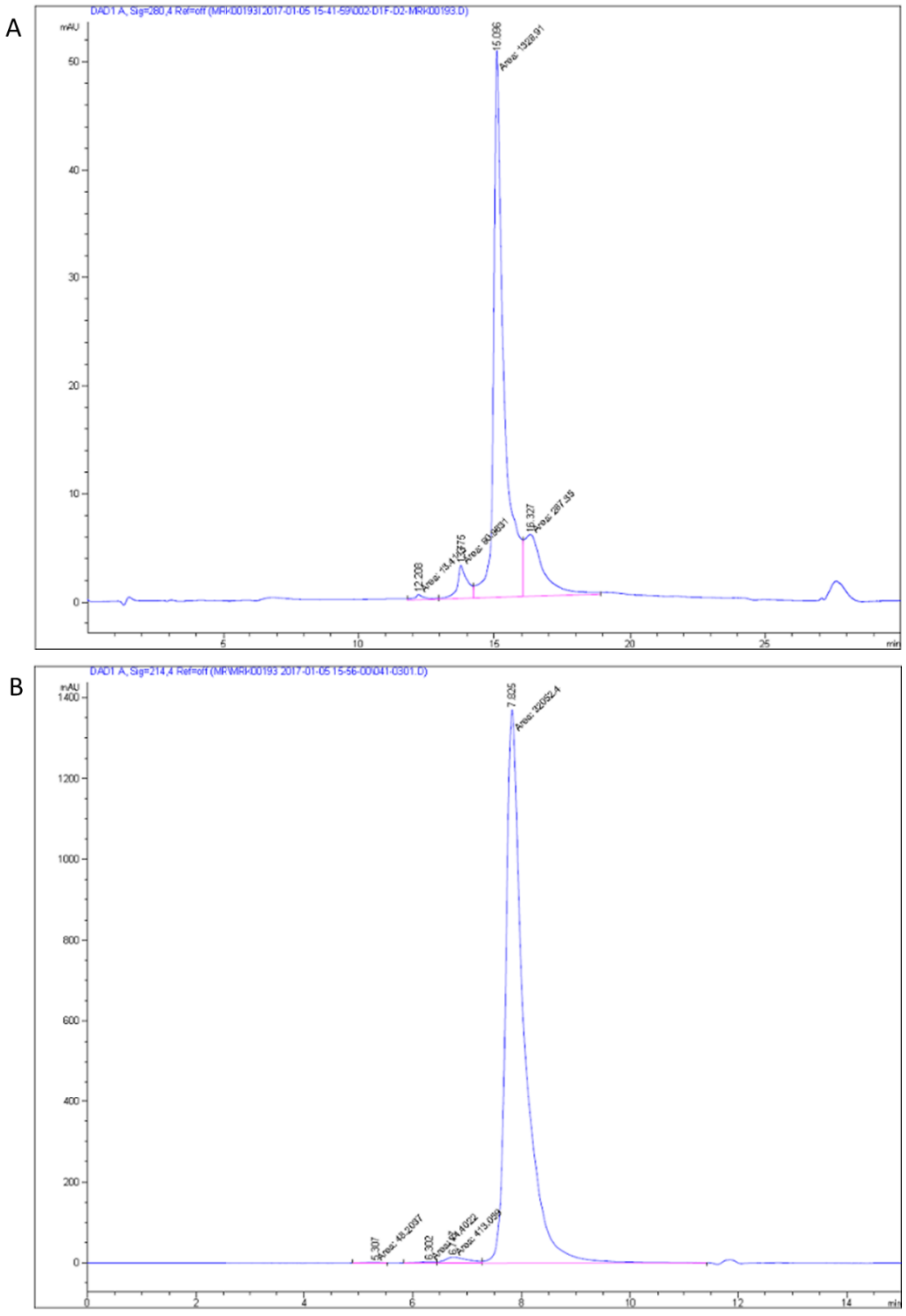

Appendix 9: Analytical data for the preparation of αMETxEGFR-**1**. A) HIC profile of the ADC at 280 nm. B) SEC chromatogram at 214 nm.

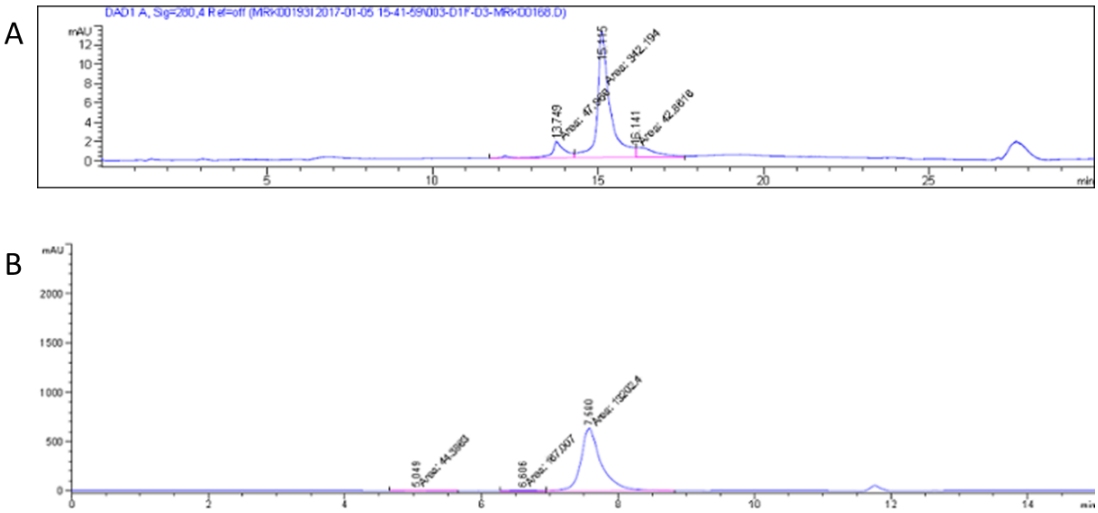

Appendix 10: Analytical data for the preparation of αMETxEGFR-**1**. A) HIC profile of the ADC at 280 nm. B) SEC chromatogram at 214 nm.

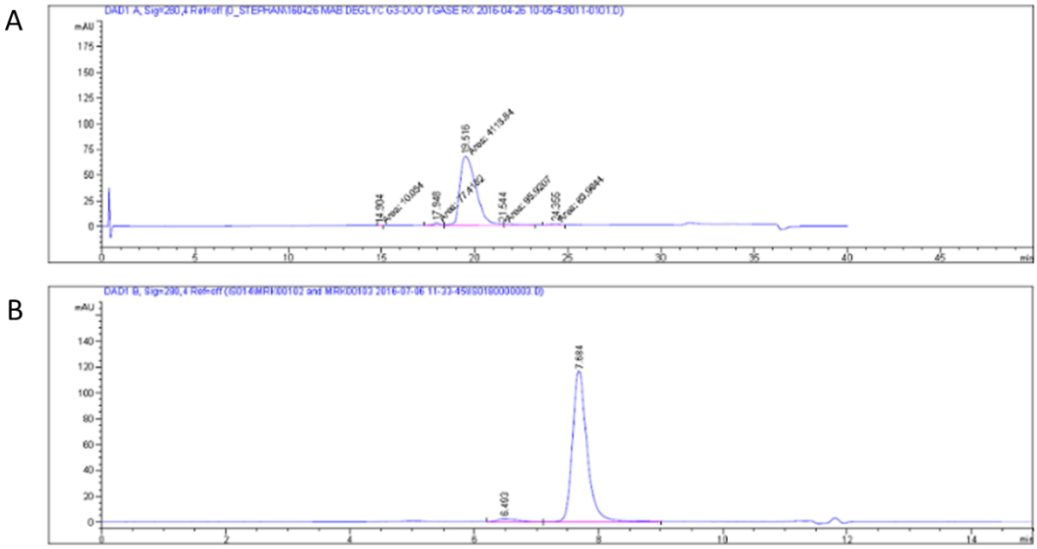

Appendix 11: Analytical data for the preparation of αHEL-**1**. A) HIC profile of the ADC at 280 nm. B) SEC chromatogram at 280 nm.

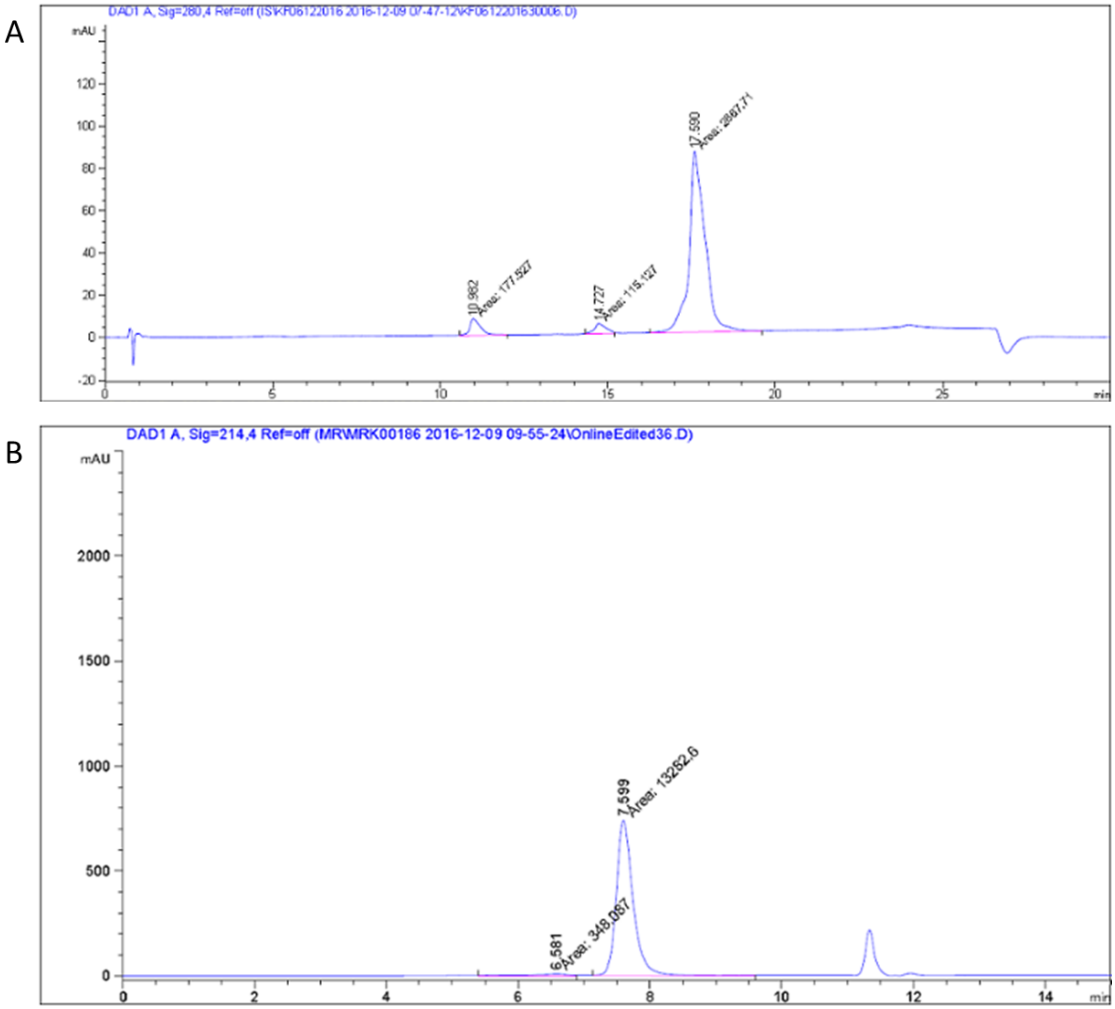

Appendix 12: Analytical data for the preparation of αHER2-**2**. A) HIC profile of the ADC at 280 nm. B) SEC chromatogram at 214 nm.

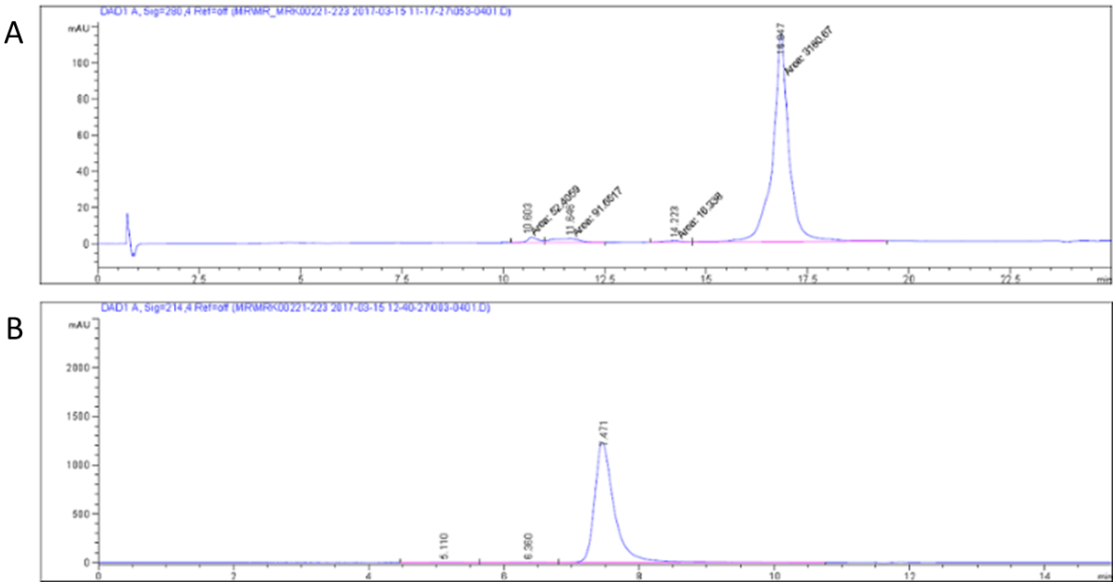

Appendix 13: Analytical data for the preparation of αHER2-**3**. A) HIC profile of the ADC at 280 nm. B) SEC chromatogram at 214 nm.

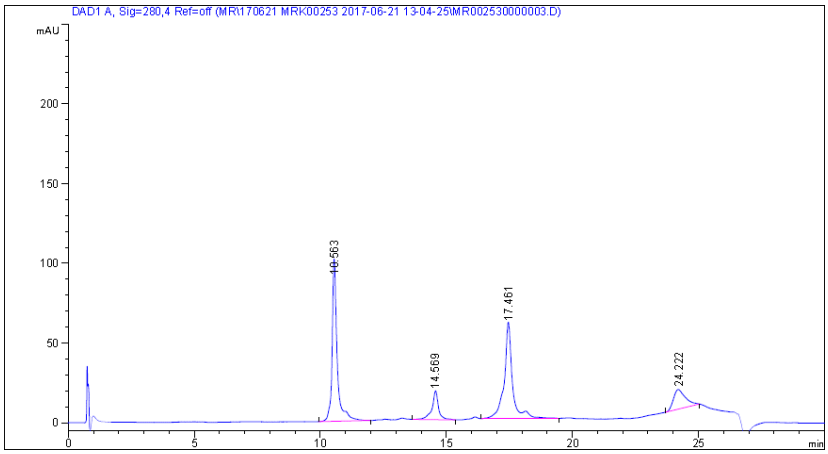

Appendix 14: Analytical data for the analytical scale reaction to generate αHER2-**5**. A) HIC profile of the ADC at 280 nm.

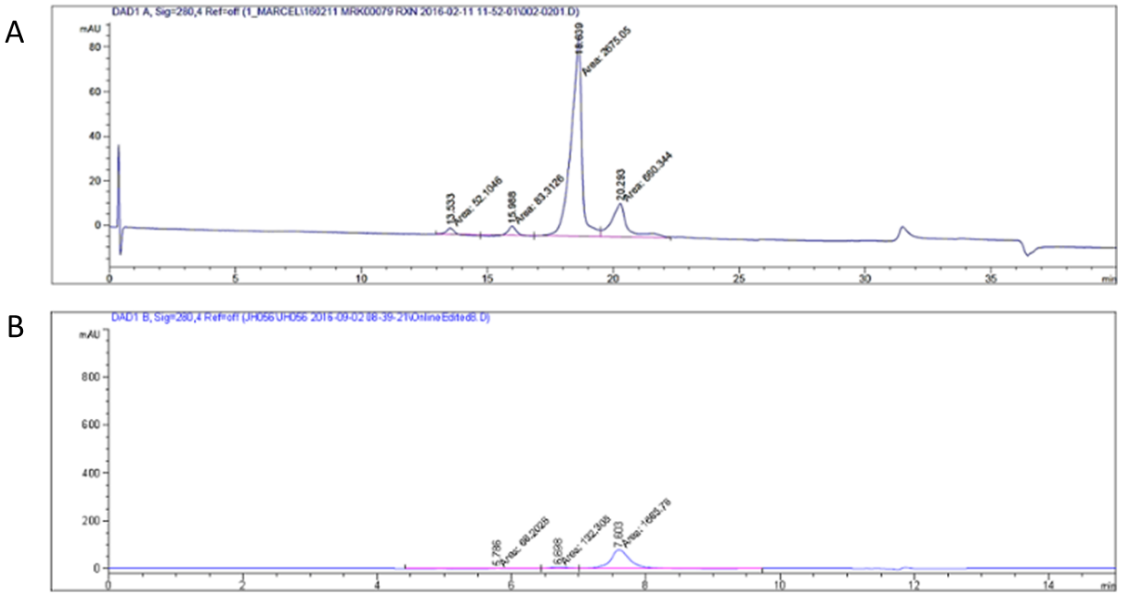

Appendix 15: Analytical data for the preparation of glycoprotein binding ADC GPB-**1**. A) HIC profile of the ADC at 280 nm. B) SEC chromatogram at 214 nm.

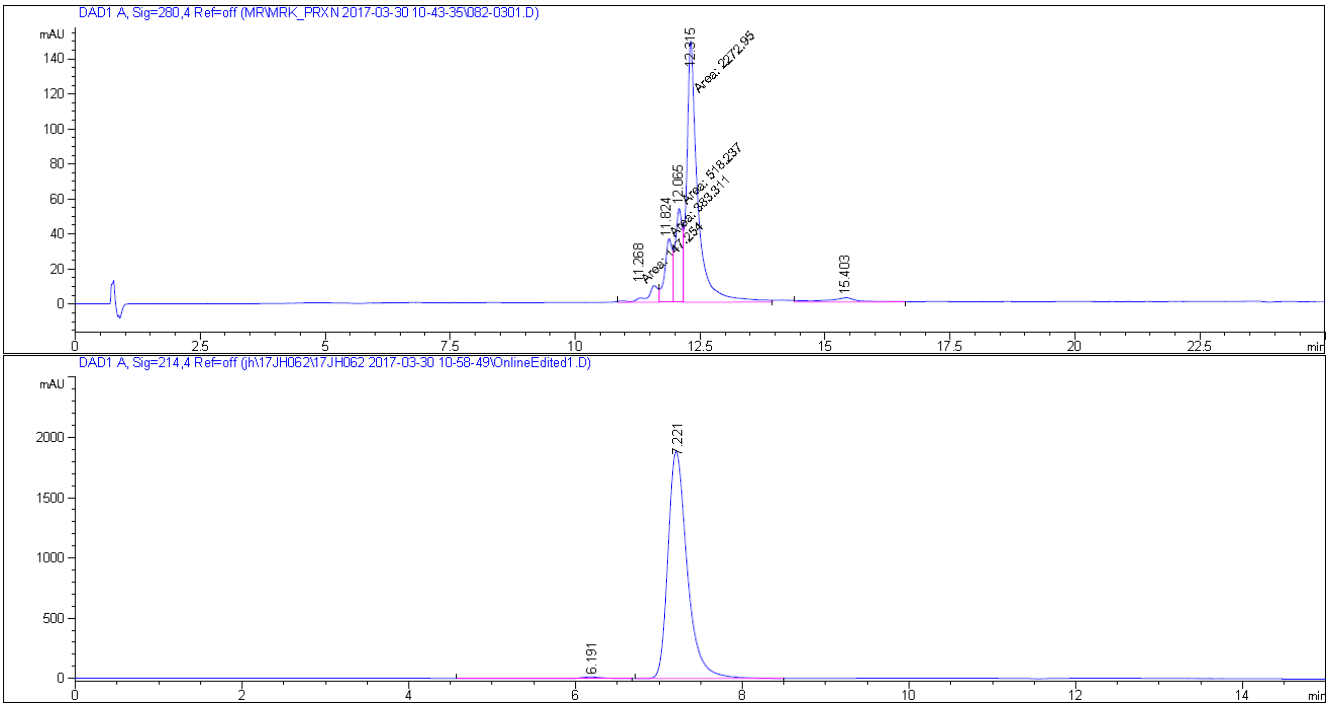

Appendix 16: Analytical data for the generation of αHER2-**9** with a DAR of 3.38. Top: Analytical HIC profile measured at a detector wavelength of 280 nm. Bottom. Analytical SEC profile measured at a detector wavelength of 214 nm.

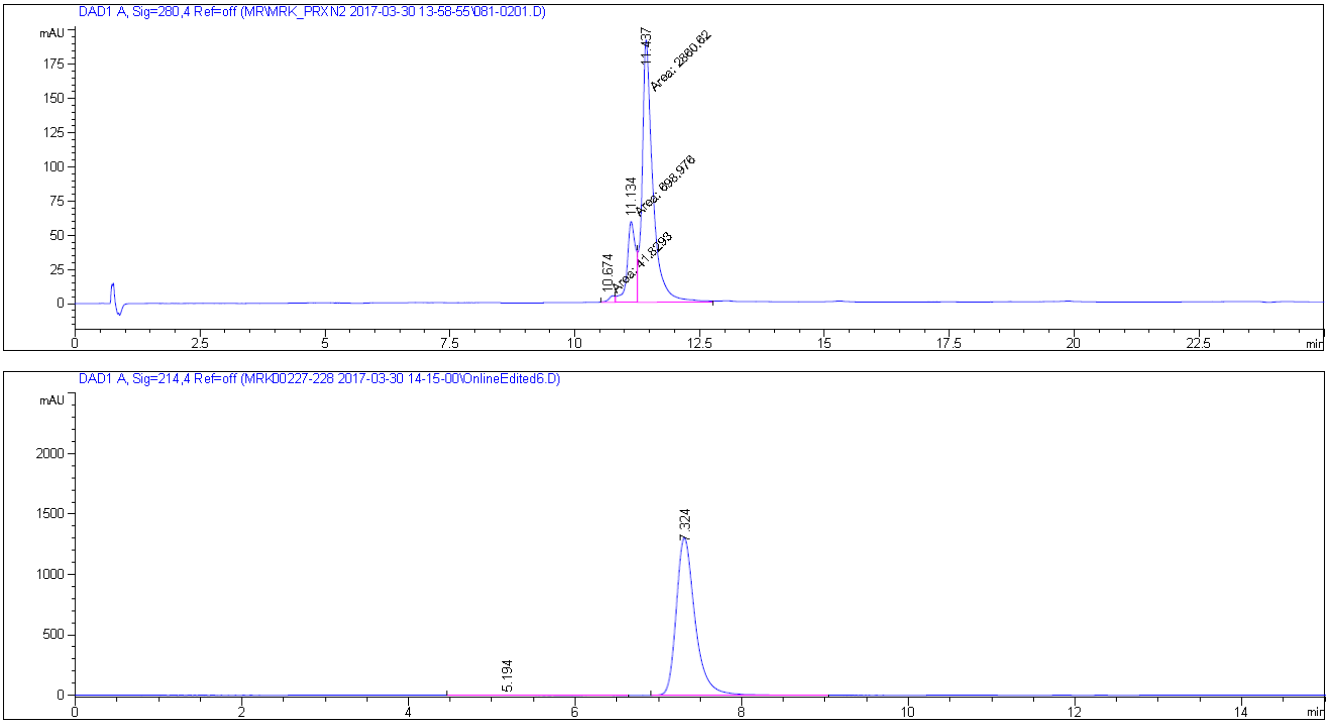

Appendix 17: Analytical data for the generation of αHER2-**9** with a DAR of 1.78. Top: Analytical HIC profile measured at a detector wavelength of 280 nm. Bottom. Analytical SEC profile measured at a detector wavelength of 214 nm.

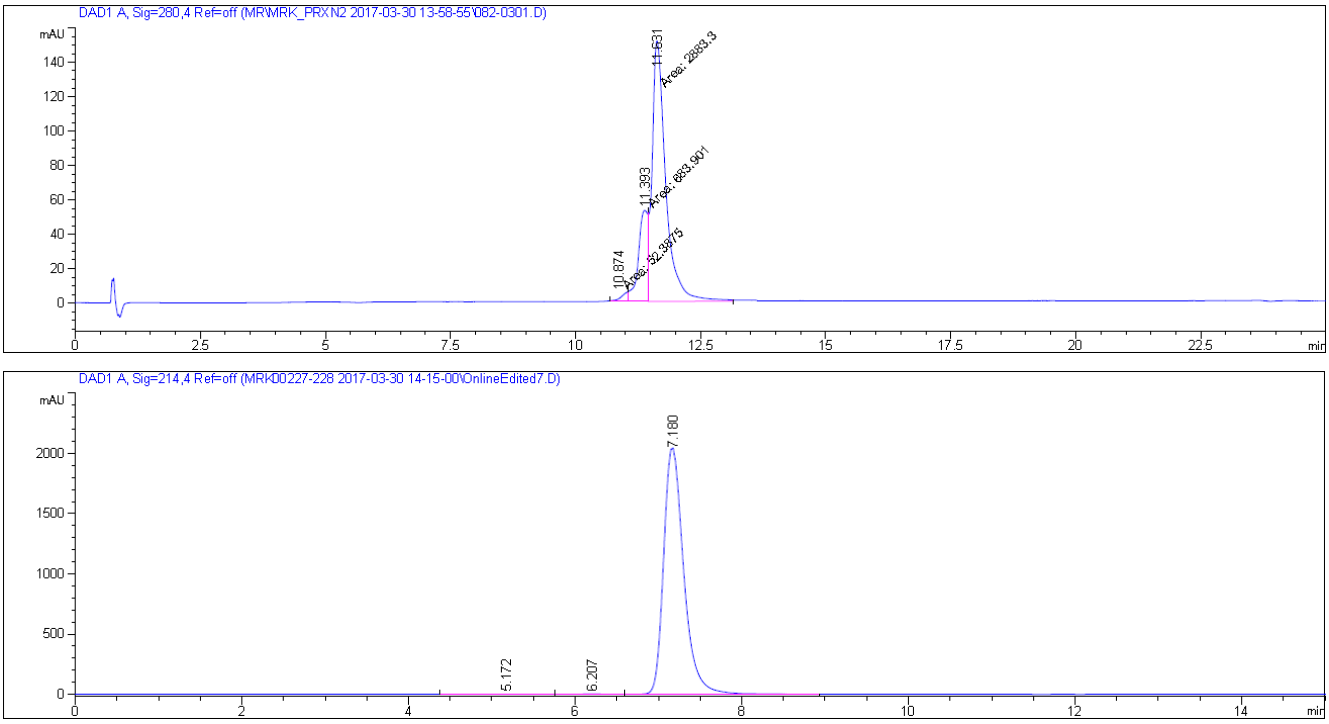

Appendix 18: Analytical data for the generation of αEGFR-**9** with a DAR of 1.78. Top: Analytical HIC profile measured at a detector wavelength of 280 nm. Bottom. Analytical SEC profile measured at a detector wavelength of 214 nm.

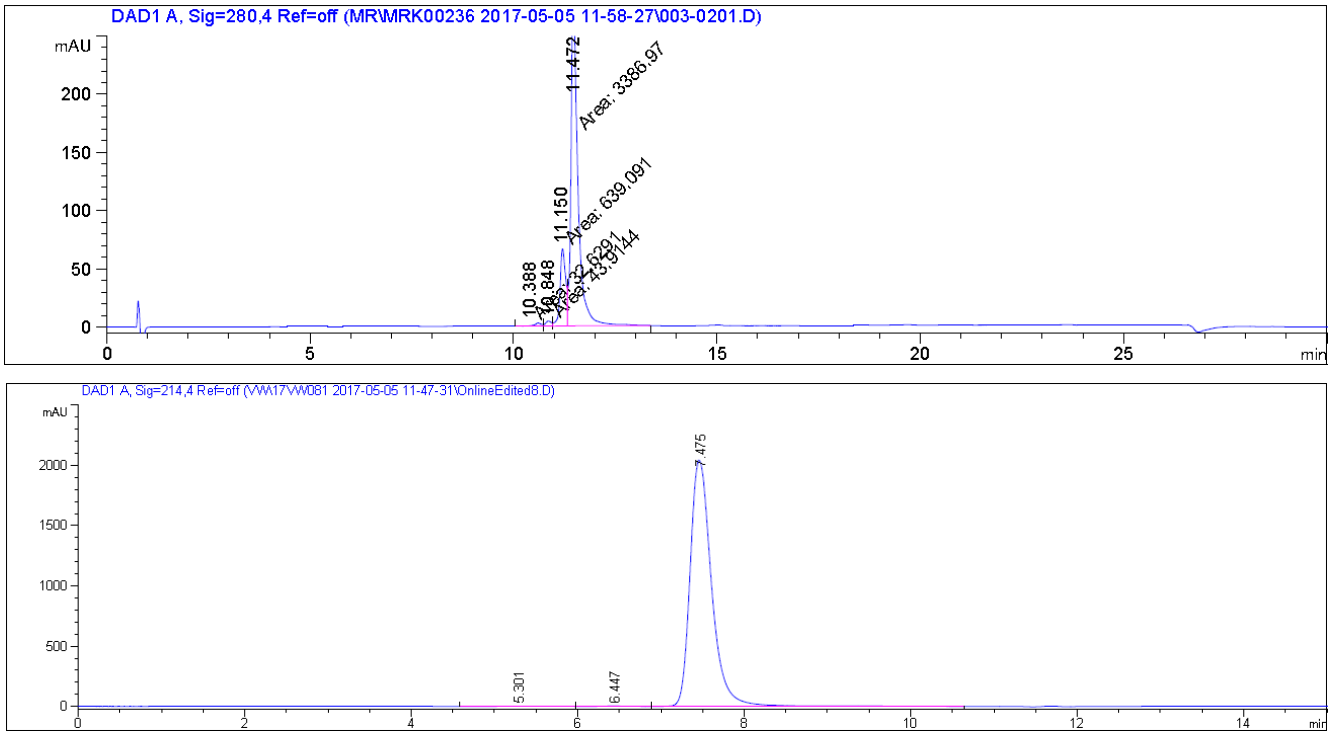

Appendix 19: Analytical data for the generation of αHEL-**9** with a DAR of 1.81. Top: Analytical HIC profile measured at a detector wavelength of 280 nm. Bottom. Analytical SEC profile measured at a detector wavelength of 214 nm.

Appendix 20: R-based code for the calculations performed in chapter 5.7. Comment characters were used to structure the code as well to comment on the functions that will be fulfilled by the subsequent section.

```
##############################################################################
# load required packages
##############################################################################
require(drc)
library(drc)
require(Matrix)
require(plot3D)
require(spatial)
require(rgl)
require(colorRamps)
##############################################################################
# annotations
##############################################################################

#name horizontally diluted drug
drug_h <- "BAY1895344"
#define starting concentration of horizontally diluted drug in nM
c0_conc_h=500

#name vertically diluted drug
drug_v <- "αHER2-2"
#define starting concentration of vertically diluted drug in nM
c0_conc_v=2.5

cell_line <- "MDA-MB-453"
exp_no <- "MRK00303"
#create working directory
setwd("Q:/Marcel/PhD/!R/")
dir.create(paste(exp_no,cell_line,drug_v,drug_h))
setwd(paste(exp_no,cell_line,drug_v,drug_h))

############################################################################## data import
##############################################################################

full_data <- read.csv(file.choose(), header=F, skip=154, nrows=17, sep=";")
#normalization
```

```
full_data_truncated <- full_data[3:16, 3:16]
#dim(full_data_truncated)
full_data_truncated_norm <- full_data_truncated/full_data_truncated[14,14]

#adjustment for evaluation of the vertically applied drug (drug_v)
drug_vert_extract <- full_data_truncated_norm[c(1:13),1:14]
#adjustment for evaluation of the horizontally applied drug (drug_h)
drug_hori_extract_t <- t(full_data_truncated_norm[c(1:14),1:13])

################################################################################
# serial dilutions
################################################################################

#this part decribes the serial dilution of the drug that is serial diluted horizontally
#define number of dilution steps
N=12
#generate serial dilution
conc_h <- rep(NA, N)
for(i in 0:N){
 conc_h[i+1] <- c0_conc_h/2^i
log_conc_h=(log(conc_h))
}
#this part decribes the serial dilution of the drug that is serial diluted vertically
#define number of dilution steps
N=12
#generate serial dilution
conc_v <- rep(NA, N)
for(i in 0:N){
 conc_v[i+1] <- c0_conc_v/2^i
}
log_conc_v=(log(conc_v))
v1 <- c(numeric(14))
for(p in 0:13){
 p <- p+1
 if(p<14){
  v1[p] <- conc_h[p]
 }
 else{
```

```
 v1[p] <- 0
}}
conc_h_names <- as.matrix(v1)
v2 <- c(numeric(14))
for(p in 0:13){
 p <- p+1
 if(p<14){
  v2[p] <- conc_v[p]
 } else{
  v2[p] <- 0
 }}
conc_v_names <- as.matrix(v2)

#############################################################################
# extract data and fit them
#############################################################################

#define matrix from which the diagonals shall be extracted
m <- as.matrix(drug_vert_extract)
#use the mid diagonal of the matrix to get the dimension of the matrix
con <- length(diag(m))
#define a matrix in which the diagonals are written column by column
m_diags <- matrix(0,con,2*con-1)
#loop runs through every column and every row and extracts the columns
j <- 0
for(l in 1:(2*con-1)){
 j <- j+1
 i <- 1
  for(n in 1:con){
  if(n+l>=con+1) {

   if(i+j<(2*con+1)){
    m_diags[n,l] <- m[i,i+j-(con)]
   }}
 i <- i+1
 }}
diagonal_data <- data.frame(m_diags)
```

```
# fits of single agents
j <- 14
fit_vert <- drm(full_data_truncated_norm[1:nrow(full_data_truncated_norm)-1,j]~conc_v,
fct=LL.4(fixed=c(NA,NA,NA,NA),names=c("HillSlope", "Bottom", "Top", "IC50")))
fit_hori <- drm(as.numeric(full_data_truncated_norm[j,1:nrow(full_data_truncated_norm)-1])~conc_h,
fct=LL.4(fixed=c(NA,NA,NA,NA),names=c("HillSlope", "Bottom", "Top", "IC50")))

# generate fit table for vertical drug
# for loop from j=2 to j=14 to skip first probably buggy line
fits_vert <- matrix(0,ncol=4,nrow=nrow(full_data_truncated_norm))
for(j in 2:14){
 fits_vert[j,1:4] <- as.numeric(coef(drm(full_data_truncated_norm[1:nrow(full_data_truncated_norm)-1,j]~conc_v,
fct=LL.4(fixed=c(NA,NA,NA,NA),names=c("HillSlope", "Bottom", "Top", "IC50")))))
}
fits_vert <- cbind(fits_vert,conc_h_names)
colnames(fits_vert) <- c("HillSlope", "Bottom", "Top", "IC50",paste("concentration of",drug_h))
fits_vert <- subset(fits_vert, fits_vert[,3]>0.8)
# HillSlope smoothing
#mean_HillSlope_vert <- mean(fits_vert[,1])
#fits_vert[,1] <- mean_HillSlope_vert

# generate fit table for horizontal drug
# for loop from j=2 to j=14 to skip first probably buggy line
fits_hori <- matrix(0,ncol=4,nrow=ncol(full_data_truncated_norm))
for(j in 2:14){
 fits_hori[j,1:4] <- as.numeric(coef(drm(as.numeric(full_data_truncated_norm[j,1:nrow(full_data_truncated_norm)-
1])~conc_h, fct=LL.4(fixed=c(NA,NA,NA,NA),names=c("HillSlope", "Bottom", "Top", "IC50")))))
}
fits_hori <- cbind(fits_hori,conc_v_names)
colnames(fits_hori) <- c("HillSlope", "Bottom", "Top", "IC50",paste("concentration of",drug_v))
fits_hori <- subset(fits_hori, fits_hori[,3]>0.8)

# calculate ratios between vertically and horizontally diluted drugs
ratio <- c(numeric(ncol(diagonal_data)))
if(c0_conc_v > c0_conc_h){
 for(j in 1:ncol(diagonal_data)){
 if(j <= 13){
  ratio[j] <- conc_h[14-j]/conc_v[1]
```

```
 }else{
  ratio[j] <- conc_h[1]/conc_v[j-12]
}}}else{
 for(j in 1:ncol(diagonal_data)){
  if(j <= 13){
   ratio[j] <- conc_v[14-j]/conc_h[1]
  }else{
   ratio[j] <- conc_v[1]/conc_h[j-12]
}}}
# define effect levels that are interesting
n_effect_levels <- seq(5,95,1)
# create empty matrices
CI_sum <- matrix(0, ncol=ncol(diagonal_data),nrow=length(n_effect_levels))
fits_diag <- matrix(0,ncol=4,nrow=ncol(diagonal_data))
# generate fit table for diagonal data
# if-else is used to exclude data that not enough data to yield a DRC
for(j in 1:ncol(diagonal_data)){
 xy_matrix <- subset(data.frame(conc_v,diagonal_data[,j]), data.frame(conc_h,diagonal_data[,j])[,2]!=0)
 if(nrow(xy_matrix) > 5){
  fit_diag <- drm(xy_matrix[,2]~xy_matrix[,1],fct=LL.4(fixed=c(NA,NA,NA,NA),names=c("HillSlope", "Bottom", "Top",
"IC50")))
  CI_sum[,j] <- as.numeric(CIcomp(ratio[j], list(fit_diag,fit_hori,fit_vert), c(n_effect_levels))[,1])
  fits_diag[j,1:4] <- as.numeric(coef(drm(xy_matrix[,2]~xy_matrix[,1], fct=LL.4(fixed=c(NA,NA,NA,NA),names=c("HillSlope",
"Bottom", "Top", "IC50")))))
 }else{
  fits_diag[j,1:4] <- c(numeric(4))
 }}
fits_diag <- cbind(fits_diag,ratio)
colnames(fits_diag) <- c("HillSlope", "Bottom", "Top", "IC50","Ratio")

#############################################################################
# global functions
#############################################################################MEE_drug_v_solve <-
function(y){
 return(fits_vert[nrow(fits_vert),4]*((1-y)/y)^(1/fits_vert[nrow(fits_vert),1]))
}
MEE_drug_h_solve <- function(y){
 return(fits_hori[nrow(fits_hori),4]*((1-y)/y)^(1/fits_hori[nrow(fits_hori),1]))
```

```
}
MEE_fits_vert_solve <- function(y){
 return(fits_vert[j,4]*((1-y)/y)^(1/fits_vert[j,1]))
}
MEE_fits_hori_solve <- function(y){
 return(fits_hori[j,4]*((1-y)/y)^(1/fits_hori[j,1]))
}
MEE_fits_diag_solve <- function(y){
 return(fits_diag[j,4]*((1-y)/y)^(1/fits_diag[j,1]))
}
DRI_vert_drug_v_MEE <- function(y){
 return(MEE_drug_v_solve(y)/MEE_fits_vert_solve(y))
}
DRI_vert_drug_h_MEE <- function(y){
 return(MEE_drug_h_solve(y)/fits_vert[j,5])
}
DRI_hori_drug_v_MEE <- function(y){
 return(MEE_drug_v_solve(y)/fits_hori[j,5])
}
DRI_hori_drug_h_MEE <- function(y){
 return(MEE_drug_h_solve(y)/MEE_fits_hori_solve(y))
}
CI_vert_MEE <- function(y){
 return(1/DRI_vert_drug_h_MEE(y)+1/DRI_vert_drug_v_MEE(y))
}
CI_hori_MEE <- function(y){
 return(1/DRI_hori_drug_h_MEE(y)+1/DRI_hori_drug_v_MEE(y))
}
get_const_conc_h <- function(j){
 return(as.numeric(fits_vert[nrow(fits_vert)-j,5]))
}
get_const_conc_v <- function(j){
 return(as.numeric(fits_hori[nrow(fits_hori)-j,5]))
}
CI_diag_MEE <- function(y){
 return(MEE_fits_diag_solve(y)/MEE_drug_v_solve(y)+(MEE_fits_diag_solve(y)*fits_diag[j,5])/MEE_drug_h_solve(y))
}
DRI_diag_drug_v_MEE <- function(y){
```

```
 return(MEE_drug_v_solve(y)/MEE_fits_diag_solve(y))
}
DRI_diag_drug_h_MEE <- function(y){
 return(MEE_drug_h_solve(y)/(MEE_fits_diag_solve(y)*fits_diag[j,5]))
}
#############################################################################
# plot CI dependent on fu and amount of horizontal drug added
#############################################################################
y=seq(.1,.9,.1)
j <- seq(1,nrow(fits_vert)-1,1)
CI_table_vert <- matrix(0,nrow=length(j),ncol=length(y))
for(j in 1:length(j)){
 CI_table_vert[j,] <- CI_vert_MEE(y)
}
j <- seq(1,nrow(fits_vert)-1,1)
png(filename =paste("3D_CI for different concentrations of",drug_h,".png") ,
  width = 1000, height = 1000, units = "px", pointsize = 18,
  bg = "white", res = NA, family = "", restoreConsole = TRUE,
  type = c("windows", "cairo", "cairo-png"))
persp3D(x=log10(get_const_conc_h(j)),y=y,z=CI_table_vert, ticktype="detailed"
   ,xlab=paste("log of concentration",drug_h,"[nM]"),ylab="Viability [%]",zlab="Combination index",main=paste(cell_line)
   ,expand=0.5, col=ramp.col(c("white","black")), border="black", nticks=9)
dev.off()
#############################################################################
# plot DRI for both drugs dependent on fu and amount of horizontal drug added
#############################################################################
j <- seq(1,nrow(fits_vert)-1,1)
DRI_table_vert_drug_v <- matrix(0,nrow=length(j),ncol=length(y))
for(j in 1:length(j)){
 DRI_table_vert_drug_v[j,] <- DRI_vert_drug_v_MEE(y)
}
j <- seq(1,nrow(fits_vert)-1,1)

png(filename =paste("3D_DRI",drug_v,"for const. conc. of",drug_h,".png") ,
  width = 1000, height = 1000, units = "px", pointsize = 18,
  bg = "white", res = NA, family = "", restoreConsole = TRUE,
  type = c("windows", "cairo", "cairo-png"))
persp3D(x=log10(get_const_conc_h(length(j)+1-j)),y=y,z=DRI_table_vert_drug_v, ticktype="detailed"
```

```
   ,xlab=paste("log of concentration",drug_h,"[nM]"),ylab="Viability [%]",zlab=paste("Dose-reduction index of",drug_v),main=paste(cell_line)
   ,expand=0.5, col=ramp.col(c("white","black")), border="black", nticks=9)
dev.off()
#####################################
DRI_table_vert_drug_h <- matrix(0,nrow=length(j),ncol=length(y))
for(j in 1:length(j)){
 DRI_table_vert_drug_h[j,] <- DRI_vert_drug_h_MEE(y)
}
j <- seq(1,nrow(fits_vert)-1,1)

png(filename =paste("3D_DRI",drug_h,"for const. conc. of",drug_h,".png") ,
  width = 1000, height = 1000, units = "px", pointsize = 18,
  bg = "white", res = NA, family = "", restoreConsole = TRUE,
  type = c("windows", "cairo", "cairo-png"))
persp3D(x=log10(get_const_conc_h(length(j)+1-j)),y=y,z=DRI_table_vert_drug_h, ticktype="detailed"
   ,xlab=paste("log of concentration",drug_h,"[nM]"),ylab="Viability [%]",zlab=paste("Dose-reduction index of",drug_h),main=paste(cell_line)
   ,expand=0.5, col=ramp.col(c("white","black")), border="black", nticks=9)
dev.off()
#############################################################################
# plot CI dependent on fu and amount of vertical drug added
#############################################################################
y=seq(.1,.9,.1)
j <- seq(1,nrow(fits_hori)-1,1)
CI_table_hori <- matrix(0,nrow=length(j),ncol=length(y))
for(j in 1:length(j)){
 CI_table_hori[j,] <- CI_hori_MEE(y)
}
j <- seq(1,nrow(fits_hori)-1,1)
png(filename =paste("3D_CI for different concentrations of",drug_v,".png") ,
  width = 1000, height = 1000, units = "px", pointsize = 18,
  bg = "white", res = NA, family = "", restoreConsole = TRUE,
  type = c("windows", "cairo", "cairo-png"))
persp3D(x=log10(get_const_conc_v(j)),y=y,z=CI_table_hori, ticktype="detailed"
   ,xlab=paste("log of concentration",drug_v,"[nM]"),ylab="Viability [%]",zlab="Combination index",main=paste(cell_line)
   ,expand=0.5, col=ramp.col(c("white","black")), border="black", nticks=9)
dev.off()
```

```
################################################################################ plot DRI of both drugs dependent on fu and amount of vertical drug added
################################################################################
j <- seq(1,nrow(fits_hori)-1,1)
DRI_table_hori_drug_v <- matrix(0,nrow=length(j),ncol=length(y))
for(j in 1:length(j)){
 DRI_table_hori_drug_v[j,] <- DRI_hori_drug_v_MEE(y)
}
j <- seq(1,nrow(fits_hori)-1,1)
png(filename =paste("3D_DRI",drug_v,"for const. conc. of",drug_v,".png") ,
  width = 1000, height = 1000, units = "px", pointsize = 18,
  bg = "white", res = NA, family = "", restoreConsole = TRUE,
  type = c("windows", "cairo", "cairo-png"))
persp3D(x=log10(get_const_conc_v(length(j)+1-j)),y=y,z=DRI_table_hori_drug_v, ticktype="detailed"
   ,xlab=paste("log of concentration",drug_v,"[nM]"),ylab="Viability",zlab=paste("Dose-reduction index of",drug_v),main=paste(cell_line)
   ,expand=0.5, col=ramp.col(c("white","black")), border="black", nticks=9)
dev.off()
#######################################
j <- seq(1,nrow(fits_hori)-1,1)
DRI_table_hori_drug_h <- matrix(0,nrow=length(j),ncol=length(y))
for(j in 1:length(j)){
 DRI_table_hori_drug_h[j,] <- DRI_hori_drug_h_MEE(y)
}
j <- seq(1,nrow(fits_hori)-1,1)
png(filename =paste("3D_DRI",drug_h,"for const. conc. of",drug_v,".png") ,
  width = 1000, height = 1000, units = "px", pointsize = 18,
  bg = "white", res = NA, family = "", restoreConsole = TRUE,
  type = c("windows", "cairo", "cairo-png"))
persp3D(x=log10(get_const_conc_v(length(j)+1-j)),y=y,z=DRI_table_hori_drug_h, ticktype="detailed"
   ,xlab=paste("log of concentration",drug_v,"[nM]"),ylab="Viability [%]",zlab=paste("Dose-reduction index of",drug_h),main=paste(cell_line)
   ,expand=0.5, col=ramp.col(c("white","black")), border="black", nticks=9)
dev.off()
################################################################################
# Plot CI for diagonal data
################################################################################y=seq(.1,.9,.1)
a <- 6
```

```
e <- 15
j <- seq(1,nrow(fits_diag),1)
CI_table_diag <- matrix(0,nrow=length(j),ncol=length(y))
for(j in 1:length(j)){
 CI_table_diag[j,] <- CI_diag_MEE(y)
}
j <- seq(1,nrow(fits_diag),1)
png(filename = "CI_for_fixed_ratio_my_functions.png",
  width = 1000, height = 1000, units = "px", pointsize = 18,
  bg = "white", res = NA, family = "", restoreConsole = TRUE,
  type = c("windows", "cairo", "cairo-png"))
persp3D(x=fits_diag[a:e,5],y=y,z=CI_table_diag[a:e,], ticktype="detailed"
   ,xlab=paste("Ratio",drug_h,"to",drug_v),ylab="Viability",zlab="Combination index",main=paste(cell_line)
   ,phi=10,inttype=2, r=2, theta=310
   ,expand=0.75, nticks=10, col=ramp.col(c("white","black")), border="black"
   ,facets=T,colkey = list(side = 1, length = 0.5, dist=-0.05, cex.clab=0.7, width=0.6)
   ,cex.main=1.2,cex.lab=1.2)
dev.off()

#############################################################################
# calculate CI values of data directly from plate
#############################################################################

CI_plate <- matrix(0, ncol=ncol(full_data_truncated_norm), nrow=nrow(full_data_truncated_norm))
for(j in 1:ncol(full_data_truncated_norm)){
 for(i in 1:nrow(full_data_truncated_norm)){
  CI_plate[i,j]                                                                                                    <-
conc_h[i]/MEE_drug_h_solve(full_data_truncated_norm[i,j])+conc_v[j]/MEE_drug_v_solve(full_data_truncated_norm[i,j]
)
 }}
colnames(CI_plate) <- conc_v_names
rownames(CI_plate) <- conc_h_names

#############################################################################
# write that stuff
#############################################################################png(filename                                =
"CI_for_fixed_ratio_CIcomp_function.png",
  width = 1000, height = 1000, units = "px", pointsize = 18,
```

```
  bg = "white", res = NA, family = "", restoreConsole = TRUE,
  type = c("windows", "cairo", "cairo-png"))
a <- 6
e <- 15
persp3D(x=n_effect_levels,y=ratio[a:e],z=CI_sum[,a:e], ticktype="detailed"
   ,phi=10, inttype=2, r=2, xlab="Effect level [%]"
   ,ylab=paste("Ratio",drug_h,"to",drug_v), zlab="Combination Index", main=paste(cell_line)
   ,expand=0.75, nticks=10, col=ramp.col(c("white","black")), border="black"
   ,colkey = list(side = 1, length = 0.5, dist=-0.05, cex.clab=0.7, width=0.6), facets=T
   ,cex.main=1.2,cex.lab=1.2)
dev.off()

# export fitting results
write.csv(fits_diag, file=paste(exp_no,cell_line,drug_h,drug_v,"diagonals fitted.txt"))
write.csv(fits_vert, file=paste(exp_no,cell_line,drug_h,drug_v,"vertical data fitted.txt"))
write.csv(fits_hori, file=paste(exp_no,cell_line,drug_h,drug_v,"horizontal data fitted.txt"))

write.csv(CI_plate, file=paste(exp_no,cell_line,drug_h,drug_v,"horizontal data fitted.txt"))
# DRI of drug h when adding constant concentrations of drug v @ IC50
# fit the data using linear model
png(filename =paste("DRI",drug_h,"at constant concentrations of",drug_v,"at IC50.png"),
  width = 1000, height = 1000, units = "px", pointsize = 18,
  bg = "white", res = NA, family = "", restoreConsole = TRUE,
  type = c("windows", "cairo", "cairo-png"))
filtered_fits_hori <- subset(fits_hori, fits_hori[,3]>0.7)
plot(filtered_fits_hori[nrow(filtered_fits_hori),4]/filtered_fits_hori[,4]~filtered_fits_hori[,5], log=""
  ,xlab=paste("Concentration of",drug_v,"[nM]"),ylab="Dose-reduction index at IC50", main=paste(cell_line),
cex.main=1.5, cex.lab=1.5)
fit_DRI_hori_at_IC50 <- lm(filtered_fits_hori[nrow(filtered_fits_hori),4]/filtered_fits_hori[,4]~filtered_fits_hori[,5])
lines(filtered_fits_hori[,5],predict(fit_DRI_hori_at_IC50))
legend("topleft",inset=.05, horiz=T, bty="n",
   c(paste("Y=",round(summary(fit_DRI_hori_at_IC50)$coefficients[2,1],digits=4),
      "*X+",round(summary(fit_DRI_hori_at_IC50)$coefficients[1,1],digits=4),
      "\nR²=",round(summary(fit_DRI_hori_at_IC50)$r.squared,digits=4))))
dev.off()

# DRI of drug v when adding constant concentrations of drug h @ IC50
# fit the data using linear model
```

```
png(filename =paste("DRI",drug_v,"at constant concentrations of",drug_h,"at IC50.png"),
  width = 1000, height = 1000, units = "px", pointsize = 18,
  bg = "white", res = NA, family = "", restoreConsole = TRUE,
  type = c("windows", "cairo", "cairo-png"))
filtered_fits_vert <- subset(fits_vert, fits_vert[,3]>0.7)
plot(filtered_fits_vert[nrow(filtered_fits_vert),4]/filtered_fits_vert[,4]~filtered_fits_vert[,5], log=""
   ,xlab=paste("Concentration of",drug_h,"[nM]"),
   ylab="Dose-reduction index at IC50", main=paste(cell_line), cex.main=1.5, cex.lab=1.5)
fit_DRI_vert_at_IC50 <- lm(filtered_fits_vert[nrow(filtered_fits_vert),4]/filtered_fits_vert[,4]~filtered_fits_vert[,5])
lines(filtered_fits_vert[,5],predict(fit_DRI_vert_at_IC50))
legend("topleft",inset=.05, horiz=T, bty="n",
    c(paste("Y=",round(summary(fit_DRI_vert_at_IC50)$coefficients[2,1],digits=4),
     "*X+",round(summary(fit_DRI_vert_at_IC50)$coefficients[1,1],digits=4),
     "\nR²=",round(summary(fit_DRI_vert_at_IC50)$r.squared,digits=4))))
dev.off()

rm(list = ls())
gc()
setwd("Q:/Marcel/PhD/!R/")
```

8.1. Sources

1. National Cancer Institute. What is cancer? *Article* (2015). Available at: https://www.cancer.gov/about-cancer/understanding/what-is-cancer.
2. Stewart, Bernhard W. and Wild, C. P. and others. *World cancer report 2014*. *International Agency for Research on Cancer Press* (2014).
3. Colditz, G. A. & Wei, E. K. Preventability of Cancer: The Relative Contributions of Biologic and Social and Physical Environmental Determinants of Cancer Mortality. *Annu. Rev. Public Health* **33,** 137–156 (2012).
4. Stewart, Bernhard W., Kleihues, P. *World Cancer Report*. *International Agency for Research on Cancer Press* (2003). doi:10.1017/S0020860400079146
5. Hanahan, D., Weinberg, R. A. Hallmarks of Cancer: The Next Generation. *Cell* **144,** 646–674 (2011).
6. Abdel-Rahman, W. M. Genomic Instability and Carcinogenesis: An Update. *Curr. Genomics* **9,** 535–541 (2008).
7. Spry, M., Scott, T., Pierce, H. & D'Orazio, J. A. DNA repair pathways and hereditary cancer susceptibility syndromes. *Front. Biosci.* **12,** 4191–4207 (2007).
8. Coussens, L. M., Zitvogel, L. & Palucka, A. K. Neutralizing Tumor-Promoting Chronic Inflammation: A Magic Bullet? *Science (80-.).* **339,** 286–291 (2013).
9. Pribluda, A. *et al.* A Senescence-inflammatory switch from cancer-inhibitory to cancer-promoting mechanism. *Cancer Cell* **24,** 242–256 (2013).
10. Bondar, T. & Medzhitov, R. The origins of tumor-promoting inflammation. *Cancer Cell* **24,** 143–144 (2013).
11. Low, K. C. & Tergaonkar, V. Telomerase: central regulator of all of the hallmarks of cancer. *Trends Biochem. Sci.* **38,** 426–434 (2013).
12. Shay, J. W. Are short telomeres predictive of advanced cancer? *Cancer Discov.* **3,** 1096–1098 (2013).
13. Lambert, A. W., Pattabiraman, D. R. & Weinberg, R. A. Emerging Biological Principles of Metastasis. *Cell* **168,** 670–691 (2017).
14. Gil-Bazo, I. Avelumab—a new programmed death-ligand 1 inhibitor against advanced non-small cell lung cancer. *Transl. Lung Cancer Res.* **6,** S35–S38 (2017).
15. Brown, J. M. & Wilson, W. R. Exploiting tumour hypoxia in cancer treatment. *Nat. Rev. Cancer* **4,** 437–447 (2004).
16. Chabner, B. a & Roberts, T. G. Timeline: Chemotherapy and the war on cancer. *Nat. Rev. Cancer* **5,** 65–72 (2005).
17. Scott, A. M., Allison, J. P. & Wolchok, J. D. Monoclonal antibodies in cancer therapy. *Cancer Immun.* **12,** 1–8 (2012).
18. Beck, A., Goetsch, L., Dumontet, C. & Corvaïa, N. Strategies and challenges for the next generation of

antibody-drug conjugates. *Nat. Rev. Drug Discov.* **16,** 315–337 (2017).

19. Chou, T. Theoretical Basis, Experimental Design, and Computerized Simulation of Synergism and Antagonism in Drug Combination Studies. *Pharmacol. Rev.* **58,** 621–681 (2006).
20. Sievers, E. L. & Senter, P. D. Antibody-Drug Conjugates in Cancer Therapy. *Annu. Rev. Med.* **64,** 15–29 (2013).
21. Pinto, A. C., Moreira, J. N. & Simões, S. *Combination Chemotherapy in Cancer: Principles, Evaluation and Drug Delivery Strategies*. *Current Cancer Treatment - Novel Beyond Conventional Approaches* (InTech, 2011). doi:10.5772/22656.
22. Krueger, A. S. *et al.* Synergistic drug combinations tend to improve therapeutically relevant selectivity. *Nat. Biotechnol.* **27,** 659–669 (2009).
23. Miles, D., Von Minckwitz, G. & Seidman, A. D. Combination Versus Sequential Single-Agent Therapy in Metastatic Breast Cancer. *Oncologist* **7,** 13–19 (2002).
24. Yadav, B., Wennerberg, K., Aittokallio, T. & Tang, J. Searching for drug synergy in complex dose–response landscapes using an interaction potency model. *Comput. Struct. Biotechnol. J.* **13,** 504–513 (2015).
25. Roell, K. R., Reif, D. M. & Motsinger-reif, A. A. An Introduction to Terminology and Methodology of Chemical Synergy — Perspectives from Across Disciplines. *Front. Pharmacol.* **8,** 1–11 (2017).
26. Ka, G., Chan, Y., Wilson, S., Schmidt, S. & Moffat, J. G. Unlocking the Potential of High-Throughput Drug Combination Assays Using Acoustic Dispensing. *J. Laboratoy Autom.* **21,** 125–132 (2016).
27. Horn, T. *et al.* High-order drug combinations are required to effectively kill colorectal cancer cells. *Cancer Res.* **76,** 6950–6963 (2016).
28. Borisy, A. A. *et al.* Systematic discovery of multicomponent therapeutics. *Proc. Natl. Acad. Sci.* **100,** 7977–7982 (2003).
29. BLISS, C. I. the Toxicity of Poisons Applied Jointly. *Ann. Appl. Biol.* **26,** 585–615 (1939).
30. Foucquier, J. & Guedj, M. Analysis of drug combinations: current methodological landscape. *Pharmacol. Res. Perspect.* **3,** 1–11 (2015).
31. Lee, S. Drug interaction: focusing on response surface models. *Korean J. Anesthesiol.* **58,** 421–434 (2010).
32. Kitson, S. L. *et al.* Antibody-Drug Conjugates (ADCs) – Biotherapeutic bullets. **31,** (2013).
33. Wagh, A., Song, H., Zeng, M., Tao, L. & Das, T. K. Challenges and new frontiers in analytical characterization of antibody-drug conjugates. *MAbs* **0,** 1–22 (2017).
34. Vidarsson, G., Dekkers, G. & Rispens, T. IgG subclasses and allotypes: From structure to effector functions. *Front. Immunol.* **5,** 1–17 (2014).
35. Kitson, S. L. *et al.* Antibody-Drug Conjugates (ADCs) – Biotherapeutic bullets. *Chem. Today* **31,** 30–36 (2013).
36. Taylor, P. *et al.* The level of HER2 expression is a predictor of antibody-HER2 trafficking behavior in cancer cells. *MAbs* **6,** 1211–1219 (2014).

37. Deonarain, M. P., Yahioglu, G., Stamati, I. & Marklew, J. Emerging formats for next-generation antibody drug conjugates. *Expert Opin. Drug Discov.* **10,** 463–481 (2015).

38. Drake, P. M. & Rabuka, D. Recent Developments in ADC Technology: Preclinical Studies Signal Future Clinical Trends. *BioDrugs* **31,** 521–531 (2017).

39. Tolcher, A. W. Antibody drug conjugates: lessons from 20 years of clinical experience. *Ann. Oncol.* **27,** 2168–2172 (2016).

40. Alagoz, M., C. Gilbert, D., El-Khamisy, S. & J. Chalmers, a. DNA Repair and Resistance to Topoisomerase I Inhibitors: Mechanisms, Biomarkers and Therapeutic Targets. *Curr. Med. Chem.* **19,** 3874–3885 (2012).

41. Tamura, N. *et al.* Analysis of type of cell death induced by topoisomerase inhibitor SN-38 in human oral squamous cell carcinoma cell lines. *Anticancer Res.* **32,** 4823–4832 (2012).

42. Lu, J., Jiang, F., Lu, A. & Zhang, G. Linkers having a crucial role in antibody–drug conjugates. *Int. J. Mol. Sci.* **17,** 1–22 (2016).

43. Shadid, M., Bowlin, S. & Bolleddula, J. Catabolism of antibody drug conjugates and characterization methods. *Bioorg. Med. Chem.* **25,** 2933–2945 (2017).

44. McCombs, J. R. & Owen, S. C. Antibody Drug Conjugates: Design and Selection of Linker, Payload and Conjugation Chemistry. *AAPS J.* **17,** 339–351 (2015).

45. Dubowchik, G. M. *et al.* Cathepsin B-labile dipeptide linkers for lysosomal release of doxorubicin from internalizing immunoconjugates: Model studies of enzymatic drug release and antigen-specific in vitro anticancer activity. *Bioconjug. Chem.* **13,** 855–869 (2002).

46. Mohamed, M. M. & Sloane, B. F. Cysteine cathepsins: Multifunctional enzymes in cancer. *Nat. Rev. Cancer* **6,** 764–775 (2006).

47. Caculitan, N. G. *et al.* Cathepsin B is dispensable for cellular processing of cathepsin B-cleavable antibody–drug conjugates. *Cancer Res.* **77,** 7027–7037 (2017).

48. Carl, P. L., Chakravarty, P. K. & Katzenellenbogen, J. A. A Novel Connector Linkage Applicable in Prodrug Design. *J. Med. Chem.* **24,** 479–480 (1981).

49. Bajjuri, K. M., Liu, Y., Liu, C. & Sinha, S. C. The Legumain Protease-Activated Auristatin Prodrugs Suppress Tumor Growth and Metastasis without Toxicity. *ChemMedChem* **6,** 54–59 (2011).

50. Doronina, S. & Bovee, T. Novel Peptide Linkers for Highly Potent Antibody− Auristatin Conjugate. *Bioconjug. Chem.* **19,** 1960–3 (2008).

51. Jeffrey, S. C., De Brabander, J., Miyamoto, J. & Senter, P. D. Expanded utility of the β-glucuronide linker: ADCs that deliver phenolic cytotoxic agents. *ACS Med. Chem. Lett.* **1,** 277–280 (2010).

52. Jeffrey, S. C. *et al.* Development and properties of β-glucuronide linkers for monoclonal antibody-drug conjugates. *Bioconjug. Chem.* **17,** 831–840 (2006).

53. Jeffrey, S. C. *et al.* Minor groove binder antibody conjugates employing a water soluble b-glucuronide linker. *Bioorg. Med. Chem. Lett.* **17,** 2278–2280 (2007).

54. Hoffmann, R. M. *et al.* Antibody structure and engineering considerations for the design and function of Antibody Drug Conjugates (ADCs). *Oncoimmunology* **7,** e1395127 (2018).
55. Gerber, H.-P., Senter, P. D., Greqal, I. S. Antibody drug-conjugates targeting the tumor vasculature Current and future developments. *MAbs* **1,** 247–253 (2009).
56. Pillow, T. H. *et al.* Modulating Therapeutic Activity and Toxicity of Pyrrolobenzodiazepine Antibody–Drug Conjugates with Self-Immolative Disulfide Linkers. *Mol. Cancer Ther.* **16,** 871–878 (2017).
57. Perez, H. L. *et al.* Antibody – drug conjugates : current status and future directions. *Drug Discov. Today* **19,** 869–881 (2014).
58. Lyon, R. P. *et al.* Reducing hydrophobicity of homogeneous antibody-drug conjugates improves pharmacokinetics and therapeutic index. *Nat. Biotechnol.* **33,** 733–736 (2015).
59. Tumey, L. N. *et al.* Site Selection: a Case Study in the Identification of Optimal Cysteine Engineered Antibody Drug Conjugates. *AAPS J.* **19,** 1123–1135 (2017).
60. Sadowsky, J. D. *et al.* Development of Efficient Chemistry to Generate Site-Specific Disulfide-Linked Protein- and Peptide-Payload Conjugates: Application to THIOMAB Antibody-Drug Conjugates. *Bioconjug. Chem.* **28,** 2086–2098 (2017).
61. Hallam, T. J., Wold, E., Wahl, A. & Smider, V. V. Antibody Conjugates with Unnatural Amino Acids. *Mol. Pharm.* **12,** 1848–1862 (2015).
62. Dennler, P. *et al.* Transglutaminase-based chemo-enzymatic conjugation approach yields homogeneous antibody-drug conjugates. *Bioconjug. Chem.* **25,** 569–578 (2014).
63. Strop, P. *et al.* Location Matters: Site of Conjugation Modulates Stability and Pharmacokinetics of Antibody Drug Conjugates. *Chem. Biol.* **20,** 161–167 (2013).
64. Agarwal, P. & Bertozzi, C. R. Site-specific antibody-drug conjugates: the nexus of bioorthogonal chemistry, protein engineering, and drug development. *Bioconjug. Chem.* **26,** 176–92 (2015).
65. Pan, L. *et al.* Sortase A-Generated Highly Potent Anti-CD20-MMAE Conjugates for Efficient Elimination of B-Lineage Lymphomas. *Small* **13,** 1–12 (2017).
66. Beerli, R. R., Hell, T., Merkel, A. S. & Grawunder, U. Sortase enzyme-mediated generation of site-specifically conjugated antibody drug conjugates with high In Vitro and In Vivo potency. *PLoS One* **10,** 1–17 (2015).
67. Sellmann, C. *et al.* Balancing Selectivity and Efficacy of Bispecific EGFR x c-MET Antibodies and Antibody-Drug Conjugates. *J. Biol. Chem.* **291,** 25106–25119 (2016).
68. Patil, P. C., Satam, V. & Lee, M. A Short Review on the Synthetic Strategies of Duocarmycin Analogs that are Powerful DNA Alkylating Agents. *Anticancer. Agents Med. Chem.* **15,** 616–630 (2015).
69. Boger, D. L., Torrey, N., Roud, P. & Jolla, L. Catalysis of the CC-1065 and Duocarmycin DNA Alkylation Reaction: DNA Binding Induced Conformational Change in the Agent Results in Activation. **5,** 263–276 (1997).

70. Smith, J. a *et al.* The structural basis for in situ activation of DNA alkylation by duocarmycin SA. *J. Mol. Biol.* **300,** 1195–204 (2000).
71. Milbank, J. B. J. *et al.* DNA Minor Groove Alkylating Agents and Structure-Activity Relationships for Their Cytotoxicity. *J. Med. Chem.* **42,** 649–658 (1999).
72. Macmillan, K. S. & Boger, D. L. Fundamental Relationships between Structure, Reactivity, and Biological Activity for the Duocarmycins and CC-1065. *J. Med. Chem.* **52,** 5771–5780 (2009).
73. McGovren, J. P., Clarke, G. L., Pratt, E. A. & DeKoning, T. F. Preliminary toxicity studies with the DNA-binding antibiotic, CC-1065. *J. Antibiot. (Tokyo).* **37,** 63–70 (1984).
74. Awada, a *et al.* Phase I study of Carzelesin (U-80, 244) given (4-weekly) by intravenous bolus schedule. *Br. J. Cancer* **79,** 1454–1461 (1999).
75. Pavlidis, N. *et al.* Carzelesin phase II study in advanced breast, ovarian, colorectal, gastric, head and neck cancer, non-Hodgkin's lymphoma and malignant melanoma: a study of the EORTC early clinical studies group (ECSG). *Cancer Chemother Pharmacol* **46,** 167–171 (2000).
76. Zhao, R. Y. *et al.* Synthesis and biological evaluation of antibody conjugates of phosphate prodrugs of cytotoxic DNA alkylators for the targeted treatment of cancer. *J. Med. Chem.* **55,** 766–782 (2012).
77. Kovtun, Y. V. *et al.* Antibody-drug conjugates designed to eradicate tumors with homogeneous and heterogeneous expression of the target antigen. *Cancer Res.* **66,** 3214–3221 (2006).
78. Suzawa, T. *et al.* Synthesis of a novel duocarmycin derivative DU-257 and its application to immunoconjugate using poly(ethylene glycol)-dipeptidyl linker capable of tumor specific activation. *Bioorganic Med. Chem.* **8,** 2175–2184 (2000).
79. Zhang, D. *et al.* Immolation of p-aminobenzyl ether linker and payload potency and stability determine the cell killing activity of antibody-drug conjugates with phenol-containing payloads. *Bioconjug. Chem.* **29,** 267–274 (2018).
80. Chari, R. V. J. *et al.* Enhancement of the Selectivity and Antitumor Efficacy of a CC-1065 Analogue through Immunoconjugate Formation. *Cancer Res.* **55,** 4079–4084 (1995).
81. Yu, L. *et al.* Promiximab-duocarmycin, a new CD56 antibody-drug conjugates, is highly efficacious in small cell lung cancer xenograft models. *Oncotarget* **9,** 5197–5207 (2017).
82. Elgersma, R. C. *et al.* Design, synthesis, and evaluation of linker-duocarmycin payloads: Toward selection of HER2-targeting antibody-drug conjugate SYD985. *Mol. Pharm.* **12,** 1813–1835 (2015).
83. Wang, H. *et al.* Pharmacokinetic characterization of BMS-936561 , an anti-CD70 antibody-drug conjugate , in preclinical animal species and prediction of its pharmacokinetics in humans. **106,** 93–106 (2016).
84. Jeffrey, S. C. *et al.* Design, Synthesis, and in Vitro Evaluation of Dipeptide-Based Antibody Minor Groove Binder Conjugates. *J. Med. Chem.* **48,** 1344–1358 (2005).
85. Scribner, J. A. *et al.* Abstract 820: Preclinical development of MGC018, a duocarmycin-based antibody-drug conjugate targeting B7-H3 for solid cancer. *Cancer Res.* **78,** Abstract Nr 820 (2018).

86. Menderes, G. *et al.* SYD985, a novel duocarmycin-based her2-targeting antibody–drug conjugate, shows antitumor activity in uterine and ovarian carcinosarcoma with HER2/Neu expression. *Clin. Cancer Res.* **23,** 5836–5845 (2017).
87. van der Lee, M. M. C. *et al.* The Preclinical Profile of the Duocarmycin-Based HER2-Targeting ADC SYD985 Predicts for Clinical Benefit in Low HER2-Expressing Breast Cancers. *Mol. Cancer Ther.* **14,** 692–703 (2015).
88. Van Herpen, C. & Banerji, U. Phase I dose-escalation trial with the DNA-alkylating anti-HER2 antibody-drug conjugate SYD985. *ESMO Annu. Meet.* **51,** Abstract #333 (2015).
89. Saura, C. *et al.* A phase I expansion cohorts study of SYD985 in heavily pretreated patients with HER2-positive or HER2-low metastatic breast cancer. *J. Clin. Oncol.* **36,** 1014 (2018).
90. NCT03262935: SYD985 vs. Physician's Choice in Participants With HER2-positive Locally Advanced or Metastatic Breast Cancer. (2017).
91. Lord, C. J. & Ashworth, A. The DNA damage response and cancer therapy. *Nature* **481,** 287–294 (2012).
92. Toledo, L., Neelsen, K. J. & Lukas, J. Replication Catastrophe: When a Checkpoint Fails because of Exhaustion. *Mol. Cell* **66,** 735–749 (2017).
93. Blackford, A. N. & Jackson, S. P. ATM, ATR, and DNA-PK: The Trinity at the Heart of the DNA Damage Response. *Mol. Cell* **66,** 801–817 (2017).
94. Forment, J. V. & O'Connor, M. J. Targeting the replication stress response in cancer. *Pharmacol. Ther.* **Article in,** (2018).
95. O'Connor, M. J. Targeting the DNA Damage Response in Cancer. *Mol. Cell* **60,** 547–560 (2015).
96. Wang, J. & Lindahl, T. Maintenance of Genome Stability. *Genomics, Proteomics Bioinforma.* **14,** 119–121 (2016).
97. Smith, J., Mun Tho, L., Xu, N. & A. Gillespie, D. The ATM-Chk2 and ATR-Chk1 pathways in DNA damage signaling and cancer. *Adv. Cancer Res.* **108,** 73–112 (2010).
98. Parker, M. W., Botchan, M. R. & Berger, J. M. Mechanisms and regulation of DNA replication initiation in eukaryotes. *Crit. Rev. Biochem. Mol. Biol.* **52,** 107–144 (2017).
99. Speck, C., Chen, Z., Li, H. & Stillman, B. ATPase-dependent cooperative binding of ORC and Cdc6 to origin DNA. *Nat. Struct. Mol. Biol.* **12,** 965–971 (2005).
100. Evrin, C. *et al.* A double-hexameric MCM2-7 complex is loaded onto origin DNA during licensing of eukaryotic DNA replication. *Proc. Natl. Acad. Sci.* **106,** 20240–20245 (2009).
101. Tsakraklides, V. & Bell, S. P. Dynamics of pre-replicative complex assembly. *J. Biol. Chem.* **285,** 9437–9443 (2010).
102. Douglas, M. E., Ali, F. A., Costa, A. & Diffley, J. F. X. The mechanism of eukaryotic CMG helicase activation. *Nature* **555,** 265–268 (2018).
103. Glanzer, J. G. *et al.* RPA inhibition increases replication stress and suppresses tumor growth. *Cancer Res.*

74, 5165–5172 (2014).

104. Poli, J. *et al.* dNTP pools determine fork progression and origin usage under replication stress. *EMBO J.* **31,** 883–894 (2012).
105. Mejlvang, J. *et al.* New histone supply regulates replication fork speed and PCNA unloading. *J. Cell Biol.* **204,** 29–43 (2014).
106. Ruff, P., Donnianni, R. A., Glancy, E., Oh, J. & Symington, L. S. RPA Stabilization of Single-Stranded DNA Is Critical for Break-Induced Replication. *Cell Rep.* **17,** 3359–3368 (2016).
107. Giannattasio, M. & Branzei, D. S-phase checkpoint regulations that preserve replication and chromosome integrity upon dNTP depletion. *Cell. Mol. Life Sci.* **74,** 2361–2380 (2017).
108. Patil, M., Pabla, N. & Dong, Z. Checkpoint kinase 1 in DNA damage response and cell cycle regulation. *Cell. Mol. Life Sci.* **70,** 4009–4021 (2013).
109. Gan, W. *et al.* R-loop-mediated genomic instability is caused by impairment of replication fork progression. *Genes Dev.* **25,** 2041–2056 (2011).
110. Pommier, Y., Sun, Y., Huang, S.-Y. N. & Nitiss, J. L. Roles of eukaryotic topoisomerases in transcription, replication and genomic stability. *Nat. Rev. Mol. Cell Biol.* **17,** 703–721 (2016).
111. Regairaz, M. *et al.* Mus81-mediated DNA cleavage resolves replication forks stalled by topoisomerase I-DNA complexes. *J. Cell Biol.* **195,** 739–749 (2011).
112. Martín, M., Terradas, M., Tusell, L. & Genescà, A. ATM and DNA-PKcs make a complementary couple in DNA double strand break repair. *Mutat. Res. - Rev. Mutat. Res.* **751,** 29–35 (2012).
113. Benada, J. & Macurek, L. Targeting the checkpoint to kill cancer cells. *Biomolecules* **5,** 1912–1937 (2015).
114. Kim, E. G. & Kim, K. M. Strategies and Advancement in Antibody-Drug Conjugate Optimization for Targeted Cancer Therapeutics. **23,** 493–509 (2015).
115. Panowski, S., Bhakta, S., Raab, H., Polakis, P. & Junutula, J. R. Site-specific antibody drug conjugates for cancer therapy. *MAbs* **6,** 34–45 (2014).
116. Ducry, L. *Antibody-Drug Conjugates*. (Humana Press, 2013). doi:10.1007/978-1-62703-541-5
117. Junutula, J. R. *et al.* Site-specific conjugation of a cytotoxic drug to an antibody improves the therapeutic index. *Nat. Biotechnol.* **26,** 925–32 (2008).
118. Poison, A. G. *et al.* Antibody-drug conjugates for the treatment of non-Hodgkin's lymphoma: Target and linker-drug selection. *Cancer Res.* **69,** 2358–2364 (2009).
119. de Goeij, B. E. C. G. & Lambert, J. M. New developments for antibody-drug conjugate-based therapeutic approaches. *Curr. Opin. Immunol.* **40,** 14–23 (2016).
120. Brody, T. *Clinical Trials: Study Design, Endpoints and Biomarkers, Drug Safety, and FDA and ICH Guidelines*. (Elsevier Inc., 2016).
121. Popp, M. W.-L. & Ploegh, H. L. Making and breaking peptide bonds: protein engineering using sortase. *Angew. Chem. Int. Ed. Engl.* **50,** 5024–5032 (2011).

122. Healthcare, G. E. *Affinity Chromatography - Principles and Methods*. (2007).
123. Scientific, T. Novel Hydrophobic Interaction HPLC Columns. 1–8 (2016). Available at: https://tools.thermofisher.com/content/sfs/brochures/BR-21089-MAbPac-HIC-BR21089-EN.pdf.
124. Brand, T. M. *et al.* Nuclear EGFR as a molecular target in cancer. *Radiother. Oncol.* **108,** 370–377 (2013).
125. Liu, X. *et al.* Homologous recombination as a resistance mechanism to replication-induced double-strand breaks caused by the antileukemia agent CNDAC. *Blood* **116,** 1737–1746 (2010).
126. Melorose, J. *et al.* DNA repair pathways as targets for cancer therapy. *Nat Rev Cancer* **14,** 1291–1295 (2008).
127. Davidson, D., Amrein, L., Panasci, L. & Aloyz, R. Small molecules, inhibitors of DNA-PK, targeting DNA repair, and beyond. *Front. Pharmacol.* **4,** 1–7 (2013).
128. Zhang, Z. *et al.* Reversing drug resistance of cisplatin by hsp90 inhibitors in human ovarian cancer cells. *Int. J. Clin. Exp. Med.* **8,** 6687–6701 (2015).
129. Niedernhofer, L. J. *et al.* The structure-specific endonuclease Ercc1-Xpf is required to resolve DNA interstrand cross-link-induced double-strand breaks. *Mol. Cell. Biol.* **24,** 5776–87 (2004).
130. Selleck Chemicals. Inhibitor catalog. (2015).
131. van Gent, D. C. & Kanaar, R. Exploiting DNA repair defects for novel cancer therapies. *Mol. Biol. Cell* **27,** 2145–8 (2016).
132. Panagiotis A. Konstantinopoulos, Raphael Ceccaldi, G. I. & Shapiro, A. D. D. Homologous recombination deficiency: Exploiting the fundamental vulnerability of ovarian cancer. *Cancer Discov.* **5,** 1137–1154 (2016).
133. Ronco, C., Martin, A. R., Demange, L. & Benhida, R. ATM, ATR, CHK1, CHK2 and WEE1 inhibitors in cancer and cancer stem cells. *Med. Chem. Commun.* **8,** 295–319 (2017).
134. Whelligan, D. K. *et al.* Aminopyrazine inhibitors binding to an unusual inactive conformation of the mitotic kinase Nek2: SAR and structural characterization. *J. Med. Chem.* **53,** 7682–7698 (2010).
135. Liu, S., Ho, C. K., Ouyang, J. & Zou, L. Nek1 kinase associates with ATR-ATRIP and primes ATR for efficient DNA damage signaling. *Proc. Natl. Acad. Sci. U. S. A.* **110,** 2175–80 (2013).
136. Xu, Z. D., Wang, M., Xiao, S. L. & Yang, M. Novel peptide derivatives of bleomycin A5: Synthesis, antitumor activity and interaction with DNA. *Bioorganic Med. Chem. Lett.* **15,** 3996–3999 (2005).
137. Gentry, A. C. *et al.* Interactions between the etoposide derivative F14512 and human type II topoisomerases: Implications for the C4 spermine moiety in promoting enzyme-mediated DNA cleavage. *Biochemistry* **50,** 3240–3249 (2011).
138. Yan, Y. *et al.* A novel function of HER2/Neu in the activation of G2/M checkpoint in response to γ-irradiation. *Oncogene* **34,** 2215–2226 (2014).
139. Wang, Y.-N. *et al.* Nuclear functions and subcellular trafficking mechanisms of the epidermal growth factor receptor family. *Cell Biosci.* **2,** 1–10 (2012).

140. Roossien, D. H., Miller, K. E. & Gallo, G. Ciliobrevins as tools for studying dynein motor function. *Front. Cell. Neurosci.* **9,** 1–10 (2015).

141. Poruchynsky, M. S. *et al.* Microtubule-targeting agents augment the toxicity of DNA-damaging agents by disrupting intracellular trafficking of DNA repair proteins. *Proc. Natl. Acad. Sci. U. S. A.* **112,** 1571–6 (2015).

142. Lambert, S. & Carr, A. M. Checkpoint responses to replication fork barriers. *Biochimie* **87,** 591–602 (2005).

143. Mullins, E. A., Shi, R. & Eichman, B. F. Toxicity and repair of DNA adducts produced by the natural product yatakemycin. *Nat. Chem. Biol.* **13,** 1002–1010 (2017).

144. Selby, C. P. & Sancar, A. ABC Excinuclease Incises both 5' and 3' to the CC-1065-DNA Adduct and Its Incision Activity Is Stimulated by DNA Helicase II and DNA Polymerase I. *Biochemistry* **19,** 7184–7188 (1988).

145. Gunz, D., Hess, M. T. & Naegeli, H. Recognition of DNA Adducts by Human Nucleotide Excision Repair. *J. Biol. Chem.* **271,** 25089–25098 (1996).

146. Beck, C., Robert, I., Reina-San-Martin, B., Schreiber, V. & Dantzer, F. Poly(ADP-ribose) polymerases in double-strand break repair: Focus on PARP1, PARP2 and PARP3. *Exp. Cell Res.* **329,** 18–25 (2014).

147. Kiakos, K. *et al.* DNA sequence – selective adenine alkylation, mechanism of adduct repair, and in vivo antitumor activity of the novel achiral seco-amino-cyclopropylbenz[e]indolone analogue of duocarmycin AS-I-145. *Mol. Cancer Ther.* **6,** 2708–2719 (2007).

148. Liu, J., Kuo, S., Beerman, T. A. & Melendy, T. Induction of DNA Damage Responses by Adozelesin Is S Phase-specific and Dependent on Active Replication Forks. *Cancer Res.* **2,** 41–47 (2003).

149. Wortmann, L. *et al.* 2-(MORPHOLIN-4-YL)-L,7-NAPHTHYRIDINES. 1–508 (2016).

150. Pastor Fernández, J., Fernández-Capetillo Ruiz, O, Martínez González, S., Blanca Aparicio, C., Rico Ferreira, M., Toledo Lázaro, L. I., Rodríguez Arísteguí, S., Murga Costa, M., Varela Busto, C., Lopes Contreras, A. J., Renner, O., Nieto Soler, M., Cebriá, D. A. International Patent No. WO 2014/140644 A1. 1–152 (2014).

151. Kawasumi, M. *et al.* Identification of ATR-Chk1 pathway inhibitors that selectively target p53-deficient cells without directly suppressing ATR catalytic activity. *Cancer Res.* **74,** 7534–7545 (2014).

152. Picture of black 384-well plate. Available at: http://www.nexcelom.co.uk/celigo/CL_01_single-colony-identification.php%0A. (Accessed: 1st August 2018)

153. Muller, P. Y. & Milton, M. N. The determination and interpretation of the therapeutic index in drug development. *Nat. Rev. Drug Discov.* **11,** 751–761 (2012).

154. Ritz, C., Baty, F., Streibig, J. C. & Gerhard, D. Dose-response analysis using R. *PLoS One* **10,** 1–13 (2015).

155. King, C. *et al.* Characterization and preclinical development of LY2603618: A selective and potent Chk1 inhibitor. *Invest. New Drugs* **32,** 213–226 (2014).

156. Zabludoff, S. D. *et al.* AZD7762, a novel checkpoint kinase inhibitor, drives checkpoint abrogation and potentiates DNA-targeted therapies. *Mol. Cancer Ther.* **7,** 2955–2966 (2008).

157. Sato, A. *et al.* A novel class of in vivo active anticancer agents: Achiral seco-amino- and seco-hydroxycyclopropylbenz[e]indolone (seco-CBI) analogues of the duocarmycins and CC-1065. *J. Med. Chem.* **48,** 3903–3918 (2005).

158. Ham, Y. & Boger, D. L. A Powerful Selection Assay for Mixture Libraries of DNA Alkylating Agents. *J. Am. Chem. Soc.* **126,** 9194–9195 (2004).

159. Cristofanilli, M. *et al.* Phase II study of adozelesin in untreated metastatic breast cancer. *Anticancer. Drugs* **9,** 779–82 (1998).

160. Vendetti, F. P. *et al.* The orally active and bioavailable ATR kinase inhibitor AZD6738 potentiates the anti-tumor effects of cisplatin to resolve ATM-deficient non-small cell lung cancer <i>in vivo</i> *Oncotarget* **6,** 44289–44305 (2015).

161. Cardillo, T. M. *et al.* Synthetic lethality exploitation by an anti-Trop-2-SN-38 antibody-drug conjugate, IMMU-132, plus PARP-inhibitors in BRCA1/2-wild-type triple-negative breast cancer - Supplementary Information. *Clin. Cancer Res.* **23,** 3405–3416 (2017).

162. He, J., Kang, X., Yin, Y., Clifford Chao, K. S. & Shen, W. H. PTEN regulates DNA replication progression and stalled fork recovery. *Nat. Commun.* **6,** 1–11 (2015).

163. Feng, J. *et al.* PTEN Controls the DNA Replication Process through MCM2 in Response to Replicative Stress. *Cell Rep.* **13,** 1295–1303 (2015).

164. Qiu, Z., Oleinick, N. L. & Zhang, J. ATR/CHK1 inhibitors and cancer therapy. *Radiother. Oncol.* **126,** 450–464 (2018).

165. Jossé, R. *et al.* ATR inhibitors VE-821 and VX-970 sensitize cancer cells to topoisomerase I inhibitors by disabling DNA replication initiation and fork elongation responses. *Cancer Res.* **74,** 6968–6978 (2014).

166. Thomas, A. *et al.* Phase I Study of ATR Inhibitor M6620 in Combination With Topotecan in Patients With Advanced Solid Tumors. *J. Clin. Oncol.* **36,** 1594–1602 (2017).

167. Oflazoglu, E., Kissler, K. M., Sievers, E. L. & Grewal, I. S. Combination of the anti-CD30-auristatin-E antibody-drug conjugate (SGN-35) with chemotherapy improves antitumour activity in Hodgkin lymphoma. *Br. J. Cancer* **142,** 69–73 (2008).

168. Ricart, A. D. Antibody-drug conjugates of calicheamicin derivative: Gemtuzumab ozogamicin and inotuzumab ozogamicin. *Clin. Cancer Res.* **17,** 6417–6427 (2011).

169. Chang, C.-H. *et al.* Combining ABCG2 Inhibitors with IMMU-132, an Anti-Trop-2 Antibody Conjugate of SN-38, Overcomes Resistance to SN-38 in Breast and Gastric Cancers. *Mol. Cancer Ther.* **15,** 1910–9 (2016).

170. Cardillo, T. M. *et al.* Synthetic Lethality Exploitation by an Anti–Trop-2-SN-38 Antibody–Drug Conjugate, IMMU-132, Plus PARP Inhibitors in BRCA1/2–wild-type Triple-Negative Breast Cancer. *Clin. Cancer Res.* **23,** 3405–3416 (2017).

171. Adams, S. *et al.* IMGN779, a Next Generation CD33-Targeting ADC, Combines Effectively with Cytarabine

in Acute Myeloid Leukemia (AML) Preclinical Models, Resulting in Increased DNA Damage Response, Cell Cycle Arrest and Apoptosis In Vitro and Prolonged. *Blood* **130,** 1357 LP-1357 (2017).

172. Fritz, C., Portwood, S. M., Adams, J. & Wang, E. S. Abstract 2820: Synergistic antileukemic activity of the antibody-drug conjugate (IMGN779) combined with PARP inhibition in preclinical human acute myeloid leukemia models. *Cancer Res.* **78,** 2820 LP-2820 (2018).
173. Portwood, S., Puchalski, R. A., Walker, R. M. & Wang, E. S. Combining IMGN779, a Novel Anti-CD33 Antibody-Drug Conjugate (ADC), with the PARP Inhibitor, Olaparib, Results in Enhanced Anti-Tumor Activity in Preclinical Acute Myeloid Leukemia (AML) Models. *Blood* **128,** 1645 LP-1645 (2016).
174. Fu, J. *et al.* Drug combination in vivo using combination index method : Taxotere and T607 against colon carcinoma HCT-116 xenograft tumor in nude mice. *Synergy* **3,** 15–30 (2016).
175. O'Carrigan, B. *et al.* Phase I trial of a first-in-class ATR inhibitor VX-970 as monotherapy (mono) or in combination (combo) with carboplatin (CP) incorporating pharmacodynamics (PD) studies. *J. Clin. Oncol.* **34,** 2504 (2016).
176. Dillon, M. T. *et al.* Abstract CT084: A Phase I dose-escalation study of ATR inhibitor monotherapy with AZD6738 in advanced solid tumors (PATRIOT Part A). *Cancer Res.* **77,** CT084--CT084 (2017).
177. Mak, M. S. & Hk, K. COMBINATIONS OF AN ANTI-HER2 ANTIBODY-DRUG CONUGATE AND CHEMOTHERAPEUTICAGENTS, AND METHODS OF USE. 1–54 (2009). doi:10.1371/journal.pone.A61P
178. Cao, P., Mchugh, M. M., Melendy, T. & Beerman, T. The DNA Minor Groove-alkylating Cyclopropylpyrroloindole Drugs Adozelesin and Bizelesin Induce Different DNA Damage Response Pathways in Human Colon Carcinoma HCT116 Cells. *Mol. Cancer Ther.* **2,** 651–659 (2003).
179. Ward, I. M. & Chen, J. Histone H2AX Is Phosphorylated in an ATR-dependent Manner in Response to Replicational Stress. *J. Biol. Chem.* **276,** 47759–47762 (2001).
180. Liu, J. S., Kuo, S. R. & Melendy, T. Comparison of checkpoint responses triggered by DNA polymerase inhibition versus DNA damaging agents. *Mutat. Res. - Fundam. Mol. Mech. Mutagen.* **532,** 215–226 (2003).
181. Couch, F. B. *et al.* ATR phosphorylates SMARCAL1 to prevent replication fork collapse. *Genes Dev.* **27,** 1610–1623 (2013).
182. Cuella-Martin, R. *et al.* 53BP1 Integrates DNA Repair and p53-Dependent Cell Fate Decisions via Distinct Mechanisms. *Mol. Cell* **64,** 51–64 (2016).
183. Williamson, C. T. *et al.* ATR inhibitors as a synthetic lethal therapy for tumours deficient in ARID1A. *Nat. Commun.* **7,** 1–13 (2016).
184. Kim, H. *et al.* Anti-tumor activity of the ATR inhibitor AZD6738 in HER2 positive breast cancer cells. *Int. J. Cancer* **140,** 109–119 (2017).
185. Walker, M. A. *et al.* Monoclonal antibody mediated intracellular targeting of tallysomycin S 10b.

Bioorganic Med. Chem. Lett. **14,** 4323–4327 (2004).

186. Dittmann, K. *et al.* Radiation-induced epidermal growth factor receptor nuclear import is linked to activation of DNA-dependent protein kinase. *J. Biol. Chem.* **280,** 31182–31189 (2005).

187. Bouquet, F. *et al.* A DNA-dependent stress response involving DNA-PK occurs in hypoxic cells and contributes to cellular adaptation to hypoxia. *J. Cell Sci.* **124,** 1943–1951 (2011).

188. Hall, A. B. *et al.* Potentiation of tumor responses to DNA damaging therapy by the selective ATR inhibitor VX-970. *Oncotarget* **5,** 5674–85 (2014).

189. Cilliers, C., Menezes, B., Nessler, I., Linderman, J. & Thurber, G. M. Improved tumor penetration and single-cell targeting of antibody–drug conjugates increases anticancer efficacy and host survival. *Cancer Res.* **78,** 758–768 (2018).

190. Ubink, R. *et al.* Unraveling the interaction between carboxylesterase 1c and the antibody-drug conjugate SYD985: improved translational PKPD by using CES1c knockout mice. *Mol. Cancer Ther.* molcanther.0329.2018 (2018). doi:10.1158/1535-7163.MCT-18-0329

8.2. List of figures

8.3. Abbreviations

$(G_4S)_3$	Linker consisting of trice the sequence glycylglycylglycylglycylseryl
°C	Degree celsius
α	alpha
µ	Micro
µg	Microgram
µM	micromolar
2xTY	Medium consisting of tryptone and yeast extract
4PL	4-point logistic, fitting function
9-1-1	Rad9-Hus1-Rad1
ABVD	doxorubicin, bleomycin, vinblastine, dacarbazine
ADC	Antibody drug conjugate
ADCC	Antibody-dependent cell-mediated cytotoxicity
Ala	alanine
ALL	Acute lymphoblastic leukemia
ATM	ataxia-telangiectasia mutated
ATR	Ataxia telangiectasia and Rad3 related
ATRIP	Ataxia telangiectasia and Rad3 related-interacting protein
AU	Alkylating unit
BA5	Bleomycin A5
BER	Base-excision repair
BU	Binding unit
C	Cetuximab
$CaCl_2$	Calcium chloride
CBI	Chloromethylbenzindoline
CCLE	Cancer Cell Line Encyclopedia
CEA	carcinoembryonic antigen
C_H1	Constant domain 1 of the heavy chain
C_H2	Constant domain 2 of the heavy chain
C_H3	Constant domain 3 of the heavy chain
CHK1	Checkpoint kinase 1
CI	Combination index
Cit	citrulline
C_L	Constant domain of the light chain

CML	chronic myleoid leukaemia
CNIO	Spanish National Cancer Research Centre
D	Dose
D_A	Dose of drug A
DAR	Drug to antibody ratio
D_B	Dose of drug B
DDM	Duocarmycin DM
DDR	DNA-damage response
DDRi	DNA-damage response inhibitor
D_m	IC_{50}
DMEM	Dulbecco's Modified Eagle's Medium
DNA	Deoxyribonucleic acid
DNA-PK	DNA-dependent protein kinase
DRC	Dose-response curve
DRI	Dose-reduction index
DSA	Duocarmycin SA
DSB	Double-strand break
DTA	DNA-targeting agent
DTT	Dithiothreitol
Dx	Dose of a drug in combination to achieve the same effect as if given as single agent
EGFR	Epidermal Growth Factor Receptor
eq.	Equivalents
eq.	equation
eSrtA	Evolved Sortase A
ETAA1	Ewing's tumor-associated antigen 1
fa	Fraction affected
Fab	Fragment antigen binding
Fc	Fragment crystalline
FCS	Fetal calf serum
FDA	Food and Drug Administration
fu	Fraction unaffected
g	Gravitational constant
G1	Growth phase 1
G2	Growth phase 2
h	Hour

HSA	Human serum albumin
HC	Heavy chain
HCl	Hydrochloride
HEL	Hen Egg Lysozyme
HEPES	(4-(2-hydroxyethyl)-1-piperazineethanesulfonic acid)
HER2	human epidermal growth factor receptor 2
HIC	Hydrophobic interaction chromatography
HMW	High molecular weight
HRR	Homologous recombination repair
Hus1	Checkpoint protein HUS1
i	Inhibitor
IBD	indilino-benzodiazepine
IC_{50}	Half-maximum inhibitory effect
IgG	Immunoglobulin G
IPTG	Isopropyl-*β*-D-thiogalactopyranosid
iv	intravenous
k	kilo
kg	Kilogram
L	Liter
LC	Light chain
LD	Linker-drug
LDS	Laureate dodecyl sulfate
Lys	Lysine
m	Milli
M	molar
mAb	Monoclonal antibody
mCRC	Metastatic colorectal cancer
MEE	Median-effect equation
MET	Mesenchymal-epithelial transition
mg	Milligram
MGB	Minor-groove binder
min	Minutes
mM	Millimolar
MMAE	Monomethyl auristatin E
MMAF	Monomethyl auristatin F

MMR	Mismatch repair
MNED	Maximum non-efficacious dose
MRN	MRN-complex consisting of MRE11, Rad50 and Nibrin
MTA	Microtubule-targeting agents
MTD	Maximum tolerated dose
MTH1	MutT homologue 1
mut	Mutated
n	Nano
N	Number, in the context of this work often number of individual experiments
N.A.	Not available
N/E	No effect
Na_2HPO_4	Disodium hydrogen phosphate
NaCl	Sodium chloride
NaH_2PO_4	Sodium dihydrogen phosphate
NER	Nucleotide excision repair
NFR	Nucleosome free region
NHEJ	Non-homologous end joining
NHL	Non-hodgkin lymphoma
nm	Nanometer
NMR	Nuclear magnetic resonance
OD_{600}	Optical density at a wavelength of 600 nm
ORC	Origin recognition complex
p	Pico
P	P value for statistical analysis
p53BP1	p53 binding protein 1
PAB	*para*-aminobenzyl moiety
PAGE	Poly amide gel electrophoresis
PBD dimer	Pyrrolobenzodiazepine dimer
PD-1	Programmed cell death protein 1
PD-L1	Programmed death ligand 1
PI3K	Phosphoinositide 3-kinase
PIKK	Phosphatidylinositol 3-kinase-related kinase
Pre-RC	Pre replication complex
qd	Quaque die, latin for every day
qPCR	Quantitative polymerase chain reaction

Rad1	DNA-damage protein Rad1
Rad51	Recombinase Rad51
Rad9	DNA-damage protein Rad9
rcf	Relative centrifugal force
R-CVP	Rituximab, cyclophosphamide, vincristine, prednisolone
rer. nat.	rerum naturalium
R-GDP	rituximab, gemcitabine, dexamethasone, cisplatin
RNA	Ribonucleic acid
RPA	Replication protein A
Rpm	Rounds per minute
rpm	Rounds per minute
RPMI-1640	Roswell Park Memorial Institute
RT	Room temperature
RTK	Receptor tyrosine kinase
S	Synergy score
sd	Single dose
SDS	Sodium dodecyl sulfate
SEC	Size-exclusion chromatography
SEED	Strand exchange engineered domain
Ser	Serine
SI	Selectivity index
siRNA	Small interfering RNA
SMCC	succinimidyl 4-(N-maleimidomethyl)cyclohexane-1-carboxylate
SN-38	Active metabolite of irinotecan, topoisomerase I inhibitor
SOC	Super Optimal Broth
SRF	Stalled replication fork
SrtA	Sortase A
SSB	Single strand break
T	Temperature
TMI	Trimethody indole
tol	Tolerated
TOP1	Topoisomerase 1
TOP2	Topoisomerase 2
TOPBP1	DNA topoisomerase 2-binding protein 1
Tris	Tris(hydroxymethyl)-aminomethan

V	Volt
val	Valine
V_H	Variable domain of the heavy chain
V_L	Variable domain of the light chain
XLF	XRCC1-like factor

8.4. Acknowledgements

Zunächst möchte ich Prof. Dr. Harald Kolmar für die Betreuung meiner Doktorarbeit an der TU Darmstadt herzlich danken. Besonders hilfreich waren auch die beiden Ausflüge ins Kleinwalsertal. Nicht nur wegen der Möglichkeit sich den ganzen Tag beim Wandern oder Snowboarden auszutoben, sondern auch um den Kontakt und den wissenschaftlichen Austausch zwischen den Doktoranden zu verbessern.

Prof. Dr. Felix Hausch möchte ich für die Übernahme des Koreferats danken. Außerdem möchte ich Prof. Dr. Boris Schmidt sowie Prof. Dr. Löbrich dafür danken, dass sie Fachprüfer meine Disputation waren. Prof. Dr. Michael Reggelin möchte ich dafür danken, dass er den Prüfungsvorsitz meiner Dispuation übernommen hat.

Dank gilt auch Dr. Björn Hock, Dr. Jan Anderl und Dr. Stefan Hecht, die mir die Promotion in diesem spannenden Forschungsfeld bei Merck erst ermöglicht haben.

Ich möchte ganz herzlich Dr. Nicolas Rasche für die Betreuung meiner Doktorarbeit bei Merck danken. Die Aufnahme in sein Labor, sein fachlicher Rat sowie seine Unterstützung, aber auch die Ermahnung mich zu fokussieren (☺), haben maßgeblich zum Erfolg dieser Arbeit beigetragen.

Weiterhin möchte ich dem gesamten Labor Rasche danken für Tips&Tricks zum Thema Konjugation und Proteinaufreinigung, das troubleshooting sowie die lockere Laboratmosphäre: Ingrid Schmidt, Jens Hannewald, Vanessa Waschk und Dr. Stephan Dickgießer.

Außerdem möchte ich Dr. Carl Deutsch für die interessanten Diskussionen, konzeptionellen Vorschläge und die Unterstützung meiner Projekte danken.

Des Weiteren möchte ich Dr. Carl Deutsch und Dr. Min Shan sowie den Chemikerinnen Antje Schöneberg, Hélène Crassier, Mirela Kunkel und Katrin Peschk für die Synthese der Duocarmycine sowie der linker-drugs danken. Und natürlich möchte ich für das Abgeben meiner Inhibitoren in die Dispensary danken.

Hélène Crassier und Mirela Kunkel möchte ich außerdem für die gemeinsame Zeit bei unseren unterhaltsamen Mittagspausen und Teamevents danken!

Katrin Peschk und Dr. Tim Knehans möchte ich weiterhin danken für unser kleines gemeinsames Projekt, das mich fachlich weit vorangebracht hat. Danke für die Synthesen an Katrin Peschk und das Modeling sowie die vielen Erklärungen an Dr. Tim Knehans.

Besonderen Dank möchte ich allen aussprechen, die am „Sahnehäubchen“ dieser Dissertation beteiligt waren: Dr. Jan Anderl und Dr. Stefan Hecht für das initiieren des Versuchs, Dr. Carl Deutsch und seinem Labor für die Synthese des Linker-Drugs und Dr. Nicolas Rasche, Jens Hannewald und Vanessa Waschk für die Konjugation des ADCs. Besonderer Dank gilt an dieser Stelle Dr. Ana Hecht für die Planung und Beaufsichtigung der Studie sowie Louisa Hüttel für die Durchführung der Studie.

Danke auch an Dr. Roland Kellner und die Mitglieder seines Labors Amanda Vanselow, Jennifer Schanz und Jason Tonillo für die MS-Analysen.

Ich möchte Marie Quillmann, Sebastian Jäger und Dr. Doreen Könning besonderen Dank aussprechen. Die erfrischenden Kaffeepausen und auch die vielen Diskussionen haben mir beim Anfertigen meiner Arbeit geholfen. Großen Dank für das Korrekturlesen meiner Arbeit!

Dr. Claudio Lademann möchte ich für die spannenden Diskussionen beim gemeinsamen Mittagessen danken.

Außerdem möchte ich Dr. Achmim Doerner für die interessanten Diskussionen danken. Ein Dankeschön an Dr. Carolin Sellmann, die mir immer mit Rat und Tat zur Seite stand.

Ich möchte Dr. Stefan Becker für die Benutzung seines Labors und der Geräte danken. Ohne ihn hätte ich nicht so viel Zeit vor der Flow verbringen können. Außerdem möchte ich Deniz Demir, Iris Willenbücher, Kerstin Hallstein für die Unterstützung in der Zellkultur danken. Ohne Stefan und sein Labor wäre die Arbeit nicht möglich gewesen, da sie immer meine Pakete angenommen haben („Da ist ein Totenkopf drauf, das muss für den Marcel sein!“).

Danken möchte ich auch Dr. Birgit Piater und ihrem Labor, dafür, dass ich Labor und Geräte nutzen durfte. Kirsten Leidinger und Dr. Stanley Sweeney-Lasch möchte ganz besonders danken für das Teilen ihres know-hows und ihre Unterstützung bei meinen Zellassays.

Danken möchte ich auch Elke Ciesielski, Dominik Reitz, Daniela Noack, Konstanze Waurisch, Angelika Helfrich, Christina Bauer, Sonja Dreher, Marion Wetter, Nils Bahl, Anja Lamack, Vanessa Lautenbach, Gernot Musch, Pia Stroh, Ramona Gaa für ihre Unterstützung im Laboralltag durch!

Des Weiteren möchte ich vielen Leuten bei Merck danken, die direkt oder indirekt an meiner Arbeit beteiligt waren, sei es durch Bereitstellung von Chemikalien, Analysen oder fachlichen Rat: Dr. Heike Dahmen, Dr. Simon Krah, Dr. Stefan Zielonka, Dr. Christian Schröter, Dr. Mireille Krier, Dr. Lars Toleikis, Dr. Christiane Amendt, Claudio Ritzert, Matthias Heil, Tanja Flachsel, Nicole Hölzer, Dr. Oscar Ortiz, Antje Ehring, Manuela Meurisch, Astrid Zimmermann, Frank Zenke, Ralf Günther, Dr. Mark Schuette, Florian Gross, Alexander Müller, Stephan Keller, Dirk Müller-Pompalla, Marion Sauer, Oliver Edler, Selma Bozkurt, Sigrid Auth, Steffen Rindfuss, Teresa Gorgol, Dr. Vanessa Siegmund, Jan Baumann, Michael Hofmann, Lars zur Bruegge, Pascal Simon, Maic Seegel, Dr. Christina Esdar, Dr. Christine Siegl, Julia Rolf, Sabrina Eisenblätter, Jutta Welge, Stefanie Gaus und Elvira Meissen.

Außerdem möchte ich den Doktoranden, der „TUD-Exklave“ bei Merck danken für die netten Mittagessen sowie wissenschaftlichen Austausch: Anna Kaempffe, Janis Rosskopf, Tim Hofmann, Sandra Müller, Martina Zimmermann, Markus Lubda, Greg Som und Lukas Roth.

Ich danke herzlich den aktuellen und ehemaligen AK-Kolmar Mitgliedern für die Gespräche und die entspannte Zeit bei Seminaren und Konferenzbesuchen. Vielen Dank an Dr. Thomas Pirzer. Bei unseren gemeinsamen Wanderungen kam schon die ein oder andere Erkenntnis! Großer Dank gilt auch Barbara Diestelmann für die organisatorische Hilfe!

Danken möchte ich auch Dr. Bernhard Seehaus, Dr. Fiona Bessoth und Dr. Claudia Blank für das Betreuen meiner Arbeit von patentrechtlicher Seite aus.

Ich danke an dieser Stelle meinen Eltern Silvia und Michael und meinen Schwestern Lena, Jasmin und Franziska aber auch meinen Freunden, da sie immer für mich da waren.
Zu guter letzt danke ich ganz besonders meiner Frau Anna für ihre Unterstützung. Sie hat mich immer motiviert und mir Rückhalt gegeben, wodurch diese Arbeit erst möglich geworden ist.

8.5. Curriculum Vitae

Marcel Tassilo Rieker
Heidelberger Str. 8
64283 Darmstadt
+49 176-43486156
marcel.t.rieker@gmail.com

Date of birth	11/07/1989
Place of birth	Bad Nauheim
Marital status	married
Nationality	German

ACADEMIC STUDIES

10/2015 – present day	**Technische Universität Darmstadt** Doctorate in biochemistry in collaboration with Merck KGaA, ADCs and Targeted NBE Therapeutics, Darmstadt under the supervision of Prof. Dr. Kolmar
10/2013 – 09/2015	**Technische Universität Darmstadt** Master of Science in Chemistry (equivalent to Chemical Engineer), Specialization: Biochemistry, Organic Chemistry and Technical Chemistry (Final grade 1.3) Master thesis in the department Protein Engineering and Antibody Technologies, Merck KGaA, Darmstadt: "Tailor-made antibody-drug conjugates: Hybrid ADCs *via* orthogonal biocatalysis" (Final grade 1.0)
10/2010 – 09/2013	**Technische Universität Darmstadt** Bachelor of Science in Chemistry (Final grade 1.8) Bachelor thesis: "Development of a Modular System for the Intracellular Delivery and Release of Bioactive Peptides" (Final grade 1.3)
09/2000 – 06/2009	**Augustinerschule, Friedberg** Abitur, Specialization: Mathematics and Chemistry (Final grade 1.9)

Darmstadt, **Error! Reference source not found.**

_____

Marcel Rieker

9. Affirmations

Marcel Rieker

ource not found.

Heidelberger Str. 8

64283 Darmstadt

Darmstadt, **Error! Reference s**

Erklärung

Ich erkläre hiermit, dass ich meine Dissertation selbstständig und nur mit den angegebenen Hilfsmitteln angefertigt habe.

_____

Marcel Rieker

Marcel Rieker
ource not found.
Heidelberger Str. 8
64283 Darmstadt

Darmstadt, **Error! Reference s**

Erklärung

Ich erkläre hiermit, noch keinen Promotionsversuch unternommen zu haben.

_____

Marcel Rieker

Marcel Rieker
ource not found.
Heidelberger Str. 8
64283 Darmstadt

Darmstadt, **Error! Reference s**

Erklärung

Ich erkläre hiermit, dass die elektronische Version der Doktorarbeit mit der schriftlichen Version übereinstimmt. Die elektronische Version liegt dem Prüfungssekretariat vor.

_____

Marcel Rieker